Université de Strasbourg

École Doctorale de Physique et Chimie – Physique (ED182)
Institut de Physique et Chimie des Matériaux de Strasbourg
(IPCMS, UMR – CNRS Unistra 7504)

THÈSE présentée par

Catalina BORDEIANU

soutenue le : 29 Septembre 2016

co-tutelle

pour obtenir le grade de : **Docteur de l'Université de Strasbourg**
Discipline / Spécialité : Chimie Organique

Discipline : Physique et chimie physique

Ingénierie d'architectures dendritiques pour la résolution de problématiques de Nanomédecine – biodistribution, toxicité, pharmacocinétique ou ciblage actif

Thèse dirigée par :		
	Dr. Delphine Felder–Flesch	IPCMS – CNRS, Strasbourg
	Dr. Sophie Laurent	Université de Mons, Belgique
Rapporteurs :		
	Dr. Jean–Michel Chezal	INSERM, Clermont–Ferrand
	Dr. Fabienne Gauffe	Université de Rennes 1, Rennes
Membres Invités :		
	Prof. Luce Vander Elst	Université de Mons, Belgique
	Prof. Robert N. Muller	Université de Mons, Belgique
	Prof. Laetitia Mespouilles	Université de Mons, Belgique
	Prof. Sylvie Begin–Colin	IPCMS, ECPM, Strasbourg

"A scientist in his laboratory is not a mere technician: he is also a child confronting natural phenomena that impress him as though they were fairy tales."

Marie Curie

Acknowledgments

Si le doctorant doit faire ses preuves, seul, par sa thèse, il n'en reste pas moins qu'il est entouré de personnes extraordinaires. La liste est longue et, bien que je me souvienne exactement de tout ce qu'elles ont su m'apporter, il reste la difficulté de ne pas pouvoir tous les citer ici. J'aimerais remercier par avance, ceux dont le nom n'est pas dans cet écrit.

Ensuite, je souhaite exprimer en premier lieu ma profonde gratitude pour les Dr. Delphine Felder Flesch et Dr. Sophie Laurent, directrices de cette thèse. Je n'aurais pu avancer dans mes travaux sans leur regard critique, pertinent et juste.

Je remercie également les membres du jury, le Dr. Fabienne Gauffre, le Pr. Laeticia Mespouilles et le Pr. Luce Vander Elst pour avoir su trouver le temps d'évaluer mes recherches. Le Dr. Jean-Michel Chezal qui m'a soutenue dans les études de radiomarquages et le Pr. Robert M. Muller qui m'a accompagné dans mes recherches méritent une distinction particulière. C'est à ce même titre que je remercie chaleureusement le Pr. Sylvie Begin-Colin pour sa participation importante dans la synthèse des nanoparticules. Merci à vous.

Je ne saurai oublier le Dr. Elisabeth Miot-Noirault, la platforme AgroResonance, ainsi que le Dr. Jean Luc Perrot, le Dr. Bruno Labeille, le Dr. Elisa Cinotti et le Dr. Sebastien Boutry. Eux-même m'ont permis d'enrichir mes travaux aux travers de leurs études IRM *in vivo* et *ex vivo* en microscopie confocale. Une mention particulière pour toi, Sébastien, car au delà de ton aide pour mes recherches, ta sympathie et ton soutien m'ont beaucoup apporté.

Le Pr. Florent Meyer et Mme. Christine Affolter-Zbaraszczuk. Une partie importante de ce manuscrit n'aurait jamais pu voir le jour sans vous et sans vos explications sur la culture *in vitro* et les interactions cellulaires avec mes produits. Merci au Dr. Carmen Burtea, merci au Dr. Céline Henoumont pour votre investissement dans les études *in vitro* et les analyses HR-Mas RMN. Je retiens de vous une très bonne collaboration, riche et extrêment formatrice.

Je remercie aussi M. Dris Ihiawakrim pour son aide dans la production des images TEM et notamment pour ses efforts de s'être rendu disponible.

Enfin, je souhaite remercier le Pr. Laurent Douce de m'avoir permis de mener mes recherches au sein de son département.

Il est certain qu'aucun mot ne saura exprimer toute ma gratitude à votre égard. Vos contributions et vos enseignements n'ont pas seulement été nécessaires, mais ont également intensifié en moi la passion de la recherche scientifique. Ainsi, j'ose espérer que ma thèse saura être un remerciement digne de ce que vous m'avez apporté.

Il importe également de souligner que le parcours d'un doctorant n'est pas seulement celui d'un scientifique.

C'est également le parcours d'une personne. A cet égard, je souhaite remercier les Dr. Jean Louis Gallani et Bertrand Donnio pour leurs conseils et leur soutien moral. Volontaires, engagés et sincères, ils m'ont offert un appui solide tout au long de ces dernières années. Si certaines choses s'oublient dans la vie, je sais que je ne vous oublierai pas.

Je dois également mentionner ceux qui m'ont aidé dans le quotidien du laboratoire, sur de petites et de grosses choses. Le Dr. Benoit Heinrich, M. Nicolas Beyer, Mme. Emilie Couzigné et Mme. Emilie Voirin. Merci à vous tous. Sans votre assistance, je me serais arraché les cheveux!

Enfin, merci à toi Audrey, j'ai trouvé en toi plus qu'une collègue. Nos moments partagés ont été pour moi des moments priviligiés qui resteront à jamais dans ma mémoire. On dit qu'un véritable ami vous encourage dans le meilleur et dans le pire ; qu'il est honnête, unique et formateur; et surtout, que c'est une personne de confiance. A l'issue de ces années, je suis ravie d'avoir trouvé en toi une véritable amie. Merci Audrey pour toutes ces années.

Je remercie aussi les Dr. Thierry Achard et Stéphane Bellemin-Laponnaz pour leur soutien tout au long de ma thèse. Leur regard critique et avisé a été un atout manifeste.

Un grand merci à Anis Amokrane, Antonio Garofalo, Pierre Olivier et aux doctorants qui ont su faire de ce milieu, un milieu où il fait bon vivre : d'une part, les doctorants du laboratoire NMR, UMons et d'autre part, Mathilde Menard, Geoffrey Cotin, Mathias Dolci, Mathilde Bouché, Damien Bissessar, Marco Monticelli et Melania Reggente.

Enfin, je dédie ce mémoire à mes parents et à mon frère, qui m'ont soutenue moralement et matériellement durant toutes ces années d'études. Je ne saurais jamais les remercier assez, mais j'espère les rendre fiers par la personne que je suis devenue ainsi que par mes actes. Parinţii mei shi Sergiu - sunteţi izvorul puterii mele şi hrana sufletului meu, vã mlţumesc pentru sprijinul vostru necondiţionat. Je termine par un grand remerciement à M. pour son soutien sans faille dans les moments les plus difficiles durant la rédaction du manuscrit.

Contents

Acronyms and Abbrevations

ABP	Amino–bisphosphonate groups
ACN	Acetonitrile
ACQ	Aggregation caused quenching
ADME	Absorption, distribution, metabolism and excretion
AIE	Aggregation–Induced Emission
ARAL	ARALPSQRSR–NH_2
6–BAT	6–[*p*–(bromoacetamido)benzyl]–1,4,8,11–tetraazacyclotetradecane–N,N",N"',N""–tetraacetic acid
BOP	(Benzotriazol–1–yloxy) tris (dimethylamino) phosphonium hexafluorophosphate
CA	Contrast agents
CBS	Carbosilane
CNDPs	Critical Nanoscale Design Parameter
CNS	Central nervous system
COX	Cyclo–oxygenase
DA	Diacetylene monomer
DAB	Diaminobutyl
DBEDA	N,N'–Dibenzylethylenediamine
DCM	Dichloromethane
DDPD	N,N–Dicyclohexyl–1,7–dibromo–3,4,9,10–perylenetetracarboxylic diimide
DENPs	Dendrimer–entrapped nanoparticles
DIBAL	Diisobutylaluminium hydride
DIPEA	N,N–Diisopropylethylamine
DMAA–IPA	3–N–[(N,N–dimethylaminoacetyl) amino]–ethyl–2,4,6–triiodo–benzenepropanoic acid
DMAP	4–Dimethylaminopyridine
DMF	N,N–Dimethylformamide
DOTA	1,4,7,10–Tetraazacyclododecane–1,4,7,10–Tetraacetic acid
DOX	Doxorubicine
DP	Dendritic probe

DSNPs	Dendrimer–stabilized nanoparticles
DTA	Diatrizoic acid
DTPA	Pentetic acid
ECM	Extracellular matrices
EDA	Ethylene diamine
EDCI	1–Ethyl–3–(3–dimethylaminopropyl) carbodiimide
EPR	Enhanced Permeation and Retention effect
FA	Folic Acid
FAM	Carboxyfluorescein or fluorescein amiditearboxyfluorescein
FAR	Folic acid receptor
FITC	Fluorescein Isothiocyanate
GAPDH	Glyceraldehyde 3–phosphate dehydrogenase
G_n	Generation
H_c	coercive field
HFD	Heterofuntional dendrimer
HOBt	Hydroxybenzotriazole
HPG	Hyperbranched Polyglycerol
IBAM–DTPA	2–(4–Isothiocyanatobenzyl)–6–Methyl–Diethylenetriaminepentaacetic acid
IEP	Isoelectric point
IONPs	Iron oxide nanoparticles
IOP	intraocular pressure
kDa	Kilodalton
LA	Lipoic acid
LDH	Lactate dehydrogenase
LyP–1	C(S−S)GNKRTRGC–NH_2
MCRs	Multicomponent reactions
MR	Remanent magnetization
Ms	Saturation magnetization
MTT	3–(4,5–Dimethylthiazol–2–yl)–2,5–Diphenyl–tetrazolium bromide
MTX	Methotrexate
NBS	N–Bromo succinimide
NHS	N–hydroxysuccinimide

NNI	National Nanotechnology Initiative
NPs	Nanoparticles
NSAI	Non–steroidal anti–inflammatory
OA	Oleic acid
PAMAM	Poly(amidoamine)
PBS	Phosphate–buffered saline
PDA	Polydiacetylene
PDs	Pharmacodynamics
PEG	Poly(Ethyleneglycol)
PGA	Poly(L–Glutamic acid)
PKs	Pharmacokinetics
PLA	Poly(lactic acid)
PLL	Poly(L–Lysine)
PPH	Polyphosphorhydrazone
PPI	Poly(propyleneimine)
PSMA	Prostate specific membrane antigen
QDs	Quantum dots
r_1	Longitudinal relaxivities
R_1	longitudinal relaxation rate
r_2	Transversal relaxivities
R_2	transversal relaxation rate
RARE	Rapid Imaging with Refocused Echoes
RES	Reticulo Endothelial System
RGD	Arginine–Glycine–Aspartic acid peptide
RhB	Rhodamine B
ROI	Region of interest
SA	Succinic acid
SAR	Specific Absorption Rate
SI	Signal intensity
SMANCS	Poly(Styrene–co–maleic acid)–neocarzino statin
SPIONs	Superparamagnetic Iron oxide nanopaarticles
SPN	Succinimyldipropyldiamine

SPR	Surface plasmon resonance
SVA	Succinimidyl valerate
T_1	Longitudinal relaxation time
T_2	Trnsversal relaxation time
T_B	Blocking temperature
TBDMSCl	*tert*–Butyldimethylsilyl chloride
TFA	Trifluoroacetic acid
THF	Tetrahydrofuran
TMEDA	N,N,N',N'–Tetramethylethylenediamine
TMSBr	Bromotrimethylsilane
TMSONa	Sodium trimethylsilanolate
TPE	Tetraphenylethylene
TsCl	4–Toluenesulfonyl chloride
UCNPs	Up–conversion nanoparticles
ZP	Zeta potential
τ_B	Brownian relaxation time
τ_N	Néel relaxation time

Part I

Introduction: Dendrimer–Nanoconjugates Engineering

1 Generalities

Nature has been an inspiration to science. Human have looked at nature for answers to complex problems throughout hundreds years of existence. Biomimetics has solved engineering problems in the fields of energy, transportation, agriculture, medicine and even communication. The occurrence of patterns in nature have instigated researchers to infer a possible law abiding configuration, for fundamental reasons but also for the challenges and applications in new technologies.

Dendritic configuration (or tree–like architecture) is omnipresent in nature, in both animate and inanimate organisms, at different scales. From the kilometer scale, in the rivers basins and deltas, on the meter scale in the branches of trees, on the centimeter scale in the roots of these trees and in their leafs, on the millimeter scale in the circulatory systems of plants and mammals, throughout the micrometer scale of bacterial colonies and of neuronal system.[1]

In chemistry, the tree–like structures are true source of inspiration, chemists reproduce the dendritic architecture on a nanometric scale. The first example of iterative synthetic procedure was envisioned by Paul J. Flory[2], who was the first to examine the idea of preparing branched macromolecules. His study was based on the polymerization potential of such branched polymers, which he called "gel"[3,4]. As for a lot of different discoveries, his ideas were in advance on the synthetic and analytical methods of that time. It was not until early–1980's that the first paper describing the synthesis of cascade molecules, was published by Fritz Vögtle[5]. Several years later, mid–1980's Donald A. Tomalia[6], George R. Newkome[7] and Robert J. Denkewalter[8] disclosed the synthesis of "Starburst Dendrimers" **(Fig.1)** using conditions with less cyclization side–reactions and therefore more suitable for repetitive growth. Step–by–step synthesis of macromolecules gave birth to a new class of molecules: the dendrimers.[9]

The name "dendrimer" comes from the Greek language, which translates as "part of a tree" (δένδρον or dendros translates to "tree–like" and meros meaning "part of"), in association with its shape and its chemical structure made by monomers.[11]

Dendrimers are often compared to their counterparts, polymers, but they are distinguished from random coil polymers by their highly branched spherical architecture. Dendritic structures can be divided

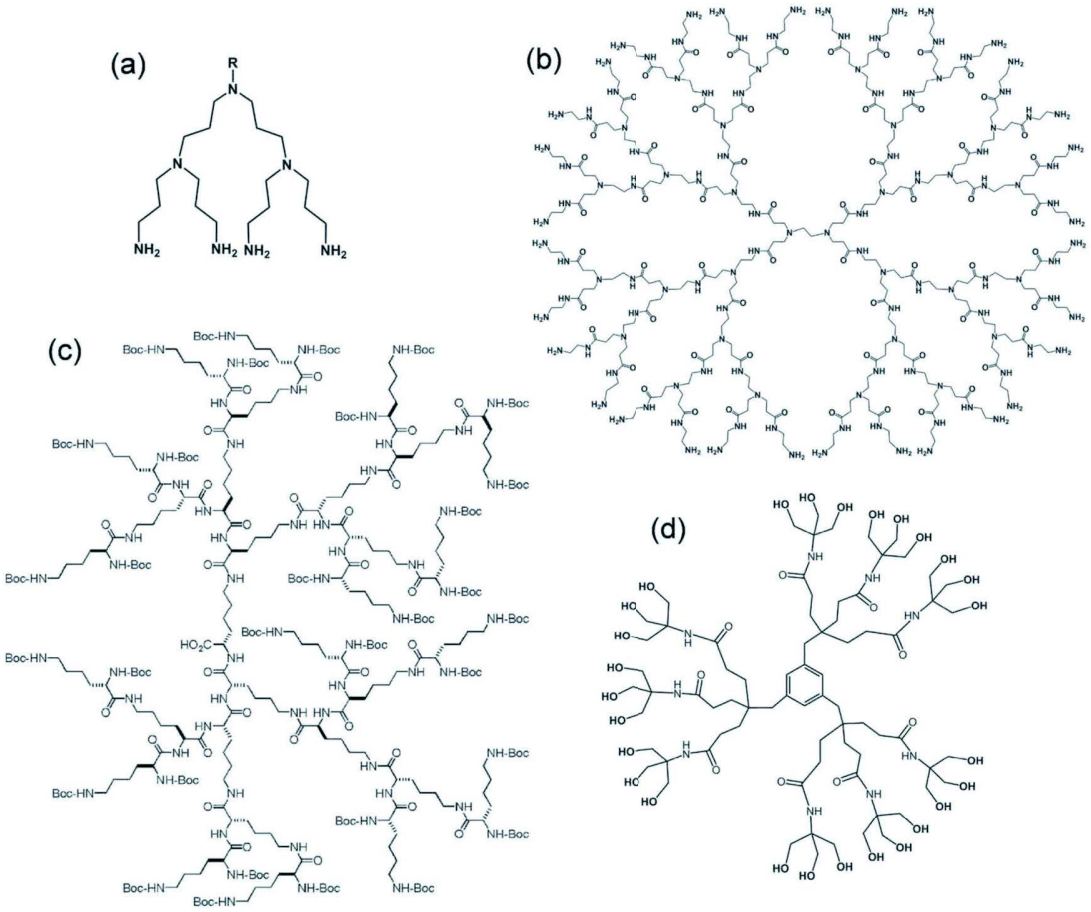

Figure 1: Chemical structures of a) Poly(amine) synthesized by Vögtle in 1978; b) Poly(amidoamine) dendrimer (PAMAM G_4) patented by Tomalia; c) Poly(lysine) dendrimer patented by Denkewalter; d) Polyol dendrimer reported by Newkome.[10]

into monodisperse dendrimers and dendrons (elementary unit), hyperbranched polymers, dendrigrafts and dendritic–linear hybrids such as dendronized polymers **(Fig.2).**[12]

Several typical traits of dendrimers are distinctly opposite to those of traditional polymers: (i) a dendrimer can be isolated as a monodisperse single compound resulting from a well–controlled synthesis, unlike most linear polymers which synthesis by polymerization affords various species differing in molecular weight[1]; (ii) as their molecular weight increases, the number of dendrimer end groups increases exponentially with generations, and therefore the properties of dendrimers are dominated by the nature of the end groups; (iii) dendritic growth is mathematically limited, the number of monomer units increases exponentially with generation, and the volume is proportional to the cube of its radius, developing a globular conformation with generation augmentation. At a certain generation, dendrimers encounter a steric limit, known as De Gennes

[1]Polymer molecular weight (molar mass distribution) – describes the relationship between the number of moles of each polymer species and the molar mass of that species.

dense packing.[13] In contrast, linear polymers can grow, in theory, to infinity.

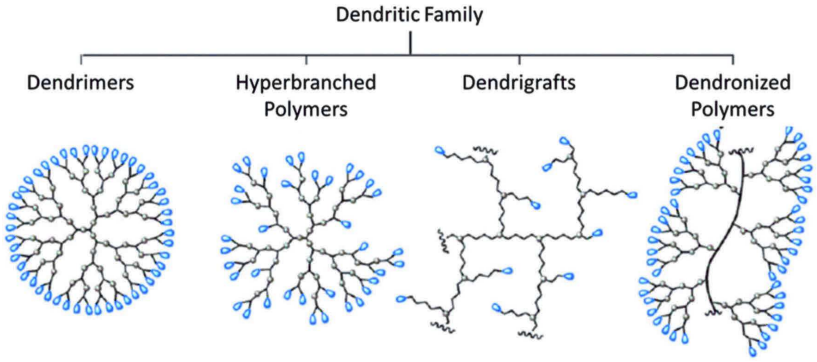

Figure 2: Schematic representation of the dendrimer family.[14]

Dendrimers exhibit three main architectural components **(Fig.3)**. These includes an interior core to which dendrons (one branch of the tree) are attached, branching layers (generations) and a high density of functional groups attached to the outer shell. Their three–dimension structure exhibits a high degree of molecular uniformity, narrow molecular weight distribution, tunable size and on–surface easily accessible functions, porosity, flexibility of the internal branches, presence of functionalized cavities, accessibility to the core and of course multivalency and cooperativity.[15] Dendrimers are typically 2 to 20nm in diameter and are composed of combinations of core types such as Ethylene diamine (EDA), Diaminobutyl (DAB), Poly(amidoamine) (PAMAM), Poly(propylene imine) (PPI). They also have different surface residues such as amine, carboxyl, and alcohol groups to name but a few.

Over the past decades a wide range of patent applications and original papers have been published in scientific journals, as evidence of the breakthrough in design and synthesis of dendrimers. Efforts were focused on the development of efficacious synthesis: fewer reaction steps, less time–consuming syntheses with higher dendritic product yields.[16]

The fact that dendrimers combine several physical and chemical properties in one molecule, made them interesting for multiple applications to the scientific community. As a result, more complex multifunctional dendrimers started to be synthesized. Thus, the first bi–functional dendrimer with alternating[17,18] or random[19] distributions of terminal group was prepared in the late–1990's. Nearly a decade later, dendrimers with at least three types of terminal functionalities that correspond a fruit–salad–tree were constructed by Steffensen and Simanek.[20]

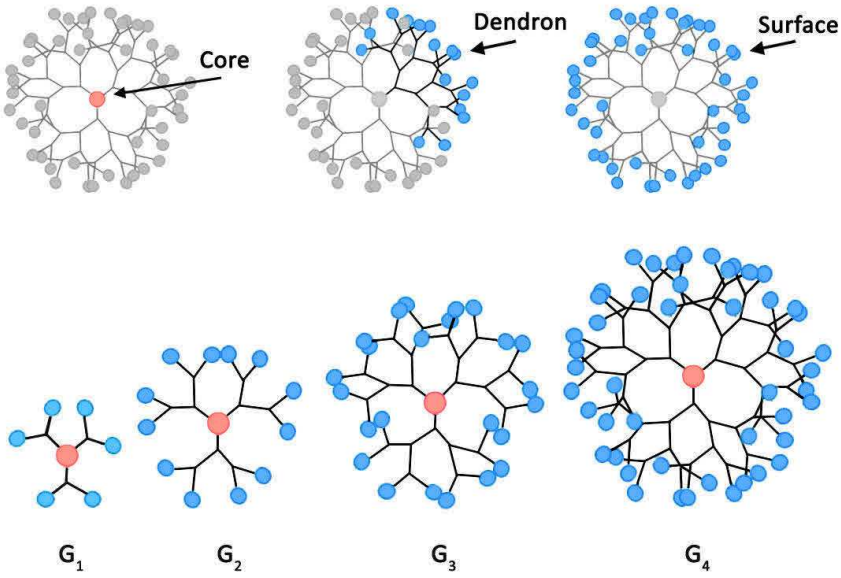

Figure 3: Schematic illustration of a dendrimer anatomy.

1.1 Synthesis and functionalization of dendrimers

The synthesis of dendrimers is accomplished with a wide variety of organic chemistry reactions, where efficient protection/deprotection and coupling reactions are of utmost importance. It might occur both in solution[7] and on solid support[21,22]. Dendrimer synthesis can be accomplished by various strategies: (i) by basic methods – divergent (inside out) and convergent (outside in) synthesis; (ii) or accelerated synthesis – which combines both divergent and convergent approaches. Even though the majority of dendrimers are built of covalent bonds, a large variety of non–covalent dendrimers have been prepared by self–assembly processes – by hydrogen bonding[23] or by coordination chemistry[24,25,26] through a chelating core moiety around a metal ion.

The singularity of dendrimers comes from the possibility to introduce various multiple functional groups at specific sites of the dendritic skeleton: (i) core, (ii) periphery, (iii) internal branches and branching point **(Fig.4)**. Dendrimers composed of different building moieties were named block–dendrimers or co–dendrimers and were initiated by Fréchet's group.[27,28] The segment–block and surface block dendrimers are often called "Janus–dendrimers" – two–faced dendrimers – with at least two different types of functional sites on the periphery and located in different parts of the dendrimer surface.[29]

The unique, tunable structure and multivalency of dendrimers made them a perfect platform for various applications: in chemistry (synthesis, analysis, catalysis...), material science (films, layers and hybrids),

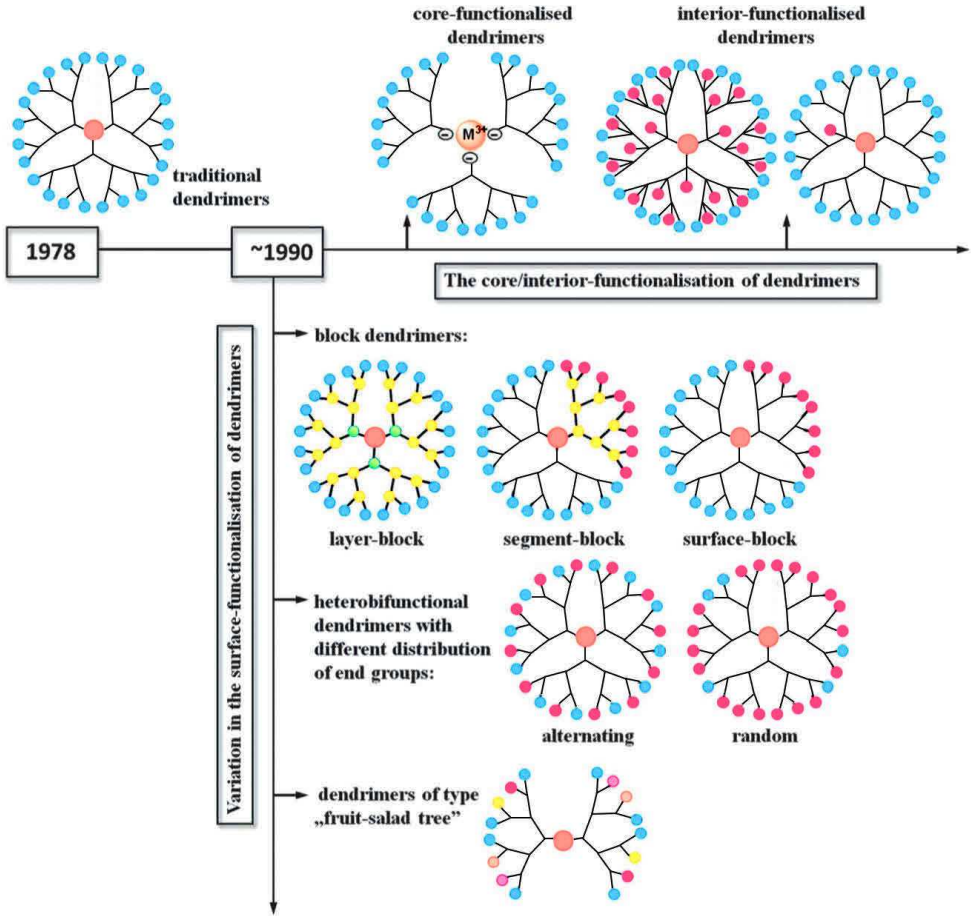

Figure 4: Evolution of dendrimer's backbone.[30]

pharmacology (drugs, medicine), nanosciences (nanoparticles), biology and medicine (immunology).[31]

1.1.1 Classic synthesis methods

From the beginning of the 1980's, dendrimers were synthesized starting from the core and growing from the inside out by increasing the number of branches equally at each branching point – Divergent approach.[32] When Donald A. Tomalia published a very extensive review[33] on the synthesis of highly branched "starbust" and "arborol" structures, Craig J. Hawker and Jean M. J. Fréchet reported their convergent approach for the synthesis of dendritic macromolecules.[27] The later raised as a solution to the potential problems in divergent–method – imperfections in high generation structures and purification difficulties.

Divergent growth In the divergent approach, the dendrimer is synthesized from the core, the starting point, and built from generation to generation towards the periphery **(Fig.5)**. So the first generation G_1 is obtained by coupling of an A_2B unit on the central core, where A is the reactive group of the monomer and

B is the protected/deactivated group of the monomer. The peripheral functionalities of the monomer A_2B are inert to the focal monomer functionality, thus preventing uncontrolled inter–monomer polymerization. The second generation G_2 is then obtained via a sequence of activation reaction of the B groups and their coupling with a new set of monomer A_2B. The repetition of such sequence allows the synthesis of higher generations "Gn".[34]

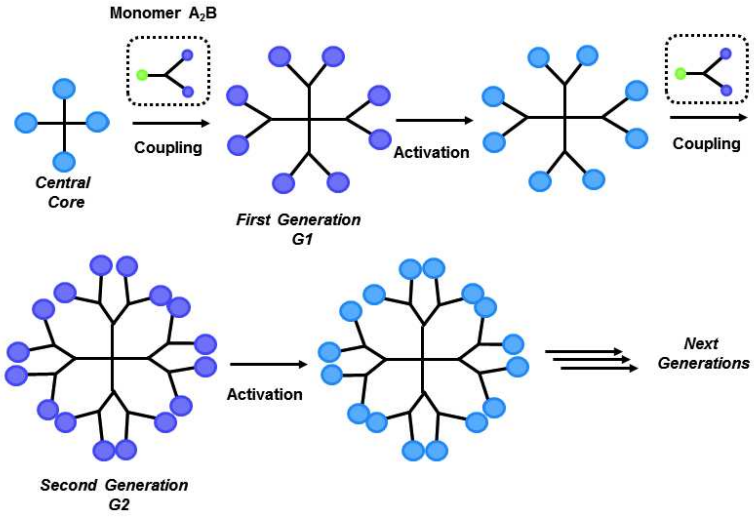

Figure 5: Divergent method of dendrimer synthesis.

The advantage of the divergent growth is the easy and fast creation of a large library of various generation dendrimers by stopping the reaction at any level and by changing their surface in the last step. Such flexibility as well as the possibility of automating the repetitive steps are the reasons for using the divergent strategy for all commercially available dendrimers.

However, with increasing generation, the divergent method leads to a number of imperfections in the dendrimer structure: indeed, any incomplete activation reaction of the end–groups brings failure sequence in the next generation, and the probability of this occurring increases with the number of terminal groups. In addition, a large excess of reagents are required in higher generation synthesis to prevent side reactions and to force reactions to completion thus causing difficulties in purification. Furthermore, the steric hindrance at the periphery, which is called "De Gennes dense packing" [13], forces the production towards dendrimers containing an appreciable number of flaws. Hence the synthesis of dendrimers through the divergent approach is a tedious, time–consuming protocol showing a low overall yield in spite of using selective reactions.[35] In order to avoid all those issues, the convergent approach appears as a good alternative.

Convergent growth In this strategy the individual dendrons (elementary building block) of various generations are synthesized first via a coupling and activation sequence, and then attached to the multi–functional

core **(Fig.6)**. The growth is initiated from the exterior of the molecule by coupling end groups to each branch of A_2B moiety. After completion, the focal point of the fragment is activated and coupled to an additional A_2B monomer unit, affording a higher generation dendron. Once a sufficient number of generations is reached, the dendrons are attached to a poly–functional core.[36]

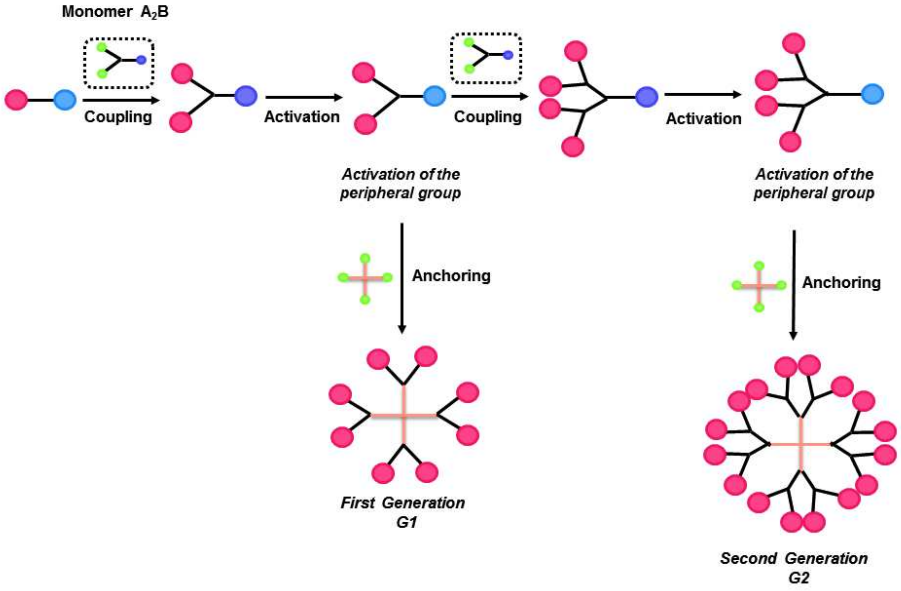

Figure 6: Convergent method of dendrimer synthesis.

Regardless the fact that it is an iterative synthesis, the convergent growth is different from the divergent method: indeed, it requires a small number of reactions per molecule and each propagation step involves two dendrons with one monomer. In addition, dendrons purification by chromatographic techniques is much easier than in the divergent synthesis. Thus by convergent method one has a greater control over the process, needs lower amounts of reagents to reach higher purity and almost flawless structures.

Nevertheless, one issue relies on the central position of the reactive groups: indeed for higher generations the focal point of a dendron is more and more isolated as buried by branches which leads to reactivity decrease.

The convergent and divergent strategies are complementary and neither is better. The choice of the synthetic approach is justified by the chemistry, functionality and features of the desired dendritic structure. In general, convergent strategy provides higher purity dendrimers with less imperfections. In contrast, divergent method is better suited for synthesis in large scales and of high generation dendrimers.

1.1.2 Accelerated synthesis methods

The accelerated approach was developed in order to respond to tedious purification and intensive iterative dendrimer synthesis, aiming to reduce the number of reaction steps, time and costs.[37,30]

Multigenerational couplings In mid–1990's scientists have revised the classical methods for dendrimer synthesis, since they had then realized the need for improvement of traditional synthesis ways. They sought for simpler routes to construct dendrimers without jeopardizing their perfection.

Hypermonomer strategy Instead of assembling monomers for dendrimer construction, this approach enables the addition of several generations during each coupling stage by using hypermonomers of the AB_4 type **(Fig.7)**. Wooly *et al.* first reported the "hypermonomer" strategy describing the synthesis of a G_5 Poly(aryl)ether dendrimer in three steps using a G_2 dendron as a hypermonomer.[38]

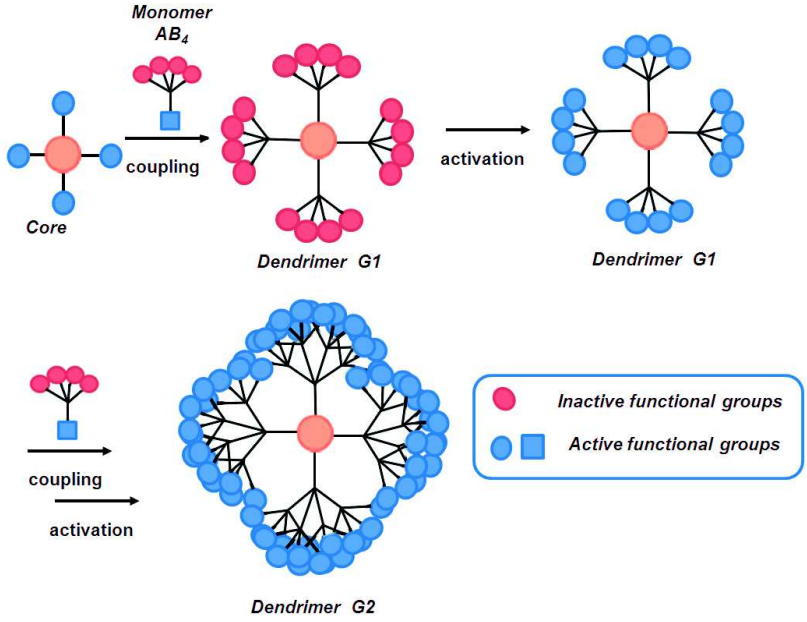

Figure 7: Hypermonomer approach for dendrimer synthesis.

Yet the product was obtained with a poor yield, caused by steric effect and low reaction efficiency. Indeed, due to the steric hindrance, the synthesis using such approach requires a very efficient coupling chemistry. On the other hand, hypermonomers are usually dendrons of low generation whose synthesis requires several steps, and in this case the acceleration is considered only for generating dendrimers, without taking into count the time demanded for hypermonomer synthesis. Currently such synthetic methodology is not largely used in the dendrimer construction since it is still a tedious method.

Hypercore approach The hypercore approach relies on three steps: (i) low–generation dendrons with protected terminal groups are coupled to a multi–functional core through their focal point, then (ii) terminal groups of the obtained dendrimer, called hypercore, are deprotected, and finally (iii) dendrons (same or different) are reacted with this hypercore, leading to the desired higher generation dendrimer **(Fig.8).**

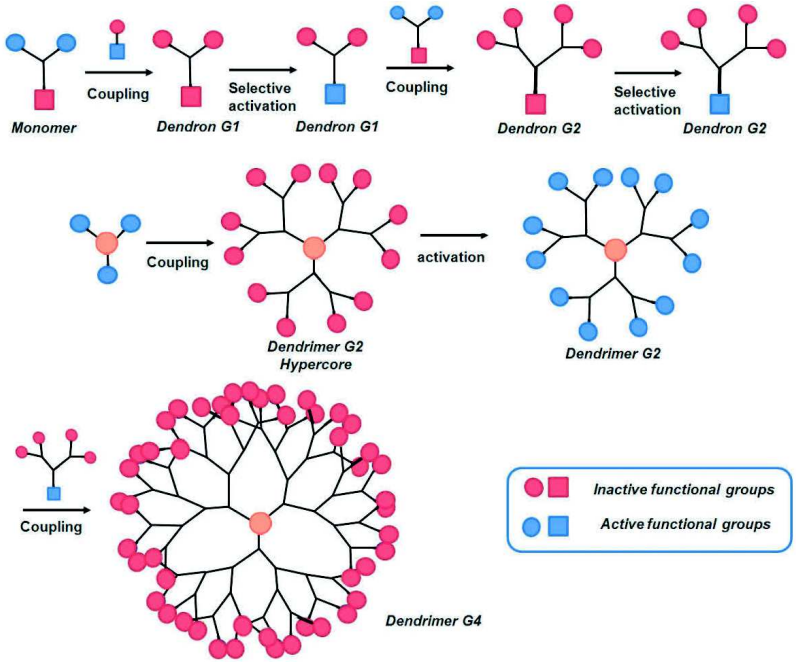

Figure 8: Hypercore approach for dendrimer synthesis.

Compared to the classical convergent synthesis, this approach uses a hypercore, which reduces steric effect and helps obtaining higher generation and monodisperse dendrimers. In addition, it allows the preparation of dendrimers with different internal and external moieties, by using different monomers in the synthesis of the hypercore and dendrons.

Fréchet *et al.* reported the synthesis of a seventh generation dendrimer using as a hypercore a second generation dendrimer, which was synthesized by convergent growth, and to which a fourth generation dendron was attached.[39] The synthesis of the hypercore and of the dendrons uses a conventional approach, which includes many synthetic steps, consequently, a time consuming method. Therefore, the use of this strategy is limited to the synthesis of high–generation dendrimers which cannot be made by traditional methods.

Double–exponential method The double–exponential growth is based on the synthesis of an entirely protected low generation dendron. Generally, an AB_2 monomer with orthogonally masked functionalities, is activated selectively, either at the focal point or at the periphery, and then coupled together to obtain a second generation of a fully protected dendron **(Fig.9).** These steps are repeated until obtaining a dendron

of desired generation. For the final step, the focal point of the dendron is activated and coupled to the multi–functional core.

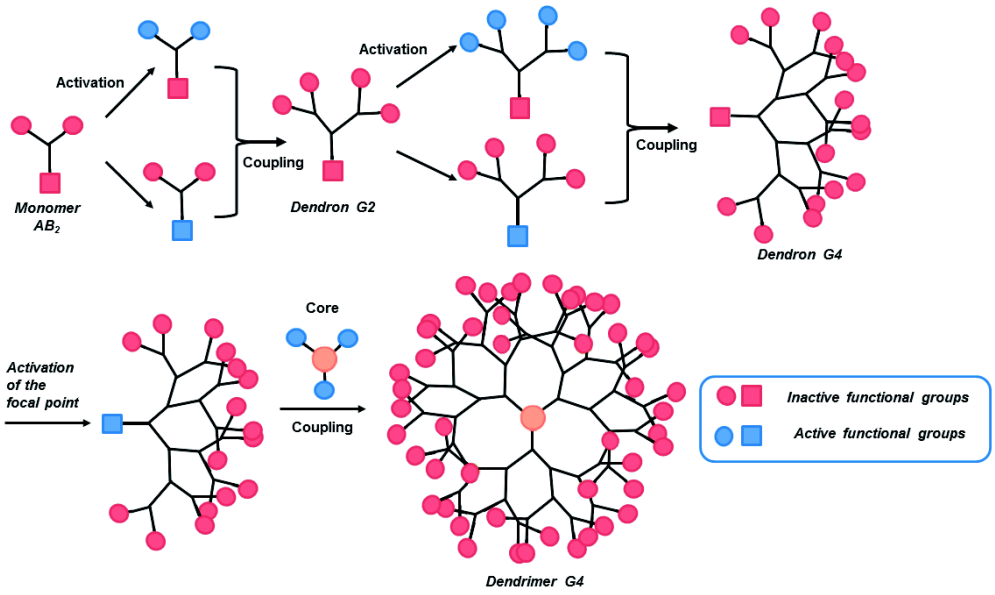

Figure 9: Double–exponential strategy.

This concept was first introduced by Moore and co–workers in 1995.[40] This method is particularly interesting as it enables the synthesis of large dendron/dendrimers in the most rapid way. The generation of dendrons is doubled at every three steps sequence of two selective activations and one coupling. The "generation jump", $G_1 \rightarrow G_2 \rightarrow G_4 \rightarrow G_8 \rightarrow ...$, leads to the reduction of reaction steps, time and costs. Furthermore, the selective deprotection of dendrons allows an easy modification of the focal point or the peripheral functions at all intermediate growing levels. According to this method, a small group of commercially available dendrimers was obtained.[41] However, with the increase of generation the overall yield decreases, suggesting that this approach is not very suited for the synthesis of high generation dendrimers requiring high–yielded coupling chemistry. The double–exponential synthesis combines the advantages and disadvantages of both convergent and divergent synthesis methods.

Orthogonal method The orthogonal strategy relies on either divergent or convergent approach for dendrimer synthesis, using two different monomers, AB_2 and CD_2, which have chemoselective functional groups **(Fig.10)**. The monomers are selected such as the focal functionalities of each individual moiety will only react with the periphery of the other monomer (A reacts only with D and B reacts only with C), thus eliminating the need for deprotection/activation steps.

Splinder *et al.* were the first to obtain a G_3 Poly(ether urethane) dendron, using 3,5 – Diisocyanatobenzyl

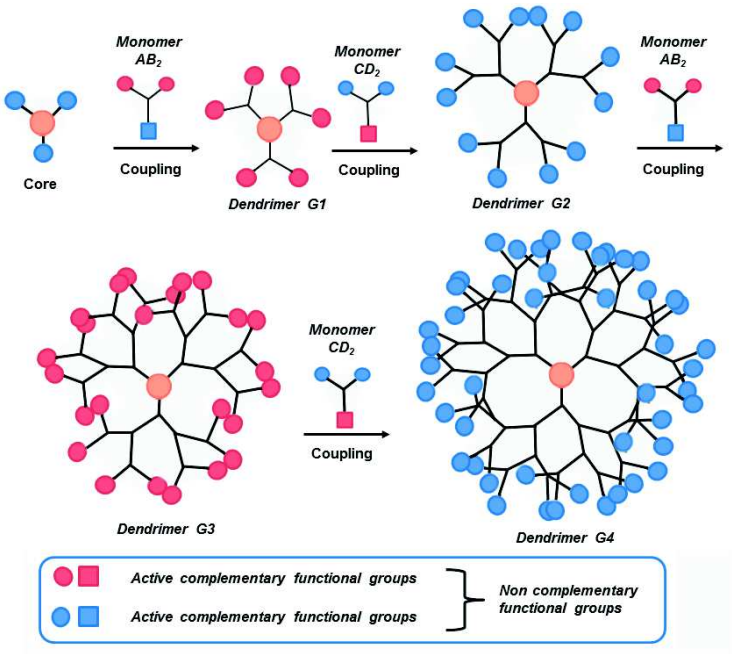

Figure 10: Orthogonal synthesis method *via* a divergent growth.

chloride and 3,5 – Dihydroxybenzyl alcohol as the AB_2 and CD_2 monomers, in a one–pot synthesis.[42] Unfortunately, the low chemoselectivity of the etherification and urethane formation reactions, prevented the preparation of higher generation dendrons. Freeman and Fréchet reported in 1999 a chemically homogeneous and highly efficient orthogonal synthesis, capable of producing high generation dendrimers.[43] In spite of the reduction of purification steps, orthogonal approach has complex synthetic parameters. In addition to requiring highly efficient coupling reactions, orthogonal synthesis requires two pairs of orthogonal coupling functionalities, which also places a greater limitation on which functionalities may be incorporated into the dendritic structure without interfering with the synthesis.

The key point of the different accelerated syntheses of dendrimers is the elimination of the iterative activation steps. Chemoselective reactions can give good results through solid–phase syntheses, click chemistry, thiol–ene coupling or Diels–Alder cycloaddition. Another possibility is to use multicomponent reactions (MCRs) combining three or more reactants in a one–pot process such as the *Passerini–3CR* or three component reaction and the *Ugi–4CR* or four component reaction.[44,45]

In order to facilitate the synthesis of dendrimers in fewer steps, scientists have been seeking the possibility to eliminate the need for purification steps. This was made possible through the use of one pot synthesis (mix between the orthogonal way and the click chemistry for example) as shown by Malkoch[46], Fréchet[47] or by Caminade[48].

1.1.3 Heterofunctional dendrimers

The major advantage of dendrimers is the ability to include a large and exact number of different functional (heterofunctional) groups within the framework without compromising the structural perfection.[49] Consequently, scientists have successfully established accelerated synthetic protocols for the development of heterofunctional dendrimers (HFDs) having heterofunctionalities that are expressed differently at defined positions. Due to the presence of different functions, only certain types of dendrimers fulfill the requirements for the synthesis, *e.g.*, the presence of specific peripheral groups, such as primary Amines or Phosphonic acids, and their compatibility towards synthetic methods. The typical variations found for such structures can be divided into subgroups by the location of the heterofunctions: external or internal.[50]

The controlled synthesis of HFD is more difficult to conduct than the synthesis of bifunctional dendrimers, which is certainly the reason for the relatively limited number of examples of such compounds. However, their "superfunctional" structure is an excellent platform for a large number of applications.

Peripheral functionalization Periphery multifunctionalization of dendrimers can be made either as a pre– or post–modification method, by introducing different desirable moieties during the dendrimer growth or by modification of existing peripheral functions after completion of the dendrimer synthesis. The HFD can be classified in three subgroups, as: (i) block dendrimers, (ii) alternating distribution of the end groups and (iii) random distribution of end groups.

The block dendrimer synthesis is obtained by coupling different dendrons, with different peripheral functions, to a common multifunctional core, giving access to entirely new dendrimers in only one step. As an example, the synthesis of "Janus–type" dendrimers. There are three commonly used methods to produce Janus or two faced structures **(Fig.11)**.

The first method consists in the direct coupling between two different dendrons with complementary functions at their focal points (Method 1). The second method is based on the connection of the focal point of the first dendron to a bi–functional core, then a second dendron is grafted through its focal point to the remaining available function of the core (Method 2). Finally, the last method, which has been rarely proposed, consists in using the focal point of a dendron to grow step–by–step a new dendron by a divergent process (Method 3).[51,52] Fréchet and co–workers reported the first synthesis of a "Janus" type dendrimer in 1993, using a convergent/convergent method.[28]

Majoral *et al.* were the first to report the synthesis of a multifunctional dendrimer with an alternating distribution of peripheral groups.[17] The synthesis of such dendrimers was performed via a convergent growth using unsymmetrical dendrons, which have different terminal groups **(Fig.12)**.

For an efficient synthesis, the monomer should be used in excess and its two functional groups should have

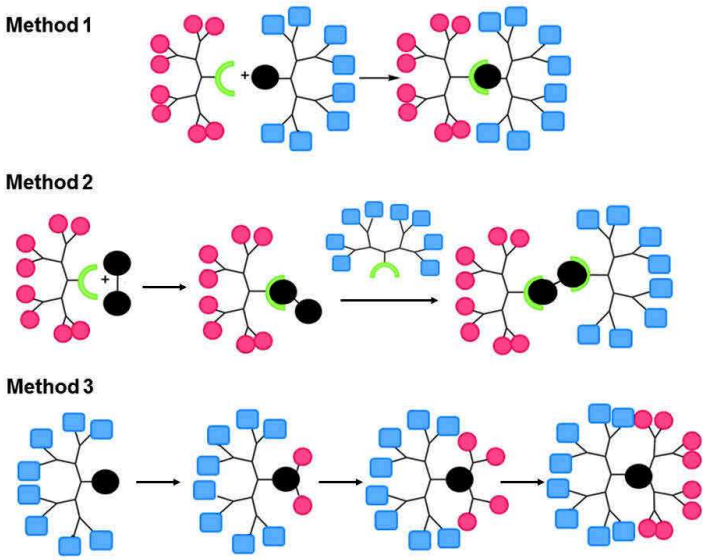

Figure 11: The commonly used methods for the elaboration of Janus dendrimers.

a different reactivity under the required synthetic conditions. Using this strategy, Fréchet and co–workers described the accelerated synthesis of HFDs through orthogonal protecting groups for the monomer functions.[53]

The post–modification synthesis relies on coupling two different functional groups to each terminal group of the dendrimer. This method was first reported by Shinkai *et al.* by introducing Anthracene and Boronic acid units through reductive amidation.[18] Amine–terminated dendrimers were post–functionalized with Sulphonyl groups and then with Alkyl, Benzyl or dendritic Halides.[54,55] Later, Fréchet and co–workers presented a post–modification method through a ring opening reaction with Amines and subsequent reaction of the activated hydroxyl groups with Propargylamine.[56] More recently, Simanek *et al.* reported a post–modification strategy by reacting Amine–terminated dendrimer with Cyanuric chloride, giving birth to either four or eight Dichlorotriazine terminated dendrimers, with a high overall yield.[57] Another post–modification stratagem is the functionalization of each dendrimer peripheral group with a trifunctional Amino–acid. A wide variety of such natural and unnatural Amino–acids was reported, as well as their post–modification. [58,59,60,61]

Internally functionalizaion Functionalization of dendrimers is often related to their cores or peripheral functions. In spite of the surface ratio of the internal dendritic framework, in almost all the cases it is assimilated as an inert scaffold, linking the core and terminal functions and arranging them in space, without any specific function. However, few scientists have been looking at changing the spectator role of the interior, by incorporating functionalities within it.[62] The first attempt was made by Fréchet *et al.* in 1993.[63]

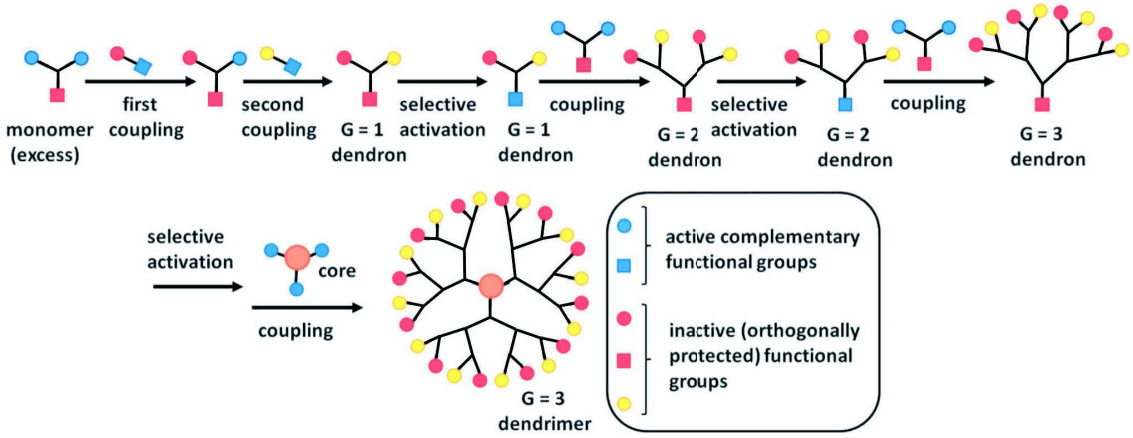

Figure 12: Synthesis of heterofunctional dendrimers with an alternating distribution of end groups.[30]

Unfortunately, their study revealed that internal functions were less reactive than peripheral ones, most probably due to their poor accessibility to the reagents. Thus the design of new monomers was presented as a necessity. The innovative aspect of the new monomer structure AB_2C, was the use of an additional functional group, C, which is inert to the synthetic cycle of the dendrimer synthesis and is recovered in the interior of the dendrimer's body. The dendrimer growth with AB_2C monomer can be done either via convergent or divergent strategies **(Fig.13)**. In addition, such remarkable method increases the dendrimer functional groups without adding extra synthetic steps.

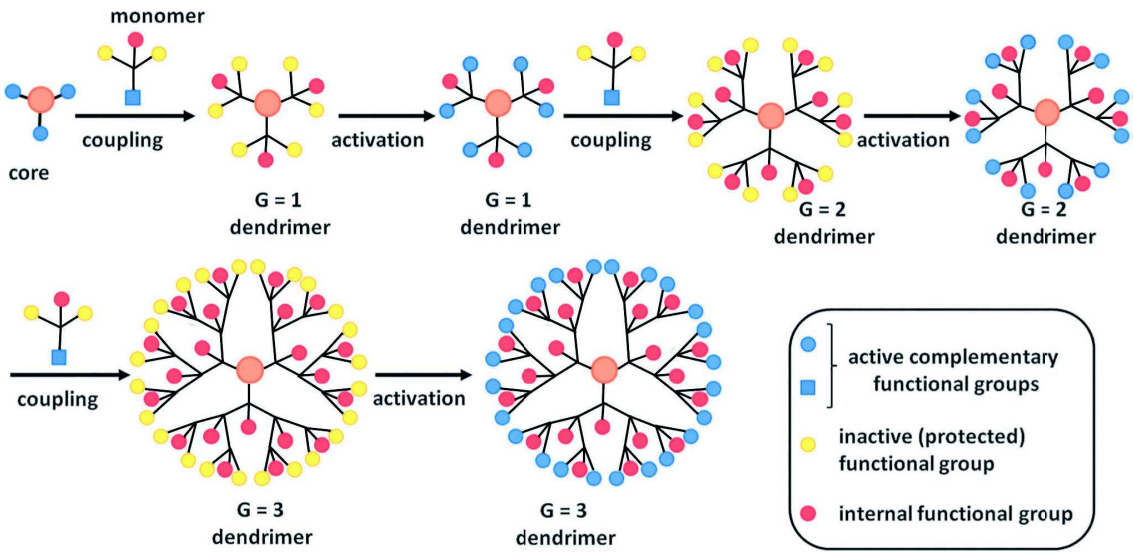

Figure 13: Internal functionalization of dendrimers using divergent strategy.[30]

This approach was first reported by McGrath and co–workers, by introducing internal Acetonide – protected vicinal diols into G_2 dendrimers via a convergent method.[64,65,66,67] However, in spite of a very inno-

vative approach, the desired product was obtained in poor yield to which side–reactions had their contribution. A beautiful example of internal functionalization of dendrimers was reported by Fréchet and co–workers in 1999, using a Fréchet–type dendrimer.[68] In addition, the deprotection of the inner functional groups was obtained in 100% yield. A very interesting example was reported by Malkoch *et al.*, synthesizing two third generation dendrimers within six reaction steps, which were compatible with post–functionalization avoiding deprotection step.[50] Later, Hawker's team described a facile and rapid synthesis of G_3 internally functionalized dendrimers by combining two orthogonal chemistrie.[69] Of extreme interest are Poly(phosphazene hydrazone) dendrimers having P=N−P(=S) linkages within the dendrimer structure, reported by Majoral *et al.*[70] The presence of this linkage is acting like an open door to a large variety of functions, regiospecifically introduced inside the dendrimer via S–alkylation using Triflates, subsequent desulphurization and coupling to the corresponding Azides (Staudinger reaction), *e.g.*, Isothiocyanates, primary Amines and Aldehydes.[71,48]

The post–modification of dendrimers is somewhat a stochastic process, depending on the size of the internal voids, dendrimers flexibility, the reactivity of the functional groups involved, among others. On the other hand, the pre–modification strategy permits the introduction of functional groups in a controlled manner and precise number.

1.2 Dendrimer design for biomedical applications

As one of the newest areas of science, nanoscale science and technology are seen by many as the key technology of the 21st century, which of course raises the question as to what role this technology will play in medicine. Nanomedicine meaning currently relies on definitions provided by the National Nanotechnology Initiative (NNI): (1) development of research and technology at the atomic, molecular or macromolecular levels, within the nanosize scale (approximately 1 to 100 nanometer in range); (2) nanobiomaterials (devices and systems) that have novel properties and functions based on their small and/or intermediate size; (3) ability to control and manipulate the atomic level.[72] The European Science Foundation reports call for a coordinated strategy to deliver new nanotechnology–based medical tools for diagnosis and therapy purposes. This is evidenced by the emergence within this field of many new high impact journals, international symposium, medical companies and start–ups, and an exponential growth in publications, patents, citations, clinical trials and projected global markets. At the current annual growth rate of 12.3%, global Nanomedicine markets are projected to reach 177.6 billion $US by 2019.[2]

The major nanomedicine growth areas are predicted to be primarily in Neurology, Oncology and Cardiovascular, Anti–inflammatory and Anti–infective applications.

[2] www.transparencymarketresearch.com

1.2.1 Diagnostic applications: Imaging

As a remarkable progress in nanomedicine, Molecular Imaging (MI) was formally introduced in 1999 and defined in 2004. MI has been emerging as a powerful tool to visualize, characterize and quantify the biological processes at the molecular and cellular levels in humans and other living systems. Traditional modalities such as X–ray, Computed Tomography (CT), and Magnetic Resonance Imaging (MRI) produce an image of anatomy. Modalities such as Positron Emission Tomography (PET), Single Photon Emission CT (SPECT), Optical Imaging (OI), Ultrasound (US), and contrast–enhanced CT or MRI produce an image with details on function **(Fig.14)**.[73] Molecular imaging monitors and measures biological processes in a way similar to a biopsy but is done non–invasively, in real time, and with potential for sequential and longitudinal monitoring.

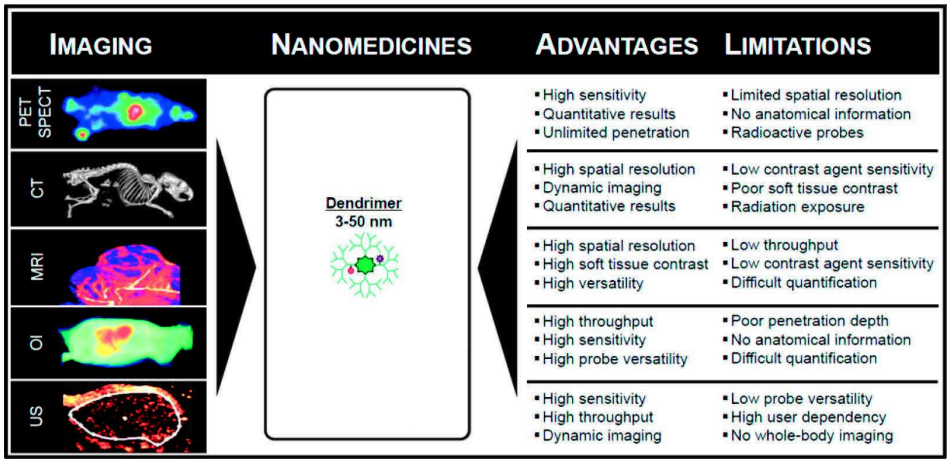

Figure 14: Schematic representation of noninvasive imaging techniques used in nanomedicine research, as well as an overview of their advantages, and limitations.[73]

Fluorescence imaging agents Fluorescence imaging has unique advantages in terms of sensitivity, multiplex detection capabilities and cost–effectiveness. Due to the limitation of small molecular imaging dyes, dendrimers have been thoroughly investigated for their stability, biocompatibility, high specificity and sensitivity providing imaging with excellent temporal and spatial resolution.

Indeed, some dendrimers present intrinsic fluorescence. In 2004, Lee *et al.* published a simple oxidation process of Hydroxyl–terminated PAMAM dendrimers generating a blue fluorescence with high quantum yield.[74] In another work, Wang *et al.* reported an intrinsic fluorescence emission under acidic conditions for both PAMAM and Poly(propylene imine) (PPI) dendrimers.[75] Recently, Tsai and co–workers reported the use of intrinsically fluorescent PAMAM dendrimers as gene vectors and nanoprobes for nucleic acids delivery.[76] Despite the importance of intrinsic fluorescence properties of dendrimers, most of the studies for biomedical imaging are limited to the cellular level due to the low fluorescence quantum yield of dendrimers.

To overcome this issue, fluorescent dyes have been conjugated to the surface of dendrimers.[77] For instance, G_5 PAMAM dendrimers have been used as a platform to conjugate Fluorescein Isothiocyanate (FITC), Folic Acid (FA), and anti–cancer drugs in the Baker laboratory for, respectively, optical imaging, targeting and cancer treatment *in vitro* and *in vivo*.[78,79,77,80]

Fluorescent dye molecules can also be loaded within the interior of dendrimers via covalent binding. For example, Amir *et al.* reported an accelerated synthesis of multifunctional dendrimer scaffolds with two different dyes: multiple Coumarin units inserted within the internal backbone through a cleavable linker, and a single Alexa647 dye conjugated to the surface through a peptide coupling.[81]

Nanosized semiconductor nanocrystals, referred as *quantum dots* (QDs) have shown promising applications as nanosensors and light–emitting bioprobes, especially in cellular imaging and drug delivery.[82] Gao *et al.* reported on stable and biocompatible dendron–coated InP/ZnS core/shell QD as a clinically translatable nanoprobe for molecular imaging applications.[83] The InP/ZnS core/shell nanocrystals can emit in the 450–750nm range, with a quantum yield as high as 40%. The bright core/shell nanocrystals are air–stable and can be dispersed in water after being coated with dendritic and PEGylated Arginine–Glycine–Aspartic acid peptide (RGD).[83] *In vivo* and *ex vivo* fluorescence imaging indicated that the QD–dendron–RGD_2 nanoprobe clearly imaged integrin $\alpha_v\beta_3$–positive tumors (human ovarian cancer cells, SKOV3) with high specificity (active targeting).

Up–conversion nanoparticles (UCNPs) are luminescent nanomaterials that generate higher energy light from lower energy radiation (usually near infrared (NIR) or IR radiation), through the use of rare earth ions doped into a solid state.[84] Water soluble and robust UCNP–HPG–RhB nanohybrid composed of a $NaYF_4$:Yb/Er core and a tunable hyperbranched Polyglycerol (HPG) shell tailored by fluorescent Rhodamine B (RhB) dye, have been recently reported to simultaneously present up–conversion and down–conversion luminescence *in vivo*.[85] The standard MTT cell–viability assay displays low cytotoxicity within 24h on breast cancer cells MCF–7. UCNP–HPG–RhB have promising properties for bioimaging applications.

X–ray CT imaging agents Computed Tomography (CT) is an X–ray–based imaging technique that is a well–established 3D technique for organs, tissues or blood vessels in a large number of research and clinical settings. CT generates high–resolution anatomical images using highly electron dense contrast agents (CAs), such as Iodine and Barium.[86,87] Commercially available iodinated small molecular CT CAs (*e.g.*, Omnipaque^{TM}) are rapidly cleared from blood after injection, display renal toxicity at a relatively high concentration and non–specificity towards tissues or organs.[88] Recently, dendrimers have been extensively used as carrier systems to load or prepare different CT CAs.[89]

In 2002 Yordanov *et al.* conjugated 3– N– [(N,N– dimethylaminoacetyl) amino]– ethyl– 2,4,6– triiodo–

benzenepropanoic acid (DMAA–IPA) on the surface of G_4 PAMAM dendrimers.[90] In another approach, PEG was used as a core to build up a dendritic macromolecule using Lysine units via a divergent synthetic strategy.[91] The terminal amines of the PEG–cored dendrimers were covalently conjugated with Triiodophthalamide, an iodinated CT CAs. The formed iodinated PEG–cored dendrimers had high X–ray attenuation intensity, prolonged intravascular enhancement in rat models, high water solubility, good chemical stability, and adjustable molecular weights. This agent represents a new development in dendrimer–based CT CAs for quantitative microvascular characterization of a variety of diseases and abnormalities.

Recently, the use of noble metals (*e.g.*, Au) as CT CAs has become a promising tool since they have a higher atomic number than Iodine and consequently stronger X–ray attenuation coefficient than iodine–based CT CAs. The versatile dendrimer nanotechnology enables the use of branched structures as facile templates to synthesize Au NPs. Their unique structural characteristics provide interior and peripheral reaction sites, thus enabling the synthesis of dendrimer–entrapped Au NPs (Au DENPs) as well as dendrimer–stabilized Au NPs (Au DSNPs).[92,93,94]

In an early study, Guo *et al.* synthesized Au DENPs, by employing amine–terminated G_5 PAMAM dendrimers (G_5NH_2) as templates and explored their X–ray attenuation properties.[95] Measurements showed higher attenuation coefficient of Au DENPs compared to Omnipaque^{TM}. *In vivo* micro–CT imaging studies have shown that an intravenous injection of acetylated Au DENPs, prepared using G_5NH_2, enables effective CT imaging of the pulmonary veins and the inferior vena cava of mice.[96]

Studies have shown that FA–conjugated dendrimers preferentially target tumor cells that overexpress FA receptors (FAR).[97,98] Wang *et al.* explored the use of (FA) – modified acetylated Au DENPs as nanoprobes for CT imaging of targeted human lung Adenocarcinoma.[99] A xenograft tumor model has been administrated with the nanoprobe through intravenous, intratumoral or intraperitoneal injections. A large amount of Au element was found in lungs, spleen and liver, which are known as the Reticulo Endothelial System (RES) organs. Zhu and co–workers have shown that partial PEGylation of G_5NH_2 renders the formation of more stable Au DENPs with improved Au loading within the dendrimer interior, prolonged blood circulation time, reduced macrophage uptake and enhanced biocompatibility.[100]

Instead of using dendrimers as templates for the synthesis of Au DENPs, under weak reducing conditions, Peng *et al.* reported the approach of forming dendrimer–stabilized Au NPs (DSNPs).[101] The so–formed Au DSNPs were relatively uniform and stable at different pH and temperature conditions, and showed much better *in vivo* performance than Omnipaque^{TM}.

To further improve the sensitivity of CT imaging, dual radio–dense elements have been incorporated within one single NP system. In a recent study, Guo *et al.* first synthesized Au DENPs using G_5NH_2 dendrimers as templates, and then complexed the Amine–functionalized Au DENPs with an Iodine–based

small molecular CT contrast agent (Diatrizoic acid – DTA).[102] Their results showed that DTA – loaded Au DENPs had significantly enhanced X–ray attenuation properties as compared to single radio–dense element–based CAs (Au DENPs or Omnipaque^{TM}). In another study, Peng and co–workers reported on the synthesis of DTA–loaded Au DSNPs, which displayed enhanced X–ray attenuation intensity, and were able to be used for CT imaging of cancer cells *in vitro* as well as for blood pool CT imaging of mice *in vivo* with dramatically improved signal enhancement.[101]

MR imaging CAs Magnetic Resonance Imaging (MRI) is based on a principle similar to the one used in chemical Nuclear Magnetic Resonance (NMR) analysis and is one of the most useful diagnostic imaging techniques in clinical medicine thanks to its excellent spatial resolution, non–invasive and non–destructive nature. For improved imaging quality including sensitivity, resolution, extended imaging time, tissue or organ specificity, CAs are generally required. In recent years considerable attention has been paid to develop various nanosized CAs, as conventional low molecular weight CAs possess disadvantages such as rapid excretion,[103] relatively low contrast efficiency,[104] renal toxicity,[105] and lack of specificity to target disease or cancerous tissues[106].

MRI is highly useful for diagnosis and therapy monitoring. Drug release and drug efficacy is monitored due to the possibility to render different signals when present within *vs* outside of a nanocarrier.[107] The latter provide an excellent soft–tissue contrast, which enables the non–invasive and highly accurate detection of *i.e.* tumors and inflammation sites.

Dendrimers have been used as T_1 positive MR CAs.[108] They often serve as a nanoplatform for multiple small molecular Gd(III)–chelates, typically Gd(III) complexed with Pentetic acid (DTPA),[109] 1,4,7,10–Tetraazacyclododecane–1,4,7,10– Tetraacetic acid (DOTA)[110], or their derivatives[111]. A pioneering work performed by Wiener *et al.* in 1994 showed that 2–(4– Isothiocyanatobenzyl)– 6– Methyl– Diethylenetriaminepentaacetic acid (IBAM–DTPA) could be covalently bound onto the surface of Amine–terminated PAMAM dendrimers. Subsequent complexation of Gd(III) ions gave then rise to nanocomplexes showing much higher r_1 relaxivity than commercially available and routinely used Gd(III)–DTPA.[112]

Kobayashi *et al.* synthesized a series of Gd(III)–DTPA functionalized PPI dendrimers of different generations: r_1 relaxivity showed almost a linear relationship as a function of the dendrimer molecular weight.[103] Similarly, by using a different linker between Gd(III)–DTPA complexes and PPI dendrimer, Meijer and colleagues showed a dramatic increase in r_1 relaxivity.[113]

Researchers have recently observed fibrosis and scar tissue in kidneys, potentially as a response to Gd(III) dissociation from the linear DTPA chelating agent in circulation. To avoid the possible leaching of Gd(III) ions from the nano–complexes, Nwe *et al.* conjugated cyclic Gd(III)–DOTA complexes onto G_4PAMAM

dendrimers, which are more stable than their linear counterparts (*e.g.*, DTPA)[114,115]The authors discovered that DOTA–based dendrimer CAs had shorter blood clearance, reducing the amount of Gd(III) ions that could leach out from the complexes.

For specific MR imaging, Gd(III)–based dendritic MR CAs have been modified with various targeting ligands. In 1997, Wiener and coworkers developed Gd(III) DTPA–based PAMAM dendrimer CAs modified with FA for ovarian cancer targeting.[116,117] In another work, Swanson e*t al.* developed a G_5 MR contrast agent by conjugating DOTA ligands onto FA–modified G_5 dendrimers, followed by chelating with Gd(III) ions.[118] Similarly, a PEG–cored dendrimer with 16 functional hydroxyl groups has also been used to conjugate FA and Gd–DTPA for FAR–targeted MR imaging in a tumor model.[119]

In addition to the use of a pre–ligation approach and the use of more stable (cyclic) chelators, non–Gd(III)– based dendrimeric MR CAs have been synthesized.[120] In a recent study, Ali and colleagues developed a Mn–PAMAM dendrimer–based contrast agent by conjugating multiple DOTAM phosphate–based chelators onto the dendrimer surface.[121] In 2014, Felder–Flesch and coworkers demonstrated the possibility to use MnO nanoparticles as T_1 vascular CAs, while enabling the excretion of more than 70% of the injected dose after 48h.[122]

Besides the discussed T_1 MR CAs, dendrimers can also be used as stabilizers for iron oxide NPs (IONPs), or be assembled onto preformed IONPs for T_2–weighted MR imaging applications. *Advanced Magnetic's Gastromark* was the first product based on IONPs which was approved in 1993 in Europe and in 1996 in the United States. The other IONPs–based MRI CAs were: 1) Resovist® approved in 2000 for liver imaging on European market (has been taken off the market because of lack of sales in November 2008[123]).[124]; 2) Sinerem®, brand name (same as Combidex®) for an ultrasmall superparamagnetic iron oxide (USPIO) to detect metastatic disease in lymph nodes.

In 2001, Strable *et al.* synthesized stable Fe_3O_4 NPs with a diameter of 20–30nm using carboxylated $G_{4.5}$PAMAM dendrimers as stabilizers.[125] They showed that the electrostatic interaction of negatively charged carboxylated PAMAM dendrimers with positively charged IONPs was crucial for their stabilization. Yang *et al.* reported the synthesis of a platform for targeted MRI of C6 glioma cells assembled from ultrasmall IONPs and RGD–modified dendrimers G_5NH_2.[126] The G_5NH_2–RGD–Fe_3O_4 NPs showed good water dispersibility, colloidal stability, excellent hemocompatibility and biocompatibility over a large concentration range. *In vitro* and *in vivo* tumor MR imaging experiments not only indicated good and active T_2–weighted MR imaging performances **(Fig.15)** but also demonstrated the specific targeting ability.

In 2011, Basly and co–workers compared the stability and magnetic properties of dendronized IONPs synthesized by co–precipitation versus by thermal decomposition.[127] In both cases homogeneous and stable aqueous suspensions were obtained. High r_2 values and r_2/r_1 ratios were obtained with the dendronized NPs

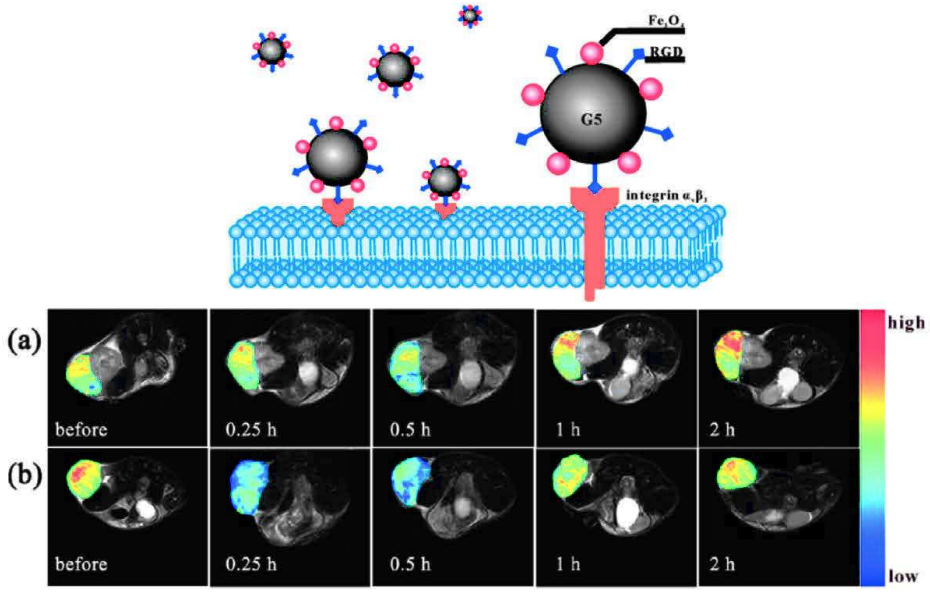

Figure 15: Schematic drawing of active targeting through RGD–mediated pathway and *in vivo* T_2–weighted MR images of tumors after intravenous injections of 0.1mL PBS solutions containing (a) G_5NH_2–Fe_3O_4 NPs (b) G_5NH_2–RGD– Fe_3O_4 NPs (600μL Fe) at different post injection times.[126]

synthesized by co–precipitation in comparison with commercial products of the same size range.

Recently, Neoh *et al.* prepared hyperbranched Polyglycerol (HPG)–grafted IONPs and evaluated their efficiency as MRI contrast agent *in vitro*.[128] They employed the carboxylic function of 6–Hydroxy caproïc acid as an anchoring group on the surface of superparamagnetic IONPs. The 'grafting from' strategy was put in use for this synthesis and *in vitro* studies showed a very low macrophage uptake. HPG–IONPs showed a high stability in both water and phosphate–buffered saline (PBS) under 1.5T which is highly advantageous for their intended applications as MRI contrast agent. A few years later, Muller and colleagues also developed an HPG–grafted IONPs approach, but through a covalent linkage (silane groups) between the NP and the organic coating.[129] *In vitro* relaxivity measurements showed negative MRI contrast enhancement and *in vivo* studies confirmed rapid renal excretion. Goodson *et al.* reported highly pH–sensitive MR responses induced by a series of superparamagnetic IONPs (SPIONs) functionalized by three generations of Melamine dendrons showing high molar relaxivities and excellent aqueous stability.[130] Cellular uptake in Henrietta Lacks (HeLa) cell cultures were performed and the high spin–spin relaxation rate (r_2) values observed were not only consistent with high cellular uptake but also reflected significant SPIONs clustering within the cells as a function of pH **(Fig.16)**.

Indeed, molar relaxivities were found to exhibit great sensitivity towards pH at physiologically relevant ionic strengths, with sharp inflections observed at pH values near the pKa of the Melamine (Poly(amine))

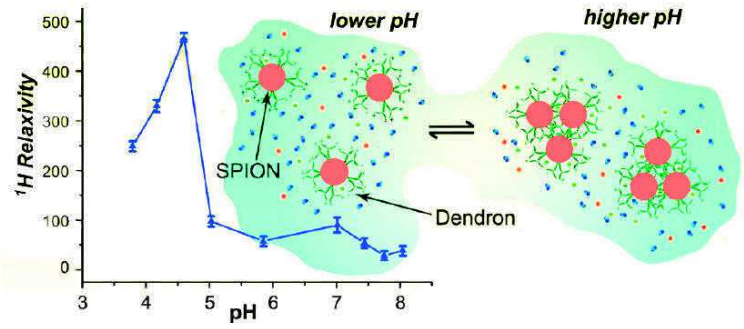

Figure 16: Representation of reversible microscale clustering of the dendron–SPIONs governed by the interplay of aggregation tendencies versus charge repulsion forces (modulated by ionic screening).[130]

dendron. Finally, by comparison with other dendrons displaying alternative functionalities (derivatives of Nitrilotriacetic acid or Poly (1–vinylimidazole)), the authors showed that these pH–sensitive MR responses were highly dependent upon chemical modification of the surface species and thus amenable to modulation through rational design.

Radionuclide–based CAs For the past decades Nuclear Medicine has demonstrated enormous potential to observe the complexity of systems *in vivo* at cellular, organ and whole body level. Positron Emission Tomography (PET) and Single Photon Emission Computed Tomography (SPECT) are the two common imaging techniques widely used in Nuclear Medicine, and are highly sensitive, highly quantitative, while showing high penetration depth.[131] Disadvantages associated with PET and SPECT imaging include the lack of anatomical information, the relatively low spatial resolution, and the necessity of using radioactive probes[132,133,134] which are rapidly cleared or metabolized and are unable to accumulate sufficiently in the targeted tissue.[135] Radionuclide–labelling of dendrimers displaying desired functionality has also been used for enhanced and specific imaging of a particular diseased tissue.[136]

Examples of routinely used Positron–Emitting isotopes in PET imaging are ^{11}C, ^{13}N, ^{15}O, ^{18}F, ^{44}Sc, ^{62}Cu, ^{64}Cu, ^{68}Ga, ^{72}As, ^{74}As, ^{76}Br, ^{82}Rb, ^{86}Y, ^{89}Zr, and ^{124}I.[137,138,139,140,141] Because of its high sensitivity, unlimited penetration depth, quantifiable results, and the broad range of available radionuclides, PET is highly suitable for pharmacokinetics, biodistribution and target site accumulation monitoring. Among the many examples available in the literature, a representative study in which PET was used to analyze the biodistribution of nanomedicine dendritic formulations has been published by Fréchet and colleagues.[142] They developed a unique approach to covalently attach on the dendrimer surface not only RGD peptides for cancer cells targeting, but also Tyrosine Amino–acids to be labelled with ^{76}Br. The developed nanoprobes had a modular multivalent core–shell architecture to which ^{76}Br was labeled in order to prevent *in vivo*

dehalogenation, while the terminal dendrimer amine functions were coupled to Lysine–modified cyclic RGD peptide. Such 12nm – sized (hydrodynamic diameter) nanoprobes showed excellent bioavailability as demonstrated by *in vivo* pharmacokinetic studies, and were able to specifically accumulate in an angiogenesis murine model of hind limb ischemia.

Wängler *et al.* reported an approach to link multiple (16 moieties) RGD peptides onto a dendrimer–based scaffold functionalized with DOTA ligands for ^{68}Ga labeling.[143] *In vitro* binding avidity towards $\alpha_v\beta_3$ integrin was evaluated on $\alpha_v\beta_3$integrin immobilized and $\alpha_v\beta_3$ integrin–expressing cells. Therefore, the developed dendrimeric platform may be used as promising contrast agent for PET imaging of $\alpha_v\beta_3$integrin–expressing tumor cells *in vivo*.

Ferrara and co–workers visualized atherosclerotic plaque in ApoE$^{-/-}$ mice with PET–CT and optical imaging using p32–targeted dendrimers. Imaging probes (FAM or 6–BAT) were conjugated to a Lysine or Cysteine (LyP or ARAL) on the dendrimer for Optical and PET studies **(Fig.17)**.[144]

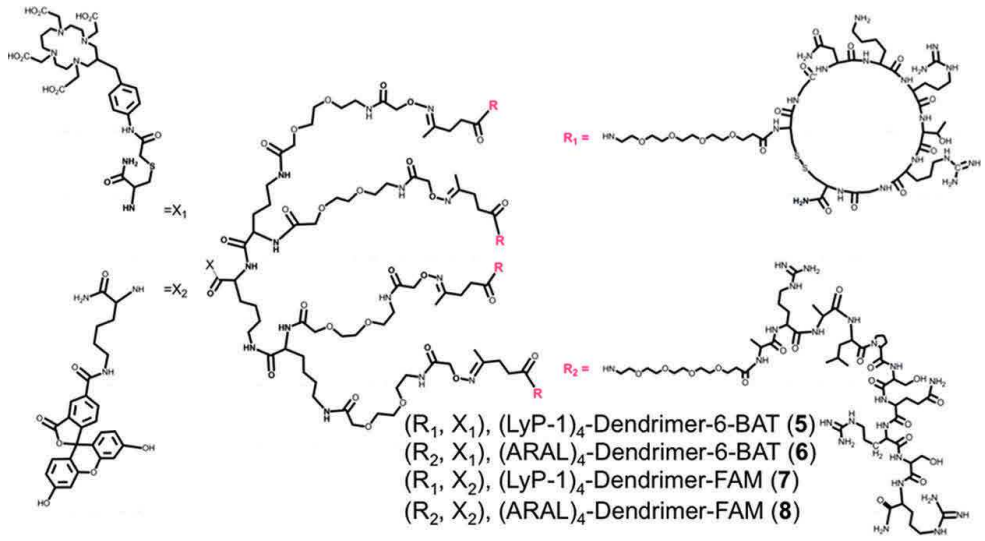

Figure 17: FAM– and 6–BAT–labeled LyP–1– and ARAL–dendrimers.[144]

For PET–CT studies, $(LyP–1)_4$– and $(ARAL)_4$– dendrimer–6–BAT were labeled with ^{64}Cu. Two hours after *iv* injection, PET–CT co–registered images demonstrated greater uptake of the $(LyP–1)_4$– dendrimer –^{64}Cu than the $(ARAL)_4$– dendrimer –^{64}Cu in the aortic root and descending aorta. *Ex vivo* images and the biodistribution acquired at three hours after injection supported the results of PET–CT imaging. In the same model system, *ex vivo* fluorescence images within aortic plaque depicted an increased accumulation and penetration of the $(LyP–1)_4$ –dendrimer–FAM as compared to the $(ARAL)_4$–dendrimer–FAM. Taken together, the results suggest that the $(LyP–1)_4$ –dendrimer can be applied for *in vivo* PET imaging of plaques and that LyP–1 could be further exploited for the delivery of therapeutics with multivalent carriers

or nanoparticles.

Analogous to PET, the most important advantages of SPECT are high sensitivity, highly quantitative results, and high penetration depth. The sensitivity of SPECT is about an order of magnitude lower than that of PET and its quantification is somewhat more difficult. Examples of radioisotopes used in SPECT are ^{99m}Tc, ^{111}In, ^{123}I, ^{88}Y and ^{201}Tl.

In a recent study carried out by Zhang *et al.*, G_5PAMAM dendrimers were used as a platform to link multiple DTPA chelates for ^{99m}Tc labeling, and FA as a targeting ligand for FAR–over expressing cancer cells.[145] The synthesized ^{99m}Tc–G_5PAMAM–FA conjugate had an excellent *in vitro* and *in vivo* stability, rapid blood clearance, and preferential accumulation at the tumor site as confirmed by SPECT imaging studies. In another study, authors linked PEGylated FA onto the dendrimer surface, followed by linking DTPA chelates for ^{99m}Tc labeling.[146] It seemed that ^{99m}Tc–labeled dendrimer–FA conjugates with PEG spacer between dendrimer and FA displayed excellent *in vitro* and *in vivo* stability, rapid blood clearance, specific accumulation in FAR–expressing tumors as confirmed by SPECT imaging studies.

Taking advantage of DTPA ligands for effective metal chelation, Kobayashi *et al.* synthesized ^{111}In and ^{88}Y–labeled G_2PAMAM dendrimers.[147] But their studies showed a very fast blood clearance and a high liver and spleen accumulation of the dendrimer conjugate. In this case, the dendrimer scaffold was not ideal for SPECT imaging applications. Therefore, dendrimers with different architectures, natures or generations may be used to improve the biodistribution of the radio–labeled conjugates.

Dual–modality CAs The idea of using multiple imaging techniques has recently gained in popularity, and researchers have come to realize that their complementary abilities (high sensitivity/poor resolution or high resolution/poor sensitivity) could be emphasized to great effect by using then in tandem. As the preponderance of recent reviews will attest, there has been a surge in research on multimodal imaging probes development over the past few years.[148,149,150,151,152]

In 2011, Begin–Colin, Felder–Flesch, and coworkers[153] investigated the synthesis of small–sized dendronized IONPs and their *in vitro* and *in vivo* MR and Optical imaging enhancement properties. Such pegylated nano–platforms showed high MR contrasting power at high magnetic fields (272 $mM^{-1}.s^{-1}$ for r_2, and with a $r_2/r_1 = 26.4$, at 7T). After post–functionalization of those dendronized IONPs with a fluorescent probe (Alexa647)[153] or with Patent Blue dye[154], no significant liver and spleen uptake was observed *in vivo* and bioelimination through both urinary and hepatobiliary pathways was highlighted both *in vivo* and *ex vivo*.[155] Begin–Colin and Felder–Flesch also reported in 2013 the biodistribution of Alexa647 – PAMAM – OligoEthyleneGlycol decorated IONPs of 10nm synthesized by thermal decomposition.[156] As shown by *in vivo* optical imaging **(Fig.18)**, such dendronized IONPs circulate freely and without RES uptake after

iv injection. They are also eliminated through urinary and hepatobiliary pathways with a faster elimination speed compared to fully pegylated dendronized IONPs.[157]

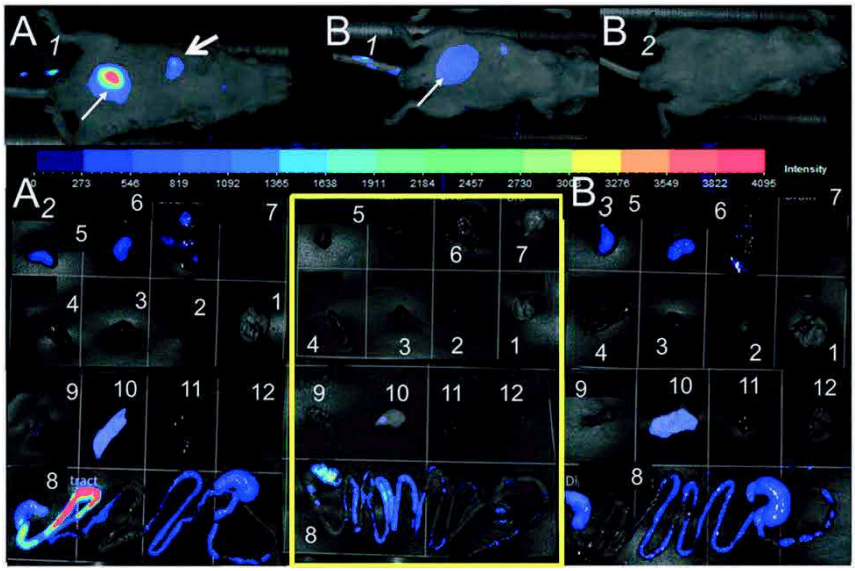

Figure 18: Bioelimination of dendronized iron oxide nanoparticles followed by optical imaging. (A1, B1 & B2) *in vivo* whole body and (A2 and B3) *ex vivo* optical images of PEGylated PAMAM dendronized IONPs labelled with Alexa647, performed at 7min (A1), 20min (B1), 30min (A2) and 24h (B2 & B3) post IV injection. The yellow square includes *ex vivo* organ images of control mouse imaged with the same parameters (1=lungs, 2=urines, 3=heart, 4=spleen, 5=kidney, 6=liver, 7=brain, 8=digestive tract, 9=bone sample, 10=skin sample, 11=blood sample, 12=muscle sample). Fine arrows indicate bladder signal, large arrow indicates liver signal.[156]

For targeted dual mode CT/MR imaging of tumors, it is essential to modify dendrimers with a targeting ligand. Li and co–workers recently designed a multifunctional FA– dendrimer– based nanoprobe for targeted dual mode CT/MR imaging of tumors.[158] G_5 dendrimers modified with DOTA– N– Hydroxysuccinimide, PEGylated FA, and PEG monomethyl ether were used as templates to entrap AuNPs, followed by complexation of Gd(III) ions and acetylation of the remaining dendrimer terminal amines. The formed Gd(III)–Au DENPs–FA probes showed specificity towards FAR–overexpressing cancer cells, and enabled targeted CT/MR (T1) dual modality imaging of the cancer cells *in vitro* and in xenograft tumor model *in vivo*.

In a proof of concept study, Cai *et al.* reported the use of Fe_3O_4@Au nanocomposite particles (NCPs) for dual mode CT/MR (T_2) imaging.[159] In their study, Fe_3O_4 NPs formed via a controlled co–precipitation method were assembled with multilayers of Poly (L–Glutamic acid) (PGA) and Poly (L–Lysine) (PLL), followed by assembly with Au DENPs. The formed Fe_3O_4@Au NCPs displayed relatively high r_2 relaxivity (71.55 $mM^{-1}.s^{-1}$at 3T) and enhanced X–ray attenuation property when compared respectively with pure Fe_3O_4 NPs or Au DENPs alone.

In an interesting study, Chrastina *et al.* reported on the applicability of hybrid SPECT–CT for the

noninvasive monitoring of a nanomedicine–based drug targeting the lungs.[160] To this end, G_5–PAMAM were functionalized with antibodies targeted to Aminopeptidase P2 (APP2), to mediate specific lung homing. Upon radiolabeling with ^{125}I, the dendrimers were followed by whole body SPECT–CT imaging 1h after *iv* injection. In case of non–targeted G_5–PAMAM–dendrimers accumulation in liver and spleen was highlighted. On the other hand, targeted G_5–PAMAM–dendrimers displayed a very strong affinity towards lung tissue, thereby nicely exemplifying the possibility of combining molecular SPECT with anatomical CT for non–invasive imaging of biodistribution.

1.2.2 Therapeutic applications

The advancement of small molecule pharmaceuticals through the regulatory approval process must involve a thorough understanding of pharmacokinetics (PKs) and pharmacodynamics (PDs). Typical PK studies investigate the absorption, distribution, metabolism and excretion (ADME) of the drug. These four parameters and the administered dose determine the concentration of a drug at the site of action and hence the intensity of its effects as a function of time. Developing a nanoparticle–based platform in combination with an approved drug may be expected to have added levels of complexity related to possible changes in the ADME of the drug. Thus, the number of dendrimers currently undergoing clinical testing for therapeutic applications is limited **(Table 2)**.

However, it is becoming widely recognized that dendrimer – *in vivo* tissue interactions such as complement activation, protein interactions (*i.e.* opsonization), excretion modes, cellular uptake, cell cytotoxicity and *in vivo* biodistribution patterns are strongly influenced by their Critical Nanoscale Design Parameter (CNDPs)[161] which can be tuned at will **(Fig.19)**.

A growing awareness of these *in vivo* CNDPs–dependent nanoperiodic property patterns in combination with the many unique dendrimer–drug relationships, have led to dramatically enhanced activity in emerging preclinical nanomedicine applications for drug administration/targeting modes and intrinsic dendrimer–targeting properties (*i.e.* inflammation targeting) **(Table 3)**.

Anti–inflammatory dendrimers Inflammation (from the latin inflammare, set on fire) processes are complex biological responses of body tissues to harmful stimuli, such as pathogens, damaged cells, or irritants. The function of inflammation is to eliminate the initial cause of cell injury, removal of necrotic or damaged tissues and initiation of the process of repair, involving immune cells, blood vessels, and molecular mediators. Inflammation treatment is often a gradual response involving a wide range of non–steroidal anti–inflammatory (NSAI) drugs and Glycocorticoid derivatives which are steroidal hormone analogs **(Fig.20)**. NSAI are used to inhibit the Prostaglandine synthase, also named Cyclo–oxygenase (COX) involved in the first step of

	Product	Composition	Condition	Phase	Identifier	Sponsor
In vivo	VivaGel® ABI– 007	Dendrimer–based topical	Treatment of bacterial vaginosis	3	NCT01577537	Starpharma Pty Ltd.
	DEP™ – Docetaxel DTX–SPL8783	Dendrimer–based conjugate	Advanced or metastatic cancer	1	Australian Clinical Trials AC-TRN12614000171617	Starpharma Pty Ltd.
	Gadomer 17	Poly(lysine) dendrimer	Contrast agent – for preclinical studies	Approved		invivoContrast GmbH
	OcuSeal®	Hydrogel–dendrimer	Ocular bandage	Approved		Beaver–Visitec International
In vitro	Stratus® CS Acute Care Diagnostic System	PAMAM dendrimer	Myocardial ischemia	Approved		Siemens
	SuperFect® Transfection Reagent	Activated dendrimer technology	DNA transfection into a broad range of cell lines	Approved		Qiagen

Table 2: Recent nanomedicine clinical activities involving dendrimer nanoplatforms.

synthesis of some inflammation mediators. Glycocorticoid derivatives produce Cortisol which affect several physiological processes, including immune response, inflammation regulation, carbohydrate and protein metabolisms.

The first use of dendrimers for anti–inflammatory purposes has been described in the late 90s. These strategies were related to drug delivery and involved either the encapsulation of known anti–inflammatory drugs within dendrimers, the conjugation of these drugs on dendrimer surfaces or the use of dendrimers having intrinsic anti–inflammatory properties.[197]

Non–covalent association of anti–inflammatory drugs with dendrimers The question of the host–guest interactions between the dendrimer and NSAI drugs depends on the nature of both components, nevertheless, based on a combinations of ionic and lipophilic interactions.[198,199,200,201] The formulation of well–known acidic NSAI drug Ibuprofen produced at 13000t per year with PAMAM dendrimers was at first considered a result of ionic surface interactions. Though, with more detail–oriented studies, researchers concluded that dendrimer/Ibuprofen stable complexes are favored by hydrogen bonding.[200] On the other hand, the affinity degree of other drugs for the dendrimers (Naproxen > Ketoprofen > Ibuprofen > Diflusinal) was found to be governed by the interaction of the drugs with the lipophilic interior of the dendrimer in

Application	Platform	Active agent	Remarks/Clinical status	References
Inflammation				
Drug delivery	PAMAM G_5	Methotrexate	Collagen– induced Arthritis.	[163]
	PAMAM G_4	Naked dendrimer	Chlamydia– induced reactive Arthritis.	[164,165]
	Phosphorus ABP terminated	Naked dendrimer	Rheumatoid Arthritis.	[166]
	PAMAM G_4	Naked indomethacin	Improved drug solubility and increased accumulation in inflammatory regions in Arthritic rats.	[167,168]
	PAMAM	Methyl–prednisolone	Allergen– induced lung inflammation.	[169]
	Mannose	Mannose–grafted dendrimer	Acute lung inflammation prevention.	[170]
	PAMAM G_4	Fluocinolone acetonide	Retinal degeneration model.	[171]
	PAMAM G_4	N– acetyl cysteine (NAC)	Single systemic administration of D–NAC on day 1 of life showed improvement in myelination and motor function in rabbit model of inflammation induced cerebral palsy.	[172]
Cancer				
Drug delivery or intrinsic dendrimer surface chemistry	PAMAM $G_{3.5}$	Cisplatin	Increased MTD and bioavailability of cisplatin, prolonged survival of mice with melanoma.	[173]
	PEG– PLL	Doxorubicin	Greater antitumor activity in breast cancer compared to liposomal formulation.	[174]
	PEG–PAMAM	Methotrexate	Greater antitumor activity compared to non– PEG dendrimer.	[175]

Table 3: Preclinical studies using dendrimer–based nanomedicine for *in vivo* therapy.[176]

Application	Platform	Active agent	Remarks/Clinical status	References
	PEG– PAMAM	Doxorubicin	RGD– conjugated PAMAM dendrimer showed greater tumor accumulation with PEG than without, and improved survival in animals with gliomas.	[177]
	PPI	Surfactants	Greater antitumor activity in brain tumors.	[178]
	PEG– PAMAM	5– fluorouracil and folate	Haemolytic toxicity was reduced with PEG– FA dendrimers, and accumulated in tumors compared to non– PEG dendrimers.	[179,180]
	PEG– PLL	Camptothecin	Enhanced survival in human colon carcinoma models.	[181]
Gene delivery	PAMAM	Oligo– DNA	Dendrimers could effectively deliver ^{111}In– labelled oligo– DNAs to tumor.	[182]
	PAMAM	Angiostatin gene	Intratumoral administration of dendrimers with the Angiostatin gene effectively inhibited tumor growth.	[183]
	PPI	DNA	Intravenous administration of transferrin–bearing PPI dendrimers led to rapid and sustained tumor regression.	[184]
Infectious disease				
Drug delivery or intrinsic dendrimer surface chemistry	PETIM– DG		Minimizes bacterial invasion in Shigella– induced gut wall damage in rabbits.	[185]

Table 4: Continue Table 3.

Application	Platform	Active agent	Remarks/Clinical status	References
	PAMAM–OH		Prevention of Escherichia coli infection in pregnant guinea pig chorioamnionitis model.	[186]
	PAMAM	Nacetyl–neuraminic acid	Inhibition of HA–mediated adhesion in influenza model.	[187]
	PEG– PPI	RIF	Tuberculosis treatment.	[188]
Gene delivery	PAMAM	siRNA	Suppressed HIV infection in humanized mouse model.	[189]
Diagnostic				
MR contrast	PAMAM G_4, G_6	Gd	Enhanced retention, reduced renal clearance.	[162,190,191,192]
CT/SPECT	PAMAM G_4	Triiodinated and chelated ^{99}Tc	Increases blood circulation time and provides effective simultaneous contrast enhancement in both CT and SPECT.	[193]
PET	Peptide dendrimer conjugate	Cyclic 9–amino acid peptide (LyP–1)	Ability to detect atherosclerotic plaques using *in vivo* PET imaging.	[144]
CEST	PPI, PAMAM G_2, G_5	DOTAM, MRI CAs	Used for pH mapping, to detect gliomas at very low agent concentrations.	[194,195,196]

Table 5: Continue Table 3. ABP – Azabisphosphonate; MTD – maximum tolerated dose; PETIM – Poly(propyl ether imine); DG – dendrimer glucosamine; HA – Hemagglutinin; RIF – Rifampicin; HIV – Human Immunoodeficiency Vvirus; HSV – Herpes Simplex Virus; siRNA – short interfering Ribonucleic Acid; LyP–1 – cyclic 9–amino acid peptide; CEST – chemical exchange saturation transfer.

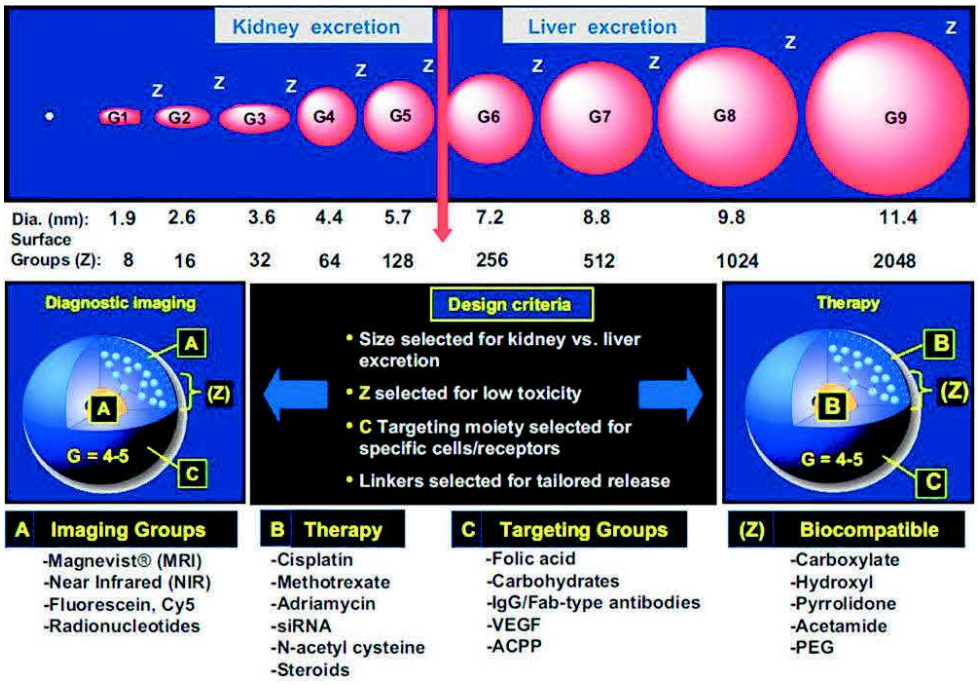

Figure 19: A schematic illustration of dendrimer CNDPs control and engineering for optimizing prototypes suitable for various nanomedical applications. (i) Size control (approximately 1nm per generation) with mathematically defined polyvalent surface functionality; (ii) polyvalent dendrimer surface chemistry can be chemically partitioned into imaging groups (A), therapy with cleavable linkers (B), targeting groups (C) and biocompatible or circulatory enhancement groups (Z).[162]

addition to the ionic interactions between the PAMAM amino terminal groups and the acidic fragments of the drugs.[202]

Introduction of PEG chains into dendrimers can increase their encapsulating properties. For instance, Mefenamic acid and Diclofenac have been formulated with PEG–cored dendrimers[203] built from biocompatible Citric acid.[204] The resulting system was found to be stable for several months and the release to be moderately accelerated at low pH. In another example, PPI dendrimers capped with PEG chains have been used to formulate a Diclofenac prodrug.[205] The loading capacity of the PPI dendrimers was significantly increased upon PEGylation, presenting more efficient *in vivo* reduction of paw edema[3] in comparison with the plain drug.[206]

In vivo studies have demonstrated that the cargo–loading strategy significantly increase the mean residence time and half–life of the dendrimer–formulated drug in comparison with the plain drug after intravenous administration.[207,208,209] It was also shown that oral administration of dendrimer–Ketoprofen formulations in mice (stomach pH 3–5)[210] leads to higher plasma drug concentration in animals.[211] In another example partially PEGylated PPI dendrimers were used to formulate Aceclofenac, a Diclofenac pro–drug. In

[3]Edema – an excessive accumulation of serous fluid in tissue spaces or a body cavity.

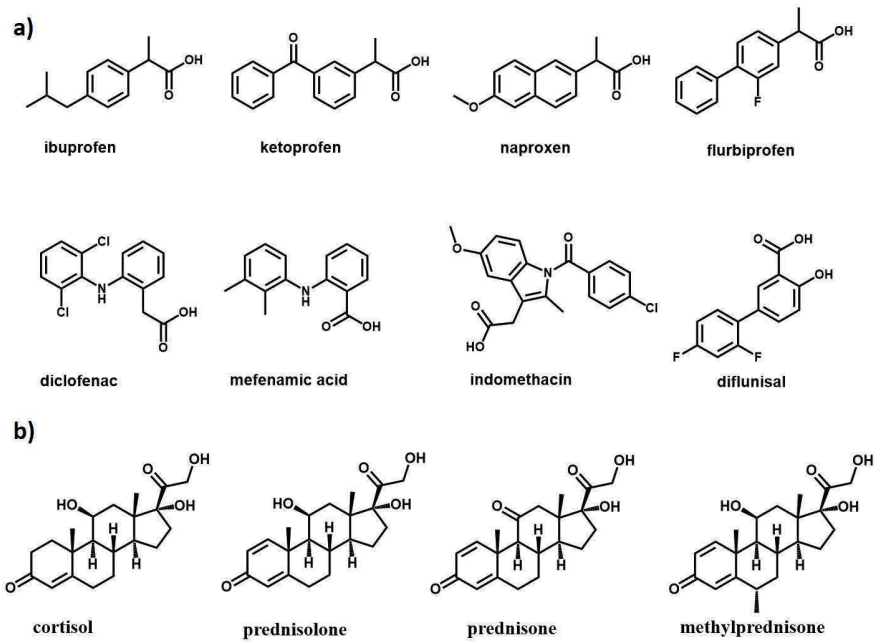

Figure 20: a) Examples of NSAI drugs and b) examples of Glycocorticoid derivatives formulated with dendrimers.

addition to the solubility enhancement provided by the PEG capping, *in vivo* studies showed an increased efficiency of the drug–dendrimer conjugate on the reduction of paw edema following *iv* administration in comparison with the plain drug.[205]

Microglial cells are immune components that regulate many inflammatory processes in the central nervous system (CNS), and their regulation is actually at the center of many therapeutic issues related to neuro–inflammation and/or neurodegeneration. In a recent study Carboxymethylchitosan–modified PAMAM–based nanoparticles have been shown to efficiently target *in vitro* and *in vivo* glial cells and neurons, proving them with the ability to cross the blood–brain–barrier and reach the desired target.[212] In another study, these systems were equipped with targeting antibody,[213] and they have been tested *in vitro* for the delivery of Methylprednisolone to microglial cells, in order to treat lateral hemisection lesions or spinal cord trauma.

Anti–inflammatory drugs linked to dendrimers Most studies are centered on the development of dendritic systems for the delivery of Methotrexate (MTX), a cytostatic drug used to treat several cancer conditions and chronic inflammatory diseases like Rheumatoid arthritis, Psoriasis or Crohn's disease.[214] The encapsulation of anti – inflammatory drugs within and/or on the surface of dendrimers preserves the chemical integrity and pharmacological properties. On the contrary, the pro–drug strategy involving a covalent attachment can alter its integrity, but it can provide a better control over drug release as demonstrated

in some isolated comparative studies.

In a pioneering study, Wiwattanapatapee and co–workers described the grafting of 5–Amino salicylic acid (5–ASA)[4] onto the surface of a G_3 PAMAM dendrimer.[215] The amount of drug released in one day was 45% and 57%, depending on the linkers, whereas the release of 5–ASA from commercial Sulfazaline was 80% in 6 hours (under the same conditions). This observation was explained by a steric hindrance of the enzyme sites in the case of dendrimer–supported 5–ASA. The group of D'Emanuele described the conjugation of Naproxen on a G_0 PAMAM dendrimer through amide or ester bonds thanks to L–Lactic acid or PEG spacers.[216] The conjugates were non–toxic when exposed to Caco–2 cells for 3h and the dendrimers significantly increased the transport of Naproxen across this model barrier.[212]

In another early example reported by the group of Kannan,[217] 58 Ibuprofen molecules have been attached to a G_4 Hydroxy–terminated PAMAM dendrimer (64 –OH groups) through an ester linkage, and FITC was coupled on the remaining hydroxyl groups. The authors observed a rapid internalization of these conjugates into lung epithelial cancer cell lines. The dendrimer–drug conjugate was found to be more efficient than the small molecular weight Ibuprofen–FITC analog in inhibiting the production of prostaglandin PGE2[5].

Dendrimers with intrinsic anti–inflammatory properties Few examples of dendrimers with intrinsic anti–inflammatory properties have been uncovered recently, in particular hydroxyl – terminated PAMAM dendrimers, Carbosilane dendrimers (CBS) and Polyphosphorhydrazone dendrimers (PPH) **(Fig.21)**, all of them displaying different backbones and surface functions.[197]

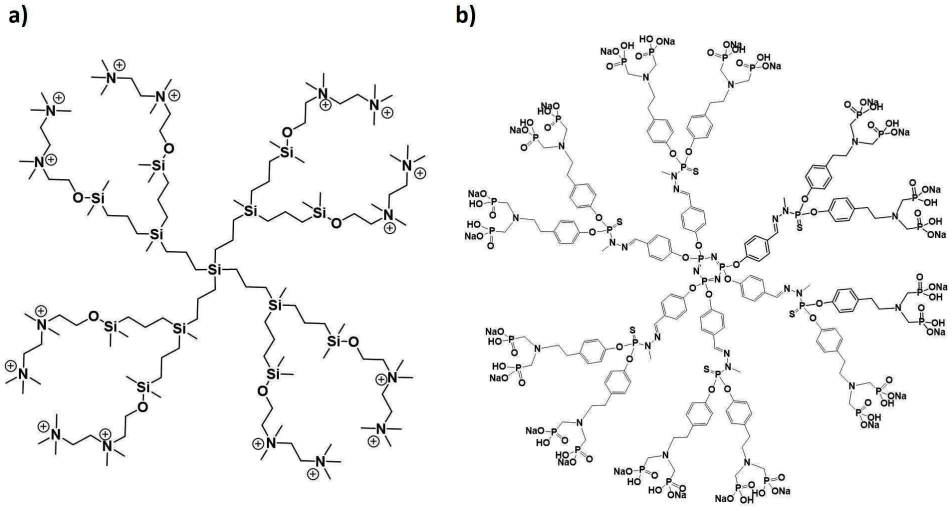

Figure 21: a) G_2–NN16 carbosilane dendrimer (CBS); b) G_1–**ABP** Polyphosphorhydrazone dendrimer (PPH).

[4] 5–ASA – the metabolite of sulfasalazine, anti–inflammatory drug used in the treatment of colon inflammatory disorders.

[5] Prostaglandin PGE2 – is also known as dinoprostone that plays a role in resolution of inflammation and it is known as fever inducer.

Among the CBS dendrimers, G_2–NN16 **(Fig.21.a)** dendrimers proved to be of particular interest due to their transfecting properties and ability to cross the blood–brain barrier.[218] For instance, it was found that G_2–NN16 was repressing Tc17 differentiation in primary TCD8+ lymphocytes, taking into account that TCD8+ lymphocytes are involved in the maintenance of inflammation in some autoimmune chronic inflammatory disease. Recently, another G_2 CBS dendrimer displaying 24 Diammonium salts on its surface was found to modify the behavior of M2 macrophages and turn them into an M1–like polarization state.[219] Basically, the M1 phenotype is associated to high levels of pro–inflammatory cytokines, whereas in contrast, M2 macrophages are likely to favor parasite containment and promote tissue remodeling and tumor progression with immuno–regulatory functions. These dendrimers could open new perspectives in oncology.

Polyphosphorhydrazone (PPH) dendrimers covered with phosphonic acids have also been identified as an emerging class of small dendrimers showing intrinsic immuno – modulatory and anti – inflammatory properties.[220,221,222,223,224] Recent studies showed that dendrimer G_1–ABP **(Fig.21.b)** activates human monocytes leading to anti–inflammatory and immuno–suppressive responses.[225] G_1–ABP dendrimer has been evaluated in several immuno–suppressive studies revealing a specific inhibition of CD4+ lymphocytes, which are pro–inflammatory monocytes.[226] Preclinical evaluation of this dendrimer in a Rheumatoid arthritis (RA) mouse model showed a complete inhibition and remission of arthritis with no adverse effect. The suppression of disease was evidenced by normal synovial membranes, reduced levels of inflammatory cytokines, absence of cartilage destruction and absence of bone erosion.[166]

In vivo studies have been endorsed on a set of G_4 and $G_{4,5}$ PAMAM dendrimers capped with various surface functions, on rats, in different anti–inflammatory assay methods.[227] Amine– and hydroxy–terminated PAMAM dendrimers showed better activity in reducing inflammation than carboxylic acid capped PAMAM. These compounds showed promising new strategies for the design of multivalent drugs systems.

Dendrimers for gene transfection Gene therapy involves the transfer (transfection) of different nucleic acids (DNA or small interfering RNA (siRNA)) into cells to repair genetic defects.[228,229,230] Efficiently turn–off gene expression has provided an enormous opportunity for exploitation in biomedical applications such as gene–based disease treatment. However, nucleic acid are highly negatively charged and hydrophilic, hence do not readily cross cell membrane to enter into cells. In addition, they are not stable and can be rapidly degraded by enzymes such as Nucleases or Esterases.[231] Efficient delivery systems which could prevent siRNA/DNA degradation and deliver nucleic acids to the site of interest are highly demanded.[232]

Vectors should be cell–specific, efficient, biodegradable, non–toxic, and non–immunogenic.[233] Viruses [234], cationic lipids and cationic peptides [235], cation ic polymers[236] such as the successful Poly(ethylene imine) (PEI)[237] and Chitosan[238] have been used. Although viral and Chitosan vectors are very effective

for nucleic acid delivery, increasing concerns over their safety and immunogenicity substantiate the need to develop alternative non–viral vectors.[234] Precise control of the size, mono–dispersity, tunable generation and peripheral functions are of great advantage for dendrimers as transfecting agents.[239,240,241,242]

Amino–terminated PAMAM and PPI dendrimers have received considerable attention for nucleic acid compaction and cell transfection.[243,244] For instance, dendronized magnetic IONPs have been employed as magnetoplexes for magnetofection, which is a powerful technology of gene delivery. In magnetofection, nucleic acid drugs were associated with G_6–PAMAM–SPIONs to form magnetoplexes which can rapidly concentrate on the target cells with the help of an additional magnetic field.[245]

Recently, Huang *et al.* prepared covalently linked PAMAM–IONPs conjugates of different PAMAM generations and used them to bind antisense Survivin oligonucleotides (asODN) to inhibit tumor cells growth.[246] The investigation was focused on gene transfection efficacy, uptake mechanism and biological effects of the nano–objects on breast (MCF–7 and MDA–MB–435) or liver (HepG2) cancer cell lines.

FA–modified Au DENPs were also used as non–viral vectors for the delivery of plasmid DNA into cancer model cell line (HeLa cells) overexpressing FA receptors.[247] In another study, Hussain and co–workers reported the synthesis of Poly (L–Lysine) dendron–DNA AuNPs and studied the release profiles of the surface–tethered DNA in water and cell culture media, together with the effect of ionic strength on dendron–Au NPs and DNA–dendron–Au NP complexes.[248,249]

Several recent attempts have combined dendrimers with other macromolecules and molecular assemblies to form better nucleic acid delivery systems and/or improve safety.[250,251,252] A recent attempt concerning α–, β–, and γ– Cyclodextrin–conjugation to the surface of PAMAM dendrimers, which significantly improved nucleic acid delivery and transfection efficiency.[253] The greatest transfection activity was attributed to α–Cyclodextrin covalently bound to the G_3 dendrimer in a 2.4:1 ratio (approximately 100 times higher for the dendrimer conjugate than for the native dendrimer or a noncovalent mixture of dendrimer and α–Cyclodextrin).

Peng and co–workers have developed Triethanolamine (TEA) core PAMAM dendrimers for nucleic acid, in particular siRNA, delivery.[254,255] The structurally flexible TEA–core dendrimers are able to bind siRNA and to form stable nanoparticles,[256,257] leading to effective protection of siRNA from degradation and significant promotion of cellular uptake via endocytosis, in particular, macropinocytosis. It was proven that G_7 PAMAM dendrimer family was the most effective for siRNA delivery and gene silencing of the luciferase gene in A549Luc cells. The excellent siRNA delivery capacity of this dendrimer was further confirmed by its effective delivery of a siRNA targeting heat shock protein 27 (Hsp27) in human castration–resistant prostate cancer PC–3 cells, generating potent down–regulation of Hsp27, and an effective anticancer activity was achieved in prostate cancer models *in vitro* and *in vivo*.[258] As Hsp27 is a molecular chaperone which

plays an important role in drug resistance, and has been recently considered as a novel target for treating drug–resistant prostate and other cancers.[259,260,261]

Weber *et al.* have developed Amino–terminated Carbosilane dendrimers (CBS) **(Fig.21.a)** for siRNA protection and transport.[262] These dendrimers were decorated with siRNA via electrostatic interactions, nevertheless, they showed a high transfection yield. Such dendriplexes were shown to silence GAPDH[6] expression and reduce HIV replication in SupT1[7] and PBMC[8] cell lines. These results point out the possibility of using CBS dendrimers to deliver and transfect siRNA into lymphocytes thus highlighting RNA interference as a potential alternative therapy for HIV infection.

However, the large–scale synthesis of high generation dendrimers with required quality for clinical translation is technically demanding. Therefore, it is highly desirable and preferable to develop small dendrimers of low generations or bifunctional dendrons with effective nucleic acid delivery capacity.

Drug delivery in cancer therapy At present about 40% of small molecule drugs in the pipeline of pharmaceutical companies are poorly water soluble and therefore can not be administrated. This exemplifies how nanotechnology may offer solutions to fundamental problems in the pharmaceutical industry. Besides, researchers have improved on the current standards in drug delivery relating to biodistribution, intra–cellular uptake, and dosing efficacy by utilizing dendrimers to encapsulate/absorb therapeutic agents and target disease sites, a strategy somewhat akin to the "Trojan Horse."[264]

Drug delivery In dendrimer–based drug delivery, a drug can be non–covalently encapsulated in the interior of the dendrimer or covalently conjugated onto its surface or within its inner backbone.

Drug loading can easily be tuned by controlling the dendrimer generation and its release could be triggered by specific stimuli like pH, degradable spacers between the drug and the dendrimer, transforming the drug into a prodrug.[265] In the past few years, the cargo loading ability of dendrimers has been one of the most flourishing field of research in dendrimer–based anticancer therapy.[266,267,268] Morgan *et al.* have studied the encapsulation of Camptothecin[9] within a G_4 Poly(glycerol)succinic acid dendrimer.[269] Improved anticancer effect resulted from the faster internalization of the dendrimer–based drug, with a higher retention time compared with the free drug in solution.[270]

In order to increase Doxorubicine (DOX) solubility in water and decrease its secondary effects on healthy tissues, it was loaded into PAMAM dendrimers (G_3 and G_4) and then encapsulated in liposomes. The

[6]Glyceraldehyde 3–phosphate dehydrogenase – is an enzyme which serves to break down glucose for energy and carbon molecules. In addition, GAPDH has recently been implicated in several non–metabolic processes, including transcription activation and initiation of apoptosis.[263]

[7]SupT1 – malignant T–cell of lymphoblastic lymphoma or lymphoblastic leukemia.

[8]PBMC – peripheral blood mononuclear cell.

[9]Camptothecin CPT – has been used in cancer chemotherapy in preliminary clinical trials but has low solubility and (high) adverse drug reaction.

dendrimer–drug complex resulted in a slower drug release, which was beneficial to increase its therapeutic index while reducing its side effects on healthy cells. This formulation was shown to be efficient against various cancer cell lines, including DU145 human prostate and MCF–7 human breast carcinomas.[271]

The therapeutic agents are internalized within the interior core space or by micellar formation of the dendrimers. A major drawback to these delivery systems is the lack of controlled drug release kinetics, with most systems releasing their payload over the course of several hours. Cisplatin cytotoxicity and release kinetics from the dendrimer was studied by Malik and colleagues in 1999.[173] Cisplatine encapsulation within, or conjugation onto, $G_{3.5}$PAMAM dendrimers revealed an increased accumulation of the drug in B16F10 melanoma cell line and decreased toxicity towards normal tissues compared to the free drug for both drug carrier forms.[173] The advantage of conjugation over encapsulation of Cisplatin resulted in a slower release of the drug, furthermore, the dendrimer–drug conjugate showed equal toxicity towards Cisplatin–sensitive and Cisplatin–resistant cancer cells.[272]

The Kannan group reported the conjugation of Methotrexate (MTX) through amide bonds to carboxylic acid–terminated $G_{2.5}$ PAMAM or amine–terminated G_3 PAMAM in order to evaluate the MTX delivery to sensitive resistant CCRF–CEM human acute lymphoblastoid leukemia and CHO Chinese hamster ovary cell lines.[273] If carboxylic acid–conjugated $G_{2.5}$ PAMAM–MTX system showed increased sensitivities towards resistant cell lines, amine–conjugated G_3 PAMAM showed similar to free Methotrexate. In another study, Paclitaxel was conjugated to PEG or G_4–PAMAM to compare the anti–cancer activity of the drug delivered by a linear or a dendritic carrier.[274] Upon exposure to human ovarian carcinoma A2780 cells, free Paclitaxel accumulated in the cytoplasm near the plasma membrane, whereas dendritic conjugate tended to distribute intracellularly in a more homogenous way compared to free drug. If PEG–Paclitaxel conjugates reduced 25–fold the drug efficacy, the dendritic PAMAM–Paclitaxel homologues decreased the IC50 compared to free drug, leading to the conclusion that the drug availability is dramatically influenced by the architecture of its conjugate.

A remarkable example of architecturally–optimized dendritic drug delivery was reported by Fréchet and Szoka reporting on the synthesis of an asymmetric Doxorubicin (DOX)–functionalized bow–tie dendrimer: DOX was conjugated to one side of a G_3 2,2–bis(Hydroxymethyl) propionic acid dendrimer with the other side of the dendrimer being PEGylated, in order to form an asymmetric bow–tie dendrimer containing 8–10 wt% DOX.[47] A pH sensitive linkage between the drug and the dendrimer was used in order to release the drug once and only it reached its target. A single intravenous injection of such PAMAM–DOX conjugate in mice bearing subcutaneous C–26 colon carcinoma tumors resulted in the complete tumor regression and survival of all mice over 60 days.

Targeted drug delivery The multifunctional dendritic architecture allows conjugation of both drugs and targeting ligands, for the selective delivery of anticancer therapeutic agents to cancer cells. Most strategies involve the use of small endogenous molecules, peptides, or monoclonal antibodies (MAb) that target overexpressed receptors at the tumor site (cell surface, angiogenic vessels).

In 2007 Hong *et al.* explicitly quantified the binding avidity of multivalent targeted G_5 PAMAM dendrimers containing different amounts of FA molecules.[275] The dendrimers demonstrated a dramatic enhancement of binding avidity of almost 5 orders of magnitude. The study present quantitative results for the multivalent effect of FA–targeted dendritic nanodevices. Baker and co–workers has investigated several variations of FA–conjugated dendrimers for targeted drug delivery. Surface conjugated FA G_5–PAMAM dendrimers were prepared where the remaining free amine groups were capped with Glycidol to neutralize the positive charges, and then further reacted with MTX.[276] FA–targeted MTX conjugates demonstrated high specificity towards KB cells overexpressing FAR.

Prostate specific membrane antigen (PSMA) is overexpressed in all prostate cancers, non–prostatic tumor neovasculature and vascular endothelium in most solid sarcoma and carcinoma tumors. PSMA J591 was conjugated to G_5–PAMAM and evaluated *in vitro* regarding binding affinities and internalization.[277] The antibody–dendrimer conjugate showed specific binding towards, and internalization into, PMSA–positive cells but not towards PMSA–negative cells. A similar study investigated two different antibody–G_5–PAMAM conjugates, 60bca and J591, for the targeting of CD14[10] and PMSA, respectively.[278] Targeting was achieved *in vitro* using two different antigen–expressing cell models including CD14–expressing HL–60 human myeloblastic leukemia cells and PMSA expressing LNCaP cells.

In another example, MTX was covalently attached to G_5–PAMAM bioconjugates containing Cetuximab, a MAb that acts as an Epidermal Growth Factor Receptor (EGFR) inhibitor and is currently used as a drug to treat colorectal, head and neck cancers. The bioconjugate showed a modest 0.8log unit reduction of its half maximal effective concentration (EC50), though its half maximal inhibitory concentration (IC50) was 2.7log units lower compared to free MTX.[279]

1.2.3 Theranostic applications

Designing nanoparticles for molecular diagnosis and targeted therapy is a challenge. Such systems have recently been described as Theranostics.[280,281] While both therapeutic compounds and imaging nanoparticles (NPs) have a long history, they have only recently begun to coalesce into the theranostic NPs.

The pioneering work in Theranostics dates back to the 1940s, when Iodine–123 (a γ–emitter) was used

[10] CD14 – has been a useful marker molecule for monocytes and macrophages. It is expressed in different cell types and in various diseases.

for diagnosis and then Iodine–131, that emits both γ– rays and β– particles, was used for imaging and radiotherapy of differentiated thyroid therapy.[282,283] The latter would be a typical clinical practice, in which molecular diagnosis is first performed to identify and stratify patients and then a corresponding theranostic agent is administered for both treatment and imaging–enabled non–invasive monitoring of the disease response.

In 2012 a system combining tumor targeting (FA), pH–responsive drug (DOX) release and SPIONs for MRI was developed by Li and coworkers.[284] (FA– PEG– PAMAM– DOX@SPIONs as represented in **Fig.22**).

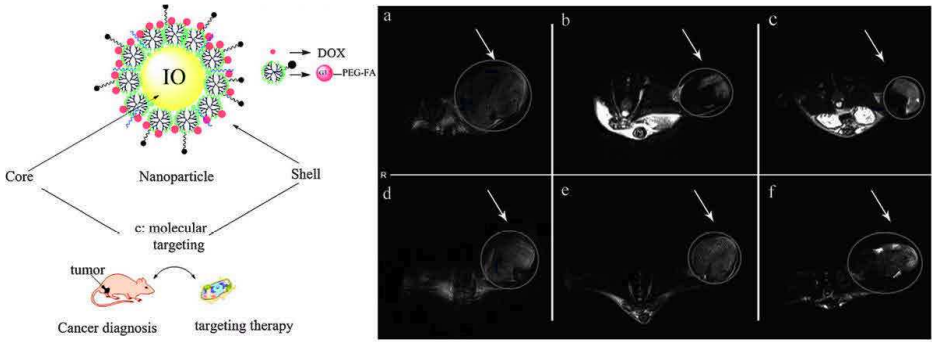

Figure 22: T_2–weighted fast spin echo images after injection of 2.5mg.mL^{-1} conjugates per mouse in 1h (a) FA–PEG–$G_{3.5}$ (b) PEG–$G_{3.5}$@IONPs (c) FA–PEG–$G_{3.5}$@IONPs (d) FA–PEG–$G_{3.5}$–DOX (e) PEG–$G_{3.5}$–DOX (f) FA–PEG–$G_{3.5}$–DOX@IONPs. The arrows denote allograft tumors, which are marked by circles.[284]

In vitro drug release studies indicated that DOX was mainly dissociated from the conjugates within the tumor cells nuclei or regions nearby. *In vivo* experiments showed great potential for application in both MRI detection and cancer therapy by virtue of their targeting function, which allowed the anticancer drug to be released directly to the target sites. In several studies, various PAMAM dendrimer–IONPs conjugates were also employed as nanocarriers of DOX[285] and Streptavidin[286] for theranostic applications.

IONPs are also developed for magnetic hyperthermia (MH).[151,287] When exposed to alternating magnetic fields of appropriate amplitude and frequency, these NPs release heat locally (where they are concentrated), which reduces the cancer cells viability. Moreover MH has been demonstrated to enhance the sensitivity of tumor cells towards chemo– or radio–therapies, to trigger a thermally–induced release of drugs or to act on cell membranes.[288]

However, one of the main limitations of MH is the low heating power of currently used magnetic NPs, requiring a local injection of large quantities of NPs. There is thus a great challenge for optimizing the heating power of magnetic NPs. The amount of heat generated by NPs is highly dependent on the NPs structural and magnetic properties. Preliminary studies have shown that IONPs with a mean size around

20nm are suitable for clinical MH.[289]

Begin–Colin and coworkers reported on the synthesis of NPs with variable and controlled shapes and core–shell structures and functionalized with small PEGylated dendrons.[290] The study revealed that oxidized nanocubes of 16nm (oxNC16) displayed high Specific Absorption Rate (SAR) values, displaying heating capacities suitable for hyperthermia treatment. At higher concentration, the SAR values strongly decreased, indicating an effect of iron concentration on the magneto–thermal properties **(Fig.23.A)**.

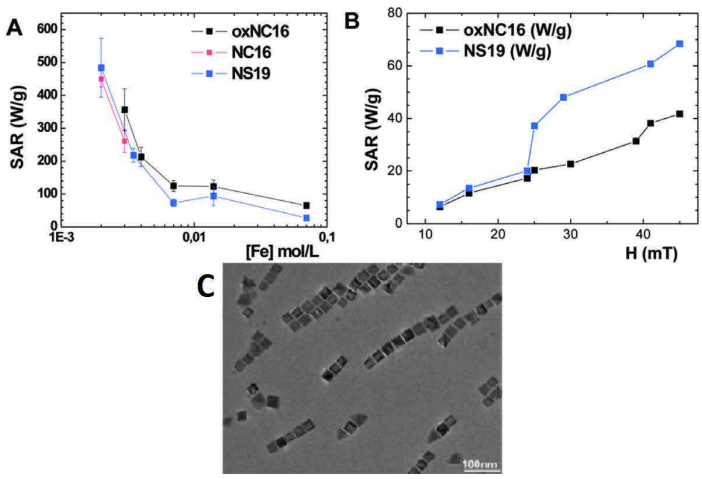

Figure 23: Magneto–thermal properties of oxNC16, NC16, and NS19. (a) SAR measurements determined as a function of iron concentration at 700kHz; (b) SAR values as a function of the magnetic field amplitude for highly concentrated oxNC16 and NS19 at 198kHz; (C) TEM images of NC16.[290]

Such a concentration effect has already been reported with nanocubes.[291] The formation of chains[292] with core–shell nanocubes was observed at low concentration by TEM without applying a magnetic field **(Fig.23.C)**, which may thus explain the high heating values due to magnetic anisotropy.

As shown in **Fig.23.B**, the SAR values increased almost linearly with the amplitude field. This confirms an aggregation of NPs when the concentration increases, leading to lower SAR values. Extensive studies of MRI properties demonstrated that core–shell $Fe_{1-x}O@Fe_{3-x}O4$ particles displayed very high *in vitro* and *in vivo* MRI contrast enhancements, even at very low concentration.[290] Furthermore, oxidized nanocubes exhibited interesting positive T_1 contrast at low concentration, allowing the envisioning of a dual contrast agent (*i.e.* positive contrast on T_1 images and negative contrast on T_2 images) with an improvement of the sensitivity related to the bright signal and thus improving the safety of the imaging interpretation procedure. In this way, such nanostructures appear very promising for combining MRI and hyperthermia.

1.2.4 Hydrogel for regenerative medicine

The field of regenerative medicine aims to regenerate, engineer or replace human cells, tissues or organs in order to establish the normal functionalities of the body. As every biomedical applications, regenerative medicine is applied only in aqueous systems, therefore hydrogels are of great promise in recreating and repairing living functional tissues. Indeed, hydrogels are three–dimensional structures similar to biological tissues having macromolecules and water as main components. Although they have been used in multiple biomedical applications (*e.g.*, contact lenses, delivery, scaffolds for tissue engineering, medical devices), supramolecular hydrogels are still challenging in controlling cellular functions, tissues morphogenesis and organogenesis .[293,294,295]

Dendrimers have been investigated as a rising class of hydrogel–based materials, as a result of their monodispersity and low viscosity with tunable size, architecture, density and surface groups. Water–soluble branched structures have multiple potential sites for covalent or non–covalent crosslinking, giving rise to three–dimensional networks with flexible physical and mechanical properties. [296]

Dendritic hydrogel's classification may be based on the nature of the crosslinking: the dendritic gel formation occurs through physical or chemical interactions between dendrimers and other similarly or complementary functionalized polymers **(Fig.24)**.

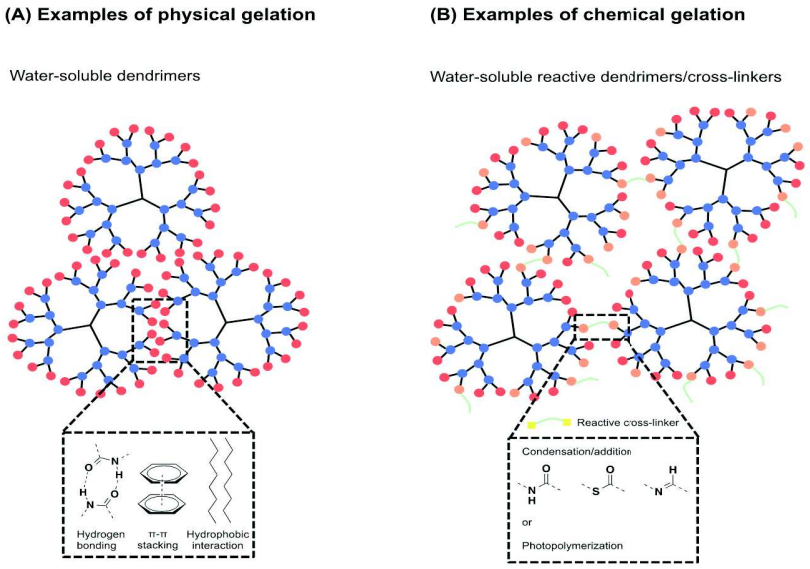

Figure 24: Representation of physical and chemical gelation of dendrimer based hydrogels.

Tissue engineering Tissue or organ transplantation is a common strategy to treat patients who suffer from loss or failure of an organ or tissue as a result of an accident or disease. However, this approach is extremely

limited by the number of donated organs or tissues. A revolutionary strategy would be the use of man–made organs or tissues engineered from the patient's own cells combined with a polymeric scaffold. The scaffold acts as an analogue to the extracellular matrices (ECM) found in tissues, allowing cell adhesion, proliferation, and interaction with other components in the matrix, as well as diffusion of nutrients, proteins, metabolites and waste products, while enhancing and controlling the tissue regeneration.[295] The biocompatibility of hydrogels is of utmost importance, else it might elicit an inflammatory response affecting the immune system and cause undesirable tissue formation.[297,298] Dendritic hydrogels are very promising as polymeric scaffolds for ECM mimic, because they are biocompatible, synthesized with a precise control of their structure, while showing crosslinking density, porosity, mechanical and degradation properties.

Grinstaff *et al.* developed *in situ* photo–crosslinkable scaffolds for articular cartilage tissue engineering.[299] The bio–dendrimer–based hydrogel was biocompatible and biodegradable, presenting high cross–linking properties with low swelling ratios, which favored their adhesion at the defected sites without causing any tissue damage. Moreover, the scaffold supported cartilaginous ECM production. Encapsulated chondrocytes showed no signs of dedifferentiation or morphological deformation, producing an ECM similar to native articular cartilage. The lower macromer concentration hydrogel scaffolds were especially supportive of cartilaginous ECM synthesis. They afforded more protein rich ECM, which might be due to beneficial diffusion characteristics for nutrients, waste products, oxygen and carbon dioxide, in a hydrogel with higher water content.

Another example of photo–induced cross–linked dendrimer–based hydrogel for tissue engineering was reported by Jia and co–workers.[300] Hydrogels composed of modified sphere–like PAMAM dendrimers and linear co–polymer of Poly(lactic acid)– b– Poly(ethylene glycol)– b– Poly(lactic acid) (PLA–PEG–PLA) as the linkage moiety, were conjugated with bioactive molecules and afforded enhanced stem–cell adhesion, differentiation and proliferation with no cytotoxic effects. The presence of PAMAM dendrimers provided PLA–PEG–PLA hydrogels with lower swelling ratios, due to the higher cross–liking density as a result of the dendritic effect, and further demonstrated their potential use in tissue engineering.

Tissue repair All type of wounds (*e.g.*, incisions, lacerations, contusions, ecchymosis, or petechiae) require immediate decontamination, closure and repair to prevent infection and stimulate healing. An ideal wound sealant needs to fulfill the following requirements: (1) quick and effective sealing of wounds, even on wet tissue, (2) adequate strength, (3) sustainable hemostasis duration, (4) preserve tissue suppleness, (5) timely biodegradable for tissue regeneration with no adverse effects to healing. Numerous wound sealants have been investigated to address specific requirements and to provide desired functions.[301] Although sutures remain a standard closure technique with high tensile strength, their placement have several disadvantages: (1) may

require anesthesia; (2) can induce infection, nerve damage, inflammatory reactions, granuloma formation, and scar tissue formation; and (3) is time–consuming. Therefore, dendrimer–based adhesives are of high clinical interest to overcome drawbacks of using sutures.

Grinstaff and co–workers have developed dendritic–based hydrogels for corneal lacerations, which can cause blindness if not treated.[302,303,304] They have evaluated photo–crosslinkable biocompatible and biodegradable copolymer composed of (Succinic acid (SA) and Glycerol (GL)) dendrons and linear PEGs, for the repair of full–thickness corneal lacerations **(Fig.25)**.

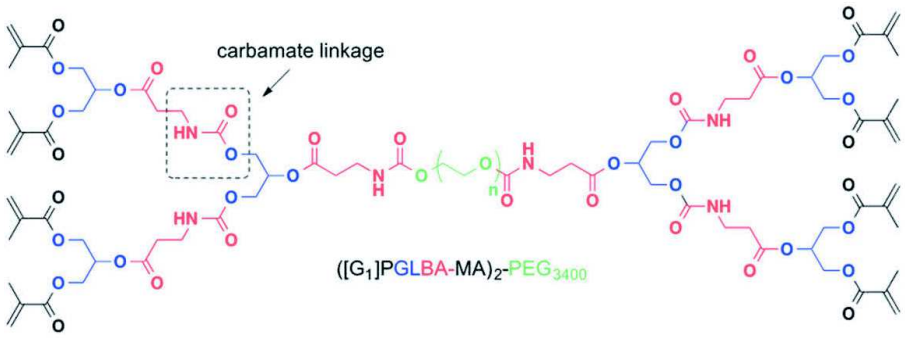

Figure 25: Structures of dendritic–linear–dendritic copolymer : β–alanate in red.

The photo–crosslinked copolymer generated a transparent hydrogel *in situ* with high adhesion properties, superior to the classical suture. The *in vivo* studies carried out using a chicken eye model, showed successful sealing of lacerations by post–operative day 2, exhibiting more uniform corneal structure with less scarring than those treated with sutures **(Fig.26)**. The dendrimer was gone from the wound site by day 14, and showed no toxic response, while nylon sutures were still present at day 28.

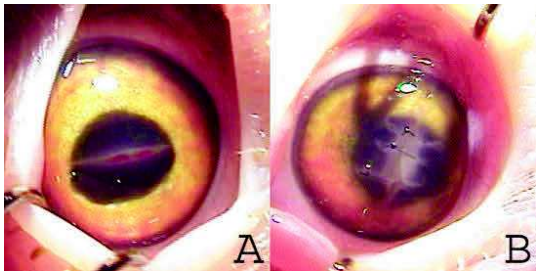

Figure 26: Full–thickness corneal lacerations secured with the photocrosslinkable dendrimer sealant (A) or with a traditional suturing technique (B). Photographs of sealed wounds at 7 days.[304]

The same group investigated alternative cross–linking dendrimer–based hydrogels that do not require photopolymerization. Their strategy was to use covalent crosslinking of amine terminated – G_1– peptide dendrons A and NHS – PEG – NHS B **(Fig.27.1)** to form A:B hydrogel sealant for the repair of scleral incisions used in *pars plana vitrectomy* procedures. *Pars plana vitrectomy* is the surgical removal of the

vitreous gel from the eye in order to redress the vision. The vitreous gel withdrawing is followed by retina repairing, then the eye is refiled with a saline solution to restore and maintain the normal intraocular pressure (IOP) and incisions are closed with sutures until the wounds are healed. The wounds treated with the A:B hydrogel attained higher pressures than those treated with sutures. The high adhesion strength of the hydrogel to the tissues was likely due to the formation of an interpenetrating network between the gel and the host tissue, as suggested by the authors, reinforced by the possible reaction of residual NHS units of the hydrogel with amino groups of proteins presented in the ECM of the tissue.

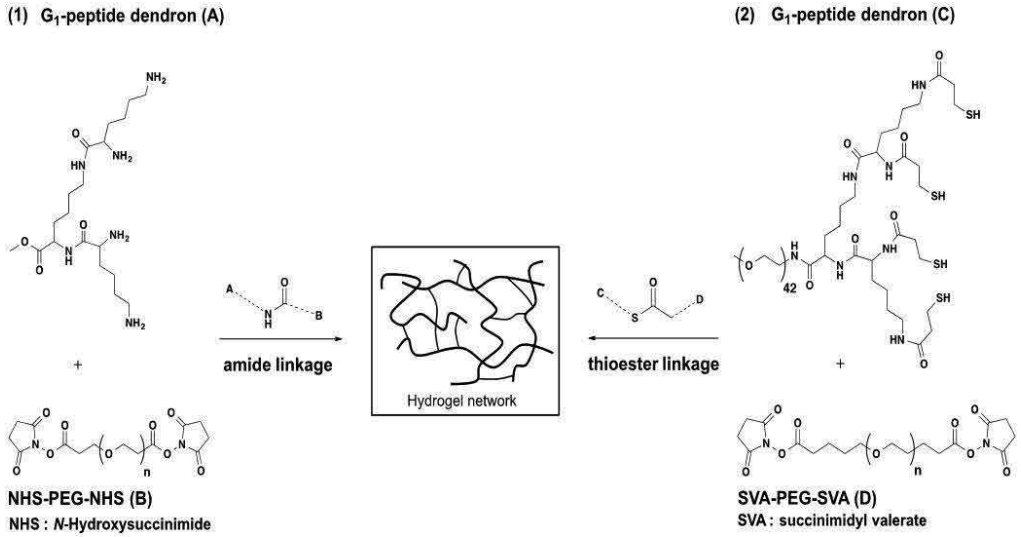

Figure 27: Examples of dendritic hydrogels based on covalent cross–linking formed via (1) amide linkage and (2) thioester linkage.

Another dendrimer–based hydrogel was developed by Grinstaff *et al.* as hemostatic adhesive, where the material can be applied on a wound to seal it and stop the bleeding, and be dissolved on–demand at a later time, for wound re–exposure and further surgical treatment.[305] The crosslinking of thiol–terminated–G_1–lysine dendrons C with SVA–PEG–SVA D **(Fig.27.2)** formed a 3D network within seconds at room temperature, through reversible thioester linkages.

The formed transparent C:D hydrogel presented no *in vitro* cytotoxicity and exhibited high sealing properties even under high pressures. Additionally, the hydrogel was completely dissolved when exposed to cysteine methyl ester solution, as a result of the thiol–thioester exchange mechanism between the thioester linkages in the hydrogel network and the added thiolate. This work is the first example of a hydrogel sealant that adheres strongly to skin tissues, secures the wound and dissolves on demand, and a big step forward in severe–burns care.

Bioactive Trizma®–based dendritic cross–linkers as adhesive primers for the stabilization and repair of

fractured bones were recently reported.[306] Dendritic scaffolds with azide/triazine and alkene groups were post–functionalized via clickable reactions and incorporated in composite materials composed of thiol–ene based matrices for further cross–linking with the adhesive primers, and E–glass fiber layers for reinforcement of the materials adhesive strength (a fiber reinforced adhesive patch (FRAP)) **(Fig.28)**.

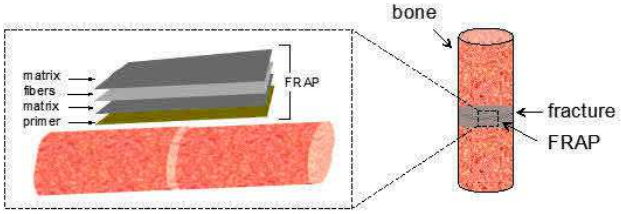

Figure 28: Schematic representation of the FRAP on fractured bones.

Both the FRAP matrix and the Trizman® based dendritic scaffolds presented no toxicity towards MG63 osteoblast cells. Furthermore azide functions within the dendrimers structure can undergo rearrangement upon irradiation and in the presence of water generate bindings to the extracellular matrices, thus reinforcing the binding strengths of FRAPs on wet bones. These composite materials based on dendritic cross–linkers are a promising strategy for polymer implants in bone fixation applications.

1.2.5 Biodistribution and pharmacokinetics

Understanding the influence of dendrimer properties – critical nanoscale design parameter (CNDPs) – on clinical translation issues, such as pharmacokinetics (PKs), pharmacodynamics (PDs), bioaccumulation and biodistribution, excretion modes and toxicology, is of utmost importance. These CNDPs include size, shape, surface chemistry, flexibility/rigidity, architecture and elemental composition. [307] The ability to structure, control and engineer CNDPs is undoubtedly the major challenge in the translation of dendrimers into approved clinical applications.

To date, numerous literature examples demonstrate improved pharmacokinetic behavior and activity of small molecule drugs in preclinical rodent models as a result of their covalent or non–covalent association with dendrimer–based carriers. However, I will refer to the pharmacokinetics of a dendrimer as meaning the absorption, distribution, metabolism and elimination (ADME) properties of the carrier, more accurately referring to 'what the body does to a dendrimer' rather than 'what the dendrimer does to the body' – known as pharmacodynamics.[308]

Intravenous pharmacokinetics Dendrimers have a resemblance in size (both molecular weight and hydrodynamic diameter) to many globular plasma proteins. As a result, dendrimers have the capacity to show

rapid clearance from the body and passage through epithelial barriers, such as the vascular wall. This, however, also restricts how dendrimers can be administered (with the intent of administration as a drug or drug delivery system). For small molecule drugs, the common method for drug administration is via the oral route. For dendrimers and other macromolecular drugs and drug carriers, however, administration is usually limited to parenteral (eg. intravenous, subcutaneous and intramuscular) injection. Once dendrimers reach the blood, they are subjected to *in vivo* clearance processes that define how rapidly the dendrimer escapes from the vascular system, the distribution in the body, biotransformation and excretion (via the urine and feces). These are classically defined by the size of the dendrimer and how it interacts with cells and tissues of the body (mainly dictated by surface charge, lipophilicity, structural flexibility, shape).

Effect of size The size of dendrimers may be increased by either increasing the dendrimer generation or by increasing the molecular weight of surface–grafted polymers (*i.e.* Poly(ethylene glycol) polymers). In general though, the size of a dendrimer is correlated to its molecular weight and the hydrodynamic diameter to the volume occupied by the dendrimer, both are not necessarily linear. Furthermore, an increase in molecular weight or hydrodynamic diameter typically has the effect of limiting urinary excretion by restricting permeability through glomerular filtration slits in the kidney (that are approximately 25nm in diameter)[309], that typically has the effect of prolonging the blood circulation time. The exclusion limit of glomerular filtration is approximately 68kDa and as a result, larger dendrimers display half–lives longer than one day, and rely on other processes for *in vivo* elimination **(Fig. 29)**.[310,311]

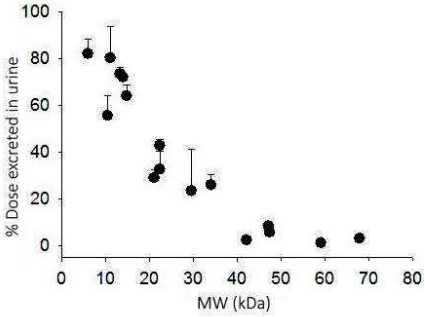

Figure 29: Correlation between dendrimer molecular weight and urinary excretion of PEGylated Poly(Lysine) dendrimers.[312]

For large dendrimers that are not eliminated via the urine and which cannot rely upon biodegradation in smaller fragments, the primary mechanism for blood clearance becomes the much slower uptake process via organs of the reticuloendothelial system (RES). These organs include liver, spleen, lungs, lymph nodes, bone marrow and thymus and are rich in macrophages that over time, recognize dendrimers as 'foreign' and remove them from blood largely via phagocytosis. For instance, a study by Kobayashi demonstrated that

an increase in generation for Gd–conjugated PAMAM dendrimers from 6 to 7, resulted in increased blood residence times and increased uptake into the liver and spleen.[313]

There is also some evidence to suggest that PEGylated dendrimers can be excreted via the feces after intravenous administration. The largest proportion of dendrimers ever quantified in feces after intravenous delivery was 37–47% after administration of PEGylated G_1 Polyester 'bow–tie' dendrimers ranging in molecular weight from 22 to 44kDa.[314]

The effect of a linear (L1) versus a PEG dendritic coating of low generation (generation 1 (G1), 2 (G2) or 3 (G3)) of Fréchet–type PEGylated dendrons, on the bio–elimination of spherical SPIONPs of 10nm (NS10) was pointed out by Felder–Flesch and co–workers through *ex vivo* optical biodistribution studies.[315] NS10 functionalized with a linear PEG (L1), and the lowest generation G1 or G2 circulated freely without significant lung uptake post *iv* injection and with both urinary and hepatobiliary eliminations as showed by *ex vivo* optical imaging studies **(Fig.30)** after coupling to an Alexa dye (Alexa647).

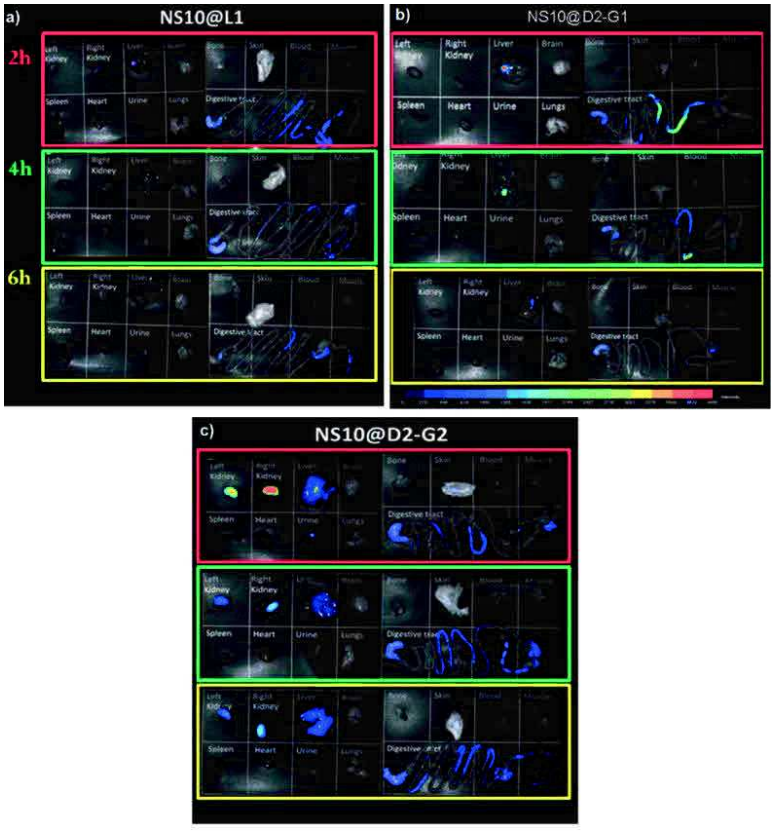

Figure 30: Optical images of mice organs removed 2, 4 and 6h post *iv* injection of NS10@L1 (a), NS10@D2-G1 (b) and NS10@D2-G2 (c).[315]

However, the kinetic of the hepatobiliary elimination is both intense and fleeting for the NP@L1, so intense but more sustainable for NP@G1 and NP@G2. At 6h post *iv* injection, the total body elimination of

NP@L1 is completed whereas a still time persistent hepatobiliary elimination process is observed for NP@G1 as evidenced by the persistent fluorescent signal in the gall bladder and the digestive tract. At the same time delay, the NP@G2 signal was still persistent and intense in kidneys and liver. These examples show the significant differences that can exist in the PKs and elimination profile of dendrimers and dendronized nanoparticles with different scaffolds and surface construction. As underlined by H. Kobayashi, other features among which flexibility and surface charge can affect *in vivo* behavior of nanosized hybrids.[316]

Effect of surface charge The surface charge is a critical determinant of how the dendrimer surface interacts with membranes, cells and plasma proteins, which has a significant impact on the dendrimers *in vivo* behavior. Dendrimer generation is also important when discussing the impact of charge on PKs. The number of charged groups on the dendrimer surface is directly proportional to the dendrimer generation and thus influences the number of electrostatic interactions with membranes, cells and plasma proteins.

Cationic dendrimers have a strong affinity for anionic charges present on membranes and cell surfaces, inducing an increased cytotoxicity which has limited their *in vivo* application.[317] However, cationic dendrimers adhere rapidly to vascular membranes after intravenous administration, leading to a rapid clearance from blood and high liver biodistribution.[318,319]

Dendrimers with an overall anionic surface display longer circulation times than cationic dendrimers, since their interaction with cells and membranes is reduced.[320] For instance, dendrimers bearing surface functionalities with relatively high pKa values (such as Carboxyl functions) and which are therefore less highly charged at physiological pH are cleared via the urine and RES organs as a function of size. For anionic dendrimers bearing surface functionalities with much lower pKa value (such as Arylsulphonate–conjugated systems), PK profiles change considerably as a result of increased binding to plasma proteins (*i.e.* opsonization). Thus, a G_4 Poly(Lysine) dendrimer bearing 32 Benzenedisulphonate groups was previously shown to display more avid opsonization in plasma and biodistribution towards the liver and spleen when compared to a G_4 dendrimer bearing 32 Benzenesulphonate groups.[321] Plasma protein binding does not always lead to extensive liver targeting since opsonization is not only dictated by how dendrimers are bound to plasma proteins, but also which plasma proteins are involved. Some plasma proteins promote liver targeting (opsonins) while others prevent liver targeting (dysopsonins).[322]

Effect of structural flexibility The composition and structure of dendrimer scaffolds impact their pore transit (*i.e.* the length of PEG chains at the periphery of dendrimers). For instance, it is already well established that linear polymers are cleared from blood more easily than more rigid, branched polymers, such as dendrimers, of similar size. The ability of linear polymers to better maneuver through glomerular

filtration slits in the kidneys conduct their excretion via urine path.[323]

Even within a given class of dendrimer, significant differences in blood clearance can be evidenced by introducing small changes in the scaffold or surface structure that impact on flexibility. A good example was demonstrated by Gillies *et al.* using Poly(ester) bow–tie dendrimers.[314] They showed that smaller generation (G_1, G_2) dendrimers conjugated with several long PEG chains displayed shorter plasma half–lives and greater urinary excretion than similar molecular–weight G_3 dendrimers with more, but shorter PEG chains. Differences in plasma PKs and urinary excretion have also been observed following a modification of a PEGylated G_4 Poly(lysine) dendrimer.[324] In this case, replacement of the G_4 Lysine layer in the Poly(Lysine) dendrimer by the symmetrical Lysine analogue Succinimyldipropyldiamine (SPN) resulted in a 10% reduction in hydrodynamic volume, also a decrease in plasma clearance and urinary excretion. This was explained by the SPN layer increasing structural rigidity, which limited the capacity of the dendrimer to traverse vascular and renal membrane barriers.

Tumor biodistribution Understanding the biological processes involved in the distribution and retention of nanomaterials inside the tumors is indispensable to the development of personalized nanomedicine approaches. It is now acknowledged that all patients do not respond equally to therapies, as a result, personalized treatment of patients is based on the genetic profile of their tumors.[325]

Passive tumor targeting General features of tumors include leaky blood vessels and poor lymphatic drainage. The increased permeability of the blood vessels in tumors is characteristic of rapid and defective angiogenesis (formation of new blood vessels from existing ones). Furthermore, the dysfunctional lymphatic drainage in tumors retains the accumulated nanocarriers and allows them to release drugs into the vicinity of the tumor cells. Given that inter– and intra–tumoral variability can affect the architecture of the neovasculature and the tumor microenvironment, it becomes apparent that the passive targeting to tumors may be more complex than originally assumed.[326] The tumor accumulation of therapeutic macromolecules was first reported for Poly(Styrene–co–maleic acid)–neocarzino statin (SMANCS). The distribution of SMANCS to the tumor vicinity was observed in early preclinical development and led Matsumura and Maeda to further show that proteins larger than 30kDa (*i.e.* SMANCS, murine and bovine albumins) could preferentially distribute to the tumor interstitium and remain there for prolonged periods of time.[327] This preferential distribution to the tumors was caused by the fenestrations present in the imperfect tumor blood vessels and by the poor lymphatic drainage in the tissue **(Fig.31.main)**. The combination of these two phenomena was coined as the Enhanced Permeation and Retention effect (EPR). Nonetheless, the EPR effect is much more complex than initially defined.

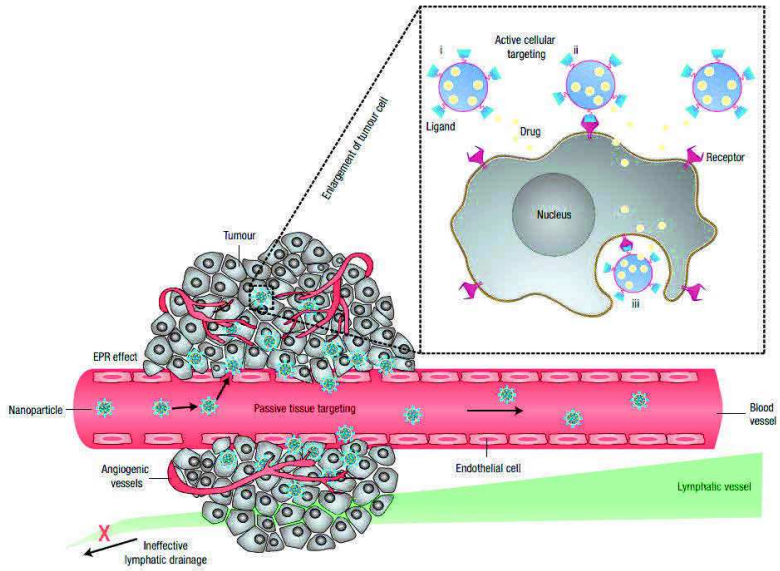

Figure 31: Schematic representation of tumor passive targeting by the EPR effect (main) and active targeting to sites on tumor cells (insert).[328]

The phenomenon has somehow embraced dozens of complex biological processes (*e.g.*, angiogenesis, vascular permeability, hemodynamic regulation, heterogeneities in tumor genetic profile, heterogeneities in the tumor microenvironment and lymphangiogenesis).[329] These factors vary among patients and their tumor types, nevertheless, they facilitate the extravasation of macromolecular therapeutics from the blood and lymphatic drainage, which collectively leads to the passive accumulation of nanomaterials in tumors. Dendrimers with longer circulation times tend to display higher accumulation in tumors, thus passive tumor biodistribution is, in large part, a function of dendrimer size.

However, while the EPR effect provides a facile means of directing dendrimers to solid tumors, this approach could also limit the tumor distribution of dendrimers, *i.e.* the presence of other concurrent pathologies which induce hypervascularization, and therefore increased intratumoral pressure.[330,331]

The last 30 years have shown the important role of EPR in the delivery to tumors, nevertheless, it has a high degree of interpatient variability and the importance of tumor heterogeneity in the EPR effect in humans has yet to be established.[332] A meaningful exploitation of the EPR effect in humans convey assessing the tumor microenvironment in individual patients and predicting their susceptibility to the EPR effect.

Active tumor targeting The main mechanism behind active targeting is the recognition of a ligand or an antibody by its receptors that are overexpressed on tumor cells **(Fig.31.insert)**. The interactions of ligand–functionalized dendrimer systems with their target antigen are enhanced by the multivalent nature of the dendrimer architecture: multiple copies of the ligand increase the avidity of the dendrimer for its target.

The targeting specificity is determined by the biodistribution of the ligand–functionalized dendrimer and by how the conjugated ligand and the dendrimer interact with off–target molecules and cells. Currently, actively targeted dendrimers are envisioned as a promising complementary strategy to EPR to further augment the efficiency of cancer nanomedicines.

FA–conjugation has most commonly been utilized to improve the tumor disposition of dendrimers, as this is a small and readily available molecule that is relatively simple to handle and attach.[333,80,334] As an example, by decorating the surface of PAMAM dendrimers with FA, the dendrimers have exhibited greater tumor uptake than similar constructs without any FA at their periphery.[80] However it must be noted that the receptor targets mentioned above are not exclusively overexpressed in cancerous tissue and in the case of folate, concurrent uptake into the lungs and kidneys occurs. Antibody targeting to HER–2 has also been employed to improve the tumor targeting of dendrimers.[335] However the large size of antibodies (approx. 150kDa) compared to much smaller peptide–based ligands (up to several hundred Da) may significantly alter the dynamics of intertumoral diffusion and PKs, which are expected to reflect the antibody, rather than the dendrimer.

The design of actively–targeted dendrimers for clinical use is often considered to be more costly than the development of non–targeted dendrimers.[336] A significant proportion of the financial burden is associated with scaling up and manufacturing, while the costs associated with large–scale clinical trials are certainly much more prohibitive. The development of one versatile targeted platform that could simultaneously treat multiple cancers is very attractive to clinicians and investors. A good compromise is using targets like Prostate Specific Membrane Antigen (PSMA) which are expressed in the neovasculature of multiple types of cancer. Despite the specificity for prostate cancer, PSMA is found in the vasculature of almost all types of solid tumors.[337] The results of a Phase 1 clinical trial on 28 patients showed one complete response (cervical cancer), 3 partial responses (prostate, non–small cell lung carcinoma (NSCLC) and ampullary cancer) and 5 stable diseases (pancreatic, colorectal, gall bladder, tonsillar and anal cancers), demonstrating that the targeted therapy could be beneficial in a variety of different solid tumors.[338,339,340]

Subcutaneous pharmacokinetics Dendrimer formulations are typically administered parenterally (*i.e.* via intravenous, subcutaneous (SC) or intraperitoneal injection), as a result of their high molecular weights and resultant low diffusion rates across epithelial barriers. In view of the large amount of literature dedicated to the subcutaneous administration of dendrimers, the absorption of dendrimers from subcutaneous injection sites appears to be very important since it is less intrusive compared to intramuscular or intravenous administration (it can be performed at home without medical supervision or significant training).

Absorption of nanomedicines from the interstitium can occur via the circulatory or the lymphatic system,

preferentially discriminated by size.[341] Kobayashi and coworkers demonstrated that gadolinium–labeled PAMAM dendrimer generation influences both subcutaneous diffusion rates and lymphatic uptake.[342,343,344] Smaller dendrimers (G_2 and G_4) showed significant nonspecific diffusion at the injection site, whereas larger scaffold G_6 dendrimers (hydrodynamic radii greater than 10nm) were largely retained in the early lymphatics resulting in improved resolution of the draining lymph vessels and downstream lymph nodes. Interestingly, as the size (and generation) of the dendrimers further increased to G_8, the benefit of retention in the early lymphatics was offset by slower diffusion through the interstitial space. Increased hydrophobicity of similarly sized dendrimers has also been shown to increase lymphatic drainage and imaging resolution for a G_5 Poly(propyleneimine) (PPI) dendrimer with a Diaminobutane (DAB) core when compared to a G_4 dendrimer of comparable molecular weight.[342]

The subcutaneous space is made up of a structural scaffold of collagens, elastins, fibrins and Polyanionic Glycosaminoglycans (GAGs).[345] The net negative charge conferred by GAGs renders charged drug delivery systems vulnerable to unwanted electrostatic interactions. Cationic species may interact directly with the GAGs preventing diffusion to the vasculature, while anionic species are repelled from the GAG rich matrix. There are only a few examples of subcutaneously administered cationic dendrimers.[346] However a cationic L– Arginine– grafted PAMAM (PAM–RG4) dendrimer has recently been successfully used in nonviral gene therapy for the treatment of diabetic skin wounds in mice.[347] While these studies did not investigate the systemic exposure of the PAM–RG4 dendrimers, they were reliant on local retention of dendrimer. Thus it can be postulated that increased skin wound healing was attributable in part to co–localization of the cationic dendrimer DNA polyplex with proliferating cells at the injection site, *i.e.* the cationic dendrimer did not diffuse into the systemic or lymphatic circulation.

More recently, a partly PEGylated G_5 Poly(Lysine) dendrimer was administered subcutaneously to rats.[348] The dendrimer, with 50% PEG surface coverage and 50% uncapped primary amines had a bioavailability of 76% which was lower than that of a similar fully PEGylated dendrimer.[349]

Generally, it can be conceded that neutral surface coatings provide improved dendrimer diffusion from subcutaneous injection sites. However, the studies described above have also investigated downstream lymph node disposition of dendrimers and while uncharged species are characterized by long circulation, their PEG coatings can also preclude efficient targeting to the site of action due to steric shielding. As a result, dendrimer surface chemistry requires a balance between sufficient surface coating to facilitate diffusion through the interstitium, longevity in the systemic circulation and adequate targeting to ensure the carrier is effective at the site of action.

Dendrimers have significant potential for systemic administration via subcutaneous injection, as lymphatic CAs for cancer staging and for the localized treatment of lymph–resident diseases, such as lymph node

metastases. Bioavailability, however, tends to decrease with increasing charge, although PEGylation provides a means to limit interstitial interactions and maximize absorption from an injection site.

Oral pharmacokinetics Oral drug administration is simple, convenient and in general, offers better compliance and outcomes. In recent times, however, oral drug delivery has become increasingly challenging with the emergence of new generations of highly potent, but poorly water soluble and poorly bioavailable compounds. Dendrimers have been suggested to enhance oral bioavailability by promoting drug solubilization in the intestinal lumen, inhibit drug–efflux transporter interactions, prevent intestinal elimination of drugs and enhance drug permeability by disrupting epithelial tight junctions in the intestines. There have been some important examples of enhanced *in vivo* bioavailability of drugs when associated with dendrimers. Indeed, the bioavailability of Doxorubicin (DOX) has been shown to be enhanced 300 fold when delivered as a complex with an amine–terminated G_3 PAMAM dendrimer, compared to delivery of the free drug.[350] More recently, both cationic and anionic G_4 PAMAM dendrimers were shown to improve the oral bioavailability of Camptothecin in mice[351]

Much of the literature related to the intestinal transport of dendrimers has been based on *in vitro* studies involving the use of Caco–2 cell monolayers[11]. This model is considered for examining the mechanisms of drug permeability across the intestinal epithelium, unfortunately it lacks a complex view on *in vivo* conditions. Nevertheless, charged dendrimers have been shown to display more efficient transcellular and paracellular transport than uncharged dendrimers in the order cationic $>$ anionic $>$ uncharged.[352] The mechanisms proposed to explain this observation include enhanced electrostatic binding of charged dendrimers to cell membranes, which promotes cellular endocytosis and disruption of interendothelial tight junctional proteins. The impact of dendrimer size, however, is more complex. For instance, increases in the size of anionic dendrimers (up to G_4) was shown to correlate with increased Caco–2 permeability, whereas increasing the size of cationic dendrimers tends more to cause cytotoxicity and a loss of membrane integrity.[240,353,354] Intestinal membrane permeability can also be enhanced by increasing dendrimer lipophilicity.[355,356,357]

In general, dendrimers may have some potential to improve the oral bioavailability of poorly soluble and poorly permeable drugs, but still yet *in vivo* evidence of significant benefit is lacking, even if evidence for the improved gastrointestinal permeability of dendrimers is based on charged (largely cationic) systems.

Transdermal pharmacokinetics Dendrimers have been explored for their potential to enhance the transdermal absorption of a number of cancer chemotherapeutics and analgesics (specifically non–steroidal anti–inflammatory drugs (NSAID's)). One advantage of this route is that it avoids first pass metabolism after

[11] Caco–2 model is based on a colon cell line that differentiates to form polarized cell layers and a brush border, similar to the intestinal lumen.

gastric absorption that limits the utility of oral delivery for some drugs and can also limit gastrointestinal irritation caused by most NSAID's.

The major barrier to transdermal drug delivery is penetration through the outer barrier of the skin. Once drugs reach the underlying epidermis, access to blood capillaries to facilitate systemic absorption is speeded up. The transdermal penetration of dendrimers has not been examined in a whole animal setting, but rather *in vitro* using excised portions of pig or rat skin. There are few *in vivo* studies that demonstrate improved percutaneous absorption of drug when associated with a dendrimer carrier and improved *in vivo* activity.[358,336]

As a general rule, smaller dendrimers appear to have more effective penetration of loaded drugs through the skin when compared to larger dendrimers, presumably due to their ability to easily pass between cells.[359] There is some divergence with regards to what dendrimer charges promote the best transdermal penetration. Generally, cationic dendrimers contribute better to transdermal absorption than uncharged dendrimers, which promote better penetration than anionic dendrimers.[360,361] This has been suggested to be a result of the ability of cationic dendrimers to adhere more effectively to lipid bilayers of the skin. In contrast, another study traced the penetration of FITC–labelled dendrimers through the skin and reported that cationic charges reduce the penetration of dendrimers through the skin when compared to anionic and uncharged dendrimers.[362] This was proposed as a result of the strong binding of cationic dendrimers to cells, which promotes enhanced retention in cells, but limited permeation through the skin. Additionally, a more recent study has shown that increasing the number of cationic charges beyond 8 may reduce drug penetration through the skin (using 5–fluorouracil as a model) **(Fig.32)**.[363] This suggests that partial cationic charge may promote good adherence and penetration through skin of dendrimers, but increasing cationic charge beyond a certain point is likely to obstruct dendrimer and drug penetration, and access to underlying vascular capillaries.

Pulmonary pharmacokinetics In recent years there has been an increase in the development of dendrimers for the inhaled delivery of drugs and genetic material. Inhaled delivery has a number of advantages over other means of administration: 1) the ability to improve drug or siRNA exposure specifically to the lungs; 2) the avoidance of first pass metabolism that can limit the utility of oral delivery for some drugs; and 3) provides a needle–free means to deliver drugs and macromolecules to the systemic circulation. Inhaled delivery is more complex in contrast to other means of drug administration, since the site of drug or macromolecule deposition (alveolar region, trachea, bronchi, bronchioles, or the back of the mouth and throat) is dictated by the size and aerodynamic properties of the inhaled aerosol or dry powder. As a general rule, droplets or particles of less than 0,5µm in size are generally exhaled and are not retained in the lungs,

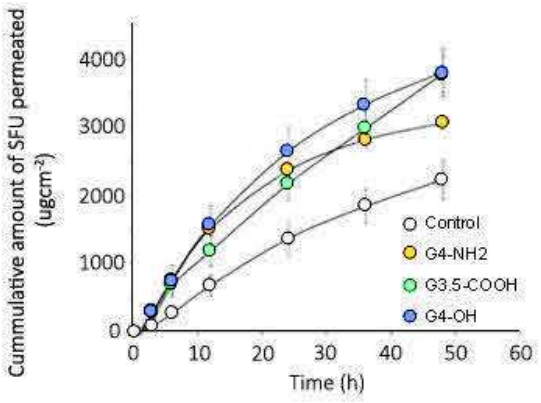

Figure 32: Permeability of 5–Fluorouracil (5FU) through pig skin after pre–treatment with Phosphate buffer (control) or PAMAM dendrimers bearing different surface functionalities.[360]

1–5µm particles are deposited primarily in the alveolar region, and $>$ 5µm particles are deposited in the upper airways and the back of the mouth.[364]

For small molecule drugs, alveolar epithelium absorption profiles almost reflects the profiles obtained after intravenous administration. By associating small molecule drugs with macromolecular drug carriers, drug retention in the lungs can be prolonged and drug liberation can be tuned to provide sustained lung exposure. For instance, a recent study has shown that small (approximately 11kDa) PEGylated Poly(Lysine) dendrimers are efficiently absorbed (approximately 30%) from the lungs of rats via both direct absorption of the intact dendrimer and absorption of dendrimer catabolism products.[365] A slightly larger dendrimer (22kDa) displayed slower absorption from the lung. A much larger 77kDa dendrimer, however, was retained in the lung for a prolonged period of time and was cleared from the lungs mainly via the expulsion of mucus. This suggests the potential to tailor dendrimers to act as systemic drug delivery vectors or drug depots to promote prolonged drug retention in the lungs **(Fig.33)**.

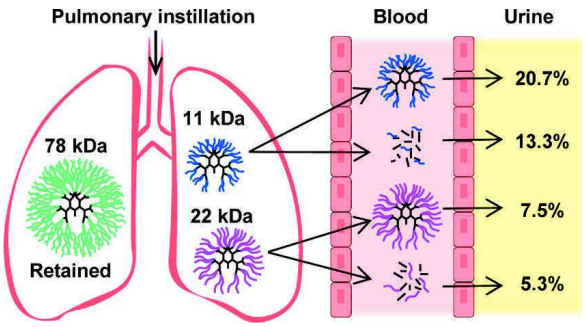

Figure 33: Size dependent pharmacokinetics and pulmonary delivery of PEGylated dendrimers into the systemic circulation.[365]

More recently, the transport of G_3 amine–terminated dendrimers across a Calu–3 monolayer model of the

pulmonary epithelium was shown to be improved by increasing the degree of PEGylation. [366] In a related study, the co–administration of G_0–G_3 PAMAM dendrimers to the lungs improved the absorption of Insulin and Calcitonin in rats.[367]

Pharmacodynamic data support the use of dendrimers as inhalable drug delivery systems. For instance, an early study showed that G_3 PAMAM–PEG micelles enhanced the bioavailability of entrapped low molecular weight Heparin in the lungs (60%) and the pulmonary delivery of the dendrimer formulation resulted in similar or better anticoagulant activity in a rat model of thrombosis when compared to the subcutaneous delivery of Heparin alone.[368] On the other hand, a Hydroxyl–terminated G_4 PAMAM dendrimer containing Methylprednisolone lowered inflammation in a rat model and prolonged the drug retention in the lungs after pulmonary administration when compared to administration of the drug alone.[169] More recently, the pulmonary administration of a 56kDa PEGylated G_5 Poly(Lysine) dendrimer conjugated to DOX displayed 13% absorption by the lungs and prolonged drug retention in the lungs of rats.[369]

Dendrimers have considerable utility as inhalable drug delivery vectors, although more work will be needed to completely evaluate the long term safety of dendrimers in the lungs, particularly given current concerns over the potential toxic effects of airborne nanoparticles on the lungs.

2 Purpose

As one of the newest areas of science, nanoscale science and technology are seen by many as the key technology of the 21st century, which of course raises the question as to what role this technology will play in medicine. An important area of nanoscale science is the development of nanostructured carriers for medical applications. For instance, various types of magnetic NPs have a widespread range of biomedical applications such as in MRI CAs, magnetically guided drug/gene delivery, magnetic hyperthermia (MH) and magnetic biosensors. Yet, these systems have a long expectations list: they should be completely nontoxic, biodegradable or capable of natural excretion, not be recognized or eliminated by the body's own immune system before they have reached their target, and not induce any allergic reactions. Ideally, they are generic, in other words, they can be 'programed' to combat a wide variety of diseases by docking onto any target structures one chooses and being capable of carrying any medicines. In regards to this wishing list, unique properties of the dendritic structures, which can be chemically tuned to reach ideal biodistribution or active targeting of high efficiency, can be considered as a perfect acolyte for magnetic NPs in order to meet those expectations.

Thousands of research articles have forecasted exciting applications of dendrimers in nanomedicine; however, the number of dendrimer–based formulations that translated to clinical studies has been somewhat deceiving, despite 40 years of research. Prospect of dendrimers' use in nanomedicine applications are directly

related to their multifunctional well–defined structure. However, most multifunctional dendrimers have been synthesized using random statistical approach leading to complex mixtures of products, which contradicts the initial purpose of building such sophisticated macromolecules. It might happen that the well–defined multifunctional dendrimers fail in achieving medical requirements, however, the reason for failure should not be non–reproducibility neither lack of control over the final dendrimer's structure.

Consequently, since 2009, our laboratory is focusing on the synthesis of dendron–Iron Oxide nanoparticles (IONPs) conjugates for MRI applications. However, the immense diversity and rapid evolution of biotechnologies create novel opportunities for exploring Dendrimer/ Dendrons diversity. Therefore, this thesis is technology driven by efforts to create new well defined small multifunctional Dendrons for theranostic applications. The main objective of this work is to build up dendronized nanoprobes in response to several biological requirements. Toward this end, after a general introduction on Dendrimer–nanoconjugates' engineering **(Chapter I)**, **Chapter II** provides synthetic routes to novel dendritic molecules which (i) apprise nanoconjugates' biodistribution under *in vivo* conditions, ii) might prevent toxicity issues of specific nanoparticles made of toxic metals (Cobalt) and iii) assess the *in vivo* nanomaterials' integrity through optical imaging. Another project I was interested in, as described in **Chapter III**, was the synthesis of dendronized IONPs, their physicochemical characterization, their *in vitro* toxicity and internalization, and *in vivo* behavior. This work includes not only the synthesis of dendrimer–based nanohybrids that open up new possibilities for the creation of novel or enhanced biological agents but also the synthesis of small dendrons or dendronized IONPs that expose new opportunities. Consequently, we studied dendronized IONPs as possible Melanoma early diagnosis contrast agents through active targeting of Melanine.

I strongly believe that using small and remarkably well–defined multifunctional dendrimers / dendrons will provide a better response to biomedical issues and a higher clinical translation. I look forward to the day when Dendrimers nanohybrids will no longer be a buzz word but a routine therapeutic.

References

[1] Miguel, A.F. Dendritic design as an archetype for growth patterns in nature fractal and constructal views. *Frontiers in Physics*, **2014**, 2(February), 1-7.

[2] Flory, J. Molecular Size Distribution in Three Dimensional Polymers. I. Gelation. *Journal of the American Chemical Society*, **1941**, 63(11), 3083-3090.

[3] Flory, P.J. Molecular Size Distribution in Three Dimensional Polymers. II. Trifunctional Branching Units. *Journal of the American Chemical Society*, **1941**, 63(11), 3091-3096.

[4] Flory, P.J. Molecular size distribution in three dimensional polymers. III. Tetrafunctional branching units. *Journal of the American Chemical Society*, **1941**, 63(5), 3096-3100.

[5] Buhleier, E., Wehner, W., Vogtel, F. Cascade and Nonskid Chain like Syntheses of Molecular Cavity Topologies. *Journal of Chemical Information and Modeling*, **1978**, 53(9), 155-158.

[6] Tomalia, D.A., Hall, M., Hedstrand, D.M. Starburst dendrimers. III. The importance of branch junction symmetry in the development of topological shell molecules. *J. Am. Chem. Soc*, **1987**, 109(5), 1601-1603.

[7] Newkome, G.R., YaolC, Z., Baker, G.R., Gupta, V.K. Cascade Molecules A New Approach to Micelles. *J. Org. Chem*, **1985**, 50(3), 2004-2006.

[8] Denkewalter, R.G., Kolc, J.F., Lukasavage, W.J. Macromolecular highly branched homogeneous compound. **1981**.

[9] Tomalia, D.A., Baker, H., Dewald, J., Hall, M., Kallos, G., S.Martin, Roeck, J., Ryder, J., SMith, P. A New Class of polymers Starburst-Dendritic Macromolecules. *Polymer Journal*, **1985**, 17(1), 117-132.

[10] Ornelas, C. Brief Timelapse on Dendrimer Chemistry Advances, Limitations, and Expectations. *Macromolecular Chemistry and Physics*, **2016**, 217(2), 149-174.

[11] Tomalia, D.A., McConnell, J.R., Padias, B.A., Hall, H.K. Starburst Polyether Dendrimers. *Journal of Organic Chemistry*, **1987**, 52(24), 5305-5312.

[12] Schluter, A.D., Rabe, J.P. Dendronized Polymers Synthesis, Characterization, Assembly at Interfaces, and Manipulation. *Angewandte Chemie International Edition*, **2000**, 39(5), 864-883.

[13] de Gennes, P.G., Hervet, H. Statistics of starburst polymers. *Journal de Physique Lettres*, **1983**, 44(9), 351-360.

[14] Svenson, S. The dendrimer paradox - high medical expectations but poor clinical translation. *Chem. Soc. Rev*, **2015**, 44(12), 4131-4144.

[15] Li, M.H., Choi, S.K., Thomas, T.P., Desai, A., Lee, K.H., Kotlyar, A., Banaszak Holl, M.M., Baker, J.R. Dendrimer-based multivalent methotrexates as dual acting nanoconjugates for cancer cell targeting. *European Journal of Medicinal Chemistry*, **2012**, 47(1), 560-572.

[16] Campagna, S., Ceroni, P., Puntoriero, F. Designing Dendrimers. *John Wiley Sons, Inc*, **2012**.

[17] Lartigue, M., Slany, M., Caminade, A., Majoral, J. Phosphorus-Containing Dendrimers Synthesis of Macromolecules with Multiple Tri- and Tetrafunctionalization. *Chemical Europeen Journal*, **1996**, 2(I), 1417-1426.

[18] James, T.D., Shinmori, H., Takeuchi, M., Shinkai, S. A saccharide sponge. Synthesis and properties of a dendritic boronic acid. *Chem. Commun*, **1996**, 705-706.

[19] Newkome, G.R., Weis, C.D., Moorefield, C.N., Baker, G.R., Childs, B.J., Epperson, J. Isocyanate-based Dendritic Building Blocks Combinatorial Tier Construction and Macromolecular Property Modification. *Angew. Chem. Int. Ed*, **1997**, submitted.

[20] Steffensen, M.B., Simanek, E.E. Synthesis and manipulation of orthogonally protected dendrimers Building blocks for library synthesis. *Angewandte Chemie - International Edition*, **2004**, 43(39), 5178-5180.

[21] Swali, V., Wells, N.J., Langley, G.J., Bradley, M. Solid-Phase Dendrimer Synthesis and the Generation of Super-High-Loading Resin Beads for Combinatorial Chemistry. *The Journal of Organic Chemistry*, **1997**, 62(15), 4902-4903.

[22] Uhrich, K.E., Boegeman, S., Frechet, J.M.J., Turner, S.R. The solid-phase synthesis of dendritic polyamides. *Polymer Bulletin*, **1991**, 25(5), 551-558.

[23] Zimmerman, S.C., Zeng, F., Reichert, D.E.C., Kolotuchin, S.V., Series, N., Feb, N. Self-Assembling Dendrimers. *Science*, **1996**, 271, 1095-1098.

[24] Frechet, J.M.J. Dendrimers and supramolecular chemistry. *Proceedings of the National Academy of Sciences of the United States of America*, **2002**, 99(8), 4782-4787.

[25] Newkome, G.R., Baker, G.R., Arai, S., Saunders, M.J., Russo, P.S., Theriot, K.J., Moorefield, C.N., Rogers, L.E., Miller, J.E., Lieux, T.R., Murray, M.E., Phillips, B., Pascal, L. Cascade molecules. Part 6. Synthesis and Characterization of Two-Directional Cascade Molecules and Formation of Aqueous Gels. *Journal of the American Chemical Society*, **1990**, 112(23), 8458-8465.

[26] Newkome, G.R. Suprasupermolecular chemistry the chemistry within the dendrimer. *Pure and Applied Chemistry*, **1998**, 70(12), 2337-2343.

[27] Hawker, C.J., Frechet, J.M.J. Unusual macromolecular architectures the convergent growth approach to dendritic polyesters and novel block copolymers. *Journal of the American Chemical Society*, **1992**, 114(22), 8405-8413.

[28] Wooley, K.L., Hawker, C.J., Frechet, J.M.J. Unsymmetrical 3-Dimensional Macromolecules - Preparation and Characterization of Strongly Dipolar Dendritic Macromolecules. *Journal of the American Chemical Society*, **1993**, 115(24), 11496-11505.

[29] Caminade, A.-M., Laurent, R., Delavaux-Nicot, B., Majoral, J.-P Janus dendrimers syntheses and properties. *New J. Chem*, **2012**, 36(2), 217-226.

[30] Sowinska, M., Urbanczyk-Lipkowska, Z. Advances in the chemistry of dendrimers. *New Journal of Chemistry*, **2014**, 38(6), 2168-2203.

[31] Caminade, A., Turrin, C., Laurent, R., Ouali, A., Delavaux-Nicot, B. Dendrimers. *John Wiley Sons, Inc*, **2011**.

[32] Tomalia, D., Baker, J.R., Dewald, J., Hall, M., Kallos, G., Martin, S., Roeck, J., Ryder, J., Smith, P. Dendritic Macromolecules Synthesis of Starburst Dendrimers. *Macromolecules*, **1986**, 19(9), 2466-2468.

[33] Tomalia, D.A., Naylor, A.M., Goddard, W.A. Starburst-Dendrimere Kontrolle von Grosse, Gestalt, Oberflachenchemie, Topologie und Flexibilitat beim Ubergang von Atomen zu makroskopischer Materie. *Angewandte Chemie*, **1990**, 102(2), 119-157.

[34] Newkome, G.R., Shreiner, C.D. Polyamidoamine, polypropylenimine, and related dendrimers and dendrons possessing different 1to 2 branching motifs An overview of the divergent procedures. *Polymer*, **2008**, 49(1), 1-173.

[35] Bosman, A.W., Janssen, H.M., Meijer, E.W. About Dendrimers Structure, Physical Properties, and Applications. *Chemical Reviews*, **1999**, 99(7), 1665-1688.

[36] Newkome, G.R., Shreiner, C. Dendrimers derived from 1 to 3 branching motifs. *Chemical Reviews*, **2010**, 110(10), 6338-6442.

[37] Walter, M.V., Malkoch, M. Simplifying the synthesis of dendrimers accelerated approaches. *Chemical Society Reviews*, **2012**, 41(13), 4593.

[38] Wooley, K.L., Hawker, C.J., Frechet, J.M.J. Verzweigte Monomere als Quelle fur einen schnelleren Zugang zu Dendrimeren. *Angew. Chem. Int. Ed*, **1994**, 106(1), 123-126.

[39] Wooley, K.L., Hawker, C.J., Frechet, J.M.J. Hyperbranched macromolecules via a novel double-stage convergent growth approach. *Journal of the American Chemical Society*, **1991**, 113(11), 4252-4261.

[40] Kawaguchi, T., Walker, K.L., Wilkins, C.L., Moore, J.S. Double Exponential Dendrimer Growth. *Journal of the American Chemical Society*, **1995**, 117(7), 2159-2165.

[41] Ihre, H., Hult, A., Frechet, J.M.J., Gitsov, I. Double-Stage Convergent Approach for the Synthesis of Functionalized Dendritic Aliphatic Polyesters Based on 2,2-Bishydroxymethylpropionic Acid. *Macromolecules*, **1998**, 31(13), 4061-4068.

[42] Spindler, R., Frechet, J.M.J. Two-step approach towards the accelerated synthesis of dendritic macromolecules. *Journal of the Chemical Society, Perkin Transactions 1*, **1993**, 1(8), 913-918.

[43] Freeman, A.W., Frechet, J.M.J. A rapid, orthogonal synthesis of polybenzyl ester dendrimers via an activated monomer approch. *American Chemical Society, Polymer Preprints, Division of Polymer Chemistry*, **1999**, 1(4), 685-687.

[44] Nenajdenko, V.G., Huang, Y., Domling, A. Isocyanide Chemistry. *Wiley-VCH Verlag GmbH Co. KGaA*, **2012**.

[45] Zhu, J., Bienayme, H. Multicomponent Reactions. *Wiley-VCH Verlag GmbH Co*, **2005**.

[46] Antoni, P., Nystrom, D., Hawker, C.J., Hult, A., Malkoch, M. A chemoselective approach for the accelerated synthesis of well-defined dendritic architectures. *Chem. Commun*, **2007**, 2249-2251.

[47] Lee, C.C., Gillies, E.R., Fox, M.E., Guillaudeu, S.J., Frechet, J.M.J., Dy, E.E., Szoka, F.C. A single dose of doxorubicin-functionalized bow-tie dendrimer cures mice bearing C-26 colon carcinomas. *Proceedings of the National Academy of Sciences of the United States of America*, **2006**, 103(45), 16649-16654.

[48] Maraval, V., Laurent, R., Donnadieu, B., Mauzac, M., Caminade, A.M., Majoral, J.P. Rapid synthesis of phosphorus-containing dendrimers with controlled molecular architectures First example of surface-block, layer-block, and segment-block dendrimers issued from the same dendron. *Journal of the American Chemical Society*, **2000**, 122(11), 2499-2511.

[49] Vogtle, F., Gestermann, S., Hesse, R., Schwierz, H., Windisch, B. Functional dendrimers. *Progress in Polymer Science Oxford*, **2000**, 25(7), 987-1041.

[50] Antoni, P., Hed, Y., Nordberg, A., Nystrom, D., Von Holst, H., Hult, A., Malkoch, M. Bifunctional dendrimers From robust synthesis and accelerated one-pot postfunctionalization strategy to potential applications. *Angewandte Chemie - International Edition*, **2009**, 48(12), 2126-2130.

[51] Feng, Y., He, Y.M., Zhao, L.W., Huang, Y.Y., Fan, Q.H. A liquid-phase approach to functionalized janus dendrimers Novel soluble supports for organic synthesis. *Organic Letters*, **2007**, 9(12), 2261-2264.

[52] Feng, X., Taton, D., Ibarboure, E., Chaikof, E.L., Gnanou, Y. Janus-Type Dendrimer-like Poly ethylene oxides. *J. Am. Chem. Soc*, **2008**, 130, 11662-11676.

[53] Grayson, S.M., Frechet, J.M.J. Synthesis and surface functionalization of aliphatic polyether dendrons. *Journal of the American Chemical Society*, **2000**, 122(42), 10335-10344.

[54] Vogtle, F., Fakhrnabavi, H., Lukin, O., Muller, S., Friedhofen, J., Schalley, C.A. Towards a Selective Functionalization of Amino-Terminated Dendrimers. *European Journal of Organic Chemistry*, **2004**, 2004(22), 4717-4724.

[55] Archut, A., Gestermann, S., Hesse, R., Kauffmann, C., Vogtle, F. Selective Activation, Different Branching and Grafting of Poly propylenimine-Dendrimers. *Synlett*, **1998**, 1998, 546-548.

[56] Goodwin, A.P., Lam, S.S., Frechet, J.M.J. Rapid, efficient synthesis of heterobifunctional biodegradable dendrimers. *Journal of the American Chemical Society*, **2007**, 129(22), 6994-6995.

[57] Patra, S., Kozura, B., Huang, A.Y.T., Enciso, A.E., Sun, X., Hsieh, J.T., Kao, C.L., Chen, H.T., Simanek, E.E. Dendrimers terminated with dichlorotriazine groups provide a route to compositional diversity. *Organic Letters*, **2013**, 15(15), 3808-3811.

[58] Janiszewska, J., Swieton, J., Lipkowski, A.W., Urbanczyk-Lipkowska, Z. Low molecular mass peptide dendrimers that express antimicrobial properties. *Bioorganic and Medicinal Chemistry Letters*, **2003**, 13(21), 3711-3713.

[59] Janiszewska, J., Urbanczyk-Lipkowska, Z. Amphiphilic dendrimeric peptides as model non-sequential pharmacophores with antimicrobial properties. *Journal of Molecular Microbiology and Biotechnology*, **2007**, 13(4), 220-225.

[60] Janiszewska, J., Sowinska, M., Rajnisz, A., Solecka, J., Lcka, I., Milewski, S., Urbanczyk-Lipkowska, Z. Novel dendrimeric lipopeptides with antifungal activity. *Bioorganic and Medicinal Chemistry Letters*, **2012**, 22(3), 1388-1393.

[61] Van Der Poll, D.G., Kieler-Ferguson, H.M., Floyd, W.C., Guillaudeu, S.J., Jerger, K., Szoka, F.C., Frechet, J.M. Design, synthesis, and biological evaluation of a robust, biodegradable dendrimer. *Bioconjugate Chemistry*, **2010**, 21(4), 764-773.

[62] Hecht, S. Functionalizing the interior of dendrimers Synthetic challenges and applications. *Journal of Polymer Science, Part A Polymer Chemistry*, **2003**, 41(8), 1047-1058.

[63] Lochmann, L., Wooley, L.K., Ivanova, P.T., Frechet, J.M.J. Multisite Functionalized Dendritic Macromolecules Prepared via Metalation by Superbases and Reaction with Electrophiles. *J. Am. Chem. Soc*, **1993**, 115, 7043-7044.

[64] McElhanon, J.R., Wu, M., Escobar, M., McGrath, D.V. Toward Chiral Dendrimers with Highly Functionalized Interiors. DEndrons from Synthetic AB2 monomers. *Macromolecules*, **1996**, 29, 8979-8982.

[65] McElhanon, J.R., Wu, M.J., Escobar, M., Chaudhry, U., Hu, C.L., McGrath, D.V. Asymmetric synthesis of a series of chiral AB2 monomers for dendrimer construction. *Journal of Organic Chemistry*, **1997**, 62(25), 908-915.

[66] Mcelhanon, J.R., Mcgrath, D.V. Constitution, Configuration, and the Optical-Activity of Chiral Dendrimers. *Journal of the American Chemical Society*, **1998**, 120(8), 1647-1656.

[67] McElhanon, J.R., McGrath, D.V. Toward chiral polyhydroxylated dendrimers. Preparation and chiroptical properties. *Journal of Organic Chemistry*, **2000**, 65(11), 3525-3529.

[68] Piotti, M.E., Rivera, F., Bond, R., Hawker, C.J., Frechet, J.M.J. Synthesis and catalytic activity of unimolecular dendritic reverse micelles with internal functional groups 13. *Journal of the American Chemical Society*, **1999**, 121(40), 9471-9472.

[69] Kang, T., Amir, R.J., Khan, A., Ohshimizu, K., Hunt, J.N., Sivanandan, K., Montanez, M.I., Malkoch, M., Ueda, M., Hawker, C.J. Facile access to internally functionalized dendrimers through efficient and orthogonal click reactions. *Chemical communications Cambridge, England*, **2010**, 46(9), 1556-1558.

[70] Larre, C., Bressolles, D., Turrin, C., Donnadieu, B., Caminade, A.M., Majoral, J.P. Chemistry within megamolecules Regiospecific functionalization after construction of phosphorus dendrimers. *Journal of the American Chemical Society*, **1998**, 120(50), 13070-13082.

[71] Galliot, C., Larre, C., Caminade, A., Majoral, J. Regioselective Stepwise Growth of Dendrimer Units in the Internal Voids of a Main Dendrimer. *Science*, **1997**, 277(5334), 1981-1984.

[72] Choi, H.S., Frangioni, J.V. Nanoparticles for Biomedical Imaging Fundamentals af Clinical Translation. *Molecular imaging*, **2010**, 9(6), 291-310.

[73] Kunjachan, S., Ehling, J., Storm, G., Kiessling, F., Lammers, T. Noninvasive Imaging of Nanomedicines and Nanotheranostics Principles, Progress, and Prospects. *Chemical Reviews*, **2015**, 115(19), 10907-10937.

[74] Lee, W.I., Bae, Y., Bard, A.J. Strong blue photoluminescence and ECL from OH-terminated PAMAM dendrimers in the absence of gold nanoparticles. *Journal of the American Chemical Society*, **2004**, 126(27), 8358-8359.

[75] Wang, D., Imae, T. Fluorescence Emission from Dendrimers and Its pH Dependence. *Journal of American Chemical Society Communications*, **2004**, 126, 12304-13205.

[76] Tsai, Y.J., Hu, C.C., Chu, C.C., Imae, T. Intrinsically fluorescent PAMAM dendrimer as gene carrier and nanoprobe for nucleic acids delivery Bioimaging and transfection study. *Biomacromolecules*, **2011**, 12(12), 4283-4290.

[77] Majoros, I.J., Myc, A., Thomas, T., Mehta, C.B., Baker, J.R. PAMAM dendrimer-based multifunctional conjugate for cancer therapy Synthesis, characterization, and functionality. *Biomacromolecules*, **2006**, 7(2), 572-579.

[78] Thomas, T.P., Choi, S.K., Li, M.H., Kotlyar, A., Baker, J.R. Design of riboflavin-presenting PAMAM dendrimers as a new nanoplatform for cancer-targeted delivery. *Bioorganic and Medicinal Chemistry Letters*, **2010**, 20(17), 5191-5194.

[79] Thomas, T.P., Majoros, I.J., Kotlyar, A., Kukowska-Latallo, J.F., Bielinska, A., Myc, A., Baker, J.R. Targeting and inhibition of cell growth by an engineered dendritic nanodevice. *Journal of Medicinal Chemistry*, **2005**, 48(11), 3729-3735.

[80] Kukowska-Latallo, J.F.J., Candido, K.K.A., Cao, Z., Nigavekar, S.S., Majoros, I.I.J., Thomas, T.P.T., Balogh, L.L.P., Khan, M.M.K., Baker, J.J.R. Nanoparticle targeting of anticancer drug improves therapeutic response in animal model of human epithelial cancer. *Cancer Res*, **2005**, 65(12), 5317-5324.

[81] Amir, R.J., Albertazzi, L., Willis, J., Khan, A., Kang, T., Hawker, C.J. Multifunctional trackable dendritic scaffolds and delivery agents. *Angewandte Chemie - International Edition*, **2011**, 50(15), 3425-3429.

[82] Wu, P., Yan, X. Doped quantum dots for chemobiosensing and bioimaging. *Chemical Society reviews*, **2013**, 42(12), 5489-5521.

[83] Gao, J., Chen, K., Luong, R., Bouley, D.M., Mao, H., Qiao, T., Gambhir, S.S., Cheng, Z. A novel clinically translatable fluorescent nanoparticle for targeted molecular imaging of tumors in living subjects. *Nano letters*, **2012**, 12(1), 281-286.

[84] Chatterjee, D.K., Gnanasammandhan, M.K., Zhang, Y. Small upconverting fluorescent nanoparticles for biomedical applications. *Small Weinheim an der Bergstrasse, Germany*, **2010**, 6(24), 2781-2795.

[85] Zhou, L., He, B., Huang, J., Cheng, Z., Xu, X., Wei, C. Multihydroxy dendritic upconversion nanoparticles with enhanced water dispersibility and surface functionality for bioimaging. *ACS applied materials interfaces*, **2014**, 6(10), 7719-7727.

[86] Kalender, W.A. X-ray computed tomography. *Physics in Medicine and Biology*, **2006**, 51(13), R29-R43.

[87] Krause, W. Delivery of diagnostic agents in computed tomography. *Advanced Drug Delivery Reviews*, **1999**, 37(1-3), 159-173.

[88] Lusic, H., Grinstaff, M.W. X-ray-Computed Tomography Contrast Agents. *Chemical Research in Toxicology*, **2013**, 113, 1641-1666.

[89] Hallouard, F., Anton, N., Choquet, P., Constantinesco, A., Vandamme, T. Iodinated blood pool contrast media for preclinical X-ray imaging applications - A review. *Biomaterials*, **2010**, 31(24), 6249-6268.

[90] Yordanov, A.T., Lodder, A.L., Woller, E.K., Cloninger, M.J., Patronas, N., Milenic, D., Brechbiel, M.W. Novel Iodinated Dendritic Nanoparticles for Computed Tomography CT Imaging. *Nano Letters*, **2002**, 2(6), 595-599.

[91] Fu, Y., Nitecki, D.E., Maltby, D., Simon, G.H., Berejnoi, K., Raatschen, H.J., Yeh, B.M., Shames, D.M., Brasch, R.C. Dendritic iodinated contrast agents with PEG-cores for CT imaging synthesis and preliminary characterization. *Bioconjugate chemistry*, **2006**, 17(4), 1043-1056.

[92] Gu, Z. Bioinspired and Biomimetic Polymer Systems for Drug and Gene Delivery. *John Wiley Sons*, **2015**.

[93] Lesniak, W., Blelinska, A.U., Sun, K., Janczak, K.W., Shi, X., Baker, J.R., Balogh, L.P. Silverdendrimer nanocomposites as biomarkers Fabrication, characterization, in vitro toxicity, and intracellular detection. *Nano Letters*, **2005**, 5(11), 2123-2130.

[94] Shi, X., Wang, S.H., Van Antwerp, M.E., Chen, X., Baker, J.R. Targeting and detecting cancer cells using spontaneously formed multifunctional dendrimer-stabilized gold nanoparticles. *The Analyst*, **2009**, 134(7), 1373-1379.

[95] Guo, R., Wang, H., Peng, C., Shen, M., Pan, M., Cao, X., Zhang, G., Shi, X. X-ray Attenuation Property of Dendrimer-Entrapped Gold Nanoparticles. *The Journal of Physical Chemistry C*, **2010**, 114(1), 50-56.

[96] Peng, C., Wang, H., Guo, R., Shen, M., Cao, X., Zhu, M., Zhang, G., Shi, X. Acetylation of Dendrimer-Entrapped Gold Nanoparticles Synthesis , Stability , and X-ray Attenuation Properties. *Journal of Applied Polymer Science*, **2010**, 119, 1673-1682.

[97] WIENER, E.C., KONDA, S., SHADRON, A., BRECHBIEL, M., GANSOW, O. Targeting Dendrimer-Chelates to Tumors and Tumor Cells Expressing the High-Affinity Folate Receptor. *Investigative Radiology*, **1997**, 32(12), 748-754.

[98] Kono, K., Liu, M., Frechet, J.M.J. Design of dendritic macromolecules containing folate or methotrexate residues. *Bioconjugate Chemistry*, **1999**, 10(6), 1115-1121.

[99] Wang, H., Zheng, L., Peng, C., Shen, M., Shi, X., Zhang, G. Folic acid-modified dendrimer-entrapped gold nanoparticles as nanoprobes for targeted CT imaging of human lung adencarcinoma. *Biomaterials*, **2013**, 34(2), 470-480.

[100] Zhu, J., Zheng, L., Wen, S., Tang, Y., Shen, M., Zhang, G., Shi, X. Targeted cancer theranostics using alpha-tocopheryl succinate-conjugated multifunctional dendrimer-entrapped gold nanoparticles. *Biomaterials*, **2014**, 35(26), 7635-7646.

[101] Peng, C., Li, K., Cao, X., Xiao, T., Hou, W., Zheng, L., Guo, R., Shen, M., Zhang, G., Shi, X. Facile formation of dendrimer-stabilized gold nanoparticles modified with diatrizoic acid for enhanced computed tomography imaging applications. *Nanoscale*, **2012**, 4(21), 6768-6778.

[102] Guo, R., Wang, H., Peng, C., Shen, M., Zheng, L., Zhang, G., Shi, X. Enhanced X-ray attenuation property of dendrimer-entrapped gold nanoparticles complexed with diatrizoic acid. *Journal of Materials Chemistry*, **2011**, 21(13), 5120-5127.

[103] Kobayashi, H., Kawamoto, S., Jo, S.K., Bryant, H.L., Brechbiel, M.W., Star, R.A. Macromolecular MRI contrast agents with small dendrimers Pharmacokinetic differences between sizes and cores. *Bioconjugate Chemistry*, **2003**, 14(2), 388-394.

[104] Raymond, K.N., Pierre, V.C. Next generation, high relaxivity gadolinium MRI agents. *Bioconjugate Chemistry*, **2005**, 16(1), 3-8.

[105] Yang, C., Chuang, K. GdIII chelates for MRI contrast agents from high relaxivity to smart, from blood pool to blood-brain barrier permeable. *MedChemComm*, **2012**, 3, 552.

[106] Cheng, C.Y., Ou, K.L., Huang, W.T., Chen, J.K., Chang, J.Y., Yang, C.H. Gadolinium-based CuInS2ZnS nanoprobe for dual-modality magnetic resonanceoptical imaging. *ACS Applied Materials and Interfaces*, **2013**, 5(10), 4389-4400.

[107] Terreno, E., Castelli, D.D., Viale, A., Aime, S. Challenges for molecular magnetic resonance imaging. *Chemical reviews*, **2010**, 110(5), 3019-3042.

[108] Margerum, L.D., Campion, B.K., Koo, M., Shargill, N., Lai, J.J., Marumoto, A., Sontum, P.C. GadoliniumIII DO3A macrocycles and polyethylene glycol coupled to dendrimers. Effect of molecular weight on physical and biological properties of macromolecular magnetic resonance imaging contrast agents. *Journal of Alloys and Compounds*, **1997**, 249, 185-190.

[109] Palinkas, Z., Baranyai, Z., Brucher, E., Rozsa, B. Kinetics of the exchange reactions between GdDTPA, GdBOPTA, and GdDTPA-BMA complexes, used as MRI contrast agents, and the triethylenetetraamine-hexaacetate ligand. *Inorganic Chemistry*, **2011**, 50(8), 3471-3478.

[110] Lauffer, R.B. Paramagnetic metal complexes as water proton relaxation agents for NMR imaging theory and design. *Chemical Reviews*, **1987**, 87(5), 901-927.

[111] Kobayashi, H., Brechbiel, M.W. Nano-sized MRI contrast agents with dendrimer cores. *Advanced Drug Delivery Reviews*, **2005**, 57(15), 2271-2286.

[112] Wiener, E.C., Brechbiel, M.W., Brothers, H., Magin, R.L., Gansow, O.A., Tomalia, D.A., Lauterbur, P.C. Dendrimer-based metal chelates A new class of magnetic resonance imaging contrast agents. *Magnetic Resonance in Medicine*, **1994**, 31(1), 1-8.

[113] Langereis, S., Lussanet, Q.G.d., van Genderen, M.H.P., Backes, W.H., Meijer, E.W. Multivalent contrast agents based on Gd-DTPA-terminated poly propylene imine dendrimers for Magnetic Resonance Imaging. *Macromolecules*, **2004**, 37, 3084-3091.

[114] Nwe, K., Bryant, L.H., Brechbiel, M.W. Polyamidoamine dendrimer based MRI contrast agents exhibiting enhanced relaxivities derived via metal preligation techniques. *Bioconjugate Chemistry*, **2010**, 21(6), 1014-1017.

[115] Nwe, K., Xu, H., Regino, C.A.S., Bernardo, M., Ileva, L., Riffle, L., Wong, K.J., Brechbiel, M.W. A new approach in the preparation of dendrimer-based bifunctional diethylenetriaminepentaacetic acid MR contrast agent derivatives. *Bioconjugate Chemistry*, **2009**, 20(7), 1412-1418.

[116] Konda, S.D., Aref, M., Wang, S., Brechbiel, M., Wiener, E.C. Specific targeting of folate-dendrimer MRI contrast agents to the high affinity folate receptor expressed in ovarian tumor xenografts. *Magma New York, N.Y*, **2001**, 12(01), 104-113.

[117] Konda, S.D., Wang, S., Brechbiel, M., Wiener, E.C. Biodistribution of a 153 Gd-folate dendrimer, generation. *Invest Radiol*, **2002**, 37(4), 199-204.

[118] Swanson, S.D., Kukowska-Latallo, J.F., Patri, A.K., Chen, C., Ge, S., Cao, Z., Kotlyar, A., East, A.T., Baker, J.R. Trageted gadolinium-loaded dendrimer nanoparticles for tumor-specific magnetic renosance contrast enhancement. *International Journal of Nanomedicine*, **2008**, 3(2), 201-210.

[119] Chen, W.T., Thirumalai, D., Shih, T.T.F., Chen, R.C., Tu, S.Y., Lin, C.I., Yang, P.C. Dynamic contrast-enhanced folate-receptor-targeted MR imaging using a gd-loaded peg-dendrimer-folate conjugate in a mouse xenograft tumor model. *Molecular Imaging and Biology*, **2010**, 12(2), 145-154.

[120] Tan, M., Ye, Z., Jeong, E.K., Wu, X., Parker, D.L., Lu, Z.R. Synthesis and evaluation of nanoglobular macrocyclic MnII chelate conjugates as non-gadoliniumIII MRI contrast agents. *Bioconjugate Chemistry*, **2011**, 22(5), 931-937.

[121] Ali, M.M., Woods, M., Caravan, P., Opina, A.C.L., Spiller, M., Fettinger, J.C., Sherry, A.D. Synthesis and relaxometric studies of a dendrimer-based pH-responsive MRI contrast agent. *Chemistry - A European Journal*, **2008**, 14(24), 7250-7258.

[122] Chevallier, P., Walter, A., Garofalo, A., Veksler, I., Lagueux, J., Begin-Colin, S., Felder-Flesch, D., Fortin, M.A. Tailored biological retention and efficient clearance of pegylated ultra-small MnO nanoparticles as positive MRI contrast agents for molecular imaging. *Journal of Materials Chemistry B*, **2014**, 2(13), 1779-1790.

[123] Miller, C., Krasnow, J., Schwartz, L.H. Medical Imaging in Clinical Trials. *Springer Science Business Media*, **2014**.

[124] Wagner, V., Dullaart, A., Bock, A., Zweck, A. The emerging nanomedicine landscape. *Nature biotechnology*, **2006**, 24(10), 1211-1217.

[125] Strable, E., Bulte, J.W.M., Moskowitz, B., Vivekanandan, K., Allen, M., Douglas, T. Synthesis and Characterization of Soluble Iron Oxide-Dendrimer Composites. *Chemistry of Materials*, **2001**, 13(21), 2201-2209.

[126] Yang, J., Luo, Y., Xu, Y., Li, J., Zhang, Z., Wang, H., Shen, M., Shi, X., Zhang, G. Conjugation of iron oxide nanoparticles with RGD-modified dendrimers for targeted tumor MR imaging. *ACS applied materials interfaces*, **2015**, 7(9), 5420-5428.

[127] Basly, B., Felder-Flesch, D., Perriat, P., Pourroy, G., Begin-Colin, S. Properties and suspension stability of dendronized iron oxide nanoparticles for MRI applications. *Contrast media molecular imaging*, **2011**, 6(3), 132-138.

[128] Wang, L., Neoh, K.G., Kang, E.T., Shuter, B., Wang, S. Superparamagnetic Hyperbranched Polyglycerol-Grafted Fe 3 O 4 Nanoparticles as a Novel Magnetic Resonance Imaging Contrast Agent An In Vitro Assessment. *Advanced Functional Materials*, **2009**, 19(16), 2615-2622.

[129] Arsalani, N., Fattahi, H., Laurent, S., Burtea, C., Vander Elst, L., Muller, R.N. Polyglycerol-grafted superparamagnetic iron oxide nanoparticles highly efficient MRI contrast agent for liver and kidney imaging and potential scaffold for cellular and molecular imaging. *Contrast media molecular imaging*, **2012**, 7(2), 185-194.

[130] Saha, I., Chaffee, K.E., Duanmu, C., Woods, B.M., Stokes, A.M., Buck, L.E., Walkup, L.L., Sattenapally, N., Huggenvik, J., Gao, Y., Goodson, B.M. pH-Sensitive MR Responses Induced by Dendron-Functionalized SPIONs. *The journal of physical chemistry. C, Nanomaterials and interfaces*, **2013**, 117(4), 1893-1903.

[131] Mather, S. Molecular imaging with bioconjugates in mouse models of cancer. *Bioconjugate Chem*, **2009**, 20(4), 631-643.

[132] Fang, W., He, J., Kim, Y.S., Zhou, Y., Liu, S. Evaluation of 99mTc-labeled cyclic RGD peptide with a PEG 4 linker for thrombosis imaging Comparison with DMP444. *Bioconjugate Chemistry*, **2011**, 22(8), 1715-1722.

[133] Shao, X., Carpenter, G.M., Desmond, T.J., Sherman, P., Quesada, C.A., Fawaz, M., Brooks, A.F., Kilbourn, M.R., Albin, R.L., Frey, K.A., Scott, P.J.H. Evaluation of 11C N-methyl lansoprazole as a radiopharmaceutical for PET imaging of tau neurofibrillary tangles. *ACS Medicinal Chemistry Letters*, **2012**, 3(11), 936-941.

[134] Shao, X., Zhang, H., Rajian, J.R., Chamberland, D.L., Sherman, P.S., Quesada, C.A., Koch, A.E., Kotov, N.A., Wang, X. 125I-labeled gold nanorods for targeted imaging of inflammation. *ACS Nano*, **2011**, 5(11), 8967-8973.

[135] Dobrucki, L.W., Sinusas, A.J Molecular imaging. A new approach to nuclear cardiology. *Q J Nucl Med Mol Imading*, **2005**, 49, 106-115.

[136] Ghobril, C., Lamanna, G., Kueny-Stotz, M., Garofalo, A., Billotey, C., Felder-Flesch, D. Dendrimers in nuclear medical imaging. *New Journal of Chemistry*, **2012**, 36(2), 310-323.

[137] Chakravarty, R., Goel, S., Valdovinos, H.F., Hernandez, R., Hong, H., Nickles, R.J., Cai, W. Matching the decay half-life with the biological half-life ImmunoPET imaging with44Sc-labeled Cetuximab Fab fragment. *Bioconjugate Chemistry*, **2014**, 25(12), 2197-2204.

[138] Herth, M.M., Barz, M., Jahn, M., Zentel, R., Rosch, F. 7274As-labeling of HPMA based polymers for long-term in vivo PET imaging. *Bioorganic and Medicinal Chemistry Letters*, **2010**, 20(18), 5454-5458.

[139] Devaraj, N.K., Keliher, E.J., Thurber, G.M., Nahrendorf, M., Weissleder, R. 18F labeled nanoparticles for in Vivo PET-CT imaging. *Bioconjugate Chemistry*, **2009**, 20(2), 397-401.

[140] Pressly, E.D., Rossin, R., Hagooly, A., Fukukawa, K.I., Messmore, B.W., Welch, M.J., Wooley, K.L., Lamm, M.S., Hule, R.A., Pochan, D.J., Hawker, C.J. Structural effects on the biodistribution and positron emission tomograpgy PET imaging of well-defined 64Cu-labeled nanoparticles comprised of amphiphilic block graft copolymers. *Biomacromolecules*, **2007**, 8(10), 3126-3134.

[141] Bar-Shalom, R., Valdivia, A.V., Blaufox, D.M. The role of hybrid cameras in oncology. *Seminars in nuclear medicine*, **2000**, 30(3), 150-185.

[142] Almutairi, A., Rossin, R., Shokeen, M., Hagooly, A., Ananth, A., Capoccia, B., Guillaudeu, S., Abendschein, D., Anderson, C.J., Welch, M.J., Frechet, J.M.J. Biodegradable dendritic positron-emitting nanoprobes for the noninvasive imaging of angiogenesis. *Proceedings of the National Academy of Sciences of the United States of America*, **2009**, 106(3), 685-90.

[143] Wangler, C., Maschauer, S., Prante, O., Schafer, M., Schirrmacher, R., Bartenstein, P., Eisenhut, M., Wangler, B. Multimerization of cRGD peptides by click chemistry Synthetic strategies, chemical limitations, and influence on biological properties. *ChemBioChem*, **2010**, 11(15), 2168-2181.

[144] Seo, J.W., Baek, H., Mahakian, L.M., Kusunose, J., Hamzah, J., Ruoslahti, E., Ferrara, K.W. 64Cu-Labeled LyP-1-Dendrimer for PET-CT Imaging of Atherosclerotic Plaque. *Bioconjugate Chemistry*, **2014**, 25(2), 231-239.

[145] Zhang, Y., Sun, Y., Xu, X., Zhu, H., Huang, L., Zhang, X., Qi, Y., Shen, Y.M. Radiosynthesis and micro-SPECT imaging of 99mTc-dendrimer polyamido-amine folic acid conjugate. *Bioorganic and Medicinal Chemistry Letters*, **2010**, 20(3), 927-931.

[146] Zhang, Y., Sun, Y., Xu, X., Zhang, X., Zhu, H., Huang, L., Qi, Y., Shen, Y.M. Synthesis, biodistribution, and microsingle photon emission computed tomography SPECT imaging study of technetium-99m labeled PEGylated dendrimer polyamidoamine PAMAM-folic acid conjugates. *Journal of Medicinal Chemistry*, **2010**, 53(8), 3262-3272.

[147] Kobayashi, H., Wu, C., Kim, M.-K., Paik, C.H., Carrasquillo, J.A., Brechbiel, M.W. Evaluation of the in vivo biodistribution of indium-11 and yttrium-88 labeled dendrimer-IB4M-DTPA and its conjugation with anti-tac monoclonal antibody. *Bioconjugate Chem*, **1999**, 10, 103-111.

[148] Garcia, J., Tang, T., Louie, A.Y. Nanoparticle-based multimodal PETMRI probes. *Nanomedicine London, England*, **2015**, 10(8), 1343-1359.

[149] El-Hammadi, M.M., Arias, J.L. Iron oxide-based multifunctional nanoparticulate systems for biomedical applications a patent review 2008 - present. *Expert opinion on therapeutic patents*, **2015**, 25(6), 691-709.

[150] Cui, X., Mathe, D., Kovacs, N., Horvath, I., Jauregui-Osoro, M., Torres Martin de Rosales, R., Mullen, G.E.D., Wong, W., Yan, Y., Kruger, D., Khlobystov, A.N., Gimenez-Lopez, M., Semjeni, M., Szigeti, K., Veres, D.S., Lu, H., Hernandez, I., Gillin, W.P., Protti, A., Petik, K.K., Green, M.A., Blower, P.J. Synthesis, Characterization, and Application of Core-Shell Co0.16Fe2.84O4NaYF4Yb, Er and Fe3O4NaYF4Yb, Tm Nanoparticle as Trimodal MRI, PETSPECT, and Optical Imaging Agents. *ACS Bioconjugate chemistry*, **2015**, A-J.

[151] Lee, N., Yoo, D., Ling, D., Cho, M.H., Hyeon, T., Cheon, J. Iron Oxide Based Nanoparticles for Multimodal Imaging and Magnetoresponsive Therapy. *Chemical Reviews*, **2015**, 115(19), 10637-10689.

[152] Qiao, Z., Shi, X. Dendrimer-based molecular imaging contrast agents. *Progress in Polymer Science*, **2015**, 44, 1-27.

[153] Lamanna, G., Kueny-Stotz, M., Mamlouk-Chaouachi, H., Ghobril, C., Basly, B., Bertin, A., Miladi, I., Billotey, C., Pourroy, G., Begin-Colin, S., Felder-Flesch, D. Dendronized iron oxide nanoparticles for multimodal imaging. *Biomaterials*, **2011**, 32(33), 8562-8573.

[154] Truong-Phuoc, L., Kueny-Stotz, M., Jouhannaud, J., Garofalo, A., Ble, F.X., Simon, H., Tellier, F., Poulet, P., Chirco, P., Begin-Colin, S., Pourroy, G., Felder-Flesch, D. Patent Blue Derivatized Dendronized Iron Oxide Nanoparticles for Multimodal Imaging. *European Journal of Inorganic Chemistry*, **2015**, 2015(27), 4565-4571.

[155] Kueny-Stotz, M., Mamlouk-Chaouachi, H., Felder-Flesch, D. Synthesis of Patent Blue derivatized hydrophilic dendrons dedicated to sentinel node detection in breast cancer. *Tetrahedron Letters*, **2011**, 52(22), 2906-2909.

[156] Ghobril, C., Popa, G., Parat, A., Billotey, C., Taleb, J., Bonazza, P., Begin-Colin, S., Felder-Flesch, D. A bisphosphonate tweezers and clickable PEGylated PAMAM dendrons for the preparation of functional iron oxide nanoparticles displaying renal and hepatobiliary elimination. *Chemical communications Cambridge, England*, **2013**, 49(80), 9158-9160.

[157] Walter, A., Parat, A., Garofalo, A., Laurent, S., Elst, L.V., Muller, R.N., Wu, T., Heuillard, E., Robinet, E., Meyer, F., Felder-Flesch, D., Begin-Colin, S., Vander Elst, L., Muller, R.N., Wu, T., Heuillard, E., Robinet, E., Meyer, F., Felder-Flesch, D., Begin-Colin, S. Modulation of Relaxivity, Suspension Stability, and Biodistribution of Dendronized Iron Oxide Nanoparticles as a Function of the Organic Shell Design. *Particle Particle Systems Characterization*, **2015**, 32(5), 552-560.

[158] Chen, Q., Li, K., Wen, S., Liu, H., Peng, C., Cai, H., Shen, M., Zhang, G., Shi, X. Targeted CTMR dual mode imaging of tumors using multifunctional dendrimer-entrapped gold nanoparticles. *Biomaterials*, **2013**, 34(21), 5200-5209.

[159] Cai, H., Li, K., Shen, M., Wen, S., Luo, Y., Peng, C., Zhang, G., Shi, X. Facile assembly of Fe3O4Au nanocomposite particles for dual mode magnetic resonance and computed tomography imaging applications. *Journal of Materials Chemistry*, **2012**, 22(30), 15110-15120.

[160] Chrastina, A., Massey, K.A., Schnitzer, J.E. Overcoming in vivo barriers to targeted nanodelivery. *Wiley Interdisciplinary Reviews Nanomedicine and Nanobiotechnology*, **2011**, 3(4), 421-437.

[161] Tomalia, D.A., Khanna, S.N. A Systematic Framework and Nanoperiodic Concept for Unifying Nanoscience HardSoft Nanoelements, Superatoms, Meta-Atoms, New Emerging Properties, Periodic Property Patterns, and Predictive Mendeleev-like Nanoperiodic Tables. *Chemical Reviews*, **2016**, 116(4), 2705-2774.

[162] Tomalia, D.A., Reyna, L.A., Svenson, S. Dendrimers as multi-purpose nanodevices for oncology drug delivery and diagnostic imaging. *Biochemical Society transactions*, **2007**, 35(1), 61-67.

[163] Thomas, T.P., Goonewardena, S.N., Majoros, I.J., Kotlyar, A., Cao, Z., Leroueil, P.R., Baker, J.R. Folate-targeted nanoparticles show efficacy in the treatment of inflammatory arthritis. *Arthritis and Rheumatism*, **2011**, 63(9), 2671-2680.

[164] Gerard, H.C., Mishra, M.K., Mao, G., Wang, S., Hali, M., Whittum-Hudson, J.A., Kannan, R.M., Hudson, A.P. Dendrimer-enabled DNA delivery and transformation of Chlamydia pneumoniae. *Nanomedicine Nanotechnology, Biology, and Medicine*, **2013**, 9(7), 996-1008.

[165] Kannan, R.M., Gerard, H.C., Mishra, M.K., Mao, G., Wang, S., Hali, M., Whittum-Hudson, J.A., Hudson, A.P. Dendrimer-enabled transformation of Chlamydia trachomatis. *Microbial Pathogenesis*, **2013**, 65, 29-35.

[166] Hayder, M., Poupot, M., Baron, M., Nigon, D., Turrin, C., Caminade, A., Majoral, J., Eisenberg, R.A., Fournie, J., Cantagrel, A., Poupot, R., Davignon, J. A phosphorus-based dendrimer targets inflammation and osteoclastogenesis in experimental arthritis. *Science translational medicine*, **2011**, 3(81), 81ra35.

[167] Chauhan, A.S., Jain, N.K., Diwan, P.V., Khopade, A.J. Solubility enhancement of indomethacin with polyamidoamine dendrimers and targeting to inflammatory regions of arthritic rats. *Journal of drug targeting*, **2004**, 12(December), 575-583.

[168] Chauhan, A.S., Diwan, P.V., Jain, N.K., Tomalia, D.A. Unexpected in vivo anti-inflammatory activity observed for simple, surface functionalized polyamidoamine dendrimers. *Biomacromolecules*, **2009**, 10(5), 1195-1202.

[169] Inapagolla, R., Guru, B.R., Kurtoglu, Y.E., Gao, X., Lieh-Lai, M., Bassett, D.J.P., Kannan, R.M. In vivo efficacy of dendrimer-methylprednisolone conjugate formulation for the treatment of lung inflammation. *International Journal of Pharmaceutics*, **2010**, 399(1-2), 140-147.

[170] Blattes, E., Vercellone, A., Eutamene, H., Turrin, C., Theodorou, V., Majoral, J., Caminade, A., Prandi, J., Nigou, J., Puzo, G. Mannodendrimers prevent acute lung inflammation by inhibiting neutrophil recruitment. *Proceedings of the National Academy of Sciences of the United States of America*, **2013**, 110(22), 8795-8800.

[171] Iezzi, R., Guru, B.R., Glybina, I.V., Mishra, M.K., Kennedy, A., Kannan, R.M. Dendrimer-based targeted intravitreal therapy for sustained attenuation of neuroinflammation in retinal degeneration. *Biomaterials*, **2012**, 33(3), 979-988.

[172] Kannan, S., Dai, H., Navath, R.S., Balakrishnan, B., Jyoti, A., Janisse, J., Romero, R., Kannan, R.M. Dendrimer-Based Postnatal Therapy for Neuroinflammation and Cerebral Palsy in a Rabbit Model. *Science Translational Medicine*, **2012**, 4(130), 130ra46-130ra46.

[173] Malik, N., Evagorou, E.G., Duncan, R. Dendrimer-platinate a novel approach to cancer chemotherapy. *Anticancer Drugs*, **1999**, 10(8), 767-776.

[174] Kaminskas, L.M., McLeod, V.M., Kelly, B.D., Cullinane, C., Sberna, G., Williamson, M., Boyd, B.J., Owen, D.J., Porter, C.J.H. Doxorubicin-conjugated PEGylated dendrimers show similar tumoricidal activity but lower systemic toxicity when compared to PEGylated liposome and solution formulations in mouse and rat tumor models. *Molecular Pharmaceutics*, **2012**, 9(3), 422-432.

[175] Jiang, Y., Tang, G., Zhang, L., Kong, S., Zhu, S., Pei, Y. PEGylated PAMAM dendrimers as a potential drug delivery carrier in vitro and in vivo comparative evaluation of covalently conjugated drug and noncovalent drug inclusion complex. *Journal of drug targeting*, **2010**, 18(5), 389-403.

[176] Kannan, R.M., Nance, E., Kannan, S., Tomalia, D.A. Emerging concepts in dendrimer-based nanomedicine from design principles to clinical applications. *Journal of internal medicine*, **2014**, 276(6), 579-617.

[177] Zhang, L., Zhu, S., Qian, L., Pei, Y., Qiu, Y., Jiang, Y. RGD-modified PEG-PAMAM-DOX conjugates In vitro and in vivo studies for glioma. *European Journal of Pharmaceutics and Biopharmaceutics*, **2011**, 79(2), 232-240.

[178] Gajbhiye, V., Jain, N.K. The treatment of Glioblastoma Xenografts by surfactant conjugated dendritic nanoconjugates. *Biomaterials*, **2011**, 32(26), 6213-6225.

[179] Singh, P., Gupta, U., Asthana, A., Jain, N.K. Folate and Folate-PEG-PAMAM Dendrimers Synthesis , Characterization , and Targeted Anticancer Drug Delivery Potential in Tumor Bearing Mice. *Bioconjugate Chemistry*, **2008**, 19, 2239-2252.

[180] Ly, T.U., Tran, N.Q., Hoang, T.K.D., Phan, K.N., Truong, H.N., Nguyen, C.K. Pegylated dendrimer and its effect in fluorouracil loading and release for enhancing antitumor activity. *Journal of Biomedical Nanotechnology*, **2013**, 9(2), 213-220.

[181] Fox, M.E., Guillaudeu, S., Frechet, J.M.J., Jerger, K., Macaraeg, N., Szoka, F.C. Synthesis and in vivo antitumor efficacy of PEGylated polyL-lysine dendrimer-camptothecin conjugates. *Molecular Pharmaceutics*, **2009**, 6(5), 1562-1572.

[182] Sato, N., Kobayashi, H., Saga, T., Nakamoto, Y., Ishimori, T., Togashi, K., Fujibayashi, Y., Konishi, J., Brechbiel, M.W. Tumor targeting and imaging of intraperitoneal tumors by use of antisense oligo-DNA complexed with dendrimers andor avidin in mice. *Clinical Cancer Research*, **2001**, 7(11), 3606-3612.

[183] Vincent, L., Varet, J., Pille, J., Bompais, H., Opolon, P., Maksimenko, A., Malvy, C., Mirshahi, M., Lu, H., Vannier, J., Soria, C., Li, H. Efficacy of dendrimer-mediated angiostatin and TIMP-2 gene delivery on inhibition of tumor growth and angiogenesis in vitro and in vivo studies. *International journal of cancer. Journal international du cancer*, **2003**, 105(3), 419-29.

[184] Koppu, S., Oh, Y.J., Edrada-Ebel, R., Blatchford, D.R., Tetley, L., Tate, R.J., Dufes, C. Tumor regression after systemic administration of a novel tumor-targeted gene delivery system carrying a therapeutic plasmid DNA. *Journal of Controlled Release*, **2010**, 143(2), 215-221.

[185] Shaunak, S., Thomas, S., Gianasi, E., Godwin, A., Jones, E., Teo, I., Mireskandari, K., Luthert, P., Duncan, R., Patterson, S., Khaw, P., Brocchini, S. Polyvalent dendrimer glucosamine conjugates prevent scar tissue formation. *Nature biotechnology*, **2004**, 22(8), 977-984.

[186] Wang, B., Navath, R.S., Menjoge, A.R., Balakrishnan, B., Bellair, R., Dai, H., Romero, R., Kannan, S., Kannan, R.M. Inhibition of bacterial growth and intramniotic infection in a guinea pig model of chorioamnionitis using PAMAM dendrimers. *International Journal of Pharmaceutics*, **2010**, 395, 298-308.

[187] Landers, J.J., Cao, Z., Lee, I., Piehler, L.T., Myc, P.P., Myc, A., Hamouda, T., Galecki, A.T., Baker, J.R. Prevention of influenza pneumonitis by sialic Acid-conjugated dendritic polymers. *The Journal of infectious diseases*, **2002**, 186(9), 1222-1230.

[188] Kumar, P.V., Agashe, H., Dutta, T., Jain, N.K. PEGylated dendritic architecture for development of a prolonged drug delivery system for an antitubercular drug. *Current drug delivery*, **2007**, 4(1), 11-19.

[189] Zhou, J., Neff, C.P., Liu, X., Zhang, J., Li, H., Smith, D.D., Swiderski, P., Aboellail, T., Huang, Y., Du, Q., Liang, Z., Peng, L., Akkina, R., Rossi, J.J. Systemic administration of combinatorial dsiRNAs via nanoparticles efficiently suppresses HIV-1 infection in humanized mice. *Molecular therapy the journal of the American Society of Gene Therapy*, **2011**, 19(12), 2228-2238.

[190] Kobayashi, H., Sato, N., Kawamoto, S., Saga, T., Hiraga, A., Laz Haque, T., Ishimori, T., Konishi, J., Togashi, K., Brechbiel, M.W. Comparison of the macromolecular MR contrast agents with ethylenediamine-core versus ammonia-core generation-6 polyamidoamine dendrimer. *Bioconjugate Chemistry*, **2001**, 12(1), 100-107.

[191] Kobayashi, H., Sato, N., Hiraga, A., Saga, T., Nakamoto, Y., Ueda, H., Konishi, J., Togashi, K., Brechbiel, M.W. 3D-Micro-MR angiography of mice using macromolecular MR contrast agents with polyamidoamine dendrimer core with reference to their pharmacokinetic properties. *Magnetic Resonance in Medicine*, **2001**, 45(3), 454-460.

[192] Sato, N., Kobayashi, H., Hiraga, A., Saga, T., Togashi, K., Konishi, J., Brechbiel, M.W. Pharmacokinetics and enhancement patterns of macromolecular MR contrast agents with various sizes of polyamidoamine dendrimer cores. *Magnetic Resonance in Medicine*, **2001**, 46(6), 1169-1173.

[193] Criscione, J.M., Dobrucki, L.W., Zhuang, Z.W., Papademetris, X., Simons, M., Sinusas, A.J., Fahmy, T.M. Development and Application of a Multimodal Contrast Agent for SPECTCT Hybrid Imaging. *Bioconjugate Chemistry*, **2011**, 22, 1784-1792.

[194] Castelli, D.D., Terreno, E., Longo, D., Aime, S. Nanoparticle-based chemical exchange saturation transfer CEST agents. *NMR in Biomedicine*, **2013**, 26(7), 839-849.

[195] Pikkemaat, J., Wegh, R., Lamerichs, R., van de Molengraaf, R., Langereis, S., Burdinski, D., Raymond, A.Y.F., Janssen, H.M., de Waal, B.F.M., Willard, N.P Dendritic PARACEST contrast agents for magnetic resonance imaging. *Contrast Media Molecular Imaging*, **2007**, 2(5), 229-239.

[196] Ali, M.M., Liu, G., Shah, T., Flask, C.A., Pagel, M.D. Using Two Chemical Exchange Saturation Transfer Magnetic Resonance Imagining Contrast Agents for Molecular Imaging Studies. *Acc. Chem. Res*, **2009**, 42(7), 915-924.

[197] Avti, P.K., Kakkar, A. Dendrimers as anti-inflammatory agents. *Brazilian Journal of Pharmaceutical Sciences*, **2013**, 49, 57-65.

[198] Cheng, Y., Li, Y., Wu, Q., Zhang, J., Xu, T. Generation-dependent encapsulationelectrostatic attachment of phenobarbital molecules by polyamidoamine dendrimers Evidence from 2D-NOESY investigations. *European Journal of Medicinal Chemistry*, **2009**, 44(5), 2219-2223.

[199] Cheng, Y., Wu, Q., Li, Y., Xu, T. External electrostatic interaction versus internal encapsulation between cationic dendrimers and negatively charged drugs Which contributes more to solubility enhancement of the drugs. *Journal of Physical Chemistry B*, **2008**, 112(30), 8884-8890.

[200] Tanis, I., Karatasos, K. Association of a weakly acidic anti-inflammatory drug ibuprofen with a poly amidoamine dendrimer as studied by molecular dynamics simulations. *The Journal of Physical Chemistry B*, **2009**, 113(31), 10984-10993.

[201] Kolhe, P., Misra, E., Kannan, R.M., Kannan, S., Lieh-Lai, M. Drug complexation, in vitro release and cellular entry of dendrimers and hyperbranched polymers. *International Journal of Pharmaceutics*, **2003**, 259(1-2), 143-160.

[202] Avila-Salas, F., Sandoval, C., Caballero, J., Guinez-Molinos, S., Santos, L.S., Cachau, R.E., Gonzalez-Nilo, F.D. Study of interaction energies between the PAMAM dendrimer and nonsteroidal anti-inflammatory drug using a distributed computational strategy and experimental analysis by ESI-MSMS. *Journal of Physical Chemistry B*, **2012**, 116(7), 2031-2039.

[203] Alavidjeh, M.S., Haririan, I., Khorramizadeh, M.R., Ghane, Z.Z., Ardestani, M.S., Namazi, H. Anionic linear-globular dendrimers Biocompatible hybrid materials with potential uses in nanomedicine. *Journal of Materials Science Materials in Medicine*, **2010**, 21(4), 1121-1133.

[204] Namazi, H., Adeli, M. Dendrimers of citric acid and poly ethylene glycol as the new drug-delivery agents. *Biomaterials*, **2005**, 26(10), 1175-1183.

[205] Gajbhiye, V., Kumar, P.V., Sharma, A., Jain, N.K. Novel PEGylated PPI Dendritic Nanostructures for Sustained Delivery of Anti-Inflammatory Agent. *Current Nanoscience*, **2008**, 4(3), 267-277.

[206] Koc, F.E., Senel, M. Solubility enhancement of Non-Steroidal Anti-Inflammatory Drugs NSAIDs using polypolypropylene oxide core PAMAM dendrimers. *International Journal of Pharmaceutics*, **2013**, 451(1-2), 18-22.

[207] Asthana, A., Chauhan, A.S., Diwan, P.V., Jain, N.K. Polyamidoamine PAMAM dendritic nanostructures for controlled site-specific delivery of acidic anti-inflammatory active ingredient. *AAPS PharmSciTech*, **2005**, 6(3), E536-42.

[208] Sun, Q., Radosz, M., Shen, Y. Challenges in design of translational nanocarriers. *Journal of Controlled Release*, **2012**, 164(2), 156-169.

[209] Mody, N., Tekade, R.K., Mehra, N.K., Chopdey, P., Jain, N.K. Dendrimer, Liposomes, Carbon Nanotubes and PLGA Nanoparticles One Platform Assessment of Drug Delivery Potential. *AAPS PharmSciTech*, **2014**, 15(2), 388-99.

[210] Kararli, T.T. Comparison of the gastrointestinam anatomy, physiology, and biochemistry of humans and commonly used laboratory animals. *Biopharmaceutics and drug disposition*, **1995**, 16, 351-380.

[211] Na, M., Yiyun, C., Tongwen, X., Yang, D., Xiaomin, W., Zhenwei, L., Zhichao, C., Guanyi, H., Yunyu, S., Longping, W. Dendrimers as potential drug carriers. Part II. Prolonged delivery of ketoprofen by in vitro and in vivo studies. *European Journal of Medicinal Chemistry*, **2006**, 41(5), 670-674.

[212] Cerqueira, S.R., Oliveira, J.M., Silva, N.A., Leite-Almeida, H., Ribeiro-Samy, S., Almeida, A., Mano, J.F., Sousa, N., Salgado, A.J., Reis, R.L. Microglia response and in vivo therapeutic potential of methylprednisolone-loaded dendrimer nanoparticles in spinal cord injury. *Small*, **2013**, 9(5), 738-749.

[213] Cerqueira, S.R., Silva, B.L., Oliveira, J.M., Mano, J.F., Sousa, N., Salgado, A.J., Reis, R.L. Multifunctionalized CMChtPAMAM Dendrimer Nanoparticles Modulate the Cellular Uptake by Astrocytes and Oligodendrocytes in Primary Cultures of Glial Cells. *Macromolecular Bioscience*, **2012**, 12(5), 591-597.

[214] Low, P.S., Henne, W.A., Doorneweerd, D.D. Discovery and development of folic-acid-based receptor targeting for imaging and therapy of cancer and inflammatory diseases. *Accounts of Chemical Research*, **2008**, 41(1), 120-129.

[215] Wiwattanapatapee, R., Lomlim, L., Saramunee, K. Dendrimers conjugates for colonic delivery of 5-aminosalicylic acid. *Journal of Controlled Release*, **2003**, 88(1), 1-9.

[216] Najlah, M., Freeman, S., Attwood, D., DEmanuele, A. Synthesis, characterization and stability of dendrimer prodrugs. *International Journal of Pharmaceutics*, **2006**, 308(1-2), 175-182.

[217] Kolhe, P., Khandare, J., Pillai, O., Kannan, S., Lieh-Lai, M., Kannan, R.M. Preparation, cellular transport, and activity of polyamidoamine-based dendritic nanodevices with a high drug payload. *Biomaterials*, **2006**, 27(4), 660-669.

[218] Jimenez, J.L., Clemente, M.I., Weber, N.D., Sanchez, J., Ortega, P., de la Mata, F.J., Gomez, R., Garcia, D., Lopez-Fernandez, L.A., Munoz-Fernandez, M.A. Carbosilane dendrimers to transfect human astrocytes with small interfering RNA targeting human immunodeficiency virus. *BioDrugs clinical immunotherapeutics, biopharmaceuticals and gene therapy*, **2010**, 24(5), 331-343.

[219] Perise-Barrios, A.J., Gomez, R., Corbi, A.L., de la Mata, J., Dominguez-Soto, A., Munoz-Fernandez, M.A. Use of carbosilane dendrimer to switch macrophage polarization for the acquisition of antitumor functions. *Nanoscale*, **2015**, 7(9), 3857-3866.

[220] Rolland, O., Turrin, C., Caminade, A., Majoral, J. Dendrimers and nanomedicine multivalency in action. *New Journal of Chemistry*, **2009**, 33(9), 1809-1824.

[221] Poupot, M., Griffe, L., Marchand, P., Maraval, A., Rolland, O., Martinet, L., LFaqihi-Olive, F., Turrin, C., Caminade, A., Fournie, J., Majoral, J., Poupot, R. Design of phosphorylated dendritic architectures to promote human monocyte activation. *The FASEB journal official publication of the Federation of American Societies for Experimental Biology*, **2006**, 20(13), 2339-2351.

[222] Rolland, O., Griffe, L., Poupot, M., Maraval, A., Ouali, A., Coppel, Y., Fournie, J.J., Bacquet, G., Turrin, C.O., Caminade, A.M., Majoral, J.P., Poupot, R. Tailored control and optimisation of the number of phosphonic acid termini on phosphorus-containing dendrimers for the ex-vivo activation of human monocytes. *Chemistry - A European Journal*, **2008**, 14(16), 4836-4850.

[223] Rolland, O., Turrin, C.O., Bacquet, G., Poupot, R., Poupot, M., Caminade, A.M., Majoral, J.P. Efficient synthesis of phosphorus-containing dendrimers capped with isosteric functions of amino-bismethylene phosphonic acids. *Tetrahedron Letters*, **2009**, 50(18), 2078-2082.

[224] Marchand, P., Griffe, L., Poupot, M., Turrin, C.O., Bacquet, G., Fournie, J.J., Majoral, J.P., Poupot, R., Caminade, A.M. Dendrimers ended by non-symmetrical azadiphosphonate groups Synthesis and immunological properties. *Bioorganic and Medicinal Chemistry Letters*, **2009**, 19(14), 3963-3966.

[225] Fruchon, S., Poupot, M., Martinet, L., Turrin, C., Majoral, J., Fournie, J., Caminade, A., Poupot, R. Anti-inflammatory and immunosuppressive activation of human monocytes by a bioactive dendrimer. *Journal of Leukocyte Biology*, **2009**, 85(3), 553-562.

[226] Portevin, D., Poupot, M., Rolland, O., Turrin, C., Fournie, J., Majoral, J., Caminade, A., Poupot, R. Regulatory activity of azabisphosphonate-capped dendrimers on human CD4+ T cell proliferation enhances ex-vivo expansion of NK cells from PBMCs for immunotherapy. *Journal of translational medicine*, **2009**, 7, 82-95.

[227] Marsolais, D., Rosen, H. Chemical modulators of sphingosine-1-phosphate receptors as barrier-oriented therapeutic molecules. *Nature reviews. Drug discovery*, **2009**, 8(4), 297-307.

[228] Jevprasesphant, R., Penny, J., Attwood, D., DEmanuele, A. Transport of dendrimer nanocarriers through epithelial cells via the transcellular route. *Journal of Controlled Release*, **2004**, 97(2), 259-267.

[229] Paleos, C.M., Tziveleka, L., Sideratou, Z., Tsiourvas, D. Gene delivery using functional dendritic polymers. *Expert opinion on drug delivery*, **2009**, 6(1), 27-38.

[230] Gao, Y.a, Gao, G.b, He, Y.a, Liu, T.a, Qi, R.a Recent advances of dendrimers in delivery of genes and drugs. *Mini-Reviews in Medicinal Chemistry*, **2008**, 8(9), 889-900.

[231] Yang, J., Zhang, Q., Chang, H., Cheng, Y. Surface-Engineered Dendrimers in Gene Delivery. *Chemical Reviews*, **2015**, 115(11), 5274-5300.

[232] Raftery, R.M., Walsh, D.P., Castano, I.M., Heise, A., Duffy, G.P., Cryan, S.A., OBrien, F.J. Delivering Nucleic-Acid Based Nanomedicines on Biomaterial Scaffolds for Orthopedic Tissue Repair Challenges, Progress and Future Perspectives. *Advanced Materials*, **2016**, Ahead of P, Ahead of publishing.

[233] Patil, S.D., Rhodes, D.G., Burgess, D.J. DNA-based therapeutics and DNA delivery systems a comprehensive review. *The AAPS journal*, **2005**, 7(1), E61-E77.

[234] Raper, S.E., Chirmule, N., Lee, F.S., Wivel, N.A., Bagg, A., Gao, G.P., Wilson, J.M., Batshaw, M.L. Fatal systemic inflammatory response syndrome in a ornithine transcarbamylase deficient patient following adenoviral gene transfer. *Molecular Genetics and Metabolism*, **2003**, 80(1-2), 148-158.

[235] Luo, D., Saltzman, W.M. Synthetic DNA delivery systems. *Nature Biotechnology*, **2000**, 8(1), 33-37.

[236] Behr, J. Synthetic Gene-Transfer Vectors. *American Chemical Society*, **1993**, 26(June 1989), 274-278.

[237] Boussif, O., Lezoualch, F., Zanta, M.A., Mergny, M.D., Scherman, D., Demeneix, B., Behr, J.P. A versatile vector for gene and oligonucleotide transfer into cells in culture and in vivo polyethylenimine. *Proceedings of the National Academy of Sciences of the United States of America*, **1995**, 92(16), 7297-7301.

[238] LeHoux, J.G., Grondin, F. Some effects of chitosan on liver function in the raat. *Endocrinology*, **1993**, 132(3), 1078-1084.

[239] Dennig, J. Gene transfer in eukaryotic cells using activated dendrimers. *Topics in current chemistry*, **2003**, 228, 227-236.

[240] Kitchens, K.M., El-Sayed, M.E.H., Ghandehari, H. Transepithelial and endothelial transport of poly amidoamine dendrimers. *Advanced Drug Delivery Reviews*, **2005**, 57(15), 2163-2176.

[241] Ramaswamy, C., Sakthivel, T., Wilderspin, A.F., Florence, A.T. Dendriplexes and their characterisation. *International Journal of Pharmaceutics*, **2003**, 254(1), 17-21.

[242] Caminade, A.M., Turrin, C.O., Majoral, J.P. Dendrimers and DNA Combinations of two special topologies for nanomaterials and biology. *Chemistry - A European Journal*, **2008**, 14(25), 7422-7432.

[243] Dufes, C., Uchegbu, I.F., Schatzlein, A.G. Dendrimers in gene delivery. *Advanced Drug Delivery Reviews*, **2005**, 57(15), 2177-2202.

[244] Liu, H., Wang, Y., Wang, M., Xiao, J., Cheng, Y. Fluorinated polypropylenimine dendrimers as gene vectors. *Biomaterials*, **2014**, 35(20), 5407-5413.

[245] Liu, W., Xue, Y., Peng, N., He, W., Zhuo, R., Huang, S. Dendrimer modified magnetic iron oxide nanoparticleDNAPEI ternary magnetoplexes a novel strategy for magnetofection. *Journal of Materials Chemistry*, **2011**, 21(35), 13306-13315.

[246] Pan, B., Cui, D., Sheng, Y., Ozkan, C., Gao, F., He, R., Li, Q., Xu, P., Huang, T. Dendrimer-modified magnetic nanoparticles enhance efficiency of gene delivery system. *Cancer research*, **2007**, 67(17), 8156-8163.

[247] Xiao, T.Y., Hou, W.X., Cao, X.Y., Wen, S.H., Shen, M.W., Shi, X.Y. Dendrimer-entrapped gold nanoparticles modified with folic acid for targeted gene delivery applications. *Biomaterials Science*, **2013**, 1(11), 1172-1180.

[248] Hussain, N. Formulation and stability of surface-tethered DNA-gold-dendron nanoparticles. *International Journal of Pharmaceutics*, **2003**, 254(1), 27-31.

[249] Singh, B., Hussain, N., Sakthivel, T., Florence, A.T. Effect of physiological media on the stability of surface-adsorbed DNA-dendron-gold nanoparticles. *The Journal of pharmacy and pharmacology*, **2003**, 55(12), 1635-1640.

[250] Choi, J.S., Nam, K., Park, J.Y., Kim, J.B., Lee, J.K., Park, J.S. Enhanced transfection efficiency of PAMAM dendrimer by surface modification with l-arginine. *Journal of Controlled Release*, **2004**, 99(3), 445-456.

[251] Sashiwa, H., Yajima, H., Aiba, S.I. Synthesis of a chitosan-dendrimer hybrid and its biodegradation. *Biomacromolecules*, **2003**, 4(5), 1244-1249.

[252] Kwok, A., Eggimann, G.A., Reymond, J., Darbre, T., Hollfelder, F. Peptide Dendrimer Lipid Hybrid Systems are Efficient DNA Transfection Generations Reagents Relationships Highlight the Role of Charge Distribution Across Dendrimer. *ACS Nano*, **2013**, 7, 4668-4682.

[253] Arima, H., Kihara, F., Hirayama, F., Uekama, K. Enhancement of gene expression by polyamidoamine dendrimer conjugates with a-, b-, and g-cyclodextrins. *Bioconjugate Chemistry*, **2001**, 12(4), 476-484.

[254] Zhou, J., Wu, J., Hafdi, N., Behr, J., Erbacher, P., Peng, L. PAMAM dendrimers for efficient siRNA delivery and potent gene silencing. *Chemical communications Cambridge, England*, **2006**, 2362-2364.

[255] Liu, X., Liu, C., Catapano, C.V., Peng, L., Zhou, J., Rocchi, P. Structurally flexible triethanolamine-core polyamidoamine dendrimers as effective nanovectors to deliver RNAi-based therapeutics. *Biotechnology Advances*, **2014**, 32(4), 844-852.

[256] Wu, J., Zhou, J., Qu, F., Bao, P., Zhang, Y., Peng, L. Polycationic dendrimers interact with RNA molecules polyamine dendrimers inhibit the catalytic activity of Candida ribozymes. *Chemical communications*, **2005**, 3, 313-315.

[257] Shen, X., Zhou, J., Liu, X., Wu, J., Qu, F., Zhang, Z., Pang, D., Quelever, G., Zhang, C., Peng, L. Importance of size-to-charge ratio in construction of stable and uniform nanoscale RNAdendrimer complexes. *Organic biomolecular chemistry*, **2007**, 5(22), 3674-3681.

[258] Liu, X.X., Rocchi, P., Qu, F.Q., Zheng, S.Q., Liang, Z.C., Gleave, M., Iovanna, J., Peng, L. PAMAM dendrimers mediate siRNA delivery to target Hsp27 and produce potent antiproliferative effects on prostate cancer cells. *ChemMedChem*, **2009**, 4(8), 1302-1310.

[259] Cornford, P.A., Dodson, A.R., Parsons, K.F., Desmond, A.D., Woolfenden, A., Fordham, M., Neoptolemos, J.P., Ke, Y., Foster, C.S. Heat Shock Protein Expression Independently Predicts Clinical Outcome in Prostate Cancer. *Cancer Research*, **2000**, 60, 7099-7105.

[260] Rocchi, P., So, A., Kojima, S., Signaevsky, M., Beraldi, E., Fazli, L., Hurtado-coll, A., Yamanaka, K., Gleave, M. Heat Shock Protein 27 Increases after Androgen Ablation and Plays a Cytoprotective Role in Hormone-Refractory Prostate Cancer Heat Shock Protein 27 Increases after Androgen Ablation and Plays a Cytoprotective Role in Hormone-Refractory Prostate Cancer. *Cancer research*, **2004**, 64, 6595-6602.

[261] Xia, Y., Rocchi, P., Iovanna, J.L., Peng, L. Targeting heat shock response pathways to treat pancreatic cancer. *Drug Discovery Today*, **2012**, 17(1-2), 35-43.

[262] Weber, N., Ortega, P., Clemente, M.I., Shcharbin, D., Bryszewska, M., de la Mata, F.J., Gomez, R., Munoz-Fernandez, M.A. Characterization of carbosilane dendrimers as effective carriers of siRNA to HIV-infected lymphocytes. *Journal of Controlled Release*, **2008**, 132(1), 55-64.

[263] Tarze, A., Deniaud, A., Le Bras, M., Maillier, E., Molle, D., Larochette, N., Zamzami, N., Jan, G., Kroemer, G., Brenner, C. GAPDH, a novel regulator of the pro-apoptotic mitochondrial membrane permeabilization. *Oncogene*, **2007**, 26(18), 2606-2620.

[264] Rowland, M., Tozer, T.N. Clinical Pharmacokinetics Concepts and Applications. *Williams Wilkins*, **1995**.

[265] Markman, J.L., Rekechenetskiy, A., Holler, E., Ljubimova, J.Y. Nanomedicine therapeutic approaches to overcome cancer drug resistance. *Advanced Drug Delivery Reviews*, **2013**, 65, 1866-1879.

[266] Wu, L.P., Ficker, M., Christensen, J.B., Trohopoulos, P.N., Moghimi, S.M. Dendrimers in Medicine Therapeutic Concepts and Pharmaceutical Challenges. *Bioconjugate Chemistry*, **2015**, 26(7), 1198-1211.

[267] Gillies, E.R., Frechet, J.M.J. Dendrimers and dendritic polymers in drug delivery. *Drug Discovery Today*, **2005**, 10(1), 35-43.

[268] Wolinsky, J.B., Grinstaff, M.W. Therapeutic and diagnostic applications of dendrimers for cancer treatment. *Advanced Drug Delivery Reviews*, **2008**, 60(9), 1037-1055.

[269] Morgan, M.T., Carnahan, M.A., Finkelstein, S., Prata, C.A.H., Degoricija, L., Lee, S.J., Grinstaff, M.W. Dendritic supramolecular assemblies for drug delivery. *Chemical communications Cambridge, England*, **2005**, 4309-4311.

[270] Morgan, M.T., Nakanishi, Y., Kroll, D.J., Griset, A.P., Carnahan, M.A., Wathier, M., Oberlies, N.H., Manikumar, G., Wani, M.C., Grinstaff, M.W. Dendrimer-encapsulated camptothecins Increased solubility, cellular uptake, and cellular retention affords enhanced anticancer activity in vitro. *Cancer Research*, **2006**, 66(24), 11913-11921.

[271] Papagiannaros, A., Dimas, K., Papaioannou, G.T., Demetzos, C. Doxorubicin-PAMAM dendrimer complex attached to liposomes Cytotoxic studies against human cancer cell lines. *International Journal of Pharmaceutics*, **2005**, 302(1-2), 29-38.

[272] Ooya, T., Lee, J., Park, K. Hydrotropic dendrimers of generations 4 and 5 Synthesis, characterization, and hydrotropic solubilization of paclitaxel. *Bioconjugate Chemistry*, **2004**, 15(6), 1221-1229.

[273] Gurdag, S., Khandare, J., Stapels, S., Matherly, L.H., Kannan, R.M. Activity of dendrimer-methotrexate conjugates on methotrexate-sensitive and -resistant cell lines. *Bioconjugate Chemistry*, **2006**, 17(2), 275-283.

[274] Khandare, J.J., Jayant, S., Singh, A., Chandna, P., Wang, Y., Vorsa, N., Minko, T. Dendrimer versus linear conjugate Influence of polymeric architecture on the delivery and anticancer effect of paclitaxel. *Bioconjugate Chemistry*, **2006**, 17(6), 1464-1472.

[275] Hong, S., Leroueil, P.R., Majoros, I.J., Orr, B.G., Baker, J.R., Banaszak Holl, M.M. The Binding Avidity of a Nanoparticle-Based Multivalent Targeted Drug Delivery Platform. *Chemistry and Biology*, **2007**, 14(1), 107-115.

[276] Patri, A.K., Kukowska-Latallo, J.F., Baker, J.R. Targeted drug delivery with dendrimers Comparison of the release kinetics of covalently conjugated drug and non-covalent drug inclusion complex. *Advanced Drug Delivery Reviews*, **2005**, 57(15), 2203-2214.

[277] Patri, A.K., Myc, A., Beals, J., Thomas, T.P., Bander, N.H., Baker, J.R. Synthesis and in vitro testing of J591 antibody-dendrimer conjugates for targeted prostate cancer therapy. *Bioconjugate Chemistry*, **2004**, 15(6), 1174-1181.

[278] Thomas, T.P., Patri, A.K., Myc, A., Thiri, M., Ye, J.Y., Norris, T.B., Baker, J.R., Nanoparticles, D., Myaing, M.T. In Vitro Targeting of Synthesized Antibody-Conjugated Dendrimer Nanoparticles In Vitro Targeting of Synthesized Antibody-Conjugated. *Society*, **2004**, 5, 2269-2274.

[279] Wu, G., Barth, R.F., Yang, W., Kawabata, S., Zhang, L., Green-Church, K. Targeted delivery of methotrexate to epidermal growth factor receptor-positive brain tumors by means of cetuximab IMC-C225 dendrimer bioconjugates. *Molecular cancer therapeutics*, **2006**, 5(1), 52-59.

[280] Sumer, B., Gao, J. Theranostic nanomedicine for cancer. *Nanomedicine London, England*, **2008**, 3(2), 137-140.

[281] Lee, D.Y., Li, K.C.P. Molecular theranostics A primer for the imaging professional. *American Journal of Roentgenology*, **2011**, 197(2), 318-324.

[282] Hertz, S., Roberts, A. Radioactive iodine in the study of thyroid physioogy. *Journal of American Medical Association*, **1946**, 131(2), 81-86.

[283] Ravdin, I.S., Rose, E., Maxwell, J.D. The treatment of thyrotoxicosis. *Journal of American Medical Association*, **1946**, 140(2), 141-146.

[284] Chang, Y., Liu, N., Chen, L., Meng, X., Liu, Y., Li, Y., Wang, J. Synthesis and characterization of DOX-conjugated dendrimer-modified magnetic iron oxide conjugates for magnetic resonance imaging, targeting, and drug delivery. *Journal of Materials Chemistry*, **2012**, 22(19), 9594-9601.

[285] Chandra, S., Mehta, S., Nigam, S., Bahadur, D. Dendritic magnetite nanocarriers for drug delivery applications. *New Journal of Chemistry*, **2010**, 34(4), 648-655.

[286] Gao, F., Pan, B., Zheng, W., Ao, L., Gu, H. Study of streptavidin coated onto PAMAM dendrimer modified magnetite nanoparticles. *Journal of Magnetism and Magnetic Materials*, **2005**, 293(1), 48-54.

[287] Hugounenq, P., Alloyeau, D., Clarke, S.P., Le, M., Bazzi, R., Brougham, D.F., Wilhelm, C., Gazeau, F. Cooperative Organization in Iron Oxide Multi-Core Nanoparticles Potentiates Their Efficiency as Heating Mediators and MRI Contrast Agents. *ACS NANO*, **2012**, 6(12), 10935-10949.

[288] Goya, G.F., Asin, L., Ibarra, M.R. Cell death induced by AC magnetic fields and magnetic nanoparticles current state and perspectives. *International Journal of Hyperthermia*, **2013**, 29(8), 810-8.

[289] Gazeau, F., Levy, M., Wilhelm, C. Optimizing magnetic nanoparticle design for nanothermotherapy. *Nanomedicine*, **2008**, 3(6), 831-844.

[290] Walter, A., Taleb, J., Laurent, S., Elst, L.V., Muller, R.N., Cnrs-ucbl, U.M.R., Claude, U., Lyon, B., Byron, A. Mastering the Shape and Composition of Dendronized Iron Oxide Nanoparticles To Tailor Magnetic Resonance Imaging and Hyperthermia. *Chemistry of Materials*, **2014**, 26, 5225-5264.

[291] Guardia, P., Corato, R.D., Lartigue, L., Wilhelm, C., Espinosa, A., Garcia-Hernandez, M., Gazeau, F., Manna, L., Pellegrino, T. Water-Soluble Iron Oxide Nanocubes with High Values of Speci fi c Absorption Rate for Cancer Cell Hyperthermia Treatment. *ACS NANO*, **2012**, 6(4), 3080-3091.

[292] de la Presa, P..., Luengo, Y., Multigner, M., Costo, R., Morales, M.P., Rivero, G., Hernando, A. Study of Heating E ffi ciency as a Function of Concentration , Size , and Applied Field in gamma-Fe2O3 Nanoparticles. *The Journal of Physiccal Chemistry*, **2012**, 116, 25602-25610.

[293] Lee, K.Y., Mooney, D.J. Hydrogels for tissue engineering. *Chemical Reviews*, **2001**, 101(7), 1869-1879.

[294] Kopecek, J. HydrogelsFrom soft contact lenses and implants to self-assembled nanomatrials. *American Chemical Society, Polymer Preprints, Division of Polymer Chemistry*, **2009**, 47, 5929-5946.

[295] Ahadian, S., Sadeghian, R.B., Salehi, S., Ostrovidov, S., Bae, H., Ramalingam, M., Khademhosseini, A. Bioconjugated Hydrogels for Tissue Engineering and Regenerative Medicine. *Bioconjugate Chemistry*, **2015**, 26(10), 1984-2001.

[296] Smith, D.K. Dendritic gels - Many arms make light work. *Advanced Materials*, **2006**, 18(20), 2773-2778.

[297] Even-Ram, S., Artym, V., Yamada, K.M. Matrix Control of Stem Cell Fate. *Cell*, **2006**, 126(4), 645-647.

[298] Lee, J., Abdeen, A.A., Zhang, D., Kilian, K.A. Directing stem cell fate on hydrogel substrates by controlling cell geometry, matrix mechanics and adhesion ligand composition. *Biomaterials*, **2013**, 34(33), 8140-8148.

[299] Sontjens, S.H.M., Nettles, D.L., Carnahan, M.A., Setton, L.A., Grinstaff, M.W., Sontjens, S.H.M., Nettles, D.L., Carnahan, M.A., Setton, L.A., Grinstaff, M.W. Biodendrimer-Based Hydrogel Scaffolds for Cartilage Tissue Repair. *Biomacromolecules*, **2006**, 7, 310-316.

[300] Wang, Y., Zhao, Q., Zhang, H., Yang, S., Jia, X. A novel polyamido amine-dendrimer-based hydrogel as a mimic for the extracellular matrix. *Advanced Materials*, **2014**, 26(24), 4163-4167.

[301] Peng, H.T., Shek, P.N. Novel wound sealants biomaterials and applications. *Expert review of medical devices*, **2010**, 7(5), 639-659.

[302] Carnahan, M.A., Middleton, C., Kim, J., Kim, T., Grinstaff, M.W. Hybrid Dendritic - Linear Polyester - Ethers for in Situ Photopolymerization. *J. Am. Chem. Soc*, **2002**, 124, 5291-5293.

[303] Grinstaff, M.W. Designing hydrogel adhesives for corneal wound repair. *Biomaterials*, **2007**, 28(35), 5205-5214.

[304] Oelker, A.M., Grinstaff, M.W. Ophthalmic adhesives a materials chemistry perspective. *Journal of Materials Chemistry*, **2008**, 18(22), 2521-2536.

[305] Ghobril, C., Charoen, K., Rodriguez, E.K., Nazarian, A., Grinstaff, M.W. A dendritic thioester hydrogel based on thiol-thioester exchange as a dissolvable sealant system for wound closure. *Angewandte Chemie - International Edition*, **2013**, 52(52), 14070-14074.

[306] Hed, Y., Oberg, K., Berg, S., Nordberg, A., von Holst, H., Malkoch, M. Multipurpose heterofunctional dendritic scaffolds as crosslinkers towards functional soft hydrogels and implant adhesives in bone fracture applications. *Journal of Materials Chemistry B*, **2013**, 1(44), 6015.

[307] Wagner, J.G. Pharmacokinetics for the Pharmaceutical Scientist. *CRC Press*, **1993**.

[308] Gabrielsson, J., Weiner, D. Pharmacokinetic and Pharmacodynamic Data Analysis Concepts and Applications, Third Edition. *CRC Press*, **2001**.

[309] Gagliardini, E., Conti, S., Benigni, A., Remuzzi, G., Remuzzi, A. Imaging of the porous ultrastructure of the glomerular epithelial filtration slit. *Journal of the American Society of Nephrology JASN*, **2010**, 21(12), 2081-2089.

[310] Kaminskas, L.M., Boyd, B.J., Karellas, P., Krippner, G.Y., Lessene, R., Kelly, B., Porter, C.J.H. The impact of molecular weight and PEG chain length on the systemic pharmacokinetics of pegylated poly L-lysine dendrimers. *Molecular Pharmaceutics*, **2008**, 5(3), 449-463.

[311] Kaminskas, L.M., Kelly, B.D., McLeod, V.M., Sberna, G., Owen, D.J., Boyd, B.J., Porter, C.J.H. Characterisation and tumour targeting of PEGylated polylysine dendrimers bearing doxorubicin via a pH labile linker. *Journal of Controlled Release*, **2011**, 152(2), 241-248.

[312] Kaminskas, L.M., Boyd, B.J., Porter, C.J. Dendrimer pharmacokinetics the effect of size, structure and surface characteristics on ADME properties. *Nanomedicine*, **2011**, 6(6), 1063-1084.

[313] Kobayashi, H., Kawamoto, S., Saga, T., Sato, N., Hiraga, A., Konishi, J., Togashi, K., Brechbiel, M.W. Micro-MR angiography of normal and intratumoral vessels in mice using dedicated intravascular MR contrast agents with high generation of polyamidoamine dendrimer core Reference to pharmacokinetic properties of dendrimer-based MR contrast agents. *Journal of Magnetic Resonance Imaging*, **2001**, 14(6), 705-713.

[314] Gillies, R.E., Dy, E., Frechet, J.M.J., Szoka, F.C. Biological evaluation of polyester dendrimer poly ethylene oxide bow-tie hybrids with tunable molecular weight and architecture. *Molecular Pharmaceutics*, **2005**, 2(2), 129-138.

[315] Walter, a., Garofalo, A., Parat, A., Jouhannaud, J., Pourroy, G., Voirin, E., Laurent, S., Bonazza, P., Taleb, J., Billotey, C., Vander Elst, L., Muller, R.N., Begin-Colin, S., Felder-Flesch, D. Validation of a dendron concept to tune colloidal stability, MRI relaxivity and bioelimination of functional nanoparticles. *J. Mater. Chem. B*, **2015**, 3(8), 1484-1494.

[316] Longmire, M.R., Ogawa, M., Choyke, P.L., Kobayashi, H. Biologically optimized nanosized molecules and particles more than just size. *Bioconjugate chemistry*, **2011**, 22(6), 993-1000.

[317] Jevprasesphant, R., Penny, J., Jalal, R., Attwood, D., McKeown, N.B., DEmanuele, A. The influence of surface modification on the cytotoxicity of PAMAM dendrimers. *International Journal of Pharmaceutics*, **2003**, 252(1-2), 263-266.

[318] Boyd, B.J., Kaminskas, L.M., Karellas, P., Krippner, G., Lessene, R., Porter, C.J.H. Cationic poly-L-lysine dendrimers pharmacokinetics, biodistribution and evidence for metabolism and bioresorption after itravenous administration to rats. *Molecular Pharmaceutics*, **2006**, 3(5), 614-627.

[319] Chernoff, D.M., Derugin, N., Rajasinghe, H.A., Hanley, F.L., Higgins, C.B., Gooding, C.A. Measurement of collateral blood flow in a porcine model of aortic coarctation by velocity-encoded cine MRI. *Journal of Magnetic Resonance Imaging*, **1997**, 7(3), 557-563.

[320] Malik, N., Wiwattanapatapee, M.R., Klopsch, R., Lorenz, K., Frey, H., Weener, J.W., Meijer, E.W., Paulus, W., Duncan, R. Dendrimers Relationship between structure and biocompatibility in vitro,and preliminary studies on the biodistribution of 125l-labelled polyamidoamine dendrimers in vivo. *Journal of Controlled Release*, **2000**, 68, 299-302.

[321] Kaminskas, L.M., Boyd, B.J., Karellas, P., Henderson, S.A., Giannis, M.P., Krippner, G.Y., Porter, C.J.H. Impact of surface derivatization of poly-L-lysine dendrimers with anionic arylsulfonate or succinate groups on intravenous pharmacokinetics and disposition. *Molecular Pharmaceutics*, **2007**, 4(6), 949-961.

[322] Kaminskas, L.M., Kelly, B.D., McLeod, V.M., Sberna, G., Boyd, B.J., Owen, D.J., Porter, C.J.H. Capping methotrexate a-carboxyl groups enhances systemic exposure and retains the cytotoxicity of drug conjugated pegylated polylysine dendrimers. *Molecular Pharmaceutics*, **2011**, 8(2), 338-349.

[323] Sadekar, S., Linares, O., Noh, G., Hubbard, D., Ray, A., Janat-Amsbury, M., Peterson, C.M., Facelli, J., Ghandehari, H. Comparative Pharmacokinetics of Pamam-Oh Dendrimers and Hpma Copolymers in Ovarian-Tumor-Bearing Mice. *Drug Deliv Transl Res*, **2013**, 3(3), 260-271.

[324] Kaminskas, L.M., Kelly, B.D., McLeod, V.M., Boyd, B.J., Krippner, G.Y., Williams, E.D., Porter, C.J.H. Pharmacokinetics and tumor disposition of PEGylated, methotrexate conjugated poly-L-lysine dendrimers. *Molecular Pharmaceutics*, **2009**, 6(4), 1190-1204.

[325] vant Veer, L.J., Bernards, R. Enabling personalized cancer medicine through analysis of gene-expression patterns. *Nature*, **2008**, 452(7187), 564-570.

[326] Tuma, R.S Oncology Fatigue The Forgotten. *Oncology Times*, **2013**, 35(4), 6-8.

[327] Matsumura, Y., Maeda, H. A New Concept for Macromolecular Therapeutics in Cancer-Chemotherapy - Mechanism of Tumoritropic Accumulation of Proteins and the Antitumor Agent Smancs. *Cancer Research*, **1986**, 46(12), 6387-6392.

[328] Peer, D., Karp, J.M., Hong, S., Farokhzad, O.C., Margalit, R., Langer, R. Nanocarriers as an emerging platform for cancer therapy. *Nature nanotechnology*, **2007**, 2(12), 751-760.

[329] Bertrand, N., Wu, J., Xu, X., Kamaly, N., Farokhzad, O.C. Cancer nanotechnology the impact of passive and active targeting in the era of modern cancer biology. *Advanced drug delivery reviews*, **2014**, 66, 2-25.

[330] Sandanaraj, B.S., Gremlich, H.U., Kneuer, R., Dawson, J., Wacha, S. Fluorescent nanoprobes as a biomarker for increased vascular permeability Implications in diagnosis and Treatment of Cancer and Inflammation. *Bioconjugate Chemistry*, **2010**, 21(1), 93-101.

[331] Azzopardi, E.A., Ferguson, E.L., Thomas, D.W. The enhanced permeability retention effect A new paradigm for drug targeting in infection. *Journal of Antimicrobial Chemotherapy*, **2013**, 68(2), 257-274.

[332] Prabhakar, U., Maeda, H., K. Jain, R., Sevick-Muraca, E.M., Zamboni, W., Farokhzad, O.C., Barry, S.T., Gabizon, A., Grodzinski, P., Blakey, D.C. Challenges and key considerations of the enhanced permeability and retention effect for nanomedicine drug delivery in oncology. *Cancer Research*, **2013**, 73(8), 2412-2417.

[333] Quintana, A., Raczka, E., Piehler, L., Lee, I., Myc, A., Majoros, I., Patri, A.K., Thomas, T., Mule, J., Baker, J.R., Mule, J., Baker, J.R. Design and function of a dendrimer-based therapeutic nanodevice targeted to tumor cells through the folate receptor. *Pharmaceutical Research*, **2002**, 19(9), 1310-1316.

[334] Abolmaali, S.S., Tamaddon, A.M., Dinarvand, R. A review of therapeutic challenges and achievements of methotrexate delivery systems for treatment of cancer and rheumatoid arthritis. *Cancer Chemotherapy and Pharmacology*, **2013**, 71(5), 1115-1130.

[335] Shukla, R., Thomas, T.P., Desai, A.M., Kotlyar, A., Park, S.J., Baker, J.R. HER2 specific delivery of methotrexate by dendrimer conjugated anti-HER2 mAb. *Nanotechnology*, **2008**, 19(29), 2951021-2951027.

[336] Cheng, Z., Al Zaki, A., Hui, J.Z., Muzykantov, V.R., Tsourkas, A. Multifunctional nanoparticles cost versus benefit of adding targeting and imaging capabilities. *Science New York, N.Y*, **2012**, 338(6109), 903-10.

[337] Rajasekaran, A. Is prostate-specific membrane antigen a multifunctional protein. *Am J Physiol Cell Physiol*, **2005**, 288(67), 975-981.

[338] Sassoon, I., Blanc, V. Antibody-Drug Conjugates Clinical Pipeline A review. *Methods in molecular biology Ducry, Laurent*, **2013**, 1-27.

[339] Garland, M., Yim, J.J., Bogyo, M. A Bright Future for Precision Medicine Advances in Fluorescent Chemical Probe Design and Their Clinical Application. *Cell Chemical Biology*, **2016**, 23(1), 122-136.

[340] Henderson, C., Wijetunge, L., Kinoshita, M.N., Shumway, M., Hammond, R.S., Postma, F.R., Brynczka, C., Rush, R., Thomas, A., Paylor, R., Warren, S.T., Vanderklish, P.W., Kind, P.C., Carpenter, R.L., Bear, M.F., Healy, a.M. Reversal of Disease-Related Pathologies in the Fragile X Mouse Model by Selective Activation of GABAB Receptors with Arbaclofen. *Science Translational Medicine*, **2012**, 4(152), 152ra128.

[341] Kaminskas, L.M., Porter, C.J.H. Targeting the lymphatics using dendritic polymers dendrimers. *Advanced Drug Delivery Reviews*, **2011**, 63(10-11), 890-900.

[342] Kobayashi, H., Kawamoto, S., Bernardo, M., Brechbiel, M.W., Knopp, M.V., Choyke, P.L. Delivery of gadolinium-labeled nanoparticles to the sentinel lymph node Comparison of the sentinel node visualization and estimations of intra-nodal gadolinium concentration by the magnetic resonance imaging. *Journal of Controlled Release*, **2006**, 111(3), 343-351.

[343] Kobayashi, H., Kawamoto, S., Choyke, P.L., Sato, N., Knopp, M.V., Star, R.A., Waldmann, T.A., Tagaya, Y., Brechbiel, M.W. Comparison of dendrimer-based macromolecular contrast agents for dynamic micro-magnetic resonance lymphangiography. *Magnetic Resonance in Medicine*, **2003**, 50(4), 758-766.

[344] Kobayashi, H., Kawamoto, S., Sakai, Y., Choyke, P.L., Star, R.A., Brechbiel, M.W., Sato, N., Tagaya, Y., Morris, J.C., Waldmann, T.A. Lymphatic drainage imaging of breast cancer in mice by micro-magnetic resonance lymphangiography using a nano-size paramagnetic contrast agent. *JNCI Journal of the National Cancer Institute*, **2004**, 96(9), 703-708.

[345] Wiig, H., Swartz, M.A. Interstitial Fluid and Lymph Formation and Transport Physiological Regulation and Roles in Inflammation and Cancer. *Physiological Reviews*, **2012**, 92(3), 1005-1060.

[346] Lee, C.C., MacKay, J.A., Frechet, J.M.J., Szoka, F.C. Designing dendrimers for biological applications. *Nature biotechnology*, **2005**, 23(12), 1517-1526.

[347] Kwon, M.J., An, S., Sunghyun, C., Nam, K., Jung, H.S., Yoon, C.S., Ko, J.H., Jun, H.J., Kim, T.K., J., J.S., Park, J.H., Lee, Y., Park, J. Effective healing of diabetic skin wounds by using nonviral gene therapy based on minicircle vascular endothelial growth factor DNA and a cationic dendrimer. *The journal of Gene medicine*, **2012**, 14, 272-278.

[348] Kaminskas, L.M., McLeod, V.M., Ascher, D.B., Ryan, G.M., Jones, S., Haynes, J.M., Trevaskis, N.L., Chan, L.J., Sloan, E.K., Finnin, B.A., Williamson, M., Velkov, T., Williams, E.D., Kelly, B.D., Owen, D.J., Porter, C.J.H. Methotrexate-Conjugated PEGylated Dendrimers Show Differential Patterns of Deposition and Activity in Tumor-Burdened Lymph Nodes after Intravenous and Subcutaneous Administration in Rats. *Molecular Pharmaceutics*, **2015**, 12(2), 432-443.

[349] Kaminskas, L.M., Kota, J., McLeod, V.M., Kelly, B.D., Karellas, P., Porter, C.J. PEGylation of polylysine dendrimers improves absorption and lymphatic targeting following SC administration in rats. *Journal of Controlled Release*, **2009**, 140(2), 108-116.

[350] Ke, W., Zhao, Y., Huang, R., Jiang, C., Pei, Y. Enhanced oral biovailability of doxorubicin in a dendrimer drug delivery system. *Journal of pharmaceutical sciences*, **2008**, 97(6), 2208-2216.

[351] Sadekar, S., Thiagarajan, G., Bartlett, K., Hubbard, D., Ray, A., McGill, L.D., Ghandehari, H. Polyamido amine dendrimers as absorption enhancers for oral delivery of camptothecin. *International Journal of Pharmaceutics*, **2013**, 456(1), 175-185.

[352] Sadekar, S., Ghandehari, H. Transepithelial transport and toxicity of PAMAM dendrimers Implications for oral drug delivery. *Advanced Drug Delivery Reviews*, **2012**, 64(6), 571-588.

[353] Kitchens, K.M., Foraker, A.B., Kolhatkar, R.B., Swaan, P.W., Ghandehari, H. Endocytosis and interaction of poly amidoamine dendrimers with Caco-2 cells. *Pharmaceutical research*, **2007**, 24(11), 2138-2145.

[354] Kitchens, K.M., Kolhatkar, R.B., Swaan, P.W., Eddington, N.D., Ghandehari, H. Transport of polyamidoamine dendrimers across Caco-2 cell monolayers Influence of size, charge and fluorescent labeling. *Pharmaceutical Research*, **2006**, 23(12), 2818-2826.

[355] DEmanuele, A., Jevprasesphant, R., Penny, J., Attwood, D. The use of a dendrimer-propranolol prodrug to bypass efflux transporters and enhance oral bioavailability. *Journal of Controlled Release*, **2004**, 95(3), 447-453.

[356] Florence, A.T., Sakthivel, T., Toth, I. Oral uptake and translocation of a polylysine dendrimer with a lipid surface. *Journal of Controlled Release*, **2000**, 65(1-2), 253-259.

[357] Pisal, D.S., Yellepeddi, V.K., Kumar, A., Kaushik, R.S., Hildreth, M.B., Guan, X., Palakurthi, S. Permeability of surface-modified polyamidoamine PAMAM dendrimers across Caco-2 cell monolayers. *International Journal of Pharmaceutics*, **2008**, 350(1-2), 113-121.

[358] Borowska, K., Wolowiec, S., Glowniak, K., Sieniawska, E., Radej, S. Transdermal delivery of 8-methoxypsoralene mediated by polyamidoamine dendrimer G2.5 and G3.5 - In vitro and in vivo study. *International Journal of Pharmaceutics*, **2012**, 436(1-2), 764-770.

[359] Venuganti, V.V.K., Perumal, O.P. Effect of polyamidoamine PAMAM dendrimer on skin permeation of 5-fluorouracil. *International Journal of Pharmaceutics*, **2008**, 361(1-2), 230-238.

[360] Venuganti, V.V.K., Perumal, O.P. PAMAM dendrimers as skin penetration enhancers influence of charge, generation and concentration. *Journal of pharmaceutical sciences*, **2009**, 98(7), 2345-2356.

[361] Chauhan, A.S., Sridevi, S., Chalasani, K.B., Jain, A.K., Jain, S.K., Jain, N.K., Diwan, P.V. Dendrimer-mediated transdermal delivery Enhanced bioavailability of indomethacin. *Journal of Controlled Release*, **2003**, 90(3), 335-343.

[362] Venuganti, V.V., Sahdev, P., Hildreth, M., Guan, X., Perumal, O. Structure-skin permeability relationship of dendrimers. *Pharmaceutical Research*, **2011**, 28(9), 2246-2260.

[363] Mutalik, S., Shetty, P.K., Kumar, A., Kalra, R., Parekh, H.S. Enhancement in deposition and permeation of 5-fluorouracil through human epidermis assisted by peptide dendrimers. *Drug delivery*, **2014**, 21(1), 44-54.

[364] Rubin, B.K. Air and soul the science and application of aerosol therapy. *Respiratory care*, **2010**, 55(7), 911-921.

[365] Ryan, G.M., Kaminskas, L.M., Kelly, B.D., Owen, D.J., McIntosh, M.P., Porter, C.J.H. Pulmonary administration of PEGylated polylysine dendrimers Absorption from the lung versus retention within the lung is highly size-dependent. *Molecular Pharmaceutics*, **2013**, 10(8), 2986-2995.

[366] Bharatwaj, B., Mohammad, A.K., Dimovski, R., Cassio, F.L., Bazito, R.C., Conti, D., Fu, Q., Reineke, J., Da Rocha, S.R.P. Dendrimer nanocarriers for transport modulation across models of the pulmonary epithelium. *Molecular Pharmaceutics*, **2015**, 12(3), 826-838.

[367] Dong, Z., Hamid, K.A., Gao, Y., Lin, Y., Katsumi, H., Sakane, T., Yamamoto, A. PAMAM dendrimers can improve the pulmonary absorption of insulin and calcitonin in rats. *Journal of pharmaceutical sciences*, **2011**, 100(5), 1866-1877.

[368] Bai, S., Thomas, C., Ahsan, F. Dendrimers as a carrier for pulmonary delivery of enoxaparin, a low-molecular weight heparin. *Journal of pharmaceutical sciences*, **2006**, 96(8), 2090-2106.

[369] Kaminskas, L.M., McLeod, V.M., Ryan, G.M., Kelly, B.D., Haynes, J.M., Williamson, M., Thienthong, N., Owen, D.J., Porter, C.J.H. Pulmonary administration of a doxorubicin-conjugated dendrimer enhances drug exposure to lung metastases and improves cancer therapy. *Journal of Controlled Release*, **2014**, 183(1), 18-26.

Part II

Dendron Engineering

The nature of the function located at the core is of utmost importance when synthesizing dendrons, particularly if a divergent process is used. Indeed, this function is present from the beginning of the synthesis and hence it must be compatible with the whole synthetic process while remaining available for the functionalization of various supports.[1] Due to the wide range of uses and applications of phosphonates in organic synthesis, biology and material chemistry, dendrons derivatized with phosphonic acids groups are being developed.[2] Among the most common routes to functional phosphonic acids for surface modification are the Michaelis–Arbuzov and Michaelis–Becker reactions,[3] hydrophosphonylation with palladium (Tanaka's[4] or Beletskaya's[5] methods) or with nickel or copper,[6] the Hirao cross–coupling,[7] the phospha–Michael addition,[8] and the Pudovik reaction starting from aldehydes. The Michaelis–Arbuzov reaction,[9] also known as the Arbuzov reaction, is one of the most versatile reactions for the formation of P–C bonds and consists of the reaction of a triester phosphite with an alkyl halide, resulting in the conversion of trivalent to pentavalent phosphorus species. While elevated temperatures are required for the transformation activation, recent data have shown that for some specific substrates this reaction can be advantageously performed at room temperature in the presence of a suitable Lewis acid.[10]

Barney *et al.* recently proposed a straightforward synthesis of benzyl or allyl phosphonates from their corresponding alcohols using Triethylphosphite and zinc iodide.[11] Benzyl phosphonate esters are usually prepared from Benzyl halides and Trialkylphosphite via an Arbuzov reaction and this procedure is a convenient alternative, although benzylic compounds bearing an electron–withdrawing group are much less reactive. Moreover, such synthetic methodology allows introducing the phosphonate group in the last steps of the synthesis, which is advantageous since the chromatographic purification of phosphonate–containing intermediates throughout the whole multistep synthesis is time–consuming.

1 Syntheses to face biodistribution issues

Although progress in the application of nanotechnology has been dramatic and successful, efforts are focused on creating more complex platforms that integrate real–time diagnostic, imaging, targeting and therapy delivery features. Various types of magnetic nanoparticles have a widespread range of applications such as in MRI as T_1 and T_2 contrast agents,[12] magnetically guided drug/gene delivery,[13] magnetic hyperthermia and magnetic biosensors.[14]

A proper surface coating can stabilize particles and avoid agglomeration and therefore may increase the sensitivity of NPs based sensor. In addition, a proper surface coating enables the nanoparticles to respond specifically towards biological species and avoids non–specific interactions with components in the complex matrix. Coating is also an effective manner of preventing the dissolution and release of core materials that may cause toxicity to biological system.[15] Furthermore, the steric hindrance of coating can affect the fate of NPs in biological system, such as cellular uptake and accumulation, circulation and clearance from body.[16] In addition, the surface can affect the maintenance of the intrinsic nanocrystal properties such as fluorescence and magnetic behavior. Hence, designing appropriate surface functionality is a perquisite for conjugating biomolecules to NPs for biomedical applications.

Felder–Flesch and co–workers reported a library of functional dendritic phosphonic acids, either fully PEGylated or derived from the PAMAM family.[17] Such a library of functional hydrophilic phosphonic acids opens new possibilities for the investigation of dendronized nanohybrids' fate in biological environment **(Fig.34)**.

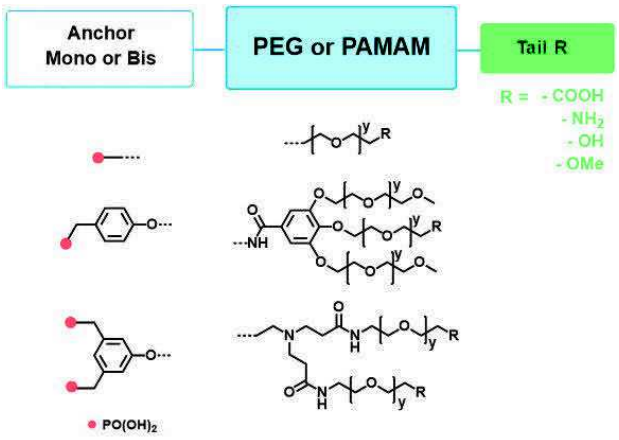

Figure 34: General structure for IONPs dendritic phosphonates as coatings.

1.1 Synthesis of 1P_G$_1$PEG_COOH

The synthesis of the dendritic Mono–ethyl–phosphonate is obtained from the key intermediate **4** which was obtained in 4 steps with a 44% overall yield **(Fig.35)**. First *para*–benzylated Methyl gallate **2** and tosylated Tetraethyleneglycol monomethyl ether **1** were obtained in good yields from the commercially available Methyl gallate and Tetraethyleneoxide monomethyl ether, respectively, following a reported one–step procedure.[18] A Williamson etherification between **1** and **2** in Acetone at 60°C, in the presence of Potassium carbonate (K_2CO_3) and Potassium iodide (KI), allowed the preparation of ester **4** in 75% yield.

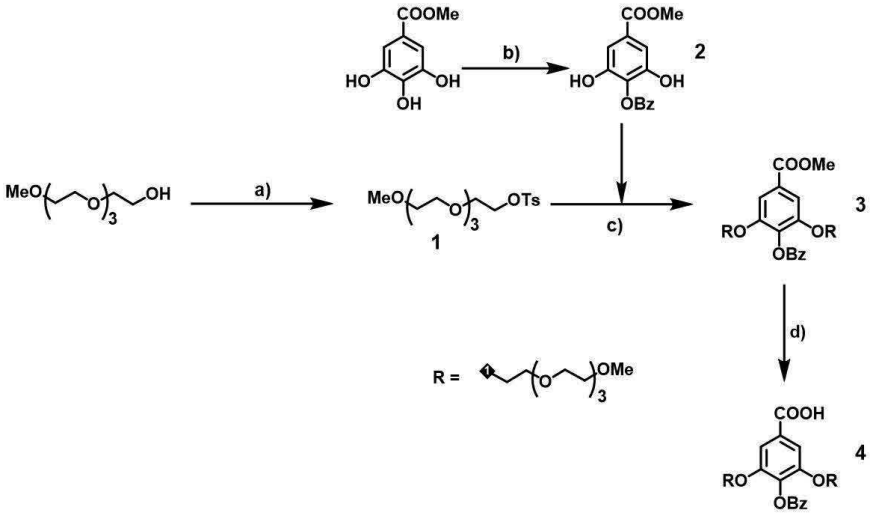

Figure 35: Synthesis of *para*–Benzyl (meta–tetraethyleneglycol monomethyl ether) methyl gallate **5**: a) TsCl, NaOH, THF/H_2O, rt, 24h, 94%; b) Benzyl bromide, $KHCO_3$, KI, DMF, 30°C, 72h, 70%; c) K_2CO_3, KI, Acetone, reflux, 24h, 75%; d) NaOH, $MeOH/H_2O$, reflux, 2h, 90%.

The synthesis of Ethyl phosphonate **7** displaying an Ethyl–amine linker in *para* position is given in **Fig.36**. The compound was obtained in 4 steps with 54% overall yield. First, 4–(benzyloxy) benzyl chloride reacted under reflux with $P(OEt)_3$ to yield **5** (92%). Phenol **6** was obtained after hydrogenolysis in the presence of Pd/C (10%) in 92% yield, and was next engaged in an etherification reaction in the presence of Boc–2–bromo–ethylamine. Subsequent treatment with Trifluoroacetic acid (TFA) yielded **7** (94%).

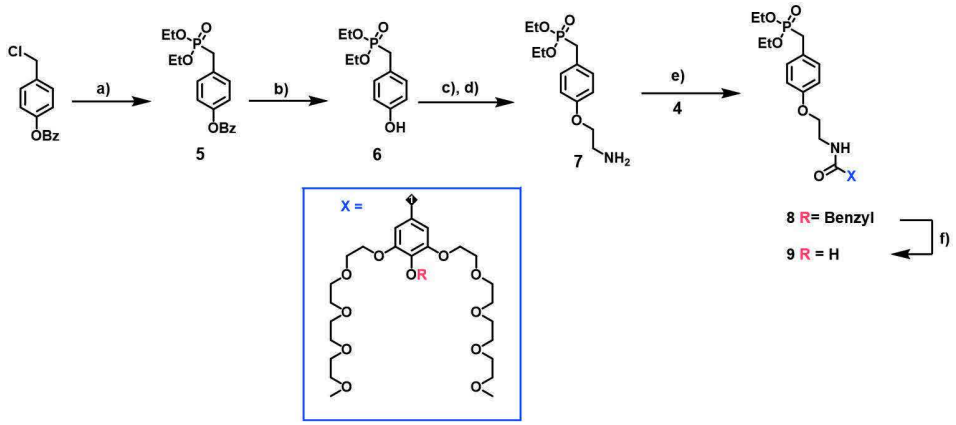

Figure 36: Synthesis of mono–ethylphosphonate **9** : a) $P(OEt)_3$, 160°C, 3h, 92%; b) Pd/C 10%, H_2, EtOH, rt, 16h, 92%; c) Boc–2–bromo–ethylamine, K_2CO_3, KI, acetone, reflux, 16h, 75%; d) TFA, CH_2Cl_2, 0°C to rt, 16h, 94%; e) **4**, BOP, DIPEA, CH_2Cl_2, rt, 24h, 70%; f) Pd/C 10%, H_2, EtOH, rt, 16h, 85%.

Amine **7** underwent a peptide coupling type reaction with Carboxylic acid **4** (obtained by saponification of **3** with NaOH, **Fig.35**) in the presence of (Benzotriazol–1–yloxy) tris (dimethylamino) phosphonium hexafluorophosphate (BOP) and *N,N* – Diisopropylethylamine (DIPEA) to obtain benzylated compound **8**

(70%). Finally, hydrogenolysis in the presence of Pd/C led to the corresponding Ethyl phosphonate **9** with 85% yield.

Refluxing in concentrated Hydrochloric acid (HCl) is an easy route for conversion of phosphonate esters into their acid analogues. However, for sensitive products requiring milder reaction conditions, McKenna's method[19] using Bromotrimethylsilane (TMSBr) remains an efficient method which allows obtaining Trimethylsilyl phosphonate ester intermediates that hydrolyze *in situ* into phosphonic acids, in protic medium (water or alcohol). In order to achieve the synthesis of phosphonic acid **12** bearing a long functionalized Oligoethylene glycol chain in *para* position, the first step was the synthesis of the common intermediate **10 (Fig.37)**, which was obtained in good yield starting from the commercially available Hydroxy–dPEGs®$_8$–*t*–butylester.[20] **10** then underwent a Williamson reaction with Ethylphosphonate **9** in Acetone at 60°C in the presence of K_2CO_3 and KI to yield the corresponding dendritic Ethyl phosphonate **11** in 85% yield. Treatment of **11** with a large excess of TMSBr generated a phosphonic acid function at the focal point and converted the terminal *tert*–butyl ester group into its corresponding carboxylic acid. This step allowed obtaining compound **12** in 90% yield after size purification chromatography on Sephadex™ LH–20[12] in Methanol.

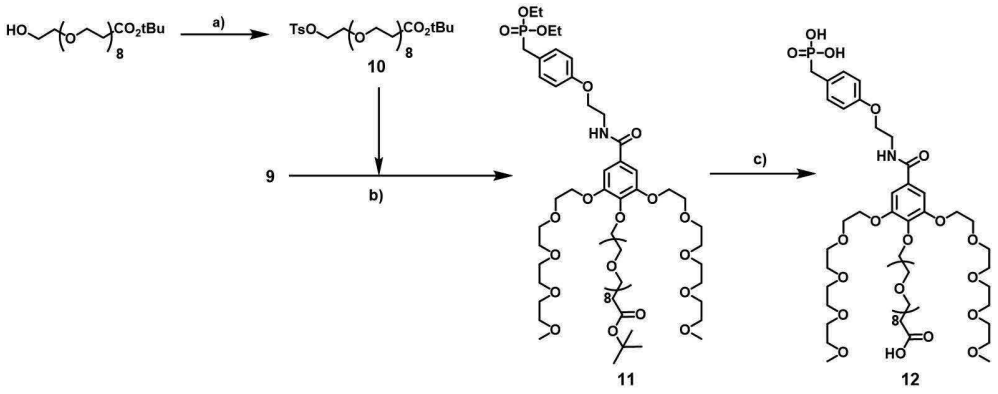

Figure 37: Synthesis of COOH–functionalized dendritic mono–phosphonic acid **12** : a) TsCl, NEt_3, CH_2Cl_2, rt, 24h, 85%; b) K_2CO_3, KI, Acetone, reflux, 16h, 70%; c) TMSBr, CH_2Cl_2, rt, 16h, 90%.

Following the purification step, Mono–phosphonic acid **12** (1P_G_1PEG_COOH) was characterized by ^{1}H, ^{31}P and ^{13}C NMR, and mass spectrometry. The dendron was obtained in 13 steps with 9% overall yield. On average every step of the synthesis gets 83% yield, which is a very honest yield. Even though, there is still room for improvement, in particularly optimizing several reagents or conditions. Compound 1P_G_1PEG_COOH has a yellowish oil appearance, and is kept at 5°C for further surface modifications of IONPs.

[12] Sephadex LH–20 is beaded, cross–linked dextran that has been hydroxypropylated to yield a chromatography medium with both hydrophilic and lipophilic character, GE Healthcare and Life Science®.

1.2 Synthesis of 2P_G$_1$PEG_COOH

The complex structure of 2P_G$_1$PEG_COOH is divided in two parts, as the earlier dendron 1P_G$_1$PEG_COOH. The dendron was synthesized by a convergent method, coupling the so called north segment, compound **18**, and the south segment, compound **4**. The synthesis of Bis–ethylphosphonate anchor **18** is detailed in **Fig.38**.

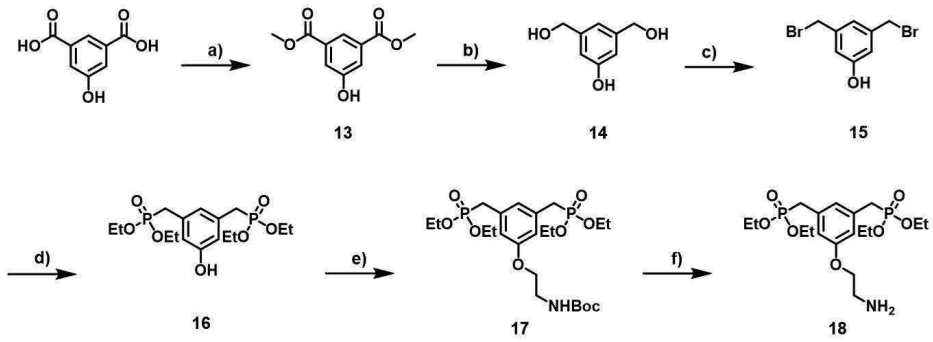

Figure 38: Synthesis of bis–ethylphosphonate anchor **18** : a) MeOH, H_2SO_4, reflux, 4h, quant.; b) $LiAlH_4$, THF, rt, 3h, 50 – 95%; c) HBr 30%, Acetic acid, rt, 24h, 96%; d) $P(OEt)_3$, reflux, 2h, 95%; e) Boc–2–bromo–ethylamine, K_2CO_3, KI, Acetone, reflux, 16h, 53 – 70%; f) TFA, DCM, rt, 24h, 88%.

Its precursor, 5–Hydroxyisophthalic acid, was converted into corresponding Dimethyl 5–hydroxyisophthalate **13** using a catalytic amount of H_2SO_4 in refluxing Methanol in a quantitative yield (over 98%). Reduction of diester **13** by an excess of $LiAlH_4$ in THF at room temperature provided triol **14**. However, the yield of this reaction was found to be poorly reproducible (50 – 95%). This is mainly associated with the poor solubility of compound **14** in usual organic solvents and its tendency to stick to the aluminum salts resulting from the oxidation of $LiAlH_4$.

Primary alcohols of compound **14** undergo a nucleophilic substitution in the presence of HBr to give **15** in 96% yield. Subsequent bromine to phosphonate conversion using Triethylphosphite at reflux gave compound **16** in 95% yield.

A Williamson coupling was carried out between **16** and a large excess of Boc–2–bromo–ethylamine in the presence of K_2CO_3 and KI, yielding **17** at maximum 70%. The etherification was followed by Amine deprotection by TFA, yielding **18** with 88%.

Compound **17** was obtained with a fair enough yield (53 – 70%), which is considered low for a relative simple Williamson coupling. The low stability of Boc– 2– bromo– ethylamine at high temperatures resulted in low–yield reactions and particularly difficult purification of compound **17**. It has been shown that Boc–2–[nucleophile]–ethylamine when subjected to basic conditions undergoes cyclization, thus decreasing reactant reactivity.[21] Another reason for poorly reproducible Williamson coupling, would be the deprotection of primary boc–group under basic conditions and relatively high temperatures.[22]

In order to increase the yield of the etherification reaction, it was decided to use as linker 2– (Z– Amino) ethanol, which is far more stable under basic conditions than Boc–equivalent. The new synthetic route is described in **Fig.39**.

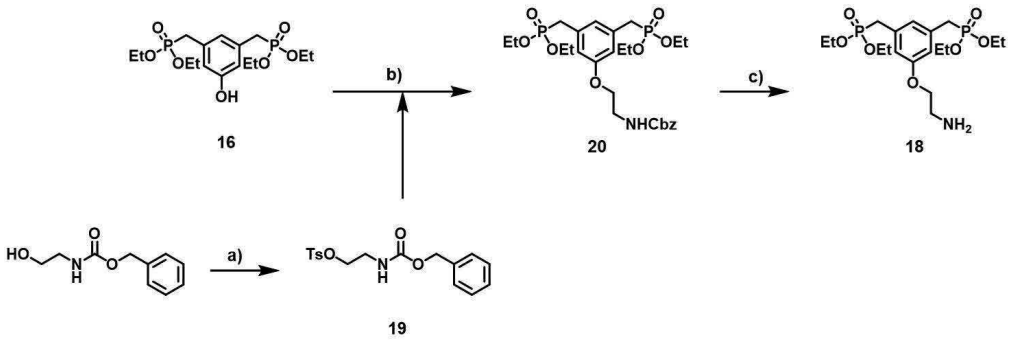

Figure 39: Alternative synthesis for Bis–ethylphosphonate anchor **18** : a) TsCl, NEt_3, DCM, rt, 16h, 75%; b) K_2CO_3, Acetone, 60°C, 48h, 85% c) $Pd(OH)_2/C$, H_2, Methanol, rt, overnight.

Primary alcohol of 2– (Z– Amino) ethanol was converted to **19** in the presence of Tosylchloride and Triethylamine with 75% yield. Etherification of **16** in the presence of **19** under classical Williamson conditions led to compound **20** in 85% yield. The amine deprotection was attempted with both 10% Pd/C and Pearlman catalyst in the presence of H_2. The best results were obtained with 20% $Pd(OH)_2/C$ catalyst in Methanol, overnight. Compound **18** was obtained in 92% yield as a yellowish oil.

Peptide coupling in the presence of BOP and DIPEA under an Argon atmosphere, between amine **18** and carboxylic acid **4**, gave the resulting benzylated compound **21** in 66% yield **(Fig.40)**. After Hydrogenolysis of the Benzyl group, compound **22** is obtained in 83% yield.

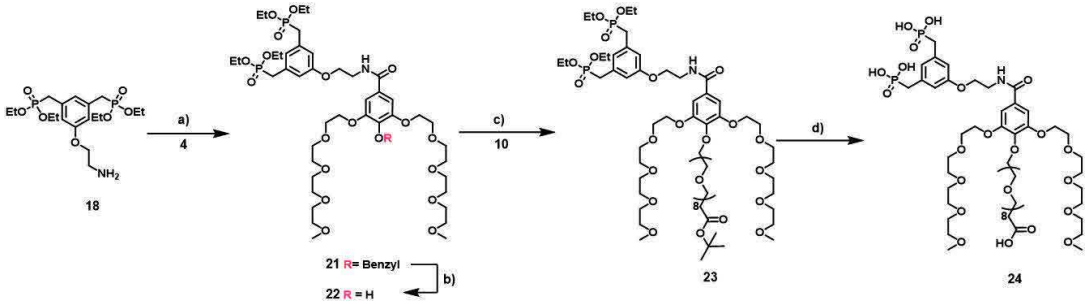

Figure 40: Synthesis of 2P_G_1PEG_COOH **24** : a) BOP, DIPEA, CH_2Cl_2, rt, 24 h, 66%; b) Pd/C 10%, H_2, EtOH, rt, 6h, 83%; c) K_2CO_3, Acetone, 60°C, 24h, 70%; d) TMSB, DCM, rt, 10h, 93%.

Phenol **22** then underwent a Williamson reaction with TsO–dPEGs®$_8$–t–butylester in Acetone at 60°C in the presence of K_2CO_3 to yield the corresponding dendritic Bis–ethyl phosphonate **23** at 70%. Treatment of **23** with a large excess of TMSBr generated phosphonic acid function at the focal point and converted the terminal *tert*–butyl ester group into its corresponding Carboxylic acid. This step allowed obtaining

compound **24** in 93% yield as a yellowish oil. Following a purification step by LH–20, COOH–functionalized Bis–phosphonic acid **24**, was characterized by ^{1}H, ^{31}P and ^{13}C NMR, and mass spectrometry.

The total synthesis of Bis–phosphonic acid dendron was performed in 15 steps with 7% overall yield, which means, on average, each step of the synthesis gets 84% yield. It still can be improved by optimizing conditions or reagents.

1.3 Synthesis of 2P_$G_{0.5}$PAMAM_COOH

Another design of a small–size dendron was based on a small Poly(amido)amine structure. Precisely, alkyne monomer **25** synthesized following a reported procedure[23], underwent deprotection of the two Methyl esters by Sodium trimethylsilanolate (TMSONa), giving **26** as a yellow solid in a quantitative yield **(Fig.41)**. Commercially available amine functionalized PEG chains were introduced within the monomer by a peptide coupling reaction in the presence of 1– Ethyl– 3– (3– dimethylaminopropyl) carbodiimide (EDCI), Hydroxybenzotriazole (HOBt) and *N,N* – Diisopropylethylamine (DIPEA) to yield bifunctional acetylenic conjugate **27**. The PEG chains were chosen for their tunable length and possible derivatization but also to counterbalance the toxicity of PAMAM motif.

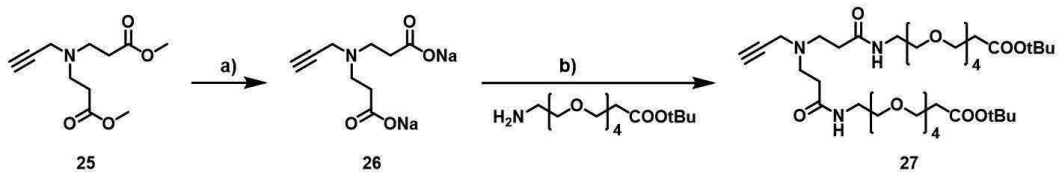

Figure 41: Introduction of functional PEG chains into a poly(amido)–amine monomer **27** : a) TMSONa 1M, CH_2Cl_2, rt, 16 h, quant.; b) EDCI, HOBt, DIPEA, CH_3CN, rt, 16 h, 67%.

In parallel, Azide–derivatized Bis–ethylphosphonate precursor **32** was synthesized in a five–step procedure with 18% overall yield as described in **Fig.**42. The commercially available Methyl 3,5– dimethylbenzoate was subjected to benzylic bromination using N–Bromo succinimide (NBS) and Benzoyl peroxide, affording compound **28** in 72% yield. Such bromination conditions afford both mono– and di– substituted benzylic bromides. The mono–benzylic bromide is easily separated from the desired di–bromide and can undergo an iterative bromination reaction leading to an increased yield of desired compound **28**.

Compound **28** was then reduced using the electrophilic reducing agent Diisobutylaluminium hydride (DIBAL) to form Dibromoethyl benzyl alcohol **29** in 92% yield. **29** underwent an Arbuzov[24] reaction in the presence of Triethylphosphite to yield compound **30** as a transparent oil. Subsequently alcohol **30** was converted into corresponding chloride **31** in the presence of Thionyl chloride. The bis–phosphonate azide precursor resulted from the nucleophilic substitution of Chlorine by Sodium azide. Compound **32**

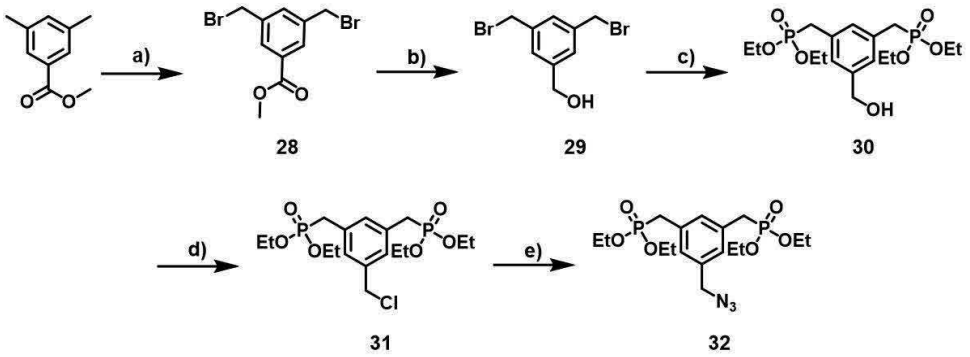

Figure 42: Synthesis of Bis–phosphonate azide precursor **32** : a) NBS, Benzoyl peroxide, CCl_4, rt, 3h, 72%; b) DIBAl, Toluene, 0°C, 3h, 92%; c) $P(OEt)_3$, 160°C, 2h, 88%; d) $SOCl_2$, $CHCl_3$, reflux, 1h, 40–60%; e) NaN_3, CH_3CN, reflux, 16h, 50 – 70%.

was obtained in 45% yield as a colorless oil. This classical route for azide synthesis suffers from complex procedures, long reaction times, non–reproducible yields, and most importantly the danger of explosion at elevated temperature and in halogenated solvents. Hence, microwave (MW)–assisted reaction of Chloride or Tosylate with Sodium azide was examined. After several attempts, *in situ* synthesis of azide **32** from alcohol **30** through Tosylation, was considered to be the most rapid with the highest yield method **(Table7)**. The precursor **30** was dissolved in DMF and, 4-Toluenesulfonyl chloride and Potassium carbonate were added to the solution. The reaction was submitted to microwaves for 20min at 80°C. Sodium azide was then added and the reaction was once more subjected to microwaves under the same conditions.

Substrate	Reagent – 1st step	Solvent	Conditions	Reagent – 2nd step	Conditions	Yield
30	$SOCl_2$	$CHCl_3$	1200t/m, 60°C, 10min	NaN_3	1200t/m, 60°C, 10min	40%
30	TsCl, K_2CO_3	DMF	1200t/m, 80°C, 10min	NaN_3	1200t/m, 80°C, 10min	58%
30	TsCl, K_2CO_3	DMF	1200t/m, 80°C, 20min	NaN_3	1200t/m, 80°C, 20min	62%

Table 7: Microwave assisted two–step synthesis of azide **32**.

MW–promoted synthesis for azides was a rapid and efficient procedure. Furthermore it reduced the overall synthesis of precursor **32** to 4 steps in a higher yield.

The Copper–catalyzed Huisgen 1,3–dipolar cycloaddition was performed between azide **32** and alkyne **27**, yielding 1,4–disubstituted triazole **33** in 75% **(Fig.43)**. The so–called "Click" reaction was carried out using Cu(II) salt in the presence of Sodium ascorbate in a mixture of Tetrahydrofuran (THF), water and

Acetonitrile (ACN).

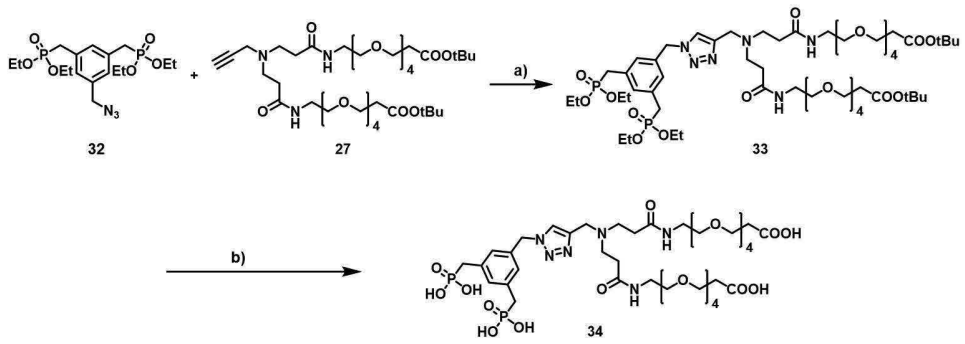

Figure 43: Synthesis of 2P_$G_{0.5}$PAMAM_COOH **34** : a) $CuSO_4$.5H_2O, L–ascorbate, THF, H_2O, ACN, rt, 16h, 75%; b) TMSBr, rt, 4h, 66%.

The final deprotection of the Bis–ethylphosphonates was achieved in the presence of TMSBr, which allowed the simultaneous deprotection of *tert*–butyl esters of compound **33**, yielding **34** as a colorless oil. Following a purification step by LH–20, COOH–functionalized Bis–phosphonic acid **34** was characterized by ^{1}H, ^{31}P and ^{13}C NMR, and mass spectrometry.

The total classical synthesis of 2P_$G_{0.5}$PAMAM_COOH was performed in 9 steps with 8% overall yield, on average, each step of the synthesis showing 76% yield. Using the alternative synthesis, which includes a MW–assisted reaction, in 8 steps, the overall yield increased up to 12% with an average 77% yield per reaction. The increase of average yield for each reaction is not very high but is significant enough to gain 4% overall yield and, most importantly, to decrease the synthesis time. Even though the overall yield was boosted up to 12%, there are still opportunities to optimize the time and the overall yield.

1.4 Synthesis of LA_G_1PEG_COOH

1.4.1 Introduction to Optoacoustic Imaging

Optoacoustic (OA) imaging is a noninvasive biomedical imaging modality with high spatial resolution and deep imaging depth.[25,26] OA imaging is an *in vivo* imaging technology[27,28] where short light energy pulses are absorbed by tissues and converted to thermal energy. The absorbing material undergoes thermal expansion, giving rise to pressure waves that propagate outwards and can be detected by ultrasound transducers (detector). Hence, lasers emitting in the spectral range from approximately 650 to 700nm (near infrared NIR) are normally used for generating OA signals (and images) due to the relatively weak absorption of biological tissues in this spectral range, also known as the window of relative tissue transparency.[29,30] Thus allowing high–resolution and whole–body imaging.

In vivo administration of exogenous contrast agents opens another opportunity for enhancement of the

OA imaging contrast in organs and tissues of interest. Standard molecular CAs such as NIR organic dyes have been extensively used in OA imaging.[31,32,33,34] Nanoparticles are especially attractive as OA CAs since the volume of a nanoparticle is significantly larger than that of a single chromophore molecule. The most effective types of exogenous CAs designed for OA imaging modalities are nanoparticles that possess strong surface plasmon resonance (SPR) absorption (such as gold nanorods, hollow nanospheres and nanocages).

Since its original inception in the 1970s[35], optoacoustic imaging has remained largely an experimental technique. Single detector and single wavelength experimental systems demonstrated aspects of biological imaging in the 90s[36], but did not offer features that enabled wide dissemination. However, considerable technical progress and advances in nanotechnology, in recent years, have brought significant contributions to the nanoparticle–based OA imaging[37,38,39,40,41,42,43,44], leading to high–quality images and the ability to resolve rich contrast with performance often not available through other imaging methods.

Plasmonic nanoparticles have been synthesized in myriad shapes and sizes, each with unique optical characteristics. The choice of nanoparticle in imaging applications dependent on imaging depth, optical wavelength range, and biological interactions. Gold nanorods are extensively used in OA imaging because of their relatively simple synthesis and tunable absorption in the NIR region.[45,39]

Likewise for IONPs, gold nanoparticle' (AuNPs) coating has to fulfill several requirements for biomedical applications. AuNPs' coating has to stabilize nanoparticles and prevent aggregation[46], increase their circulation time, decrease their cytotoxicity and easily conjugate a variety of relevant molecules for targeting or treatment of different diseases.

The most common ligands used for AuNPs stabilization involve Thiol–derivatives. Nowadays, a wide variety of thiolated molecules **(Fig.44)** is used for AuNPs stabilization, achieved either directly during AuNPs synthesis[47] or by ligands–exchange reactions.[48]

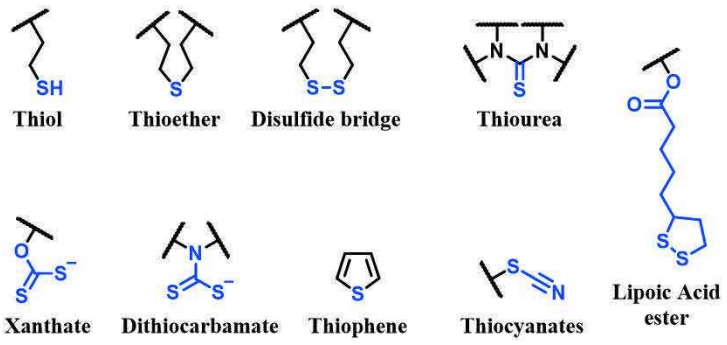

Figure 44: Examples of Thiol–anchoring group derivatives for AuNPs stabilization.

The nature of Thiol–derivatives bond toward gold surface relies upon the anchoring group structure. Therefore, Thioethers do not adsorb onto the gold surface in the same way as Thiols or Disulfide bridges.

For Thioethers bonding to AuNPs surface, analytical studies indicated the formation of a dative bond, much weaker and less stable than Thiol S–Au bond.[49,50] Lipoic Acid (LA) is presented as a perfect candidate for AuNPs stabilization, as a result of its bifunctional character: the Disulfide bridge ensures a strong binding to the nanoparticle surface while the peripheral acid function allows post–functionalization with a wide variety of beneficial moieties.

To this end, it was decided to develop the synthesis of a PEGylated dendron with LA as anchoring group for AuNPs. At first, the synthesis of a control sample was developed, in order to establish the grafting procedure and evaluate the stability of different shape and size dendronized gold nanoparticles.

1.4.2 Synthesis of LA_G_1PEG_OMe as control sample

The convergent synthesis of LA_G_1PEG_OMe – control sample – is based on the synthesis of the South part **(Fig.45)** which is linked to the Lipoic Acid by a peptide coupling in the last step. The synthesis of the South part starts with a Williamson coupling of Methyl gallate with 3 equivalents of compound **1**. PEGylated Methyl gallate **35** was subjected to a base hydrolysis of the ester in the presence of NaOH, in order to yield **36** in 92%.

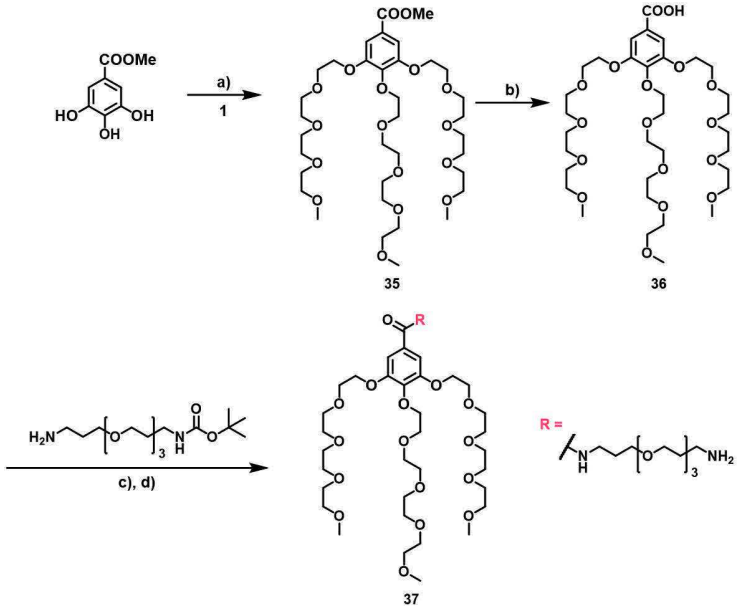

Figure 45: Synthesis of compound **37** : a) K_2CO_3, DMF, 60°C, 48h, 88%; b) NaOH, MeOH/H_2O, rt, overnight, 92%; c) EDC, NHS, DCM, 24h, rt, 88% d) TFA, DCM, overnight, rt, 95%.

Benzoic acid **36** reacted with the commercially available *t*– boc– *N*– amido– dPEG®$_3$– amine[13] in the presence of EDC and NHS. This preparative procedure of amides is highly tolerant to various functional

[13]Quanta Biodesign, CAS: 194920–62–2.

groups. Subsequent to peptide coupling, TFA was used for Boc–Amine deprotection, as shown in **Fig.45**, leading to the corresponding amine **37** in 95%.

For the synthesis of LA_G_1PEG_OMe, LA was used in a racemic mixture, since our objective is not influenced by its stereochemistry.

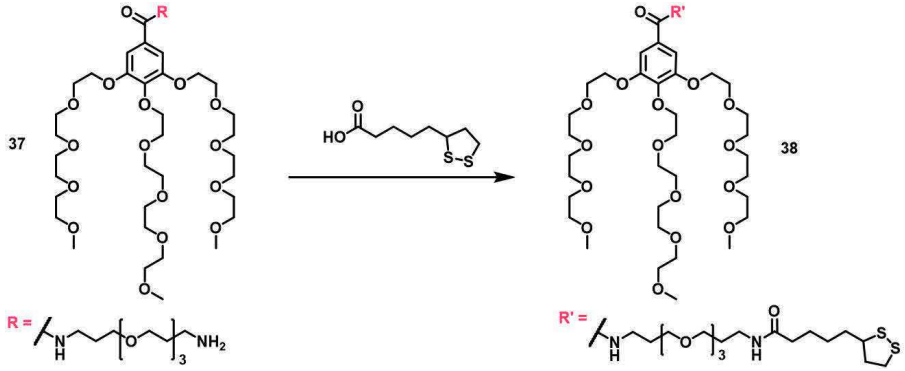

Figure 46: Synthesis of LA_G_1PEG_OMe **38** : EDC, NHS, MeOH/H_2O (1:1), rt, 24h, 72%.

Compound **37** underwent peptide coupling with (±) LA, in the presence of EDC and N– Hydroxysuccinimide (NHS) in a mixture of MeOH / H_2O in a 1:1 ratio **(Fig.46)**. The reaction was stirred for 24h at room temperature. The desired compound **38** was purified using size exclusion chromatography and obtained in 72% as an orange oil. Following the purification step, LA_G_1PEG_OMe **38** was characterized by ^{1}H and ^{13}C NMR, and mass spectrometry. The total synthesis of LA_G_1PEG_OMe was performed in 5 steps with 49% overall yield, each step of the synthesis with 87% yield.

1.4.3 Synthesis of LA_G_1PEG_COOH

The synthesis of COOH–functionalized PEGylated LA dendron was performed in 5 steps following a convergent method. It was decided at first, to link the LA to the commercially available *t*–boc–*N*–amido–dPEG®$_3$–amine, and afterwards, couple it to the *t*Bu–COOH – functionalized PEGylated Gallate precursor **42**. The synthesis of compound **40** is detailed in the **Fig.47**.

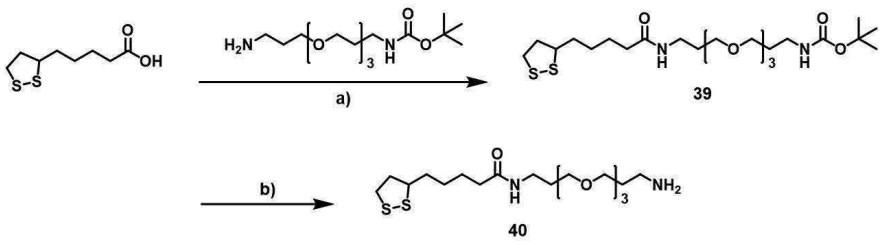

Figure 47: Synthesis of **40** : a) EDC, NHS, NEt_3, DCM/MeOH, rt, overnight, 53%; b) TFA, DCM, rt, 10h, 94%.

LA was dissolved in a mixture of DCM/MeOH (1:1) and cooled down to 0°C. EDC, NHS and few drops of NEt_3 were then added to the mixture, in order to increase the kinetics of acid activation. After addition of *t*– boc– *N*– amido– dPEG®$_3$– amine, the reaction was stirred overnight at room temperature. The desired compound **39** was obtained in 53% yield. The peptide coupling was followed by Amine deprotection in the presence of TFA leading to the corresponding amine **40** in 94% yield.

The synthesis of the South part is detailed in **Fig.48** and starts with the deprotection of *para*–alcohol of Methyl gallate in the presence of 10% Pd/C.

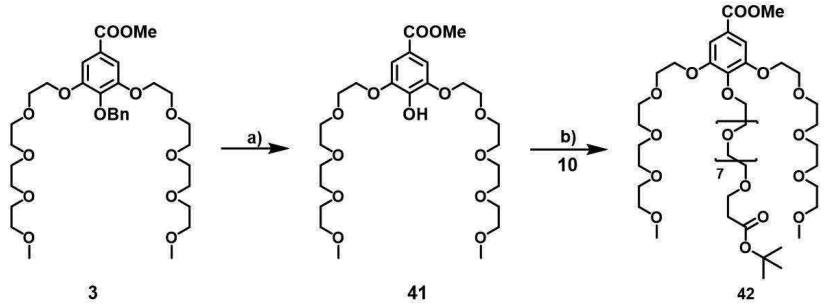

Figure 48: Synthesis of compound **42** : a) 10% Pd/C, H_2, Ethanol, rt, 12h, 84%; b) K_2CO_3, DMF, 60°C, 48h, 89%.

The obtained product **41** was submitted to a classical Williamson coupling with **10**, in the presence of K_2CO_3 for two days. The desired product **41** was obtained in 89% yield and showed a yellowish oil aspect. In order to obtain LA_G_1PEG_COOH dendron, compound **42** underwent an *in situ* two–step reaction. Base hydrolysis of **42** in the presence of KOH followed by peptide coupling with **40** was performed *in situ*, as shown in **Fig.49**. The compound **43** was obtained in maximum 56% yield as an orange oil.

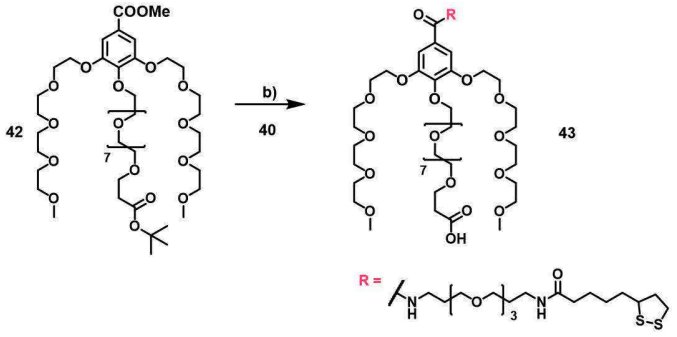

Figure 49: Synthesis of LA_G_1PEG_COOH dendron, **43** : 1st step) KOH, MeOH/H_2O/THF, 60°C, overnight; 2nd step) EDCI, NHS, THF/MeOH, **40**, rt, 24h, 30–56%.

Following the purification step using size exclusion chromatography, LA_G_1PEG_OMe **38** was characterized by ^{1}H and ^{13}C NMR (**Fig.50**). NMR profiles correspond to the expected structure of LA–dendron. As one can see on the **Fig.50**, important pics are highlighted, which correspond to both LA and COOH–functionalized

PEGylated gallate structures.

The *in situ* deprotection of **42** and coupling with **40** was a good idea in order to decrease time and synthesis step–number. Either way, the saponification of **42** lead to carbonate, which makes, in theory, peptide coupling undergo easier. On the contrary, the last step yield is low and not reproducible. Deprotection of the Boc–group under basic conditions, as mentioned earlier, might be an explanation to the low yield. As a result, having two different acid groups in the reaction mixture, one can ask the question: which one will have a higher kinetics for peptide coupling?

During the saponification reaction two intermediates are possible, thus two possibilities for Amine binding to the PEGylated gallate (**43** and **44**) **(Fig.51)**. Several analytical techniques have been applied in order to determine the exact structure of the final compound.

The structure difference between **43** and **44** couldn't be determined by ^{1}H NMR profiles since the chemical shift of $PEG_7C\mathbf{H_2}$–CO–NH– is very close to the one of $PEG_7C\mathbf{H_2}$–COOH. Furthermore J–couplings cannot be compared as several peaks overlap. On the other hand, results obtained from ^{13}C, homonuclear Correlation Spectroscopy (COSY) and Heteronuclear Single–Quantum Correlation (HSQC) NMR sequences sustain the structure of compound **43**. As shown on ^{13}C **(Fig.50.down)** NMR profile, PEG_7–**C**OOH is the most shielded peak at 174ppm, than comes –CH_2–**C**O–NH– peak at 172.14ppm and less shielded carbonyle is Ph–**C**O–NH– at 159.3ppm. These results confirm the structure of compound **43**, nevertheless, last step is not reproducible, with a high probability to obtain side–products, which will impede further grafting on AuNPs.

A decision was taken to overcome the problems of side–products and low reproducible yields, by changing the synthetic route. To this end, it was decided to bond t–boc–N–amido–dPEG®$_3$–amine to the PEGylated gallate precursor, and to perform the peptide coupling on phenol **46**. The synthesis of the south part is detailed in **Fig.52**. Compound **4** undergoes a peptide coupling in the presence of EDC and NHS in a mixture of Methanol/Water. The reaction is stirred for 24 hours at room temperature, followed by size exclusion purification (LH–20). Product **45** was obtained in 68% yield.

Compound **46** was obtained in two step deprotections. First the Benzyl function was deprotected in the presence of 10% Pd/C catalyst, in order to give the corresponding *para*–alcohol. Then, the Amine deprotection was achieved in the presence of a large excess of TFA, to obtain compound **46** in 85% as a colorless oil.

Further synthesis of LA_G_1PEG_COOH dendron was accomplished in 3 steps **(Fig.53)**. Compound **46** reacted with LA under classical peptide coupling conditions to give **47** in 65% yield. Following the amide formation, Williamson coupling was performed on compound **47** with TosylO– dPEGs®$_8$– t– butylester in DMF at 60°C in the presence of K_2CO_3. Treatment of resulted compound with a large excess of TFA converted the terminal *tert*–Butyl ester group into its corresponding carboxylic acid.

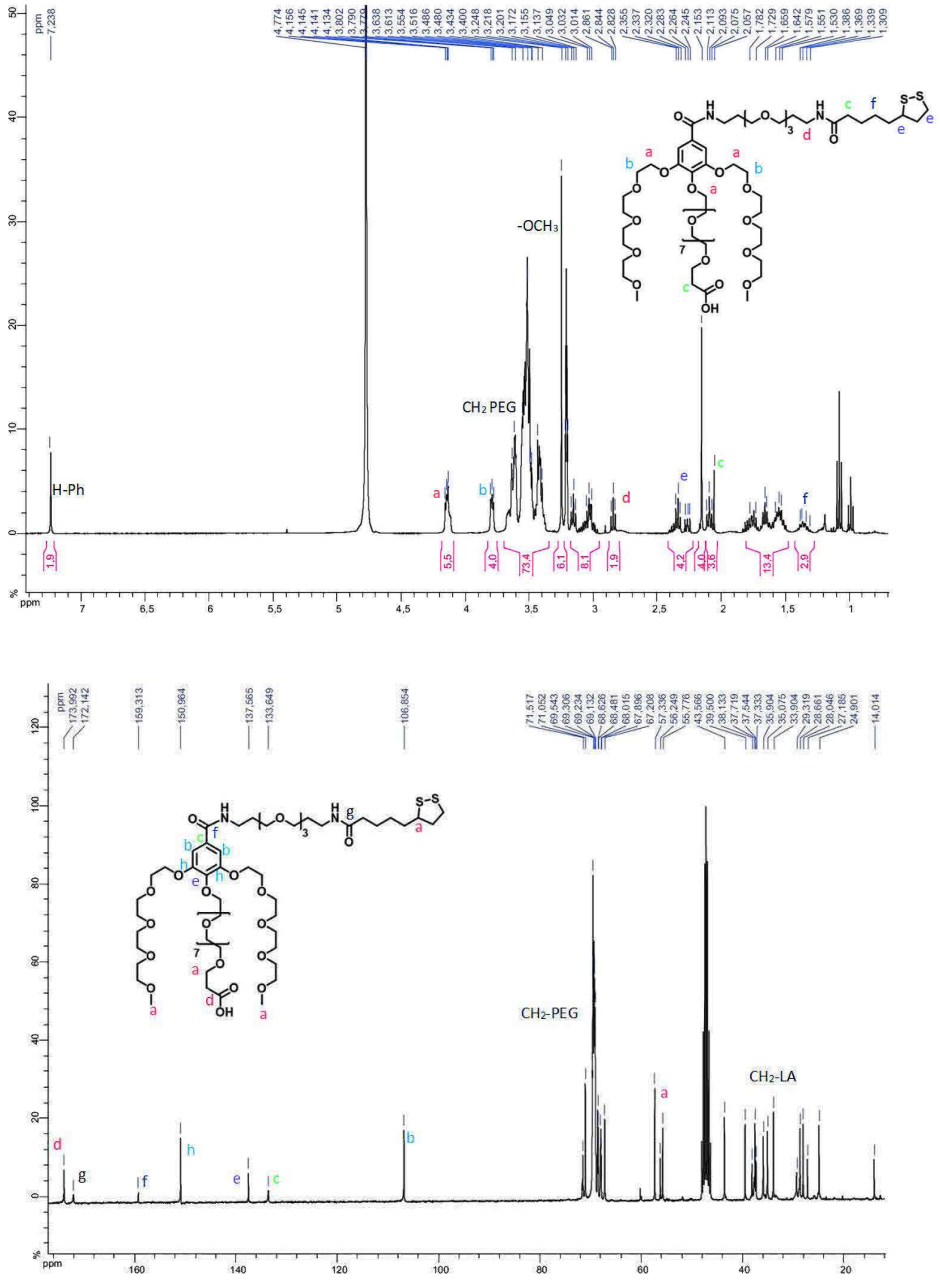

Figure 50: ^{1}H (top) and ^{13}C (down) NMR (MeOD, 300MHz) profiles of compound **43**.

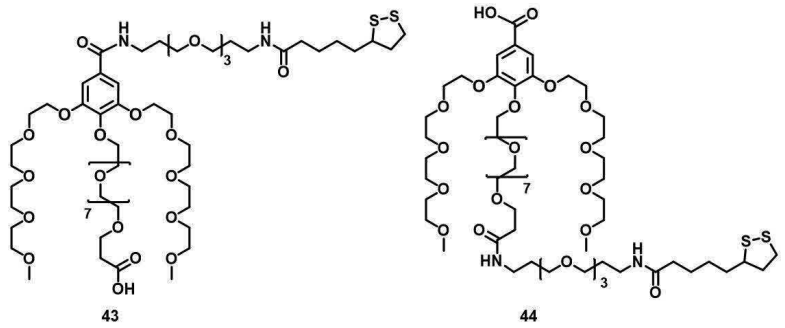

Figure 51: Two possible combination for peptide coupling with deprotected compound **42**.

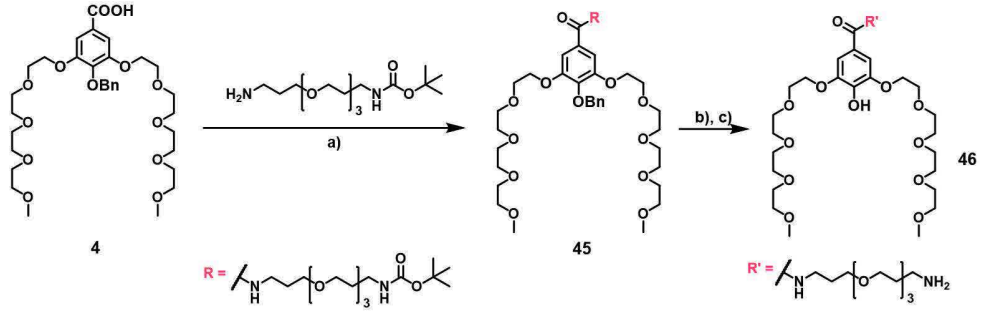

Figure 52: Synthesis of compound **46** : a) EDC, NHS, MeOH/H_2O (1:1), rt, 24h, 68%; b) 10% Pd/C, H_2, Ethanol, rt, 12h, 85%; c) TFA, DCM, rt, 10h, quant.

This step allowed obtaining **48** in 45% yield as an orange oil. Following a purification step by LH–20 COOH–functionalized LA dendron **48** was characterized by ^{1}H and ^{13}C NMR, and mass spectrometry. The total synthesis of bis–phosphonic acid dendron **48** was performed in 9 steps with 17% overall yield, which means each step of the synthesis gets 2% yield. It still can be improved by optimizing either conditions or reagents.

2 Synthesis for toxicity prevention

Cobalt–based nanoparticles (CoNPs) have been suggested as possible alternative to IONPs for MRI applications, due to their greater saturation magnetization value.[51] For example, Bouchard *et al.* demonstrated in MRI studies that T_2 contrast is clearly visible at concentrations as low as 2.5pM in phantoms and 50pM in tissues for CoNPs.[52] These detection thresholds are 7 orders of magnitude lower than those demonstrated for monocrystalline IONPs.[53] This improved performance is in large part due to the high saturation magnetization of Cobalt (3.42 times larger than magnetite) leading to a per–particle relaxivity that is nearly 12 times larger. CoNPs can therefore find applications as highly sensitive MRI CAs.

However, both the oxidation–induced instability and toxicity of metallic Cobalt or Cobalt oxide nanopar-

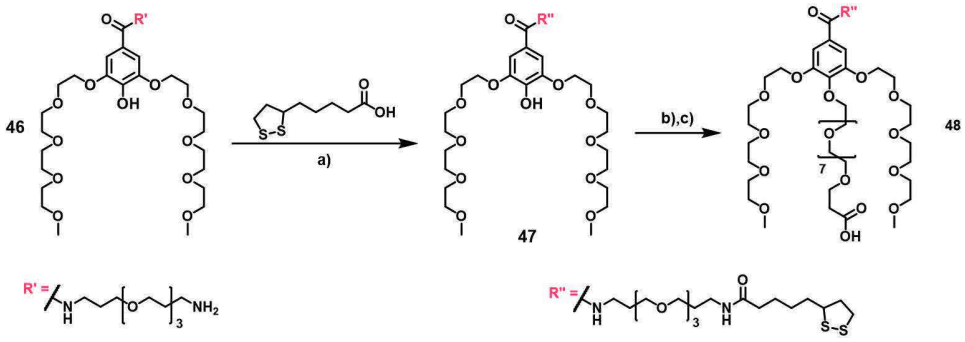

Figure 53: Synthesis of compound **48** : a) EDC, NHS, MeOH/H_2O (1:1), rt, 24h, 65%; b) **10**, K_2CO_3, DMF, 60°C, 48h, 45%; c) TFA, DCM, rt, 10h, quant.

ticles, have prohibited so far their wide use as MRI CAs. The International Agency on Research on Cancer (IARC)[14] has classified this metal and its compounds as possibly carcinogenic to humans, which can cause lung diseases in exposed workers as well as cardiac toxicity[54,55]. Studies have attributed CoNPs' toxicity either to their direct uptake by cells or to their dissolution leading to increased level of Co^{2+} ions[56] in the growth media, with consequent effects on cells.[57] CoNPs were found to exert DNA damage in fibroblasts[58,59,60] and inflammatory response in endothelial cells[61,62], human mononuclear cells[63] and neutrophils[15][64]. In addition, it was shown that CoNPs induce genotoxic effects in human peripheral leukocytes[65].

It is important to note that toxicity effects of Cobalt in human are difficult to evaluate, as they are also dependent on nutritional factors.[66] Indeed, many patients have taken up to 50mg Cobalt/day as Roncovite® for refractory anemia for long periods with little or no toxicity. There are currently no data on the toxicity of CoNPs on humans, in addition the amount of solubilized Cobalt, which is responsible for particle toxicity is still unknown for human body. CoNPs biological effects are mainly driven by the interaction of the nanoparticle' surface and its environment. Therefore, toxicity can probably be modulated by means of a suitable coating with tailored characteristics.

Our aim was to design an appropriate coating–shell for CoNPs in order to keep them stable from chemical oxidation and retain the magnetization of the nanoparticles, while also preventing the release of toxic Co^{2+} ions *in vivo*.

[14] http://www.iarc.com

[15] Neutrophils – are the most abundant type of granulocytes and the most abundant (40% to 75%) type of white blood cells in most mammals.

2.1 Introduction to photopolymerization for biomedical use

Molecules having ene–diynes feature occur in some pharmaceuticals, *e.g.* Calicheamicin – in one of the most aggressive antitumor drugs known, the ene–diyne subunit is sometimes referred to as a *warhead*, by generating highly reactive radical intermediates that attack DNA within the tumor.[67]

Polydiacetylene (PDA) is a conjugated polymer, formed through the topochemical 1,4 – photopolymerization of self–assembled Diacetylene (DA) monomers **(Fig.54)**, forming ene–yne alternating polymer chains without additional catalysts or initiators.

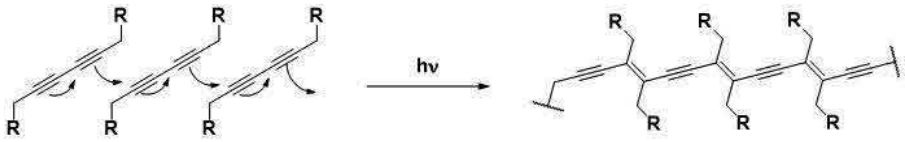

Figure 54: Schematic representation of the photopolymerization of Diacetylene compounds upon irradiation with UV light.

PDAs are very promising in terms of stress–induced colorimetric and fluorogenic transitions for biomedical applications.[68,69,70,71] Displaying a characteristic blue absorption peak at around 640nm, which can shift to be fluorescent and red colored upon environmental stimuli such as heat[72,73], virus[74], magnetic field[75], pH[76], electrochemical reactions[77], mechanical perturbations[78] and organic solvents[79].

Schmuck *et al.* have shown that PDA containing oligo–Lysine groups and Naphthalic acid functions works as a fluorescent turn–on sensor for the detection of bacterial Lipopolysaccharides (LPS).[80] Lee and co–workers have very recently reported PDAs probes displaying both antibacterial efficacy and also a distinct colorimetric change from blue to red upon their binding to bacteria.[81] *In vitro* studies showed low cytotoxicity of PDAs on Caco–2[16] cell line. In contrast, the electrostatic interactions between the PDA and the negatively charged bacteria lead to structural perturbations and cell death. PDAs show a great potential to be used as a dual probe–killers for bacteria.

Molecules containing DA form nanoaggregates in aqueous environments under UV irradiation at 254nm as a result of the formation of PDA supramolecules.[82] We hypothesized that because phosphonic acid allows strong anchoring at any oxide surface, addition of DA–featured dendrons to Cobalt oxides (or Cobalt–doped IONPs) shall result in DA–dendronized CoNPs, which subsequent to irradiation at 254nm, might lead to the formation of PDA–dendron/Co NPs nanoconjugates.

The aim of this project was the surface–modification of CoNPs by the grafting of hydrophilic DA–dendrons followed by photopolymerization of the DA moieties. The presence of an immobilized hydrophilic PDA layer on the surface of nanoparticles is expected to stabilize the morphology, physical properties, including magnetic

[16] Caco–2 cells – is a continuous cell line of heterogeneous human epithelial colorectal adenocarcinoma cells.

and relaxivity properties, and of the highest interest, to lower the toxicity of CoNPs by precluding the diffusion of Co^{2+} ions into the media.

Hydrogen bonding between DA monomers have previously been utilized for the self–assembly of a PDA layer coating on the surface of IONPs, which acted as a stabilizing layer by inhibiting aggregation.[75,83]

2.2 Synthesis of 2P_G_1PEG_PP

One of the main challenges of the project was the use of DA moieties for dendron design, and in the same time keep the hydrophilicity of the final DA–dendron. All of the current literature concerning PDA–based compounds are made of surfactants bearing hydrophobic chains of 12–20 carbon atoms and a polar head containing either an acid group or a PEG chain. Our goal was to develop new hydrophilic PDA systems, by introducing photopolymerizable DA motifs into the structure of a PEG chain. Indeed, regarding MRI application and efficient contrast enhancement, the structure of such DA–containing dendron has still to allow the contact and circulation of water molecules close to the magnetic core. Second challenge was the elaboration of a Phosphonic acid dendron containing DA–PEG chains. The decision was to use the same architecture as for 2P_G_1PEG_COOH dendron, and introducing the DA moieties in the middle of the PEG chains, as shown in **Fig.55**.

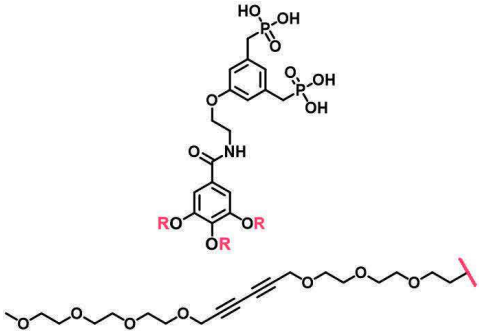

Figure 55: Representation of 2P_G_1PEG_PP dendron final structure.

The synthesis of 2P_G_1PEG_PP dendron starts with the design of such DA–PEGylated chains. To our knowledge, this is the first work describing the synthesis of DA moieties within hydrophilic chains **(Fig.56)**. Compound **51** was synthesized in 4 steps with an overall yield of 14%. At first, commercially available Triethylene glycol undergoes a Nucleophilic Substitution with Propargyl bromide under basic conditions. Compound **49** is obtained in 42% yield, the low yield is mainly due to the formation of one side product – Diethylene glycol propargyl ether – proven by ^{1}H, ^{13}C NMR and Mass spectrum. It appears that, Triethylene glycol propargyl ether is the kinetic product of the first reaction, and with time course, the thermodynamic product – Diethylene glycol propargyl ether – dominates the reaction outcome.

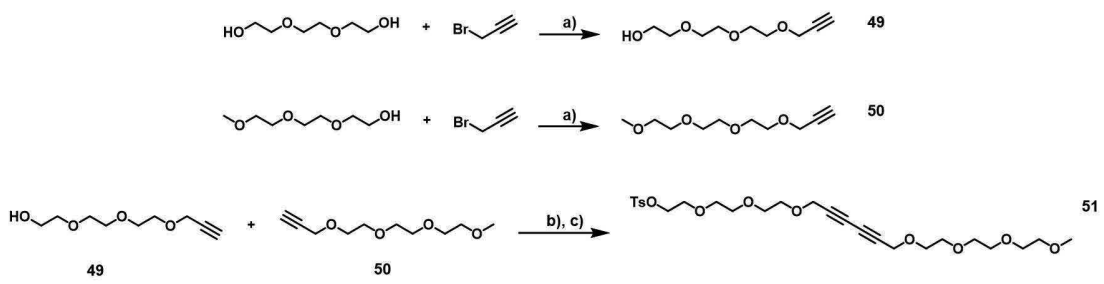

Figure 56: Synthesis of DA–PEG chains **51** : a) *t*BuOK, THF, rt, overnight, 42% and 97%; b) CuCl, TMEDA, DCM, 48h, rt, 40%; k) TsCl, NEt_3, DMAP, DCM, 90%.

On the other side, the reaction of Propargyl bromide with commercially available Triethylene glycol monomethyl ether, has no side products, and compound **50** is obtained in a quantitative yield. The hetero–coupling of both terminal alkynes **49** and **50** was then attempted under several conditions **(Table8)**.

Coupling Agent	Temperture (°C)	Time (h)	Results
$Cu(OAc)_2 \cdot H_2O$, Pyridine	Rt	48	failed
$Cu(OAc)_2 \cdot H_2O$, Pyperidine	Rt	24	failed
CuI, *t*BuOK, DBEDA	100	12	failed
CuI, K_2CO_3, DBEDA	100	12	failed
CuCl, TMEDA, [Alkynes]= 5%	Rt	24	20%
CuCl, TMEDA, [Alkynes]= 2%	Rt	24	40%

Table 8: Terminal alkyne hetero–coupling attempts.

At first, the coupling was experimented under Eglinton conditions[84,85]. The synthesis of DA via the reaction of terminal alkynes in the presence of a stoichiometric amount of a Copper(II) salt in Pyridine or Pyperidine at room temperature resulted in too many inseparable side products. Another attempt was performed under oxidative Glaser–Eglinton–Hay coupling conditions.[86] Reactions with Cu(I) iodide catalyst, *N,N'* – Dibenzylethylenediamine (DBEDA) as complex agent in the presence of O_2 and small amounts of base failed in DA synthesis. In another attempt of Glaser–Eglinton–Hay coupling, Cu(I) chloride in the presence of *N,N,N',N'* – Tetramethylethylenediamine (TMEDA) as complex agent at low reagent–concentrations gave encouraging results. Optimization of both the reaction time and reagent concentrations led to the desired product in 40% yield. Under these conditions, the formation of all three statistic products (two homo–coupling compounds and one hetero–coupling) is inevitable, therefore 40% yield is a very good result in comparison with the statistic yield of 33%. Subsequent to the coupling, Tosylation of the hetero–coupling product in the presence of NEt_3 and DMAP afforded compound **51** in 90% yield and as a translucent oil. Compound **51** is kept at low temperatures and protected from light as DA moieties undergo photopolymerization under day light.

Williamson coupling was performed between Methyl gallate and compound **51**, under classical conditions,

to yield **52** in 75% as an orange oil **(Fig.57)**. All the reactions involving DA–PEGylated chains must be covered from day light, in order to avoid PDA formation.

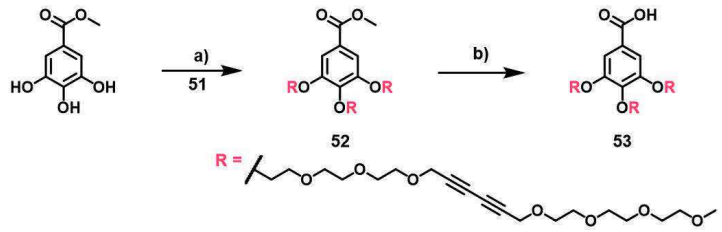

Figure 57: Synthesis of compound **53** : a) K_2CO_3, acetone, 70°C, 48h, 75%; b) KOH, THF / MeOH / H_2O, 80°C, overnight, 30–97%.

Compound **52** underwent then base hydrolysis in the presence of KOH in a mixture of THF/ MeOH/ H_2O and led to compound **53** in 30 to 97% yield. The yield was not reproducible since the reactivity of DA moieties during the ester cleavage reaction can be extremely different, from completely inactive to very reactive. Production of side–products, Diolefins, depends on the time, temperature and base choice, as evidenced by ^{1}H NMR.

Direct amidation between carboxylic acid **53** and amine **18**, in the presence of BOP reagent and molecular sieves at room temperature, yielded **54** in 40% **(Fig.58)**.

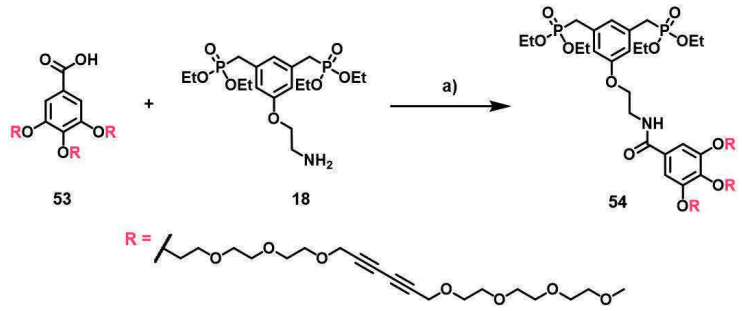

Figure 58: Synthesis of Bisphosphonate precursor **54** of 2P_G_1PEG_PP : BOP, DCM, rt, 72h, 40%.

The reaction was performed under dry and oxygen free conditions, therefore, the use of molecular sieves is not mandatory but advised. The desired product **54** was purified by size exclusion chromatography, LH–20, and analyzed by ^{1}H, ^{13}C, ^{31}P NMR and mass spectrometry. For instance, on ^{1}H NMR spectrum **(Fig.59)** important peaks are highlighted, representative of the structure of **54**.

The most shielded peaks correspond to the amide proton (7.52ppm) and to protons of both aromatic rings, 7.08ppm Gallate protons and 6.8–6.76ppm aromatic protons of the anchoring part. Phosphonate anchoring group is also represented by the triplet at 1.22–1.26ppm, which corresponds to $\mathbf{H_3}$C–CH_2–P(O)–, and by the doublet at 3.04–3.11ppm, corresponding to the Ar–C$\mathbf{H_2}$–P(O)–. It is more complicated to

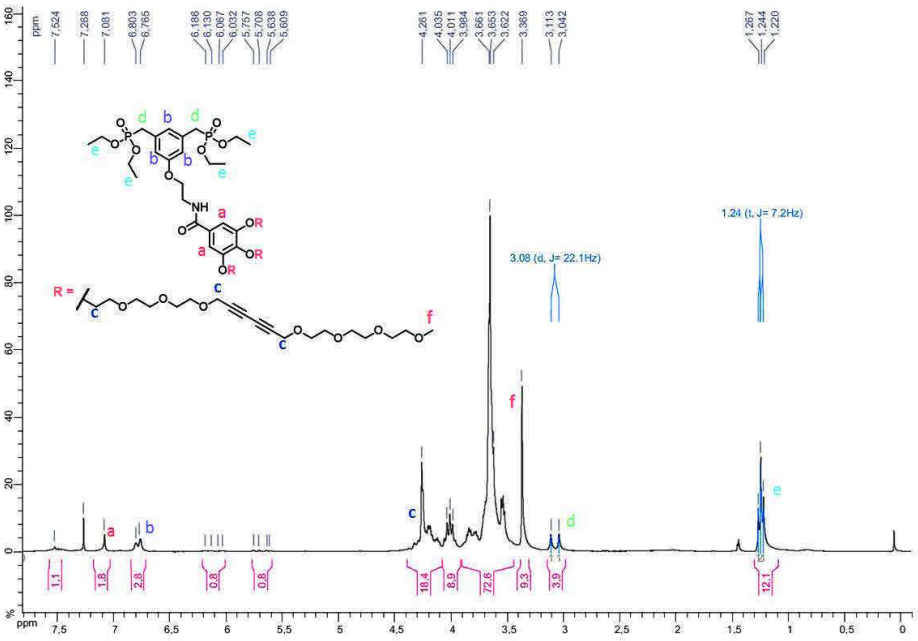

Figure 59: ^{1}H NMR ($CDCl_3$, 300MHz) profile of compound **54**.

distinguish the singlet of the 12 α–alkyne protons at 4.26ppm due to the overlap with H_3C–C**H$_2$**–P(O)– and Ar–C**H$_2$**–CH_2–O– protons.

^{1}H NMR profile corresponds to the structure of compound **54**. However, one can see a small signature of Diolefin side–product at 5.6–6.18ppm, corresponding to almost 10% impurity, which might be enough to either poison the photopolymerization reaction or preclude grafting on the nanoparticle surface. At this stage, these two products are impossible to separate using classical purification methods: same polarity and molecular mass. In order to circumvent the problem, using DA–PEGylated chains at the end of the synthesis might be a solution, thus limiting their exposure to temperature and light.

The intermediate Bisphosphonate **54** was then subjected to a two–step deprotection process to restore the phosphonic acids by using first TMSBr followed by a Methanolysis step **(Fig.60)**.

The first step is known to transform Phosphonates into their corresponding Trimethylsilyl phosphonates which are then cleaved to the Phosphonic acids under hydrolytic conditions. According to McKenna's recent results, the use of methanol instead of water should lead to the selective deprotection of these Trimethylsilyl phosphonates.[87] In our case, careful examination of ^{1}H NMR profile of reaction mixture showed the absence of deprotected product **54**. Concentrating the reaction mixture provided high amounts of Hydrogen bromide (originated from TMSBr methanolysis) which is incompatible with Diacetylene moieties. Indeed, HBr reacts with DA moieties leading either to corresponding alkene or, depending on the amount of hydrogen halide, to

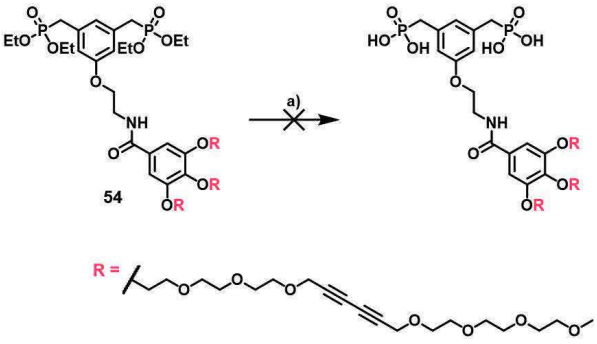

Figure 60: Deprotection of the Ethylphosphonate groups of compound **67** in the presence of a large excess of TMSBr in DCM.

geminal dihalide. This type of electrophilic addition of hydrogen halides on alkynes is a common knowledge. Thus the decision to change the synthetic route for 2P_G_1PEG_PP has been taken.

In order to overcome the use of TMSBr as deprotection agent for Ethylphosphonates, employing Methylphosphonates gives the opportunity to perform their deprotection in Methanol. The new retrosynthetic method is described in **Fig.61**. Additionally, the new synthetic pathway allows the introduction of DA–PEGylated chains close to the end of the process, which should lower the yield of Diolefin side–product.

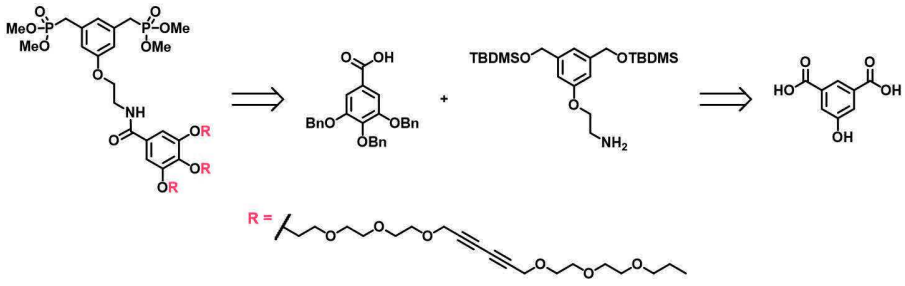

Figure 61: New retrosynthetic analysis for 2P_G_1PEG_PP preparation.

The divergent synthesis of 2P_G_1PEG_PP starts, as previously, with 5–Hydroxyisophthalic acid. During this synthetic strategy, Methylphosphonates shall be introduced into the structure near by the end of the synthesis, in order to avoid complicated purifications due to phosphonates polarity. This work is still under progress, therefore some of the following reactions are not optimized.

The new synthesis of the dendritic Bis–Methyl–phosphonate starts with the key intermediate **56** which was obtained in 3 steps from compound **14** with 56% overall yield **(Fig.62)**.

Both Benzylic and Phenol functions of compound **14** underwent protection in the presence of *tert*–Butyldimethylsilyl chloride (TBDMSCl) and Imidazole, while subsequent deprotection with TBAF was selective towards Phenol function and led to compound **55** in 75% yield. **55** was then subjected to Williamson coupling with **19** in the presence of K_2CO_3 in Acetone to afford **56** in 73% yield. The synthesis of the second

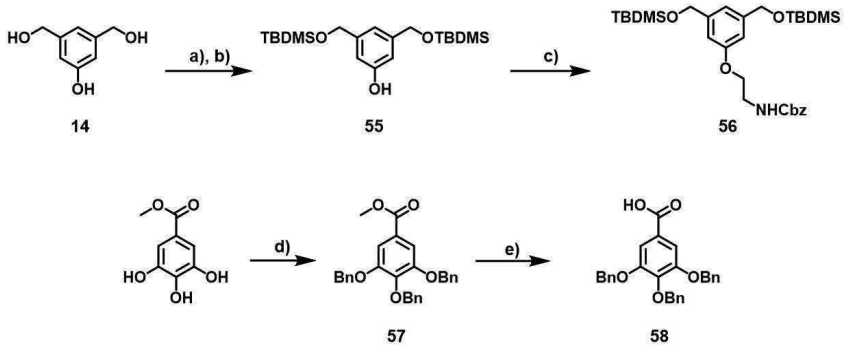

Figure 62: Synthesis of two key intermediates **56** and **58** : a) TBDMSCl, Imidazole, DMF, 0°C, 3h, 80%; b) TBAF, THF, 0°C, 20min, 95%; c) **19**, K_2CO_3,Acetone, 60°C, 48h, 73%; d) BnBr, K_2CO_3, KI, DMF/ACN, 80°C, overnight, 95%; e) KOH, THF/MeOH/H_2O, 80°C, 6h, 98%.

key intermediate **58** was performed in 2 steps in 88% overall yield. For the synthesis of Benzyl ether **57**, Benzyl bromide was introduced as protective groups of Methyl gallate alcohol functions using Williamson ether synthesis in 95% yield. The latter underwent base hydrolysis using KOH in a mixture of THF/MeOH/H_2O. The key intermediate **58** was prepared in 98% yield.

Remaining reactions in order to accomplish the synthesis of dendron 2P_G_1PEG_PP are described in **Fig.63**.

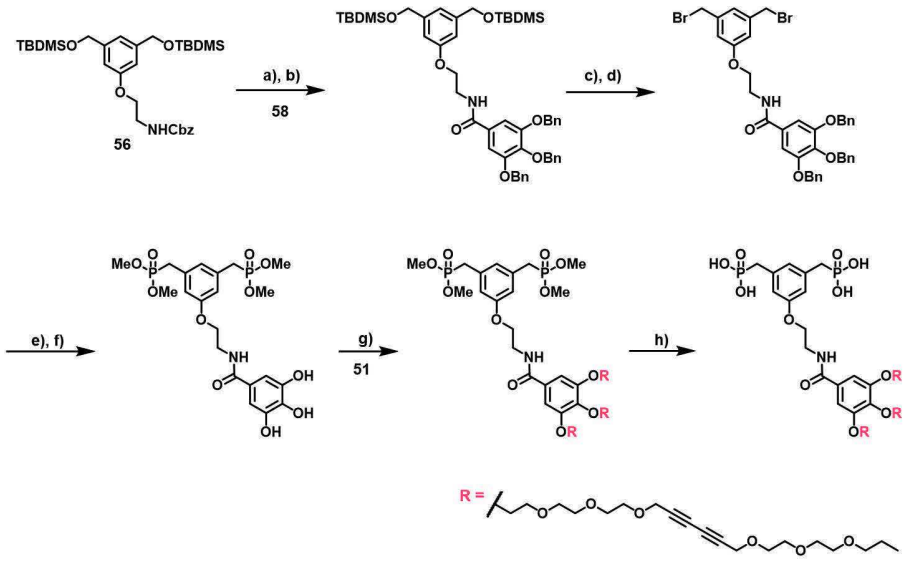

Figure 63: Synthetic route to follow for 2P_G_1PEG_PP synthesis completion: a) 10% Pd/C, H_2, ethanol, rt; b) BOP, DIPEA, DCM; c) TFA, DCM, rt; d) HBr, Acetic acid, 0°C; e) $P(OMe)_3$, reflux; f) 10% Pd/C, H_2, ethanol, rt; g) K_2CO_3, acetone, 60°C; h) MeOH, 80°C.

The connection of the two key intermediates shall start with the deprotection of Benzyl carbamate protecting group in the presence of 20% $Pd(OH)_2/C$, followed by a peptide coupling with **58**. Subsequent to the

deprotection of *tert*–butyldimethylsilyloxy group, Benzyl alcohols undergo substitution with Methyl phosphonates under Arbuzov reaction conditions. Deprotection of Benzyl ethers in the presence of 10% Pd/C is followed by Williamson ether coupling with DA–PEGylated chains **(51)**. The most challenging step remains the deprotection of Methyl phosphonates, avoiding TMSBr as deprotection reagent. Recently, such deprotection was reported using a mixture of MeOH/ H_2O at 90˚C.[88] In our case, such mild conditions should allow deprotection of Methyl phosphonates functions without damaging DA–moieties.

3 Synthesis for integrity assessment of nanomaterials

3.1 Introduction to Aggregation–Induced Emission (AIE)

Development of sensitive and selective fluorescent biosensors is of great importance in the fields of biological science and technology, as they allow direct visualization of biological analytes at the molecular level and offer useful insights into complex biological structures and processes. To achieve desired signal output and high signal–to–noise ratio, a variety of fluorescent probes based on both discrete molecules and colloidal nanoparticles have been explored for biomedical research.[89,90,91] The emission of these dyes, however, is often weakened or even annihilated at high concentrations or in aggregate state, which is known as concentration quenching or aggregation caused quenching (ACQ).[92,93]

A typical example of ACQ effect is shown in **Fig.64.A**. A dilute THF solution of *N,N* – Dicyclohexyl–1,7– dibromo– 3,4,9,10– perylenetetracarboxylic diimide (DDPD) is highly emissive under UV illumination. The fluorescence is weakened upon addition of water and is diminished when the water fraction (fw) reaches 70%. Such behavior has been widely observed in conventional fluorophore systems, especially in amphiphilic far–red/near IR (FR / NIR) emitters.[94]

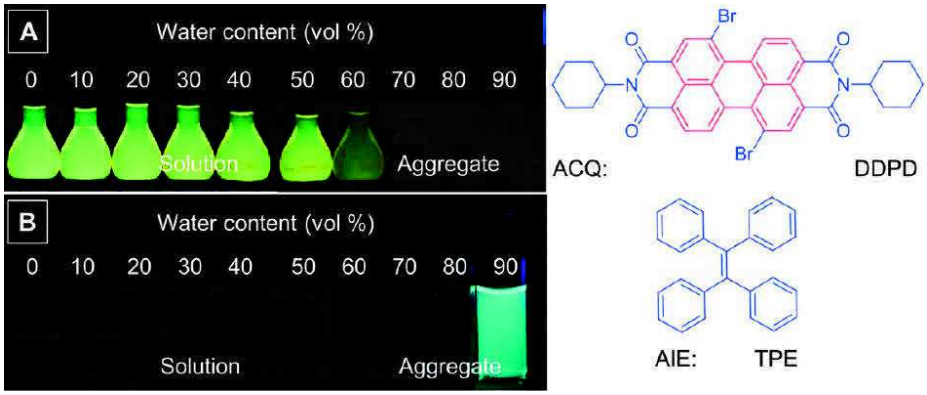

Figure 64: Fluorescence photographs of (A) DDPD with ACQ feature and (B) TPE with aggregation–induced emission (AIE) attribute in THF/water mixtures with different water contents upon UV illumination.[95]

Oppositely to such ACQ, an Aggregation Induced Emission (AIE) phenomenon has been extensively investigated by Tang *et al.* since 2001,[96,97] and by now, a great number of AIE molecules has been designed. For example, Tetraphenylethylene (TPE) is an iconic AIE fluorophore: it is non–fluorescent in THF solution, becomes emissive in a THF/water mixture, with high water fraction TPE molecules aggregate **(Fig.64.B)**.

The AIE phenomenon is generally observed in molecules that contain rotor structures (*e.g.*, phenyl groups), which undergo low–frequency motions in dilute solutions, causing fast non–radiative decay of the excited states that makes the fluorogens non–emissive. In the aggregates, these motions are blocked by intermolecular steric interactions, which open the radiative pathway. Fascinating features (*e.g.* low fluorescence as molecular species, high brightness in aggregates and large Stokes shifts[17]) of AIE fluorogens led to booming development of AIE–based nanoconjugates in the past two years. These AIE–based fluorescent nanoparticles have been extensively exploited for a variety of biomedical applications, which include *in vitro* and *in vivo* MI[98,99,100,101], gene delivery[102], therapy[103], biological sensors[104,105,106] and elaboration of dual–mode platforms or theranostics.[107]

For instance, very recently Yuan *et al.* have developed light–responsive AIE nanoparticles showing Cytosolic[18] drug release upon light irradiation **(Fig.65)**[108]: those AIE–NPs/DOX significantly inhibit the growth of DOX resistant breast cancer cells (MDA–MB–231/DOX), moreover, when exposed to light irradiation, AIE nanoparticles can trigger drug release in the cytosol. Such drug loaded nanoparticles showed significantly improved cytotoxicity towards drug resistant cancer cells compared to free DOX treatment.

In another study, Wang and co–workers reported the preparation of fluorescent Silica NPs doped with AIE molecules.[109] The morphology results showed that AIE–based SiO_2 NPs have narrow particle size distribution around 50nm and spherical shapes. They show no apparent cytotoxicity to both MCF–7S[19] and HepG–2[20] cells. Furthermore, cellular images highlighted potential advantages in *in vivo* imaging because not only of strong fluorescence intensity but also stability in complicated bio–environments.

Structure restriction of AIE molecules is usually affected by microenvironments including viscosity, polarity, temperature and compatibility. Therefore, building an appropriate microenvironment to restrict rotations of AIE molecules may be the key factor to obtain materials with stable and high fluorescence.

For a long time now, we have been asking the same question: what is the fate of your dendronized nanoparticles, and in particular, what is the fate of the dendritic shell in physiological media? As the particles enter a biological milieu, it is likely that they are coated with biomolecules that modify the properties

[17] Stokes shifts – is the difference (in wavelength or frequency units) between positions of the band maxima of the absorption and emission spectra (fluorescence and Raman being two examples) of the same electronic transition.
[18] Cytosolic – or cytoplasmic matrix is the liquid found inside cells.
[19] MCF–7 – breast cancer cell line.
[20] HepG2 – human liver cancer cell line.

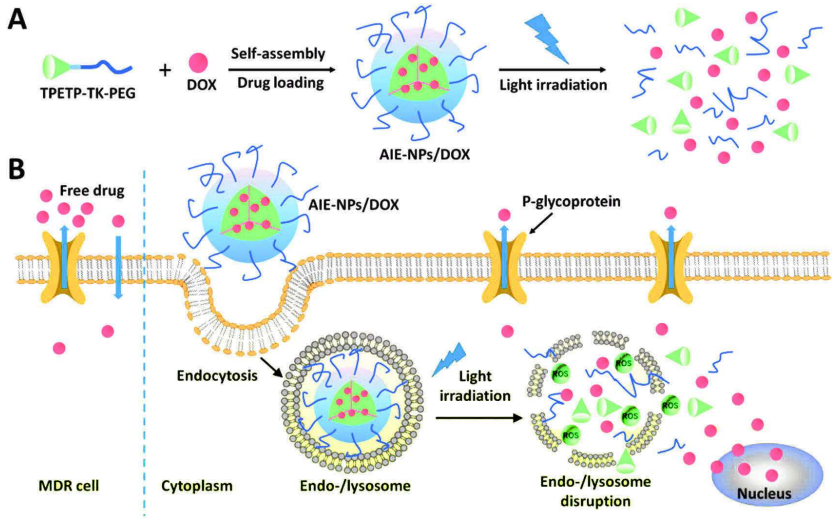

Figure 65: (A) Schematic illustration of light–responsive polymeric micelles from a thioketal (TK)–bridged TPETP–TK–PEG polymer in aqueous media with the encapsulation of anticancer drug (DOX). (B) The itinerary of AIE–NPs/DOX to overcome drug resistance in cancer cells.[108]

of the nanoparticles (*e.g.* size, surface charge, flexibility) and the way in which they interact with cells (*Protein–corona*). Wong *et al.* recently demonstrated that quantum dot–gelatin nanoparticles shrink from 100nm in diameter to 10nm after they extravasate from leaky regions of the tumor vasculature and are exposed to matrix metalloproteinases in the tumor microenvironment.[110] To this end, it is important to assess the evolution of the shell as a nanoparticle is transferred from one biological compartment to another.

In the past two years, there have been few successful attempts to introduce AIE moieties within dendrimer structure.[111,112,113] Arseneault *et al.* reported the synthesis of different generation dendrimers with ethylene oxide core and decorated with TPE molecules.[113] They showed a strong correlation between dendrimer generation and TPE enhanced photoluminescence. Liu and co–workers have also reported a study on the AIE–based PAMAM dendrimer of different generations and their enhanced emission.[112] Their results confirmed that the absolute fluorescence quantum yield of AIE–based PAMAM dendrimer increases with increasing the generation and reaches a plateau, nevertheless it remains much higher than the corresponding forms of AIE moiety.

In our case, do the dendronized nanoparticles stay integer *in vivo*? Meaning does the organic shell stay anchored at the IONP' surface upon *iv* injection?

Our idea was the design of a smart coating for IONPs, which will assess those questions. The use of AIE moieties within the dendron backbone occurred to us as a central part of the research project. We hypothesized that organizing AIE–based dendrons around IONPs acting as nanoscale templates, could possibly block rotational modes of AIE molecules and thus open the radiation pathway **(Fig.66)**. *In vivo* OI

of dendronized nanoparticles will be much more representative of the real fate of the integer nanohybrids.

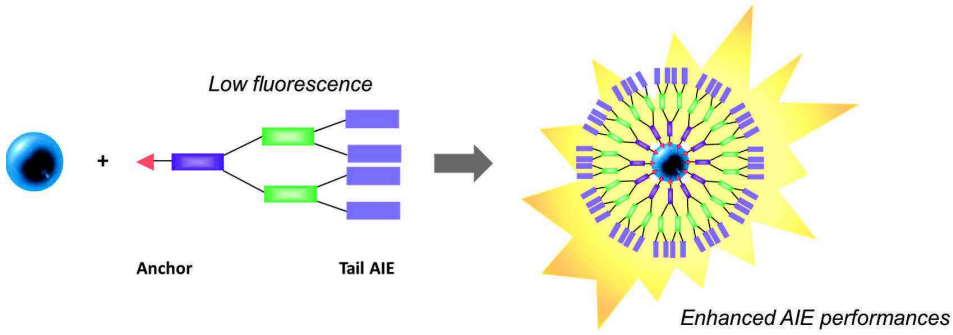

Figure 66: Schematic representation of enhancement upon grafting of AIE–based dendrons on NPs surface.

The goal of the project is then to design and synthesize AIE–based PEGylated dendrons and to graft them onto IONPs. The ability to follow only integer nanohybrids by OI, will open great possibilities in biomedical applications. For instance, learning more about adsorption or metabolim of nanomaterials, drug release tracking or mapping lymph nodes under direct visual guidance.

3.1.1 Synthesis of 2P_G_1PEG_AIE

The structure of AIE–based dendrons had to fulfill several requirements: 1) hydrophilicity (since AIE moieties are hydrophobic), then dendron structure must present PEG unit, 2) Ethylphosphonates as anchoring functions, as they allow strong binding to IONPs surface. The decision was to use an alike pattern as for 2P_G_1PEG_COOH dendron, but replacing PEGylated chains by AIE–PEGylated ones, as shown in **Fig.67**. The structure of AIE dendron presents only two AIE–PEG chains since AIE moieties induce a bulky environment.

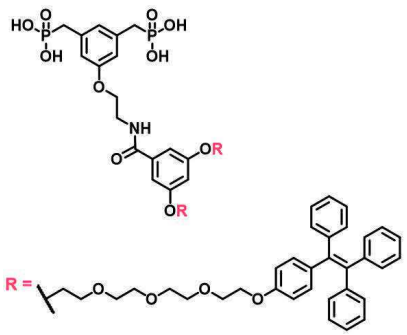

Figure 67: Representation of 2P_G_1PEG_AIE desired structure.

The choice of TPE resulted from its emission wave–length, around 500nm (depending on the combined functions), its small size and its use for the development of different *in vitro* and *in vivo* biological sensors.

The synthesis of 2P_G_1PEG_AIE starts with the key intermediate **63** synthesized in 6 steps with 40% overall yield **(Fig.68)**. At first, commercially available 4–Hydroxybenzophenone underwent electrophilic Methylation via Williamson coupling in the presence of Methyl iodide. Resulting compound **59** was subjected to a nucleophilic addition of Diphenylmethane followed by alcohol elimination performed in the presence of a catalytic amount of *p*–Toluenesulfonic acid (TsOH). TPE precursor **60** was obtained in 63% yield as a white solid.

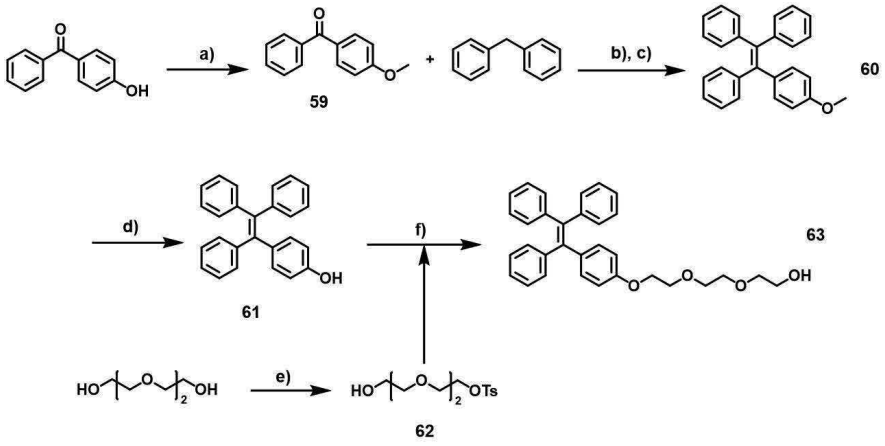

Figure 68: Synthesis of intermediate **63** : a) MeI, K_2CO_3, acetone, 65°C, 72h, 96%; b) Diphenylmethane, n–BuLi, THF, 0°C, overnight, 63%; c) TsOH, reflux, 8h, quant.; d) BBr_3, DCM, 0°C, overnight, 88%; e) NaOH, TsCl, THF/H_2O, 0°C, 24h, 85%; f) K_2CO_3, Acetone, 60°C, 24h, 88%.

Cleavage of Phenolic ether **60** under mild conditions using Tribromoborane (BBr_3) reagent led to **61** in 88% yield. Meanwhile, Triethylene glycol was transformed in 85% yield into its corresponding Tosylated ester **62** via Williamson alkylation. Then, alkylation of **61** by **62** in the presence of K_2CO_3 in acetone allowed the production of **63** which was obtained in 88% yield as a yellowish oil, showing an intense blue luminescence when exposed to UV (254 nm) light. Activation of primary alcohol **63** in the presence of TsCl, DMAP and Pyridine gave intermediate **64** in 86% **(Fig.69)**.

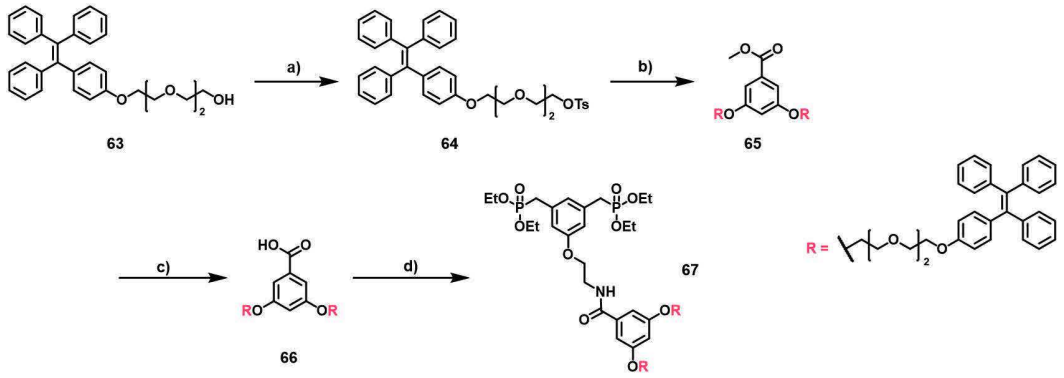

Figure 69: Synthesis of 2P_G_1PEG_AIE dendron precursor **67** : a) TsCl, DMAP, Pyridine, DCM, 86%; b) Methyl 3,5–dihydroxybenzoate, K_2CO_3, Acetone, 60°C, 48h, 84%; c) KOH, THF/MeOH/H_2O, 80°C, 6h, quant.; d) BOP, DIPEA, DCM, rt, 72h, 60%.

Alkylation of Methyl 3,5–dihydroxybenzoate with **65** in the presence of K_2CO_3 in acetone at reflux for 2 days, led to **65** in 84%. Subsequent base hydrolysis of **65** using KOH in a THF / MeOH / H_2O mixture , yielded carboxylic acid **66** in quantitative yield as a yellowish oil. Peptide coupling between **66** and Amine **18** in the presence of BOP and DIPEA afforded **67** in 60%.

The desired Ethyl phosphonate **67** was purified using size exclusion chromatography, LH–20, and analyzed by ^{1}H, ^{13}C, ^{31}P NMR and mass spectrometry. For instance, on ^{1}H NMR spectrum **Fig.70** important peaks are highlighted, which confirm the structure of compound **67**.

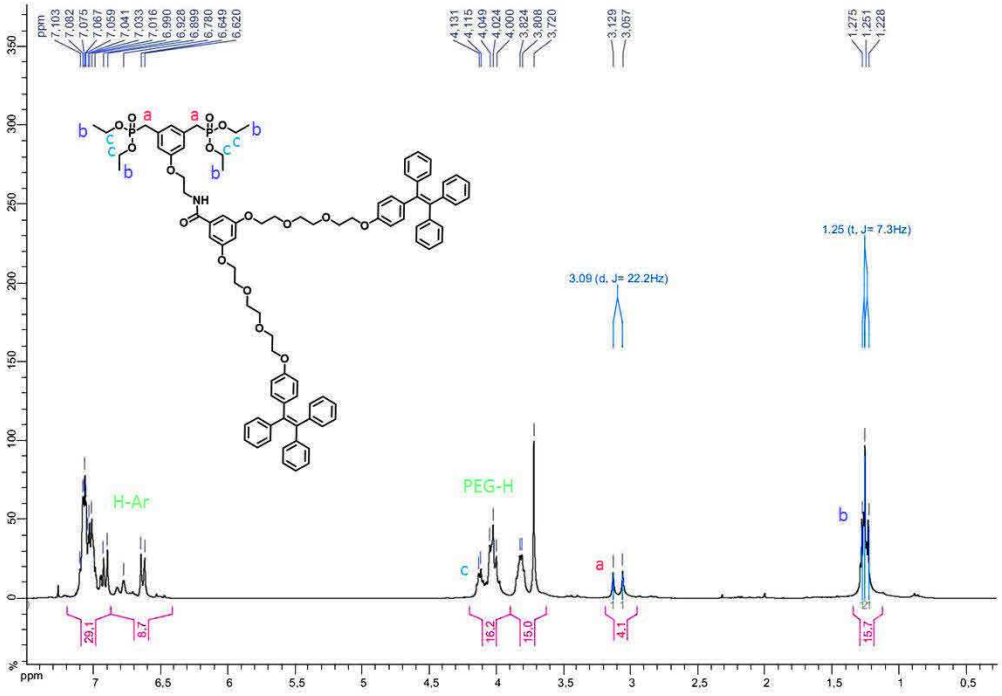

Figure 70: ^{1}H NMR ($CDCl_3$, 300MHz) profile of compound **67**.

All aromatic protons of the anchoring part, Gallate and both TPE moieties are located between 6.62–7.10ppm. Phosphonate anchoring group is also represented by the triplet at 1.22–1.27ppm with J = 7.3Hz, which correspond to **H$_3$**C–CH$_2$–P(O)–, and the doublet at 3.04–3.11ppm with J = 22.2Hz, corresponding to the Ar–C**H$_2$**–P(O)–. It is more complicated to distinguish quartet peaks of H$_3$C–C**H$_2$**–P(O)– protons due to their overlap with PEG protons.

The intermediate Bisphosphonate **67** was then subjected to a two–step deprotection process to restore the Phosphonic acids by using first TMSBr followed by Methanolysis **(Fig.71)**.

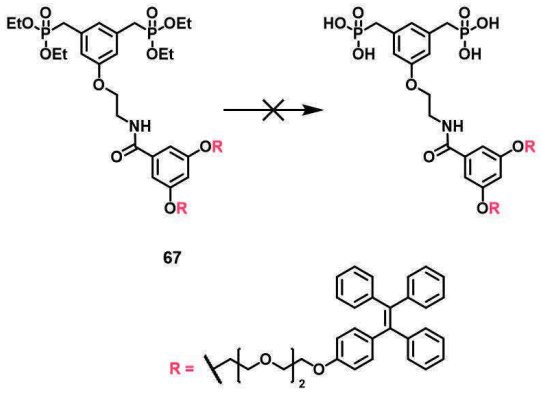

Figure 71: Deprotection of compound **67** Ethylphosphonate groups in the presence of a large excess of TMSBr in DCM.

TMSBr was added dropwise to a mixture of 2P_G_1PEG_AIE precursor **67** in DCM at 0˚C. After 4 hours, the reaction mixture was quenched with Methanol, in order to cleave Trimethylsilyl phosphonates group and release corresponding Phosphonic acids. Careful examination of ^{1}H NMR profile of reaction mixture showed the presence of deprotected product **67 (Fig.72)**. All aromatic protons of the anchoring part, Gallate and both TPE moieties are located between 6.51–6.99ppm, as expected. Somehow, one can notice a singlet peak shielded at 5.21ppm that appeared on the spectra. After attentive investigation, this singlet does not correspond to any of the reagents (TMSBr, MeOH, *in situ* produced HBr), neither to the deprotected compound **67**. However, it can belong to the product structure B, more precisely to the $(Ar)_2$–C**H**–COH–$(Ar)_2$– (TPE precursor) **(Fig.72.B.)**. We suppose that structure A was subjected to an addition reaction in the presence of a strong Brønsted acid, HBr, leading to Tetraphenylethane derivative (1,1,2,2–tetraphenylethan–1–ol). Indeed, in theory $(Ar)_2$–C**H**–COH–$(Ar)_2$– proton should be shielded at around 5ppm. Additionally, integration of **H**–O···H peak at 4.35ppm for six protons, qualitative data, supports the hypothesis of compound structure B. ^{13}C NMR sequence could not give any information regarding the structure, since several peaks overlap.

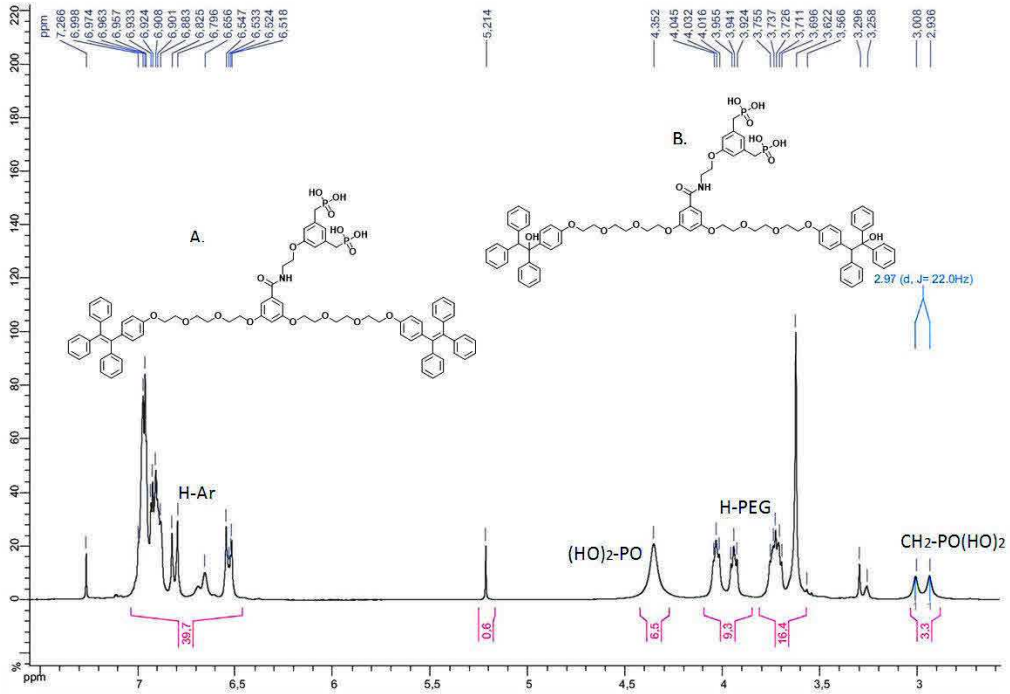

Figure 72: ^{1}H NMR ($CDCl_3$, 300MHz) profile of deprotected compound **67**.

As the deprotection of Ethylphosphonate of compound **67** led to a mixture of structure A and B, both structure being moreover insoluble in water, decision to change 2P_G_1PEG _AIE structure and synthetic method was taken, in order to obtain a hydrophilic compound and to avoid TMSBr as deprotection reagent.

Synthesis of 2P_G_1PEG_AIE should follow a similar divergent path as for 2P_G_1PEG _PP, moreover longer PEG chains will be attached to the AIE moieties, to increase hydrophilicity of the final dendron **(Fig.73)**. During this synthetic strategy, Methylphosphonates shall be introduced into the structure near by the end of the synthesis, in order to avoid complicated purifications due to Phosphonates polarity. This work is still under progress.

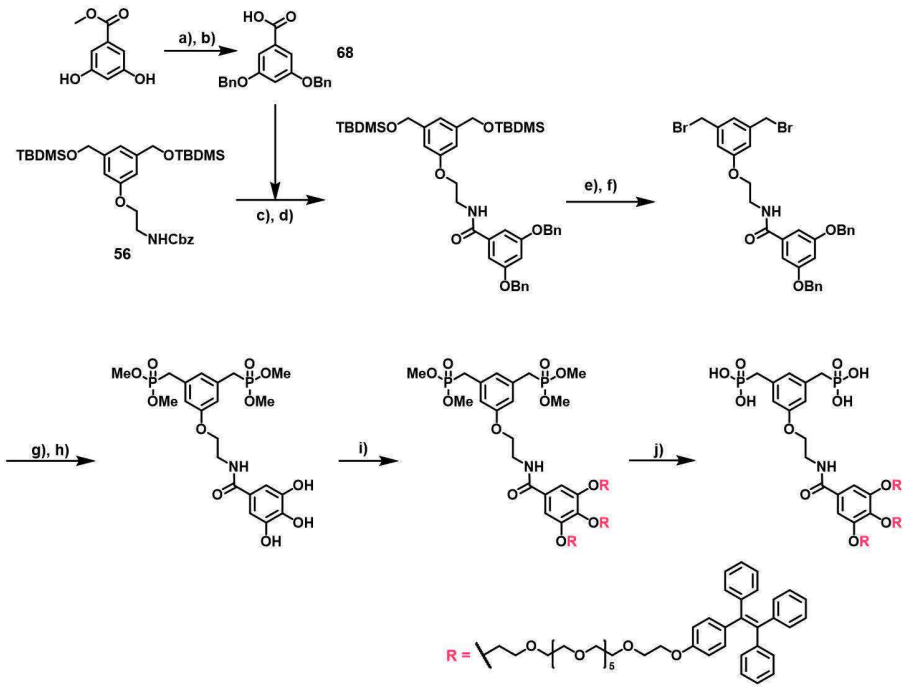

Figure 73: Synthesis of compound **68** and the new path for 2P_G_1PEG_AIE synthesis.

Conclusion In conclusion, we have developed and successfully synthesized two hydrophilic dendritic Phosphonic acids useful for the functionalization of IONPs, 1P_G_1PEG_PP and 2P_G_1PEG _PP and two dendritic Lipoic acids for further AuNPs functionalization for biomedical applications. The syntheses of 2P_G_1PEG_PP and 2P_G_1PEG_AIE and their subsequent grafting onto magnetic NPs (Fe and Co NPs) are under progress. Taken together, we have shown that organic shells properties for inorganic NPs can be adjusted in order to respond to biomedical issues: biodistribution, toxicity, nanohybrid integrity. Here exemplified by molecular engineering of 2P_G_1PEG_PP using Diacetylene moieties for decreasing CoNPs toxicity and by 2P_G_1PEG_AIE engineering for assessing material integrity upon *in vivo* application. With the results obtained herewith, one can definitely infer that, with minor manipulation and fine–tuning, these dendritic structures do possess excellent potential for applications in the field of biotechnology and biochemical engineering.

References

[1] Tully, D.C., Frechet, J.M.J. Dendrimers at surfaces and interfaces chemistry and applications. *Chemical Communications*, **2001**, 2(14), 1229-1239.

[2] Sebastian, R., Griffe, L., Turrin, C., Donnadieu, B., Caminade, A., Majoral, J. Synthesis and Core and Surface Reactivity of Phosphorus-Based Dendrons. *European Journal of Inorganic Chemistry*, **2004**, 2004(12), 2459-2466.

[3] Snyder, S.A., Breazzano, S.P., Ross, A.G., Lin, Y., Zografos, A.L. Total synthesis of diverse carbogenic complexity within the resveratrol class from a common building block. *Journal of the American Chemical Society*, **2009**, 131(5), 1753-1765.

[4] Zhao, C., Han, L., Goto, M., Masato Tanaka Rhodium-Catalyzed Hydrophosphorylation of Terminal Alkynes Leading to Highly Selective Formation of E -Alkenylphosphonates Complete Reversal of Regioselectivity to the Palaldium-Catalyzed Counterpart. *Angewandte Chemie International ed*, **2001**, 40(10), 1929-1932.

[5] Alonso, F., Beletskaya, I.P., Yus, M. Transition-metal-catalyzed addition of heteroatom-hydrogen bonds to alkynes. *Chemical reviews*, **2004**, 104(6), 3079-3159.

[6] Gao, Y., Wang, G., Chen, L., Xu, P., Zhao, Y., Zhou, Y. Copper-Catalyzed Aerobic Oxidative Coupling of Terminal Alkynes with H -Phosphonates Leading to Alkynylphosphonates. *Journal of American Chemical Society*, **2009**, 131, 7956-7957.

[7] Hirao, T., Masunaga, T., Yamada, N. Palladium-catalyzed New Carbon-Phosphorus Bond Formation. *Belletin of Chemical Society of Japan*, **1982**, 55, 909-913.

[8] Enders, D., Chow, S. Organocatalytic Asymmetric Michael Addition of 2,2-Dimethyl-1,3-dioxan-5-one to Nitro Alkenes Employing Proline-Based Catalysts. *European Journal of Organic Chemistry*, **2006**, 2006(20), 4578-4584.

[9] Bhattacharya, A.K., Thyagarajan, G. The Michaelis-Arbuzov Rearrangement. *Chemical reviews*, **1981**, 81, 415-430.

[10] Rajeshwaran, G.G., Nandakumar, M., Sureshbabu, R., Mohanakrishnan, A.K. Lewis Acid-Mediated Michaelis - Arbuzov Reaction at Room Temperature A Facile Preparation of Arylmethyl Heteroarylmethyl Phosphonates. *Organic letters*, **2011**, 13(6), 2645-2648.

[11] Barney, R.J., Richardson, R.M., Wiemer, D.F. Direct conversion of benzylic and allylic alcohols to phosphonates. *The Journal of Organic Chemistry*, **2011**, 76(8), 2875-2879.

[12] Lee, J., Huh, Y., Jun, Y., Seo, J., Jang, J., Song, H., Kim, S., Cho, E., Yoon, H., Suh, J., Cheon, J. Artificially engineered magnetic nanoparticles for ultra-sensitive molecular imaging. *Nature medicine*, **2007**, 13(1), 95-99.

[13] Thomas, C.R., Ferris, D.P., Lee, J., Choi, E., Cho, M.H., Kim, E.S., Stoddart, J.F., Shin, J., Cheon, J., Zink, J.I. Noninvasive remote-controlled release of drug molecules in vitro using magnetic actuation of mechanized nanoparticles. *Journal of the American Chemical Society*, **2010**, 132(31), 10623-10625.

[14] Lee, H., Sun, E., Ham, D., Weissleder, R. Chip-NMR biosensor for detection and molecular analysis of cells. *Nature Medicine*, **2008**, 14(8), 869-874.

[15] Chen, L., Razavi, F.S., Mumin, A., Guo, X., Sham, T., Zhang, J. Multifunctional nanoparticles for rapid bacterial capture, detection, and decontamination. *RSC Advances*, **2013**, 3(7), 2390-2397.

[16] Louie, A. Multimodality imaging probes design and challenges. *Chemical reviews*, **2010**, 110(5), 3146-3195.

[17] Garofalo, A., Parat, A., Bordeianu, C., Ghobril, C., Kueny-Stotz, M., Walter, A., Jouhannaud, J., Begin-Colin, S., Felder-Flesch, D. Efficient synthesis of small-sized phosphonated dendrons potential organic coatings of iron oxide nanoparticles. *New Journal of Chemistry*, **2014**, 38, 5226-5239.

[18] Gentilini, C., Boccalon, M., Pasquato, L. Straightforward Synthesis of Fluorinated Amphiphilic Thiols. *European Journal of Organic Chemistry*, **2008**, 2008(19), 3308-3313.

[19] Mckenna, C.E., Higa, M.T., Cheung, N.H., Mckenna, M. The Facile Dealkylation of Phosphonic Acid Dialkyl Ethers by Bromotrimethylsilane. *Tetrahedron Letters*, **1977**, 2, 155-158.

[20] Schrigten, D., Breyholz, H., Wagner, S., Hermann, S., Schober, O., Schafers, M., Haufe, G., Kopka, K. A New Generation of Radiofluorinated Pyrimidine-2,4,6-triones as MMP-Targeted Radiotracers for Positron Emission Tomography. *Journal of Medicinal Chemistry*, **2012**, 55, 223-232.

[21] Gurjar, M.K., Pal, S., Rama Rao, A.V. STUDIES DIRECTED TOWARD THE SYNTHESIS OF MARTINELLINES ONE POT SYNTHESIS OF PYRROLOQUINOLONE RING SYSTEM. *Heterocycles*, **1997**, 45(2), 231-234.

[22] Tom, N.J., Simon, W.M., Frost, H.N., Ewing, M. Deprotection of a primary Boc group under basic conditions. *Tetrahedron Letters*, **2004**, 45(5), 905-906.

[23] Lee, J.W., Kim, B., Kim, H.J., Han, S.C., Shin, W.S., Jin, S. Convergent Synthesis of Symmetrical and Unsymmetrical PAMAM Dendrimers. *Macromolecules*, **2006**, 39(6), 2418-2422.

[24] Arbuzov, B.A., Nikonov, G.N. Phosphorus Heterocycles from a-Hydroxyalkylphosphines and Vinylphosphines. *Advances in heterocycling chemistry*, **1994**, 61, 60-133.

[25] Wang, L.V. Photoacoustic imaging and spectroscopy. *CRC Press*, **2009**.

[26] Oraevsky, A.A. Optoacoustic Tomography From fundamentals to diagnostic imaging of breast cancer. *Biomedical Photonics Handbook Biomedical Diagnosis*, **214**, 715-757.

[27] Ntziachristos, V. Going deeper than microscopy the optical imaging frontier in biology. *Nature methods*, **2010**, 7(8), 603-614.

[28] Wang, L.V., Hu, S. Photoacoustic Tomography In Vivo Imaging from Organelles to Organs. *Science*, **2012**, 335(6075), 1458-1462.

[29] Welch, A.J., Van Gemert, M.J.C. Overview of Optical and thermal laser-tissue interaction and nomenclature. *Optical-Thermal Response of Laser-Irradiated Tissue*, **2011**, 1-958.

[30] Weissleder, R. A clearer vision for in vivo imaging Progress continues in the development of smaller , more penetrable probes for biological imaging . Toward the phosphoproteome. *Nature biotechnology*, **2001**, 19(4), 316-317.

[31] Lin, A.W.H., Lewinski, N.A., West, J.L., Halas, N.J., Drezek, R.A. Optically tunable nanoparticle contrast agents for early cancer detection model-based analysis of gold nanoshells. *Journal of biomedical optics*, **2005**, 10(6), 0640351-06403510.

[32] Yang, X., Maurudis, A., Gamelin, J., Aguirre, A., Zhu, Q., Wang, L.V. Photoacoustic tomography of small animal brain with a curved array transducer. *Journal of biomedical optics*, **2009**, 14(5), 0540071-0540075.

[33] Razansky, D., Distel, M., Vinegoni, C., Ma, R., Perrimon, N., Koster, R.W., Ntziachristos, V. Multispectral opto-acoustic tomography of deep-seated fluorescent proteins in vivo. *Nature Photonics*, **2009**, 3(7), 412-417.

[34] Ntziachristos, V., Razansky, D. Molecular imaging by means of multispectral optoacoustic tomography MSOT. *Chemical Reviews*, **2010**, 110(5), 2783-2794.

[35] Wong, Y.H., Thomas, R.L., Hawkins, G.F. Surface and subsurface structure of solids by laser photoacoustic spectroscopy. *Applied Physics Letters*, **1978**, 32(9), 538-539.

[36] Kruger, R.A. Photoacoustic ultrasound. *Medical physics*, **1994**, 21(1), 127-131.

[37] Torchilin, V.P. PEG-based micelles as carriers of contrast agents for different imaging modalities. *Advanced Drug Delivery Reviews*, **2002**, 54(2), 235-252.

[38] Shim, S., Lim, D., Nam, J. Ultrasensitive optical biodiagnostic methods using metallic nanoparticles. *Nanomedicine London, England*, **2008**, 3(2), 215-232.

[39] Luke, G.P., Yeager, D., Emelianov, S.Y. Biomedical applications of photoacoustic imaging with exogenous contrast agents. *Annals of Biomedical Engineering*, **2012**, 40(2), 422-437.

[40] Pramanik, M., Swierczewska, M., Green, D., Sitharaman, B., Wang, L.V. Single-walled carbon nanotubes as a multimodal-thermoacoustic and photoacoustic-contrast agent. *Journal of Biomedical Optics*, **2009**, 14(3), 0340181-0340188.

[41] Yang, X., Stein, E.W., Ashkenazi, S., Wang, L.V. Nanoparticles for photoacoustic imaging. *Wiley Interdisciplinary Reviews Nanomedicine and Nanobiotechnology*, **2009**, 1(4), 360-368.

[42] Choi, Y., Kwak, J., Park, J.W. Nanotechnology for Early Cancer Detection. *Sensors*, **2010**, 10(1), 428-455.

[43] Pan, D., Pramanik, M., Senpan, A., Ghosh, S., Wickline, S.A., Wang, L.V., Lanza, G.M. Near infrared photoacoustic detection of sentinel lymph nodes with gold nanobeacons. *Biomaterials*, **2010**, 31(14), 4088-4093.

[44] Manohar, S., Ungureanu, C., Van Leeuwen, T.G. Gold nanorods as molecular contrast agents in photoacoustic imaging The promises and the caveats. *Contrast Media and Molecular Imaging*, **2011**, 6(5), 389-400.

[45] Nikoobakht, B., El-Sayed, M.A. Preparation and Growth Mechanism of Gold Nanorods NRs Using Seed - Mediated Growth Method. *Chemistry of Materials*, **2003**, 15(16), 1957-1962.

[46] Niidome, T., Yamagata, M., Okamoto, Y., Akiyama, Y., Takahashi, H., Kawano, T., Katayama, Y., Niidome, Y. PEG-modified gold nanorods with a stealth character for in vivo applications. *Journal of Controlled Release*, **2006**, 114(3), 343-347.

[47] Lao, Y., Xing, D., Yang, S., Xiang, L. Noninvasive photoacoustic imaging of the developing vasculature during early tumor growth. *Physics in medicine and biology*, **2008**, 53(15), 4203-4212.

[48] Laufer, J., Zhang, E., Beard, P. Evaluation of absorbing chromophores used in tissue phantoms for quantitative photoacoustic spectroscopy and imaging. *IEEE Journal on Selected Topics in Quantum Electronics*, **2010**, 16(3), 600-607.

[49] Takiguchi, H., Sato, K., Ishida, T., Abe, K., Yase, K., Tamada, K. Delicate surface reaction of dialkyl sulfide self-assembled monolayers on Au111. *Langmuir*, **2000**, 16(4), 1703-1710.

[50] Beulen, M.W.J., Huisman, B., van der Heijden, P.A., van Veggel, F.C.J.M., Simons, M.G., Biemond, E.M.E.F., de Lange, P.J., Reinhoudt, D.N. Evidence for Nondestructive Adsorption of Dialkyl Sulfides on Gold. *Langmuir*, **1996**, 12(10), 6170-6172.

[51] Parkes, L.M., Hodgson, R., Lu, L.T., Tung, L.D., Robinson, I., Fernig, D.G., Thanh, N.T.K. Cobalt nanoparticles as a novel magnetic resonance contrast agent-relaxivities at 1.5 and 3 Tesla. *Contrast media molecular imaging*, **2008**, 3(4), 150-156.

[52] Bouchard, L., Anwar, M.S., Liu, G.L., Hann, B., Xie, Z.H., Gray, J.W., Wang, X., Pines, A., Chen, F.F. Picomolar sensitivity MRI and photoacoustic imaging of cobalt nanoparticles. *Proceedings of the National Academy of Sciences of the United States of America*, **2009**, 106(11), 4085-4089.

[53] Lu, J., Yang, S., Ng, K.M., Su, C., Yeh, C., Wu, Y., Shieh, D. Solid-state synthesis of monocrystalline iron oxide nanoparticle based ferrofluid suitable for magnetic resonance imaging contrast application. *Nanotechnology*, **2006**, 17, 5812-5820.

[54] Linna, A., Oksa, P., Groundstroem, K., Halkosaari, M., Palmroos, P., Huikko, S., Uitti, J. Exposure to cobalt in the production of cobalt and cobalt compounds and its effect on the heart. *Occupational and environmental medicine*, **2004**, 61(11), 877-885.

[55] Monteiller, C., Tran, L., MacNee, W., Faux, S., Jones, A., Miller, B., Donaldson, K. The pro-inflammatory effects of low-toxicity low-solubility particles, nanoparticles and fine particles, on epithelial cells in vitro the role of surface area. *Occupational and Environmental Medicine*, **2007**, 64(9), 609-615.

[56] Horev-Azaria, L., Kirkpatrick, C.J., Korenstein, R., Marche, P.N., Maimon, O., Ponti, J., Romano, R., Rossi, F., Golla-Schindler, U., Sommer, D., Uboldi, C., Unger, R.E., Villiers, C. Predictive toxicology of cobalt nanoparticles and ions Comparative in vitro study of different cellular models using methods of knowledge discovery from data. *Toxicological Sciences*, **2011**, 122(2), 489-501.

[57] Chattopadhyay, S., Dash, S.K., Tripathy, S., Das, B., Mandal, D., Pramanik, P., Roy, S. Toxicity of cobalt oxide nanoparticles to normal cells An in vitro and in vivo study. *Chemico-Biological Interactions*, **2015**, 226(November), 58-71.

[58] Papageorgiou, I., Brown, C., Schins, R., Singh, S., Newson, R., Davis, S., Fisher, J., Ingham, E., Case, C.P. The effect of nano- and micron-sized particles of cobalt-chromium alloy on human fibroblasts in vitro. *Biomaterials*, **2007**, 28(19), 2946-2958.

[59] Ponti, J., Sabbioni, E., Munaro, B., Broggi, F., Marmorato, P., Franchini, F., Colognato, R., Rossi, F. Genotoxicity and morphological transformation induced by cobalt nanoparticles and cobalt chloride An in vitro study in Balb3T3 mouse fibroblasts. *Mutagenesis*, **2009**, 24(5), 439-445.

[60] Papis, E., Gornati, R., Prati, M., Ponti, J., Sabbioni, E., Bernardini, G. Gene expression in nanotoxicology research Analysis by differential display in BALB3T3 fibroblasts exposed to cobalt particles and ions. *Toxicology Letters*, **2007**, 170(3), 185-192.

[61] Peters, K., Unger, R.E., Kirkpatrick, C.J., Gatti, A.M., Monari, E. Effects of nano-scaled particles on endothelial cell function in vitro Studies on viability, proliferation and inflammation. *Journal of Materials Science Materials in Medicine*, **2004**, 15(4), 321-325.

[62] Larese Filon, F., Crosera, M., Timeus, E., Adami, G., Bovenzi, M., Ponti, J., Maina, G. Human skin penetration of cobalt nanoparticles through intact and damaged skin. *Toxicology in Vitro*, **2013**, 27(1), 121-127.

[63] Petrarca, C., Perrone, A., Verna, N., Verginelli, F., Ponti, J., Sabbioni, E., Di Giampaolo, L., Dadorante, V., Schiavone, C., Boscolo, P., Mariani Costantini, R., Di Gioacchino, M. Cobalt nanoparticles modulate cytokine in vitro release by human mononuclear cells mimicking autoimmune disease. *International journal of immunopathology and pharmacology*, **2006**, 19(4 Suppl), 11-14.

[64] Mo, Y., Zhu, X., Hu, X., Tollerud, D.J., Zhang, Q. Cytokine and NO release from peripheral blood neutrophils after exposure to metal nanoparticles in vitro and ex vivo studies. *Nanotoxicology*, **2008**, 2(2), 79-87.

[65] Colognato, R., Bonelli, A., Ponti, J., Farina, M., Bergamaschi, E., Sabbioni, E., Migliore, L. Comparative genotoxicity of cobalt nanoparticles and ions on human peripheral leukocytes in vitro. *Mutagenesis*, **2008**, 23(5), 377-382.

[66] Alexander, C.S. Cobalt-beer cardiomyopathy. A clinical and pathologic study of twenty-eight cases. *The American Journal of Medicine*, **1972**, 53(4), 395-417.

[67] Walker, S., Landovitz, R., Ding, W.D., Ellestad, G.A., Kahne, D. Cleavage behavior of calicheamicin gamma1 and calicheamicin T. *Proceedings of the National Academy of Sciences of the United States of America*, **1992**, 89(10), 4608-4612.

[68] Yoon, B., Lee, S., Kim, J. Recent conceptual and technological advances in polydiacetylene-based supramolecular chemosensors. *Chem. Soc. Rev*, **2009**, 38(7), 1958-1968.

[69] Lauher, J.W., Fowler, F.W., Goroff, N.S. Single-crystal-to-single-crystal topochemical polymerizations by design. *Accounts of Chemical Research*, **2008**, 41(9), 1215-1229.

[70] Reppy, M.A., Pindzola, B.A. Biosensing with polydiacetylene materials structures, optical properties and applications. *Chemical communications Cambridge, England*, **2007**, 4317-4338.

[71] Sun, X., Chen, T., Huang, S., Li, L., Peng, H. Chromatic polydiacetylene with novel sensitivity. *Chemical Society reviews*, **2010**, 39(11), 4244-4257.

[72] Chance, R.R., Muller, H., Eckhardt, C.J. Thermochromism in a polydiacetylene crystal. *The Journal of Chemical Physics*, **1977**, 67(8), 36163618.

[73] Ahn, D.J., Lee, S., Kim, J.M. Rational design of conjugated polymer supramolecules with tunable colorimetric responses. *Advanced Functional Materials*, **2009**, 19(10), 1483-1496.

[74] Seo, S., Lee, J., Choi, E.J., Kim, E.J., Song, J.Y., Kim, J. Polydiacetylene liposome microarray toward influenza A virus detection Effect of target size on turn-on signaling. *Macromolecular Rapid Communications*, **2013**, 34(9), 743-748.

[75] Chen, X., Li, L., Sun, X., Liu, Y., Luo, B., Wang, C., Bao, Y., Xu, H., Peng, H. Magnetochromatic Polydiacetylene by Incorporation of Fe3O4 Nanoparticles. *Angewandte Chemie International Edition*, **2011**, 50, 5486-5489.

[76] Cheng, Q., Stevens, R.C. Charge-Induced Chromatic Transition of Amino Acid-Derivatized Polydiacetylene Liposomes. *Langmuir*, **1998**, 14(8), 1974-1976.

[77] Peng, H., Sun, X., Cai, F., Chen, X., Zhu, Y., Liao, G., Chen, D., Li, Q., Lu, Y., Zhu, Y., Jia, Q. Electrochromatic carbon nanotubepolydiacetylene nanocomposite fibres. *Nature nanotechnology*, **2009**, 4(11), 738-741.

[78] Carpick, R.W., Sasaki, D.Y., Burns, A.R. First observation of mechanochromism at the nanometer scale. *Langmuir*, **2000**, 16(3), 1270-1278.

[79] Bloor, D. Dissolution and spectroscopic properties of the polydiacetylene poly10,12-docosadiyne-1,12-diol-bisethylurethane. *Macromolecular Chemistry and Physics*, **2001**, 202(8), 1410-1423.

[80] Wu, J., Zawistowski, A., Ehrmann, M., Yi, T., Schmuck, C. Peptide functionalized polydiacetylene liposomes Act as a fluorescent turn-on sensor for bacterial lipopolysaccharide. *Journal of the American Chemical Society*, **2011**, 133(25), 9720-9723.

[81] Lee, S., Cheng, H., Chi, M., Xu, Q., Chen, X., Eom, C.Y., James, T.D., Park, S., Yoon, J. Sensing and antibacterial activity of imidazolium-based conjugated polydiacetylenes. *Biosensors and Bioelectronics*, **2016**, 77, 1016-1019.

[82] Kim, J.M., Lee, J.S., Choi, H., Sohn, D., Ahn, D.J. Rational design and in-situ FTIR analyses of colorimetrically reversibe polydiacetylene supramolecules. *Macromolecules*, **2005**, 38(22), 9366-9376.

[83] Vinod, T.P., Chang, J.H., Kim, J., Rhee, S.W., Ji, H.C., Kim, J., Seog, W.R. Self-Assembly and Photopolymerization of Diacetylene Molecules on Surface of Magnetite Nanoparticles. *Bulletin of the Koren Chemical Society*, **2008**, 29(4), 799-804.

[84] Eglinton, G., Galbraith, A.R. Cyclic diynes. *Chemistry Industry London, United Kingdom*, **1956**, 737-738.

[85] Hay, A.S. Oxidative Coupling of Acetylenes. *Journal of Organic Chemistry*, **1960**, 296(25), 1275.

[86] Shi, W., Lei, A. 1,3-Diyne chemistry Synthesis and derivations. *Tetrahedron Letters*, **2014**, 55(17), 2763-2772.

[87] Marma, M.S., Khawli, L.A., Harutunian, V., Kashemirov, B.A., McKenna, C.E. Synthesis of alpha-fluorinated phosphonoacetate derivatives using electrophilic fluorine reagents Perchloryl fluoride versus 1-chloromethyl-4- fluoro-1,4-diazoniabicyclo2.2.2octane bistetrafluoroborate Selectfluortextregistered. *Journal of Fluorine Chemistry*, **2005**, 126(11-12), 1467-1475.

[88] Aliouane, N., Helesbeux, J., Douadi, T., Khan, M.a., Bouet, G., Chafaa, S., Duval, O. Synthesis of New Benzylic Di-, Tri-, and Tetraphosphonic Acids as Potential Chelating Agents. *Phosphorus, Sulfur, and Silicon and the Related Elements*, **2011**, 186(2), 354-364.

[89] De, M., Ghosh, P.S., Rotello, V.M. Applications of Nanoparticles in Biology. *Advanced Materials*, **2008**, 20, 4225-4241.

[90] van de Linde, S., Heilemann, M., Sauer, M. Live-cell super-resolution imaging with synthetic fluorophores. *Annual review of physical chemistry*, **2012**, 63, 519-540.

[91] Tsien, R.Y. The Green Fluorescent protein. *Annual review of Biochemistry*, **1998**, 67(11), 509-544.

[92] Birks, J.B. Photophysics of Aromatic Molecules. *John Wiley Sons Ltd*, **1970**.

[93] Zhelev, Z., Ohba, H., Bakalova, R. Single Quantum Dot Micells Coated with Silica Shell as Potentially Non Cytotoxic Fluorescent Cell Tracers.pdf. *J. Am. Chem. Soc*, **2006**, 128, 6324-6325.

[94] Borisov, S.M., Wolfbeis, O.S. Optical Biosensors. *Optical Biosensors*, **2008**, 108(2), 423-461.

[95] Ding, D., Li, K., Liu, B., Tang, B.Z. Bioprobes based on AIE fluorogens. *Accounts of Chemical Research*, **2013**, 46(11), 2441-2453.

[96] Luo, J., Xie, Z., Lam, J.W.Y., Cheng, L., Tang, B.Z., Chen, H., Qiu, C., Kwok, H.S., Zhan, X., Liu, Y., Zhu, D. Aggregation-induced emission of 1-methyl-1,2,3,4,5-pentaphenylsilole. *Chemical Communications*, **2001**, 381(18), 1740-1741.

[97] Tang, B., Zhan, X., Yu, G., Lee, P. Efficient blue emission from siloles. *Journal of Materials Chemistry*, **2001**, 11(12), 2974-2978.

[98] Liu, M., Zhang, X., Yang, B., Liu, L., Deng, F., Zhang, X., Wei, Y. Polylysine crosslinked AIE dye based fluorescent organic nanoparticles for biological imaging applications. *Macromolecular Bioscience*, **2014**, 14(9), 1260-1267.

[99] Wan, Q., Liu, M., Xu, D., Huang, H., Mao, L., Zeng, G., Deng, F., Zhang, X., Wei, Y. Facile fabrication of amphiphilic AIE active glucan via formation of dynamic bonds self assembly, stimuli responsiveness and biological imaging. *J. Mater. Chem. B*, **2016**, 4(22), 4033-4039.

[100] Jayaram, D.T., Ramos-Romero, S., Shankar, B.H., Garrido, C., Rubio, N., Sanchez-Cid, L., Gomez, S.B., Blanco, J., Ramaiah, D. In Vitro and in Vivo Demonstration of Photodynamic Activity and Cytoplasm Imaging through TPE Nanoparticles. *ACS Chemical Biology*, **2016**, 11(1), 104-112.

[101] Li, K., Liu, B. Polymer-encapsulated organic nanoparticles for fluorescence and photoacoustic imaging. *Chemical Society reviews*, **2014**, 43(18), 6570-97.

[102] Yuan, Y., Zhang, C.J., Liu, B. A Photoactivatable AIE Polymer for Light-Controlled Gene Delivery Concurrent EndoLysosomal Escape and DNA Unpacking. *Angewandte Chemie - International Edition*, **2015**, 54(39), 11419-11423.

[103] Hu, Q., Gao, M., Feng, G., Liu, B. Mitochondria-targeted cancer therapy using a light-up probe with aggregation-induced-emission characteristics. *Angewandte Chemie - International Edition*, **2014**, 53(51), 14225-14229.

[104] Seo, Y.H., Singh, A., Cho, H., Kim, Y., Heo, J., Lim, C., Park, S.Y., Jang, W., Kim, S. Rational design for enhancing inflammation-responsive in vivo chemiluminescence via nanophotonic energy relay to near-infrared AIE-active conjugated polymer. *Biomaterials*, **2016**, 84, 111-118.

[105] Hong, Y., Lam, J.W.Y., Tang, B.Z. Aggregation-induced emission phenomenon, mechanism and applications. *Chemical Communications*, **2009**, 4332.

[106] Wang, M., Zhang, G., Zhang, D., Zhu, D., Tang, B.Z. Fluorescent biochemosensors based on silole and tetraphenylethene luminogens with aggregation-induced emission feature. *Journal of Materials Chemistry*, **2010**, 20(10), 1858-1867.

[107] Zhang, X., Zhang, X., Tao, L., Chi, Z., Xu, J., Wei, Y. Aggregation induced emission-based fluorescent nanoparticles fabrication methodologies and biomedical applications. *Journal of Materials Chemistry B*, **2014**, 2(28), 4398-4414.

[108] Yuan, Y., Xu, S., Zhang, C., Liu, B. Light-responsive AIE nanoparticles with cytosolic drug release to overcome drug resistance in cancer cells. *Polym. Chem*, **2016**, 7(21), 3530-3539.

[109] Kwok, R.T.K., Leung, C.W.T., Lam, J.W.Y., Tang, B.Z. Biosensing by luminogens with aggregation-induced emission characteristics. *Chemical Society reviews*, **2015**, 44(13), 4228-4238.

[110] Wong, C., Stylianopoulos, T., Cui, J., Martin, J., Chauhan, V.P., Jiang, W., Popovic, Z., Jain, R.K., Bawendi, M.G., Fukumura, D. Multistage nanoparticle delivery system for deep penetration into tumor tissue. *Proceedings of the National Academy of Sciences of the United States of America*, **2011**, 108(6), 2426-2431.

[111] Xiang, K., He, L., Li, Y., Xu, C., Li, S. Dendritic AIE-active luminogens with a POSS core synthesis, characterization, and application as chemosensors. *RSC Advances*, **2015**, 5, 97224-97230.

[112] Liu, X., Zeng, Y., Liu, J., Li, P., Zhang, D., Zhang, X., Yu, T., Chen, J., Yang, G., Li, Y. Highly emissive nanoparticles based on AIE-active molecule and PAMAM dendritic molecular glue. *Langmuir*, **2015**, 31(15), 4386-4393.

[113] Arseneault, M., Leung, N.L.C., Fung, L.T., Hu, R., Morin, J., Tang, B.Z. Probing the dendritic architecture through AIE challenges and successes. *Polymer Chemistry*, **2014**, 5(20), 6087-6096.

Part III

Dendronized superparamagnetic probes as highly efficient cancer targeting tools

1 Generalities of iron oxide nanoparticles

In all biological applications, iron oxide nanoparticle (IONPs) colloidal stability is of utmost importance. It has been shown that the blood half–life, opsonization, biokinetics and biodistribution of IONPs is determined by both the surface chemical nature and the particle size.[1] There is a group of requirements that functionalized nanoparticles need to fulfill in order to have a practical use in the biomedical field:

- hydrophilicity and biocompatibility;
- furtivity;
- colloidal stability in water and protein–rich physiological media;
- hydrodynamic size < 100nm;
- multimodality.

Indeed, functionalized NPs are disposed to opsonization when entering the bloodstream, a non–specific adhesion of the plasma proteins (to form a protein corona) on the surface of NPs and ingestion by the macrophages. All the physicochemical parameters of the colloids affect their extravasation by influencing, among other things, their diffusivity, their permeability through the vascular wall, their drag coefficient in the fluid and their interactions in the tumor with the cells and the extracellular matrix.[2]To this end, NPs shape, structure, composition, synthesis method and coating play a crucial role in the nontoxicity, biocompatibility, stability, reticulo–endothelial system (RES) escape, internalization by cancer cells and relaxometric properties of IONPs.[3]

1.1 Synthesis

Iron oxide nanoparticles are synthesized through chemical path, which provides a simple, powerful and a non–expensive way to form colloidal suspensions with controlled shape, size and structure.[4] During last decades, numerous synthetic routes were developed to produce IONPs.[5,6,7,8] Their synthetic routes are rundown in the **Table10**.

Synthetic Methods	Synthesis comments	Reaction Tempera-ture	Reaction time	Solvent	Size Distribution	Shape control	Yield
Co– precipitation	Very simple	ambient conditions	20 – 90 Minutes	Water	Relatively narrow	Bad	High/ scalable
Thermal De-composition	Complicated	100 – 400	Minutes– Hours	Organic	Very narrow	Very good	High/ scalable
Microemulsion	Complicated	ambient conditions	20 – 50 Hours	Water/ Organic	Very narrow	Very good	High/ scalable
Hydrothermal synthesis	Simple, high pressure	130 – 250	Hours – Days	Water or/ and Organic	Relatively narrow	Good	Low
Polyol	Simple, high temperature and inert conditions	120 – 280	Minutes – Days	Polyol	Relatively broad	Good	High/ scalable
Sol– gel	Complicated, high temperature	200 – 400	Minutes – Days	Water or/and organic	Relatively broad	Good	Medium

Table 10: Summary of IONPs synthetic methods.

The co–precipitation method is the most efficient and simplest synthetic way to obtain magnetic nanoparticles. It is the cheapest and most environmentally friendly procedure. It consists of mixing ferric and ferrous salts in aqueous solution at low temperature and atmospheric pressure. The precipitation occurs after adding a base. The adjustment of pH, ratio between iron(II) and iron(III) concentrations, medium ionic strength, salt type, base nature and reaction temperature, allow a better control of final nanoparticles' characteristics (size, shape and composition).[9,10] The resulting nanoparticles present a broad size distribution, a medium level of crystallinity and not well controlled shape. After the synthesis, this method requires a size selection step to reduce the size standard deviation. Other methods, such as synthesis by microemultion[11], hydrothermal synthesis[12,13], polyol[14] method or sol–gel[15] have been developed and allow a better control of NPs size and morphology. Since 2000,[16,17,18] the synthesis by thermal decomposition is highly developed for production of magnetic nanoparticles with high level of monodispersity and size control. It consists in the decomposition of a metal complex in a high boiling point organic solvent in the presence of surface active agents, acting as stabilizers. This technique allows obtaining well crystallized NPs *in situ* functionalized with an organic hydrophobic layer ensuring their high colloidal stability in organic solvents.[19]

Begin–Colin and co–workers reported the production of monodisperse IONPs from thermal decomposition of Iron (II) stearate in the presence of Oleic acid in high boiling point solvents. They also focused on the relationship between synthesis parameters and nanoparticle properties in order to better understand and control the nanoparticle formation via this synthetic route.[20] Their results underlined that synthesis parameters affect the NPs nucleation and growth steps by modifying the stability of iron stearate on which depend the monomer formation and concentration. The monomer formation, which is reaction time and/or temperature dependent, is also found to vary as a function of the nature of solvents and ligands.

The exact mechanism of the formation of the uniform–sized nanocrystals has still not been clarified. However, the size control is steered by three different processes like: 1) nucleation, 2) growth and 3) Ostwald ripening. In particle synthesis, nucleation is considered as a first stage where the nuclei are formed from atoms assembling in a supersaturated solution and present a small size.[21] Generally, three kinds of nucleation processes are described: homogeneous, heterogeneous and secondary nucleation. The homogeneous nucleation occurs by the combination of solute molecules to produce nuclei in the absence of the solid interface. On the contrary, heterogeneous nucleation forms nucleus on a pre–existing surface of another material. An example of the heterogeneous nucleation is the nucleation of nanoparticles at the surface of carbon nanotubes.[22] The secondary nucleation can be defined as a phase that occurs at a pre–existing 'seed' of some materials, or by the particle aggregation. The growth is the deposition of the precursors at the surface of the pre–existing nuclei, inducing an increase of particle size. In practice, when the concentration of precursor species decreases below the minimum concentration for nucleation step, the primary species keep growing until the equilibrium

concentration of nuclei. Ostwald ripening (also referred to as coarsening) is a phase in which the large particles increase their sizes at the expense of the smaller nanoparticles.[23] The simplified explanation would be that the particle relative size (r) solely depends on the average size of the particles ($\bar{r}$) **(Fig.74)**. Therefore, if the radius is inferior to the average radius, a decrease of the particle size is observed, indicating the dissolving process of the particles. On the contrary, when the radius is larger than the average size, the particles keep on growing until a value limited by the double of the average radius.

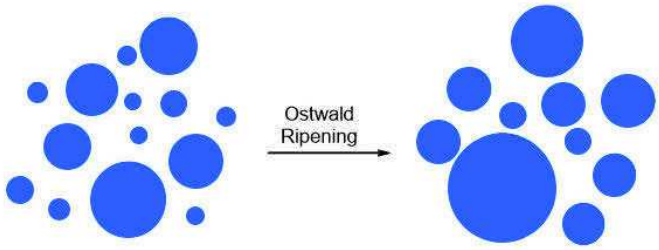

Figure 74: Illustration of Ostwald ripening.

The most famous theory for the understanding of the nanoparticle formation in numerous nanosystems was described by LaMer and co–workers.[24] As shown in **Fig.75**, the concentration of solute molecules increases in the pre–nucleation stage (step I) from the decomposition of the iron precursors. However, below minimum concentrations (C_{min}) (commonly called critical concentration), the precipitation of solute molecules does not occur and thus nucleation is not observed due to the high energy barrier of nucleation and the unfavorable condition of supersaturation.

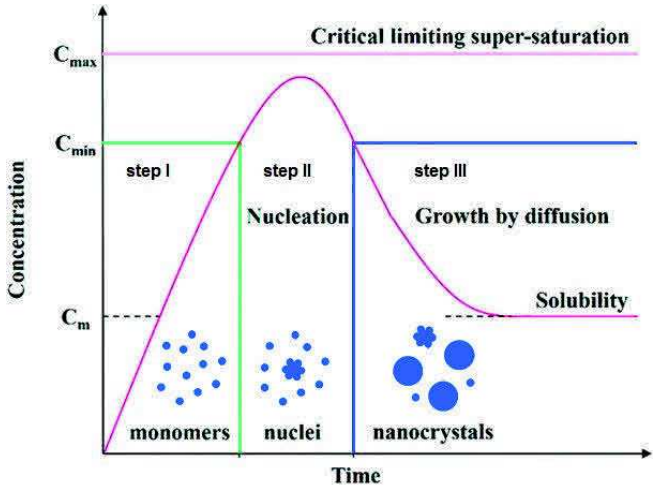

Figure 75: LaMer mechanism of nucleation and growth phases as a function of reaction time and iron precursor concentration.[24]

Nevertheless, the solute molecule concentration accumulates until C_{min} at which the initial nucleation

takes place (step II). During this period, the concentration increases until a maximum and then gradually decreases as the solute molecules gather together to form nuclei. This stage is irreversible and corresponds to the nucleation period in which the previous step has a favorable supersaturation condition. Below the minimal concentration (step III), the pre–formed nuclei continue to grow. Finally, the growing stop stage occurs when the concentration is lower than the solubility level for the bulk solid.

In this process, most of the nuclei are formed and then grow to give the final nanoparticles without additional nuclei formation. The separation between nucleation and growth is at the origin of the ability to control size distribution of the nanomaterial suspension. The LaMer theory is often used in the case of IONPs.

Colloidal stability A colloidal dispersion is a suspension of small solid pieces (size range from 1nm to 1µm) in solution. A dispersion of solid particles is defined as a stable colloidal suspension when particles do not aggregate in time. Due to their high surface volume ratio, uncoated nanoparticles tend to aggregate in order to minimize the interfacial energy. Moreover, under the action of a magnetic field, magnetic cores also aggregate due to interactions between their magnetic dipoles. The stability of nanoparticle suspensions results from two opposite forces: attractive and repulsive forces defined in the theory developed by Derjaguin, Landau, Verwey and Overbeek, kown as the DLVO theory.[25,26] It describes the concept of nanoparticle stability and the way to avoid agglomeration. DLVO theory is a kinetic and microscopic approach related to the interaction potential between two particles **(Fig.76)**.

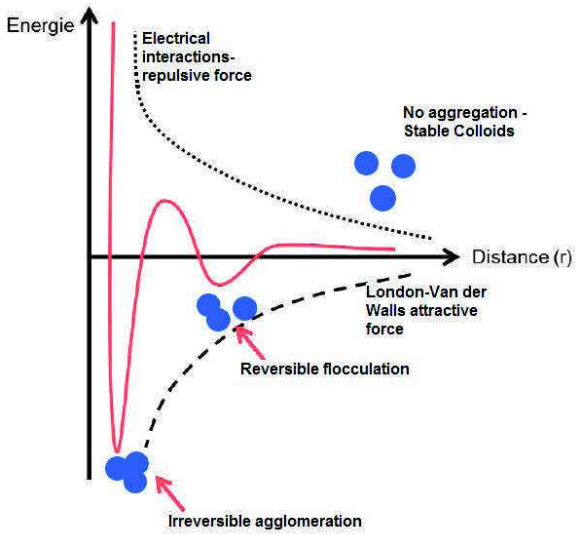

Figure 76: Schematic representation of the potential energy evolution with the inter–particles distance.

The attractive forces are essentially due to London–van der Walls forces based on dielectric or magnetic

interactions between dipoles. These interactions depend on the material nature and the distance between two particles. Consequently, at a short inter–particles distance, the attractive forces predominate and thus induce an irreversible agglomeration. The repulsive forces are due to the presence of charges on the nanoparticle surface which induce electrical interactions. The repulsive energy exponentially decreases as a function of the distance between two particles. As a result, the colloidal dispersion is mainly induced by the presence of charges on the nanoparticle surface.

To keep the stability of a colloidal system, repulsive (steric or electrostatic) forces should be dominant, because if a repulsion mechanism does not exist, flocculation or coagulation will appear. In order to describe different stabilization methods, it is first important to define the IONPs surface nature. For all oxides, the surface is covered by hydroxyl groups due to the water chemisorption **(Fig.77.a)**: the epoxy groups on the metal (here iron) surface react with water molecules to form hydroxyl groups.

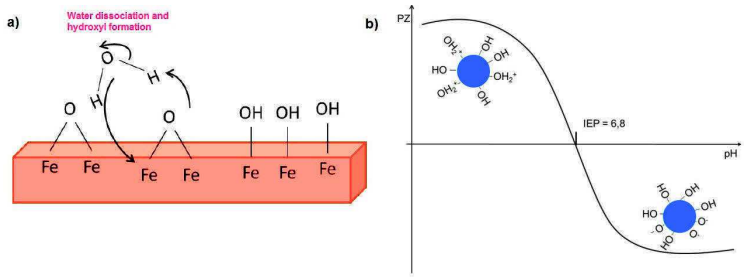

Figure 77: a) Schematic representation of hydroxyl formation on iron oxide surface; b) Surface charge and Zeta Potential evolution according to the pH.

A part of hydroxyl groups exhibit amphoteric properties meaning that their charge can be modified by pH modulation. Thus, the surface of iron oxide can be positively or negatively charged, depending on the pH of the solution **(Fig.77.b)**. The isoelectric point (IEP) corresponds to the pH value when the nanoparticle carriers have no net electrical charge. For magnetite the IEP is around 6.8.[27] Below IEP, hydroxyl sites are protonated to form Fe–OH^{2+} species. Above IEP, the hydroxyl functions are deprotonated and lead to negative species Fe–O^-. The magnitude of zeta potential (ZP) gives an indication of the stability of nanoparticle colloids. In the case of high ZP values (either negative or positive) IONPs suspension are considered stable (electrostatic interactions). On the contrary, when low ZP values are observed, flocculation generally occurs in solution.

IONPs' IEP is exactly in the pH range of physiological media. Therefore, for biomedical applications, IONPs have to be functionalized with molecules ensuring steric or/and electrostatic stabilization. The electrostatic stabilization is an effective way to disperse particles in aqueous media. The major disadvantage of charge stabilization is its high sensitivity towards the dispersion media ionic strength: indeed, when the ionic strength is high, the electrostatic repulsions are insufficient to counterbalance the attractive forces and

consequently lead to the nanoparticle aggregation. Steric stabilization can be achieved by attaching (covalently or by chemisorption) molecules to the particle surface. Such coating avoids direct contact between nanoparticles creating a strong steric repulsion among nanoparticles, leading to stable colloidal suspensions.

The current trend is to graft molecules allowing both electrostatic and steric stabilizations. These molecules are large enough to induce steric repulsions and are charged , thus leading to electrostatic repulsion, hence the name *electrosteric* stabilization. Recently, small dendrons displaying peripheral charges have been shown to induce such *electrosteric* stabilization.[28] For oxides coating, various grafting procedures have been described involving bonding through different types of anchoring groups **(Fig.78)** such as Catechol[29], Carboxylate[30] or stronger anchoring groups such as Silane[31] or Phosphonates[32].

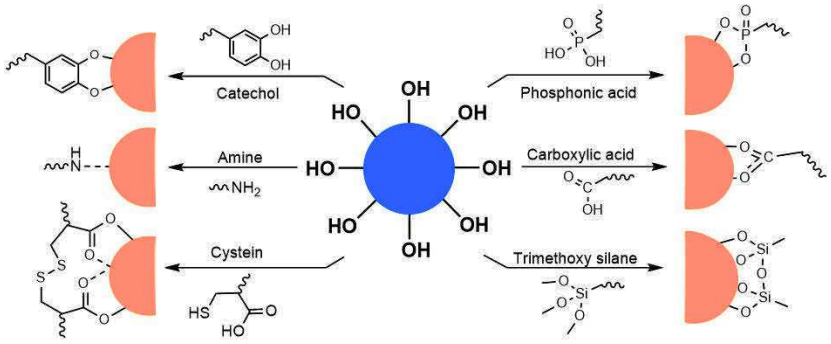

Figure 78: Possible surface complexes of iron oxide nanoparticles according to the coupling agent.

1.2 Physical properties and characterization

Crystal structure The majority of studied IONPs are composed of Magnetite (Fe_3O_4) ans its oxidized form Maghemite (γ–Fe_2O_3). Both oxides abide by an inverse spinel structure with AB_2X_4 as general formula, in which A and B stay for cations and X for anions.[33]

The crystalline structure of Magnetite is composed of 32 O^{2-} anions arranged in a face–centered cubic structure, and contains both divalent and trivalent cations. Considering one Magnetite unit cell containing 32 oxygens, 64 tetrahedral (A sites) and 32 octahedral (B sites) sites are generated, among which 8 divalent atoms and 8 trivalent atoms of iron fill the octahedral sites and 8 trivalent iron ions fill the tetrahedral sites.[34] The composition of a Magnetite unit cell is written down as $[Fe^{3+}]_{\text{tetrahedral}}[Fe^{3+}Fe^{2+}]_{\text{octahedral}}O_4$ or $FeO.Fe_2O_3$.

The inverse spinel structure of one Magnetite unit of contains 56 atoms among which 32 oxygen ions, 16 iron(III) ions and 8 iron(II) ions **(Fig.79)**. Thus, the quarter of a unit cell is filled with a divalent and a trivalent iron ion.

On the other hand, Maghemite is exclusively composed of iron(III) ions. The oxidation of iron(II) to

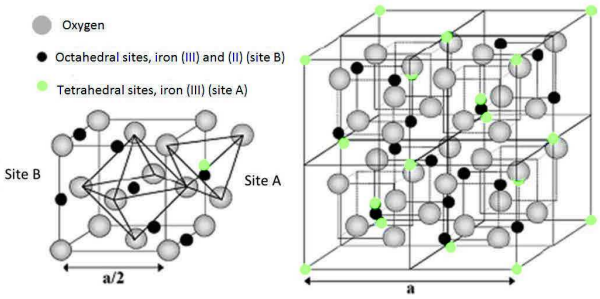

Figure 79: Schematic representation of inverse spinel structure of magnetite, were 8 octahedral sites are surrounded by 6 oxygen ions and 16 tetrahedral sites are surrounded by 4 oxygen ions.

iron(III) increases the development of vacancies ($\square$) in the octahedral sites. One iron ion among nine is replaced by a vacancy. The composition of a Maghemite unit cell is written down as $[Fe^{3+}]_{\text{tetrahedral}}$ $[Fe^{3+}{}_{2/3}\square_{1/3}]_{\text{octahedral}}$ O_4.[18]

The structure and magnetic properties of IONPs synthesized by thermal decomposition have been studied by various techniques (XRD, FTIR, Mössbauer spectroscopy, etc.). The results showed that the composition of NPs evolves from Maghemite for small sizes (typically $<$ 8nm) up to a core of Magnetite surrounded by an oxidized shell (typically $>$ 12nm).[35,36,37] For intermediate sizes (8–12nm), the composition is found to be intermediate between those of Magnetite and Maghemite without a clear core–shell structure and with the occurrence of a perturbed oxidized state with defects.[20]

Magnetic properties of superparamagnetic nanoparticles The magnetism of Magnetite is a result of the antiparellel coupling of the unpaired 3d electrons of iron ions located in tetrahedral and octahedral sites of the face–centered cubic lattice. A Ferrimagnetic behavior is defined by the non–compensation of spins' magnetic moments at low temperatures. Moreover, a critical temperature at which paramagnetic state transitions to superparamagnetic behavior is called the Curie temperature. In the case of Magnetite the Curie temperature is 580˚C.

In bulk, Magnetite magnetic domains are divided in Weiss domains[38] separated by Bloch walls[39]. Inside each domain, magnetic moments possess a uniform direction, while at the same time the surrounding magnetic domains exhibit different directions of magnetic moments **(Fig.80)**.

When an external field (H) is applied, Bloch walls move and induce an increase in magnetic domains oriented in the same direction as H. A high magnetic field is required to remove completely Bloch walls. This phenomenon is at the origin of the remanent magnetization (M_r) and the hysteresis observed[40,41] during the measurement of magnetic moments as a function of applied magnetic field **(Fig.81)**.

When an external field is applied, Bloch walls move and the magnetic moment increases **(a)** until reaching

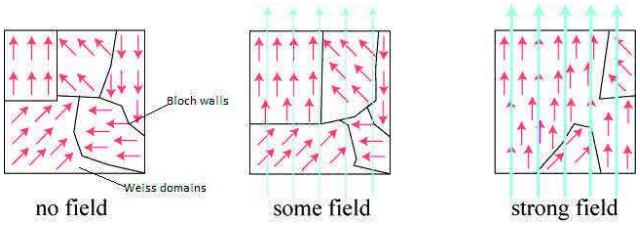

Figure 80: Organization of magnetic domains for ferromagnetic materials and their arrangement as a function of applied magnetic field (blue arrows).

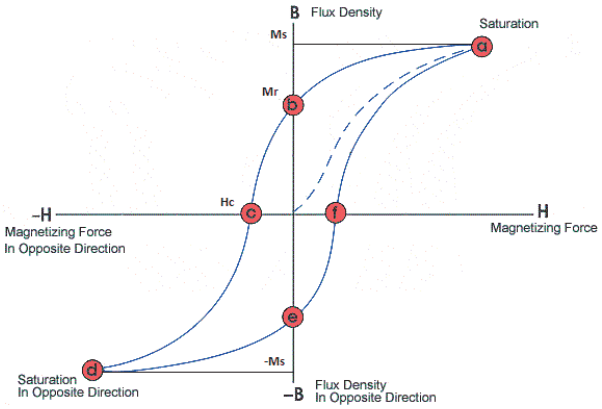

Figure 81: Hysteresis curve of a ferromagnetic compound with the representation of the saturation magnetization (M_s), the coercive field (H_c) and the remanent magnetization (M_r).

the saturation magnetization (M_s) corresponding to the state at which all the magnetic moments are aligned with the external magnetic field. At zero magnetic field **(b)**, the magnetic moment is equal to the remanent magnetization (M_r). M_s is a fundamental characteristic of ferromagnetic materials, due to the presence of domains within the structure.[42] Material is demagnetized **(c)** by applying an apposite magnetic field called coercive field (H_c). Increasing the external magnetic field in opposite direction **(d)**, the magnetic moment decreases to a minimum value ($-M_s$). The final curve **(e,f)** describes H increase in order to reach zero magnetization **(f)**. The hysteresis cycle is an important characteristic of ferromagnetic compounds. Both remanent magnetization (M_r) and coercive field (H_c) depend on the nature and the size of the material, whereas the saturation magnetization does not depend on the material size but only on the chemical composition.

If the material size is small enough (less than a Weiss domain of the corresponding bulk material) to form a single crystal domain, where all of the spins are aligned in the same direction, H_c will become equal to zero and the remanent magnetization will disappear. This phenomenon is called *Superparamagnetism*.

The magnetization curve of superparamagnetic compounds is not defined by a hysteresis as for ferromagnetic materials. The curve is reversible with no remanence and no coercive field **(Fig.82)**.

The size and the saturation magnetization of superparamagnetic particles can be determined from the

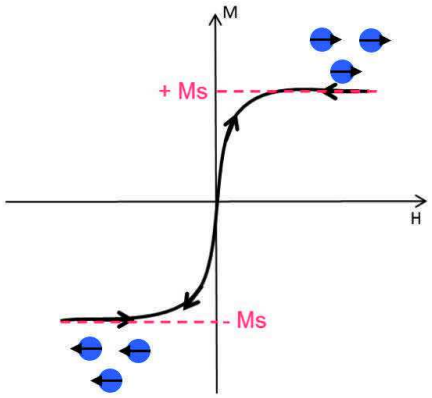

Figure 82: Magnetization curve of superparamagnetic materials.

measurements of magnetization curve, assuming that all particles exhibit the same volume and that the saturation magnetization is an average value.[43,44]

Relaxometric properties For superparamagnetic particles, the direction of the magnetization vector is aligned on a preferred position called *easy direction magnetization* or *anisotropy axis*. The anisotropy energy is defined as the energy required to move the magnetization vector between two positions of easy magnetization axis.[45] A changeover of magnetic moment vector from an axis to another is observed when thermal energy is high enough to break the anisotropy energy barrier. The average time to switch from one direction to another is called "Néel relaxation time" (τ_N) and depends on the temperature and the crystal volume.

Superparamagnetic crystals which are dispersed in a liquid medium to form a colloidal suspension, see their magnetic moment defined by two different processes: the Néel and the Brownian relaxations **(Fig.83)**.[46]

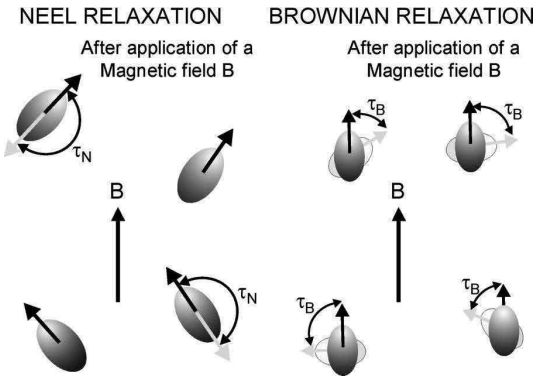

Figure 83: Illustration of Néel and Brownian relaxation processes observed for superparamagnetic materials. [46]

For large crystals, Néel relaxation time becomes longer and any changeover of observed magnetization is due to the blockage of magnetic moments on easy axis. The crystal blocking volume, defined as critical

volume, leads to the magnetization lock during the measurement at a given temperature. Therefore, only the total rotation of particles, submitted to the thermal agitation, is considered. The characteristic time of the rotation is defined as Brownian relaxation time (τ_B).

In summary, the global magnetic relaxation time rate of colloidal suspensions is regulated by Néel and Brownian relaxation times. The Néel relaxation thus governs small crystals, whereas the relaxation time of large crystals is almost exclusively dominated by Brownian contribution.

The concept of relaxation times for MRI contrast agents The high magnetization of superparamagnetic nanoparticles exhibits a great influence on the surrounding water protons relaxation rate. The understanding of the superparamagnetic relaxation phenomena is linked to the theory established by Roch–Muller–Gillis (commonly called RMG model).[47,48,45] The relaxation induced by superparamagnetic nanoparticles is due to the coupling between the magnetic moments of water protons and the electron magnetic moments of the nanoparticles. Its modulation is caused by Néel relaxation (flip of the magnetization vector of particles from an easy axis to another), by the diffusion of water protons and the strength of the external magnetic field.[49]

The relaxation time exploited in MRI are the water proton nuclear relaxation influenced by the presence of superparamagnetic compounds. The parameters that define the efficiency of a compound as an MRI contrast agent are the longitudinal (r_1) and transversal (r_2) relaxivities. These proton relaxivities give the efficiency of magnetic nanoparticles to increase the longitudinal (R_1) or transversal (R_2) relaxation rate of water protons induced by one millimolar of iron **(Eq.1)**:

$$R_i^{obs} = \frac{1}{T_i^{obs}} = \frac{1}{T_i^{dia}} + r_i \cdot C \ (i = 1 \, or \, 2) \tag{1}$$

Where R_i^{obs} is the global relaxation rate of the system (s^{-1}), T_i^{obs} is the global relaxation time of the system, T_i^{dia} is the relaxation time of the system before the addition of the contrast agent (s), C is the iron concentration of the superparamagnetic compound ($mmol^{-1}.L^{-1}$) and r_i is the relaxivity.

The relaxometric properties are inferred from the measurements of longitudinal (T_1) and transversal (T_2) relaxation times. The evolution of relaxivity as a function of external magnetic field is studied by Nuclear Magnetic Resonance Dispersion (NMRD) profiles.

Characterization techniques NMRD profiles are essential tool to evaluate the relaxometric properties of MRI contrast agent's as a function of magnetic field. The method allows a rapid analysis of new contrast agent properties and results can be exploited to control the reproducibility of nanoparticle synthetic protocol. The fitting of NMRD profiles with suitable theoretical models provide information on average radius of magnetic crystals, their saturation magnetization, their anisotropy energy and their Néel relaxation time. It

is important to notice that the RMG model is based on the assumption that nanoparticle size is homogeneous, and consequently, all theoretical parameters extracted from the fitting curves are average values.

Although NMRD measurements give a good description of magnetic compounds, other techniques are used to complete their characterization **(Table 11)** such as the hydrodynamic and core size, their colloidal stability, the surface and structure analysis.

Different methods can be used to determine nanoparticle characteristics. The size of the particle core can be determined by TEM images.[50,51] This technique reports the total particle size of the core (crystalline and amorphous parts). Furthermore, it provides details on the size distribution and the shape. XRD can be performed to obtain the crystalline structure of the particles. In a diffraction pattern, the intensity can be used to quantify the proportion of iron oxide formed in a mixture by comparing experimental peak and reference peak intensities.[52] The crystal size can be calculated also from the line broadening from the XRD pattern using the Scherrer formula.[53,54,55] Dynamic light scattering (DLS) is a common technique to obtain the hydrodynamic sphere of nanoparticles. Additionally, magnetometry and relaxivity profiles recorded over a wide range of magnetic fields can be used to determine the mean crystal size, among numerous other parameters. Other physicochemical techniques, such as Atomic and Chemical Force Microscopies (AFM and CFM), Thermogravimetric Analysis (TGA), Differential Scanning Calorimetry (DSC), X–ray Photoelectron Spectroscopy (XPS), Thermally Programmed Desorption, Infrared Spectroscopy (IR), Fourier Transform Infrared Spectroscopy (FTIR), Secondary Ion Mass Spectra (SSIMS and TOF–SIMS), conductimetry, potentiometry, and solid–state NMR, have been used to investigate the surface properties of coated IONPs.[56] It is worth noting that some of these techniques are used to describe the nature and strength of the bonding between the iron oxide surface and the coating, while others are used to understand the coating' influence on the NPs' magnetic properties.

2 Dendronized iron oxide nanoparticles

Lately, there has been a steady increase in the number of IONPs–based therapeutics approved by the FDA (US Food and Drug Administration). *Advanced Magnetic's Gastromark* was the first product based on IONPs which was approved in 1993 in Europe and in 1996 in the United States. The other IONPs–based MRI CAs were: 1) Resovist® approved in 2000 for liver imaging on European market (has been taken off the market because of lack of sales in November 2008 [57]).[58]; 2) Sinerem®, brand name (same as Combidex®) for an ultrasmall superparamagnetic iron oxide (USPIO) to detect metastatic disease in lymph nodes. Feraheme® (Ferumoxytol) was approved in 2009 and used to treat iron–deficiency anemia in adults with chronic kidney disease, and in 2015 FDA ordered stricter warnings and contraindications, stating that there have been 79

Method	Characteristics
Dynamic light scattering (DLS)	• determination of hydrodynamic diameter. • evaluation of aggregate formation before and after nanoparticle functionalization.
Zeta potential	• evaluation of charges present on the nanoparticle surface. • determination of the pH range for colloidal stability of suspensions. • determination of isoelectric point before and after surface functionalization.
Fourier transform infrared spectroscopy (FTIR)	• determination of atomic bonds on the nanoparticle surface. • observation of Fe–O bonds of in both magnetite and maghemite.
Transmission electron microscopy (TEM)	• two dimensional images of nanoparticles. • determination of size and size distribution of the magnetic core. • evaluation of aggregates formation.
Superconducting quantum interference device (SQUID)	• evaluation of NPs' magnetic behavior. • determination of magnetometric radius and saturation magnetization. • determination of Curie temperature.
NMRD profiles measured by fast field cycling relaxometer	• evaluation of longitudinal relaxivities as a function of external magnetic field. • determination of relaxometric radius, saturation magnetization and Néel relaxation time.
Measurements of relaxation times (T_1 and T_2) at 20 and 60MHz	• determination of longitudinal and transversal relaxivities. • efficiency evaluation as MRI contrast agent. • determination of iron(III) concentration (no distinction between several magnetic ions).
X–ray diffraction (XRD)	• analysis of crystalline phase of nanoparticles. • size determination of crystalline domain.
Thermogravimetry analysis (TGA)	• evaluation of the coating weight %. • coarse estimation of nanoparticle grafting rate.
High–resolution magic angle spinning (HR–MAS)	• determination of the coating chemical structure. • rough estimation of grafting rate.
Atomic absorption spectroscopy (AAS)	• determination of iron(III) concentration (distinction between a mix of different elements in the same sample).

Table 11: Characterization techniques used to define iron oxide nanoparticles' properties.

anaphylactic reactions resulting in 18 deaths since the drug approval.key "Ault2015,U.S.FoodandDrug2015"

Although progress in the application of nanotechnology has been dramatic and successful, substantial opportunities exist for the development of future generation nanotherapeutics by improving upon certain recognized nanoparticle limitations associated with the present prototypes.[59] Efforts are focused on creating more complex platforms that integrate real–time diagnostic, imaging, targeting and therapy delivery features. Currently a number of IONPs–based therapeutics are engaged in pre–clinical and clinical studies **(Table 12)**.

	Technique	**Therapeutic agent**	**Disease state**	**Target**	**Reference**
Pre – Clinical	MRI	Anti – EGFR IgG	Brain Cancer	EGFR	Mao *et al.*[60]
	Ultrasound, MRI	Paclitaxel	Many	FA	Zink *et al.*[61]
	MRI	antisense *survivin* oligonucleotides (asODN)	Many	EPR	Pan *et al.*[62]
	MRI	Doxorubicin	Many	FA	Chang *et al.*[63]
Clinical Trials	MRI	Injected cell	Healthy volunteers	None	Univ.of Edinburgh (NCT00972946)
	MRI	Feraheme	Pancreatic Cancer	EPR	Massachusetts General Hospital (NCT00920023)
	MRI	Feraheme	Cancer of lymph node	EPR	M.D. Anderson Cancer Center (NCT01815333)
	MRI	Feraheme	Myocardial infarction, inflammation	N/A	Univ. of Edinburgh (NCT01995799)
	MRI / Radio therapy	Heat	Glioblastoma multiform	EPR	MagForce AG[64]
	MRI / Ultrasound	Doxorubicin/ Paclitaxel	Many	$\alpha_v\beta_3$ Integrin	Kereos, Inc [65,66,67,68]

Table 12: Examples of nanomedicine recent clinical activities involving various IONPs–based therapeutics.

A dendritic approach as a coating strategy for the design of functional nanoparticles is particularly interesting in the field of cancer diagnostics. In addition to a controlled multifunctionalization, dendrimers and dendron units allow a versatility of size (according to the generation) and of physicochemical properties (hydrophilicity and hydrophobicity) which can be precisely tuned. The resulting effects on stability (dendrimer effect), pharmacokinetics and biodistribution can then clearly be identified. There is no doubt that dendrimer–based organic/inorganic hybrids represent highly advanced pharmaceutical tools, able to target a specific type of cell or organ, be tracked while doing it and deliver a specific drug *in situ*.

M. Textor *et al.* have recently compared IONPs colloidal stability functionalized with linear or dendritic PEG chains of various molecular weight.[69] They demonstrated the reversible aggregation of NPs functionalized with dendrons at increased temperature, while NPs functionalized with linear molecules aggregate and sediment irreversibly. The influence of the dendron generation has been the subject of several articles. In particular, C. Duanmu and co–workers showed the influence of the dendron generation on MRI properties of IONPs: r_2 increases as NPs are functionalized with higher generation dendrons.[70] Additionally, Walter et al. have shown that the relaxivity depends on the nature of the surface coating, thus evidencing that the water diffusion and circulation is much easier through the dendritic PEGylated shell in comparison with its linear counterpart.[71]

In this chapter I will present the synthesis of spherical 10nm IONPs by thermal decomposition in the presence of surface active agents acting as stabilizers and offering a good colloidal stability in non–polar organic solvents. IONPs hydrophilicity and suitability for biomedical applications is provided by their functionalization with two types of dendrons: ii) 1P_G_1PEG_COOH and ii) 2P_G_1PEG_COOH – fully oligoethyleneglycol dendrons displaying either one (1P) or two (2P) phosphonic acids at their focal point and a long functional octaethyleneglycol chain in *para*–position bearing a carboxylate end–group. Subsequently, the resulting dendronized IONPs will be characterized, their physico–chemical and biodistribution properties discussed and compared as a function of the coating.

2.1 Synthesis and characterization

Employed IONPs have been synthesized by thermal decomposition. This technique consists in iron salt decomposition in a high boiling temperature solvent in the presence of surfactants. In order to obtain nanoparticles with a homogeneous size and form, it is important to control temperature, times of nucleation and growth steps. For this purpose, a specific device was developed within Pr. S. Begin–Colin team for a proper control of the system temperature during the synthesis. Two different thermocouples are placed within the solution and outside the round–bottom flask, and all the temperature gradient parameters are software–operated **(Fig.84)**. The software–operated control system allows for tight temperature, speed and time regulations of all synthesis steps (decomposition, germination and growth). All procedure conditions allowing spherical 10nm IONPs (NPs10) synthesis have been well established within Pr. S. Begin–Colin team.

Procedure for NPs10 synthesis: 1.38g (2.22mmol) of Fe(stearate)$_2$ and 1.25g (4.44mmol) of Oleic acid (OA) were added to 20mL of Dioctyl ether (b.p. 287°C). Subsequent to 30 seconds of sonication, reaction mixture was kept at 110°C, without the condenser, for one hour, in order to ensure reactants decomposition.

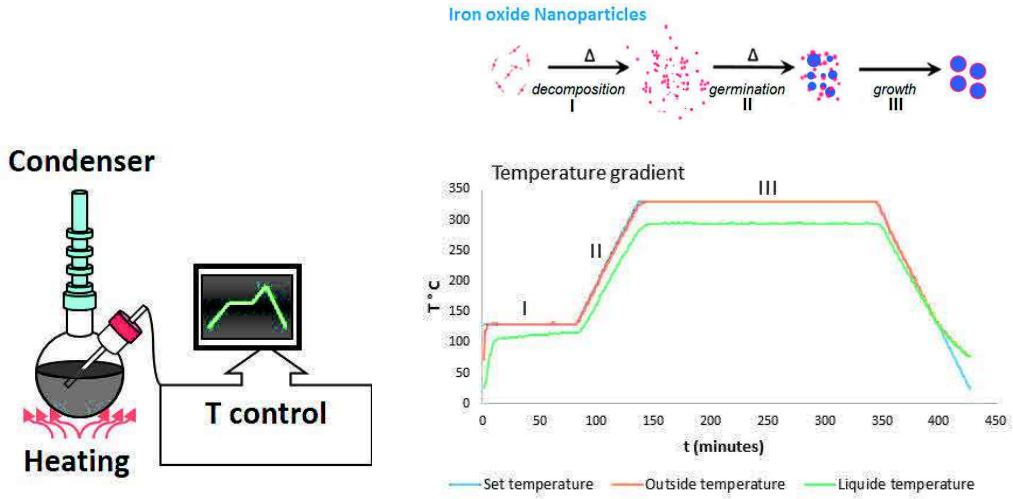

Figure 84: Schematic representation of IONPs synthesis device by thermal decomposition (left) and temperature gradient as a function of decomposition, germination and growth steps (right).

After placing the condenser on the round–bottom flask, the solution was heated up to 300 °C with a heating rate of 5°C/minute and was refluxed for 120min under air. The reaction mixture was then cooled down to room temperature.

At the end of the synthesis, a viscous black liquid characteristic of NPs formation was obtained. This liquid contains NPs10, undecomposed Iron Stearate and the excess of OA. NPs10 were then purified and separated from reactants and by–products using a series of precipitation/redispersing (washes) in a mixture of good/bad solvents.

At first, NPs10 were precipitated by adding Acetone (bad solvent 3/4 v/v) to the reaction mixture followed by centrifugation at 10,000 rpm for 10min. Subsequently, the supernatant was removed and the sediment was dispersed in Cyclohexane (good solvent 1/4 v/v) to which was added Acetone (bad solvent 3/4 v/v) and the mixture was centrifuged at 10,000 rpm for 10min. NPs10 purification was FTIR monitored.

The FTIR profiles of NPs10 washed 3 and 6 times are represented in **Fig.85** and display three distinct zones: the bands between 3000 and 2800cm^{-1} which are attributed to alkyl chains of OA, those between 1800 and 900cm $^{-1}$ to the asymmetric and symmetric COO $^{-}$ bands of Oleate and those between 800 and 500cm $^{-1}$ to Fe–O bands of iron oxide.

The narrow band between 1800 and 1700cm^{-1} correspond to the vibration of COO $^{-}$ double bond of free OA molecules in the suspension of NPs10. Furthermore, the bands located at 1660 and 1390cm $^{-1}$ are characteristic of asymmetric and symmetric vibrations of OA grafted to IONPs surface via carboxylate function. The band at 719 cm^{-1} is characteristic of the presence of Iron Stearate and IONPs magnetite phase displays one Fe–O characteristic band at around 570cm^{-1}.

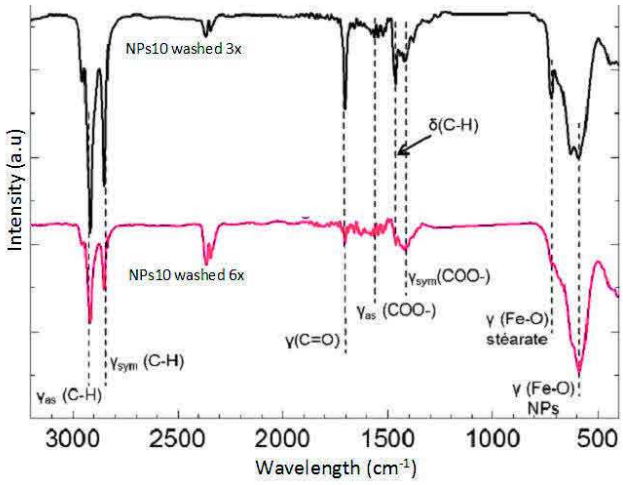

Figure 85: FTIR profiles of NPs10 washed 3 and 6 times by precipitation/redispersing technique.

The purification efficiency of IONPs by centrifugation is determined evaluating the intensity ratios between bonded and free OA, and between Fe–O bond relative to Iron stearate and NPs10. The intensity ratio of C–H and Fe–O bonds decreases with the number of washes, indicating elimination of residual organic molecules (Stearate and OA). Similarly, the peaks corresponding to COO^- bond of free OA and Fe–O of Iron Stearate decrease with the number of washes. NPs10 are considered as *"washed"* when Iron stearate band disappears, and the band intensity of the C=O double bond is low. Purification process is tricky due to the equilibrium between bonded and free OA in the solution. If NPs10 are too *"washed"*, OA tend to maintain the equilibrium and desorb from IONPs surface, leading to aggregation. Following the previous purification process, it results to a just sufficient amount of OA on the surface of NPs, which is very important for further functionalization with dendrons.

The sized distribution of NPs10 stabilized with OA (NPs10@OA) has been determined by TEM and DLS analysis **(Fig.86)**. NPs10@OA demonstrate a spherical morphology with an average size of 10nm with a narrow size distribution ($< 9\%$) and a low polydispersity index (PDI) equal to 0.98nm. On the high resolution TEM image **(Fig.86.middle)** crystallographic planes are continuous for overall nanoparticles, showing a single crystalline domain in accordance with what has been achieved within our group. NPs10@OA hydrodynamic diameter was evaluated by DLS measurements and compared to TEM size distribution **(Fig.86.right)**. DLS data show the presence of a unique size population with an average hydrodynamic diameter of 12nm and a PDI = 0.043. TEM and DLS size distributions are unimodal, indicating a monodisperse colloidal system.

NPs10@OA magnetic and relaxometric properties were further characterized by SQUID magnetometry and NMRD profiles.

Magnetization curve of NPs10@OA measured at 4K (–269.15°C) presents a loop, representative of spin

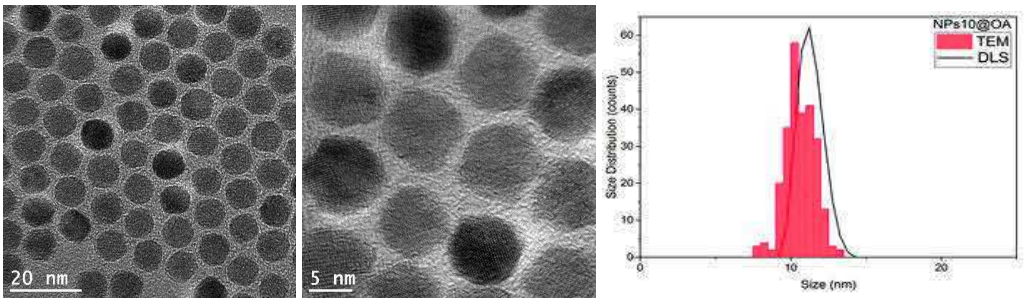

Figure 86: TEM images of NS10@AO at 20nm zoom (left) and at high resolution (middle); DLS and TEM size distribution of NPs10@OA (right).

blocking at low temperatures, thus a ferrimagnetic behavior **(Fig.87.left)**. Obtained saturation magnetization of M_s= 65A.m^2.Kg^{-1} confirms a high crystalline order in synthesized IONPs, and low coercivity value of the sample Hc = 0.03T leans toward the idea that NPs10@OA present weak particles interactions, little spin canting and surface anisotropy.

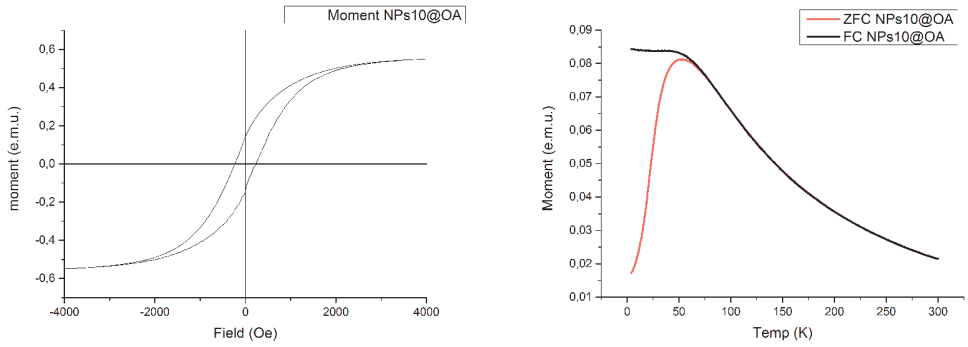

Figure 87: Hysteresis loop recorded at 4K (left) and temperature dependence of ZFC and FC magnetization (right) for NPs10@OA sample.

Representative Zero Field Cooled (ZFC) and Field Cooled (FC) of *superparamagnetic* behavior **(Fig.87.right)**: ZFC curve exhibits a peak at 51K, indicating a transition from magnetically blocked state (low temperature) to a superparamagnetic state (at high temperatures). Above the *superparamagnetic* transition temperature, called blocking temperature (T_B), particles behave as *paramagnets* due to the dominance of the thermal fluctuations over the magneto–crystalline anisotropy energy. At low temperatures, below T_B= 51K, the orientations of the particle's magnetic moments are frozen (so called blocked) in random directions and cannot rotate freely. Therefore, the sample magnetization becomes very small.Moreover, narrow ZFC curve in **Fig.87.right** reflects the fact that NPs10@OA sample has a very thin size distribtion (10.6 $\pm$ 0.98nm).

NMRD profile has been measured with Stelar fast field cycling NMR relaxometer at 37˚C and displays the evolution of proton longitudinal relaxivity as a function of the applied magnetic field. NMRD profile

recorded for NPs10@OA in THF is represented in **Fig.88**. According to the fitting of NMRD profile, one can extract theoretical values such as the relaxometric diameter (d^{NMRD}) (this value represents the shorter distance between magnetic core and THF molecules) and saturation magnetization (Ms).

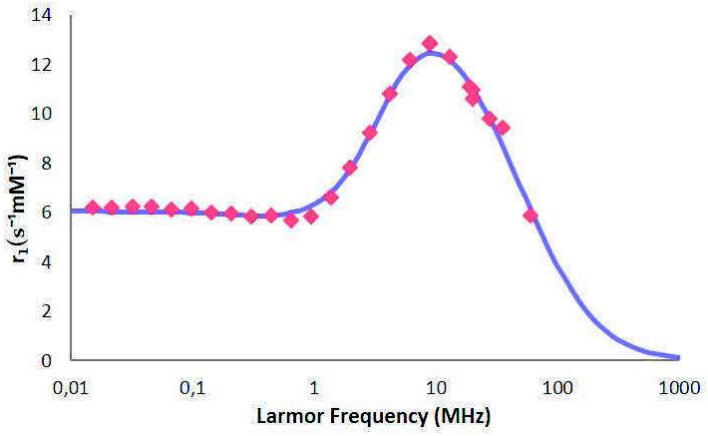

Figure 88: Relaxation evolution with Larmor frequency of NPs10@OA (dots) and the theoretical simulation according to superparamagnetic theory (line).

The general shape of NMRD profile is similar and match very well to the NMRD curve of superparamagnetic colloidal suspensions.[48] The obtained NMRD diameter d^{NMRD}= 10.9nm is slightly higher than TEM diameter. This observation is due to the thickness of OA, moreover, TEM calculations depend on the crystal volume.

Proton longitudinal relaxivity maximum is situated around 10MHz, which fits the superparamagnetic model. M_s calculated from NMRD profile is close to 32A.m².$Kg^{-1}$of iron. The saturation magnetization estimated from NMRD profile can be considered as an approximated value. Indeed, the estimated magnetization is correlated to the distance of the solvent molecules surrounding the magnetic core. Else, OA at the NPs surface limits the approach of THF molecules near to the magnetic core, inducing inevitably the decrease of M_s estimated by the fitting of NMRD curve. Moreover, at high Larmor frequencies some differences can be observed on NMRD profile in comparison to the theoretical data. This can be explained by the influence of the solvent, as in THF all hydrogens are not equivalent and the heterogeneity of the proton signal increases with Larmor frequency. In theory,the evolution of relaxation time should be multi–exponential. However, in order to facilitate the measurements, a mono–exponential behavior was assumed. These assumptions can thus explain the small differences at high magnetic field.

Table 13 summarizes diameter values obtained by various techniques (DLS, TEM and NMRD) and shows good correlation. Moreover, all of the values are coherent, since the theoretical order is followed $d^{DLS} > d^{NMRD} > d^{TEM}$. Fe^{3+} concentration values were measured with several techniques (Inductively Coupled

Plasma (ICP), Atomic Absorption Spectroscopy (AAS) and Relaxometry).

	DLS	**TEM**	**NMRD**
diameter (nm)	12±0.043	10.6±0.98	10.9±1
	ICP–OES	**AAS**	**Relaxometry**
$[Fe^{3+}]$ (mg/mL)	2±0.02	2.2±0.02	2.08±0.06
$[Fe^{3+}]$ (mM)	35.8±1	39.4±1	37.2±3

Table 13: Summary of NPs10@OA sample size distribution and concentration values determined by different techniques.

Boutry *et al.* have established a robust relaxometric method for Fe^{3+} quantification in solutions, based on magnetic influence of Iron ions on water protons relaxometry.[72] However, this technique can be applied to solutions containing only one type of magnetic ions, else there will be an impending for one ion quantification.

2.2 Grafting and characterization

Synthesized NPs10@OA by thermal decomposition have a good colloidal stability in organic solvents. However, for biomedical applications surface ligands have to render IONPs hydrophilic, biocompatible and provide colloidal stability in water and physiological media. In this section, physico–chemical properties of IONPs functionalized with two different dendrons, 1P_G_1PEG_COOH and 2P_G_1PEG_COOH will be discussed and we'll put into evidence their dependence on the anchoring group (mono– *versus* bi– phosphonic acid).

Procedure for dendronization of IONPs by direct ligand exchange: 7mg of dendron molecules were added to a mixture of 5mg of NPs10@OA in 5mL of THF, and the solution was magnetically stirred (400 rpm) for 48h. NPs were then precipitated by adding Cyclohexane. After centrifugation (10,000 rpm, 10min), grafted particles were easily dispersed in distilled water, and suspensions were purified by ultra–filtration **(Fig.89.left)**.

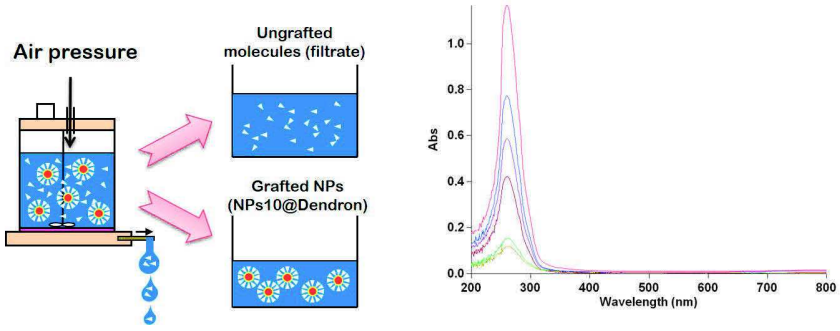

Figure 89: Schematic representation of ultra–filtration device (left) and UV–monitoring of dendron concentration in the supernatant (right).

The water suspension was introduced in the apparatus and purification occurred by pressurizing the

solution flow. The water and ungrafted molecules (released OA and the excess of dendrons) went through the membrane while grafted NPs remained. Ultrafiltration was UV–monitored due to high absorbency of 1P_G_1PEG_COOH and 2P_G_1PEG_COOH at 360nm wavelength. Dendronized NPs were considered *"clean"* when the supernatant was free of dendrons **(Fig.89.right)**.

In order to simplify writing, NPs10@1P_G_1PEG_COOH and NPs10@2P_G_1PEG_COOH are being referred to as NPs10@D2 and NPs10@D2–2P respectively. Both stability and size distribution of dendronized NPs were determined by DLS and TEM measurements **(Fig.90)**.

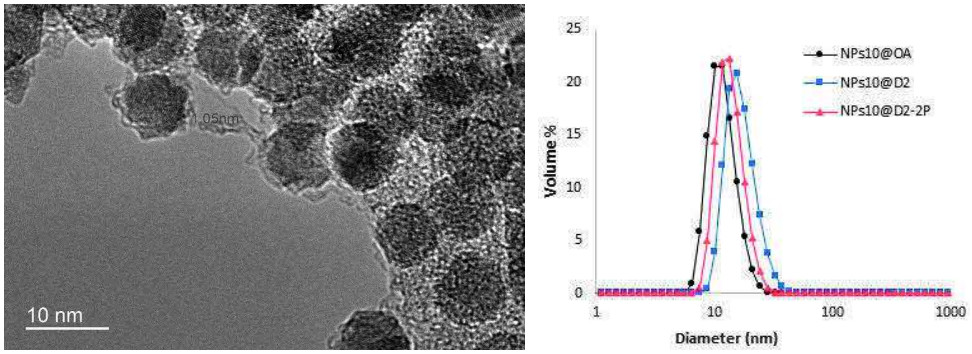

Figure 90: An example of dendronized NPs TEM image, NPs10@D2 (left) and size distribution by volume before and after grafting of NPs10@OA with D2 and D2–2P (right).

After dendronization, size distributions of NPs10@D2 and D2–2P suspensions are monomodal with an average hydrodynamic diameter slightly larger than the one of NPs10@OA in THF **(Fig.90. right)**. This slight increase is due to the larger length of the dendrons (2 – 3nm) by comparison with OA (from 1 to 2nm) **(Table 14)**.

	d^{DLS} (nm)	PDI	Z potential (mV)	IEP
NPs10@OA	12±1.3	0.043	–	–
NPs10@D2	17±1.5	0.33	–16.9	2.94
NPs10@D2–2P	14±1.1	0.29	–18.5	2.53

Table 14: Comparison between size distribution by volume of NPs10@D2 and NPs10@D2–2P determined by DLS, corresponding Zeta potential values measured at pH = 7.4.

Zeta potential measurements were done at physiological pH, around 7.4 **(Table 14)**. The isoelectric point (IEP) for uncoated IONPs is equal to pH = 6.5 and thus naked IONPs are not stable in water suspension. The Zeta potential negative values obtained for dendronized NPs confirm the dendron grafting and are due to the presence of peripheral Carboxylic acid functions (pKa = 4), which are deprotonated at physiological pH. Colloidal stability is due to the electrostatic interactions introduced by the deprotonated Carboxylate end groups and also to steric hindrance induced by the dendron architecture.

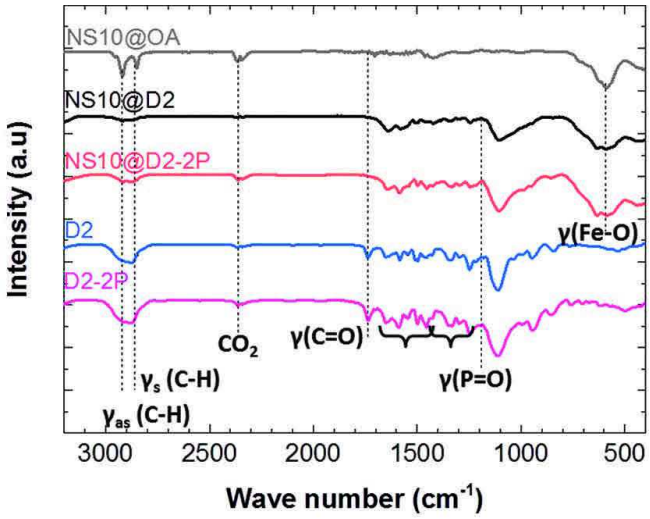

Figure 91: FTIR spectra of dendrons D2 and D2–2P and of NPs10 before and after functionalization with D2 and D2–2P.

The surface modification of NPs10@OA with D2 and D2–2P has been assessed by FTIR spectroscopy **(Fig.91)**, comparing profiles of free dendrons with those of NPs before and after ligand exchange.

The FTIR profiles of NPs10 before and after functionalization with D2 and D2–2P display several bands characteristic of asymmetric and symmetric vibrations of CH_2 groups identified as γ_{as} (C–H) = 2920cm^{-1} and γ_s (C–H) = 2850cm^{-1}. The band at 1734cm^{-1} belongs to the Carboxylic acid function. After the grafting of both D2 and D2–2P dendrons, the band belonging to the Carboxylic acid function is not visible, which can be certainly attributed to the lower amount of carboxylate group carried by D2 and D2–2P (one COOH per 3 PEG chains). The C–O–C groups of PEG chains are characterized by bands at 1100cm^{-1}. This last band should also include the C–C–C groups of the aromatic cycle. The band at 1180cm^{-1} is attributed to the P=O double bond and bands at 1054 and 993cm^{-1} to P–OH bonds. IR spectrum of NPs10@OA displays a single broad band for Fe–O located at 570cm^{-1}, whereas, dendronized NPs present small shoulders between 800 and 600cm^{-1}, attributed to a small surface oxidation.

According to the NMRD profiles **(Fig.92)** the maximum longitudinal relaxivity peaks for dendronized and OA coated NPs are observed at the same positions, around 10MHz, since the size of all nanocrystals is similar. One must than notice that the NMRD profile of NPs10@0A has been recorded in THF, whereas it was recorded in water for both dendronized NPs10@D2 and NPs10@D2–2P, rendering the comparison of relaxivity values r_1 impossible between OA–coated or dendronized NPs.

Regarding only dendronnized NPs10, the r1max value of NS10@D2 is slightly lower than the ${r_1}^{max}$ value of NS10@D2–2P. The experimental data were fitted using the usual model assuming a spherical shape of the particles. The M_s and diameter fitted values are shown in **Table15**.

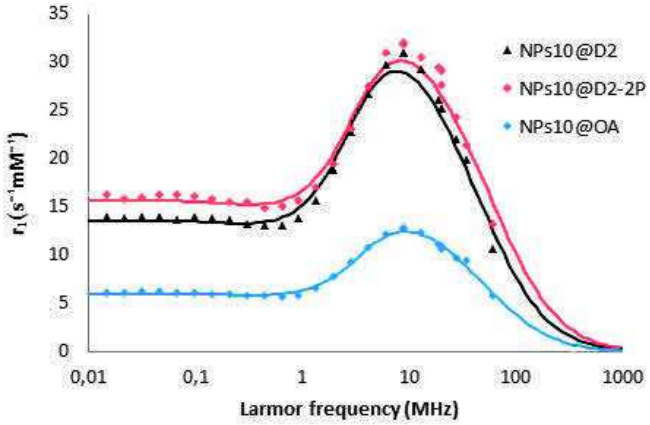

Figure 92: NMRD profiles of NPs10 before and after functionalization with both dendrons.

	d^{NMRD} (nm)	r_1 ($s^{-1}mM^{-1}$)	r_2 ($s^{-1}mM^{-1}$)	r_2/r_1	$M_s{}^{NMRD}$ ($A.m^2.kg_{-1}$)	$M_s{}^{SQUID}$ ($A.m^2.kg_{-1}$)
NPs10@D2	10.6±1.6	10.7±1	74.5±3	6.9±0.5	46±0.2	63
NPs10@D2–2P	10.1±1.7	13.2±2	70.7±5	5.3±0.3	53±0.3	65

Table 15: Values of r_1 and r_2 relaxivities at 1.5T, diameter deduced from the NMRD profiles, and saturation magnetization (M_s) deduced from NMRD and SQUID profles.

The saturation magnetization determined for NPs10@D2 and D2–2P from NMRD profiles are lower by comparison with SQUID measurements. This phenomena can be explained by the nature of the measurements. For SQUID measurements only the spinel phase contributes to the magnetization of the nano–objects, whereas NMRD profiles allow deducing sample's magnetization as a function of water diffusion around the magnetic core.

Longitudinal r_1 and transverse r_2 relaxivity values, measured at 1.5T and 37°C, are given in **Table 15**. The values reported are good if we compare them to commercial products displaying similar mean hydrodynamic size.[32]

Magnetization curves of NPs10@D2 and D2–2P measured at 4K (–269.15°C) present a loop, representative of ferrimagnetic behavior **(Fig.93.left)**. Saturation magnetization (M_s) of 63 and 65$A.m^2.Kg^{-1}$ were recorded for NPs10@D2 and NPs10@D2–2P , respectively, and don't differ from the M_s value before grafting, thus confirming a high crystalline order after the ligand exchange. Else, dendronized NPs present a slightly higher coercivity value, H_c =0.036T, which may be due to the small oxidized shell formed during ligand exchange. This phenomena is also confirmed by ZFC/FC curves of dendronized NPs **(Fig.93.right)**. Blocking temperatures present a small increase, T_B = 68K, in comparison with NPs10@OA for which T_B = 51K. The increase of H_c and T_B denote the existence of a surface layer with reduced magnetization, and some diamagnetic contribution from the surfactant shell, since dendrons are longer in comparison with OA.

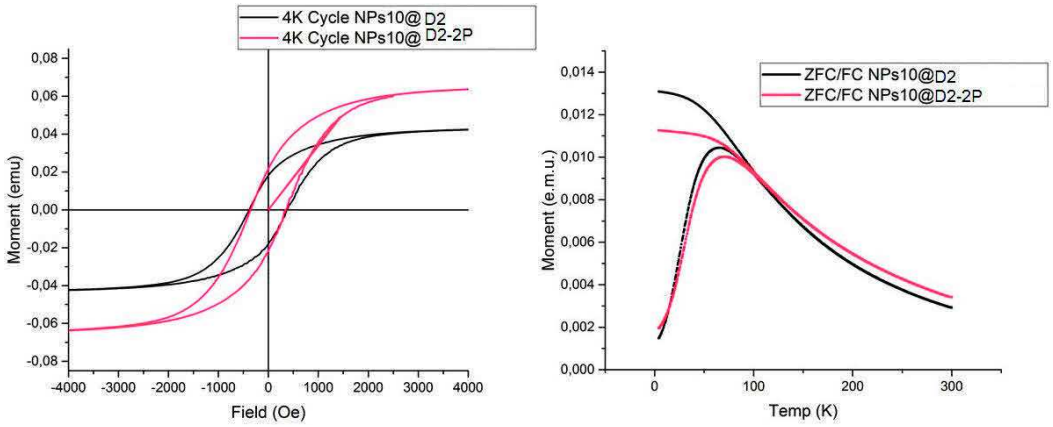

Figure 93: Hysteresis loop recorded at 4K (left) and temperature dependence of ZFC and FC magnetization (right) for NPs10@D2 and NPs10@D2–2P samples.

The grafting rate was determined by correlation between Iron to Phosphorus amounts in each sample, and by considering that NPs are perfectly spherical **(Table 16)**. Iron concentration, as discussed previously, was determined by three different techniques: ICP–OES, AAS and Relaxometry. For the quantification of Phosphorus, a colorimetric method was performed using Ammonium heptamolybdate. Indeed, in the presence of Ammonium heptamolybdate, a mineralized sample of dendronized NPs gives an intense blue color due to the formation of a stable complex between free Phosphates, originated from the dendrons, and Ammonium heptamolybdate **(Eq.2)**.

$$H_3PO_4 + 12(NH_4)_2MoO_4 + 21H^+ \rightarrow (NH_4)_3PO_4 \cdot 12MoO_3 + 21NH_4^+ + 12H_2O \quad (2)$$

Obtained results show a small grafting rate difference between the two dendrons, D2 and D2–2P, which can be attributed to the surface covered by the dendrons, since D2–2P shows a Bi–phosphonate anchor occupying a higher surface in comparison to dendron D2 displaying a Mono–phosphonate anchor.

The experimental grafting rates were found very close to the theoretical ones showing a whole coverage of the NP surface by the dendron.

	[Fe^{3+}] (mM)	[Dendron] (nbr/L)	[NPs] (nbr/L)	Dendron/ NPs	Dendron/ nm^2	Theory Dendron/nm^2
NPs10@D2	10.03	1.83E+20	2.85E+17	648±12	2.1	1.4
NPs10@D2–2P	10.03	1.61E+20	2.85E+17	573±9	1.85	1.4

Table 16: Grafting rates determined by the elemental analysis of Iron and Phosphorus.

All the previous analysis showed good physico–chemical properties of dendronized NPs for biomedical applications. However, a suitable characterization of NPs' organic shell is a real challenge and of utmost importance since Oleic acid promotes apoptosis and necrosis of healthy cells[73,74,75].

FTIR spectroscopy gives a qualitative description of grafted molecular species on NPs' surface. Consequently, in order to better identify the coating' chemical structure, ^{1}H NMR spectroscopy was investigated. Yet, this technique is not suitable for magnetic particles due to the presence of nano–magnets influencing magnetic field heterogeneity and the decrease of ligand mobility bound to the NPs' surface. This effect induces broadening of NMR characteristic peaks, thus complicating spectrum interpretation. To this end, High Resolution – Magic Angle Spinning (HR–MAS) was performed on dendronized NPs.[76]

The general principle of HR–MAS is based on recording an NMR spectrum under rotation of the sample at a magic angle (54°74'). The sample rotation at high frequencies minimizes the dipolar interactions responsible for the NMR peaks broadening in conventional NMR.

Fig.94 shows an example of conventional ^{1}H NMR spectra of OA in $CDCl_3$ and D2–2P in D_2O compared to NPs10@D2–2P ^{1}H HR–MAS spectra in D_2O.

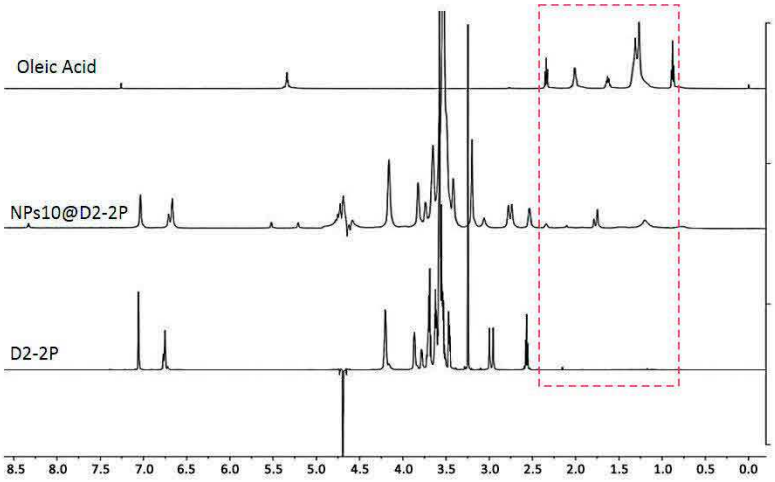

Figure 94: Oleic acid ^{1}H NMR spectra in $CDCl_3$ (top), NPs10@D2–2P ^{1}H HR–MAS spectra in D_2O (middle) and D2–2P ^{1}H NMR spectra in D_2O (bottom) recorded with a NMR Bruker Avance 500MHz.

The ^{1}H HR–MAS spectrum shows OA representative peaks at 0.9 – 2.5ppm corresponding –C$\mathbf{H_2}$– groups and at 5.2ppm signal of vinyl bond –C**H**=C**H**–. D2–2P representative peaks are present between 2.5 and 4.5ppm, and also at 6.4 and 7ppm. Moreover, one can notice that OA peaks represented on the ^{1}H HR–MAS profile are shifted and not all of the peaks can be observed. This phenomena can be explained by the influence of the solvent nature. Polito *et al.* reported that the appearance of NMR signals on a HR–MAS profile, changes as a function of solvent nature due to the modification of ligand mobility.[76] Dendronized NPs are soluble in D_2O, which is not the case for OA. In deuterated water, OA chains are probably not completely extended since the solvent is much more polar than THF. This could have an effect on the OA molecular mobility, thus reducing the signal intensity and only the signals related to the end of OA chains are visible. These observations confirm thus the presence of OA at the surface of NPs10@D2–2P, leading to

the conclusion that the dendrons grafting rate is not 100%, as assumed by theoretical calculations. Further studies have to be performed in order to determine OA quantity at the dendronized NPs surface, in order to predict nano–material cytotoxicity.

In this section, IONPs have been successfully synthesized and functionalized with two different dendrons, D2 and D2–2P. Their colloidal stability and physico–chemical characterizations assessed their importance as MRI CAs. Thereafter, *in vitro* and *in vivo* studies are performed, in order to examine their *in vitro* cytotoxicity and bioavailability, and *in vivo* biodistribution.

2.3 *In vitro* studies

Biocompatibility was determined *in vitro* on 2D culture cell models by evaluating the bioavailability of dendronized nanoparticles towards four different cell types: i) Human hepatic stem cell line (HepaRG), ii) Hepatocyte derived cellular carcinoma cell line (HuH7–luc), iii) Adenocarcinomic human alveolar basal epithelial cells (A549–luc) and iv) Human neuroblastoma cell line (Kelly). Cytotoxicity was established through MTT[21] assay and LDH[22] release test.

The cell viability was determined by MTT colorimetric assay developed by Mosmann for *in vitro* cytotoxicity and cell proliferation measurements.[77] It was reported that the mitochondrial enzyme Succinate–dehydrogenase within viable cells is able to cleave the MTT salt into Formazan, a blue colored product. The amount of Formazan produced, read on scanning multi–well spectrophotometer, is proportional to the number of viable cells present[78,79], thus examining the percentage of dead cells caused by external factors, in our case – dendronized IONPs.

Complementary, LDH assay quantifies the enzyme Lactate dehydrogenase, which is a soluble cytoplasmic enzyme that is present in almost all cells and is released into extracellular space when the plasma membrane is damaged. LDH reduces INT (2–(4–Iodophenyl)–3–(4–nitrophenyl)–5–Phenyl tetrazolium chloride) in the presence of NADH + H^+ (reduced β–Nicotinamide Adenine Dinucleotide) yielding a red water–soluble Formazan, which is quantified by light absorption measurement.[80] Damaged plasma membrane initiates inflammatory response in surrounding tissues, thus preventing phagocytes from eliminating dead cells. The loss of cell membrane integrity is a key signature for necrosis.[81]

The *in vivo* blood half–life of IONPs varies, depending on particle size and surface properties[82], from 2 hours for Dextran–coated 120 – 180nm Ferumoxide particles (Endorem®, Feridex®) to 24 – 36 hours for Dextran–coated 15 – 30nm Ferumoxtran particles (Sinerem®, Combidex®). In a recent study, the half–life of starch–coated IONPs and those with 5 and 2kDa PEG coatings was found to be 0.12, 7.3 and 11.8h,

[21] MTT – 3–(4,5–Dimethylthiazol–2–yl)–2,5–Diphenyl–tetrazolium bromide or Thiazolyl blue tetrazolium bromide salt.
[22] LDH – Lactate dehydrogenase.

respectively, in male rats.[82] To mimic the potential *in vivo* contact time, biocompatibility/ toxicity effects were investigated for periods of 24 or 48h of incubation, at 37 °C, with 5 % CO_2. Cells were plated into 96–wells flat–bottom plates at a starting density of 10^4 cells per well. After an equilibration time (12 to 24h for A549–luc, Huh7–luc and Kelly, and 7 days for HepaRG), until they reached 70%–80% confluency, culture media was removed and cells were treated in triplicate with increasing concentrations (0.82, 2.05, 5.12, 12.8, 32, 80, 200 and 500µg/mL) of NPs10@D2 and NPs10@D2–2P suspended in culture media.

MTT cell–viability assay Briefly, the MTT assay was conducted by incubating cells with a 2 mg/mL solution of MTT (50µL) for 3 hours. The supernatant was then aspirated and 150µL of Dimethyl sulfoxide (DMSO) was applied to the cells to solubilize the formed Formazan crystals. Plates were agitated and then 100µL of the supernatant was collected and transferred into a clean 96–well flat–bottom plate. Optical density was measured at 570nm and a reference wavelength at 630nm was used. Cell viability percentage viability was calculated as the ratio of mean absorbency of triplicate readings of sample wells (A_{sample}) compared to the mean absorbency of control wells ($A_{control}$). At each experiment DMSO was used as a negative control, A_{DMSO}, as shown in **Eq.3**:

$$Cell\ viability\ \% = \frac{A_{sample} - A_{DMSO}}{A_{control} - A_{DMSO}} \times 100\% \tag{3}$$

MTT cytotoxicity assay of *transfected* cells with NPs10@D2 demonstrated both an incubation time and concentration dependent cell loss **(Fig.95)**. The toxic effect was taken into consideration when the survival rate was below 80%.

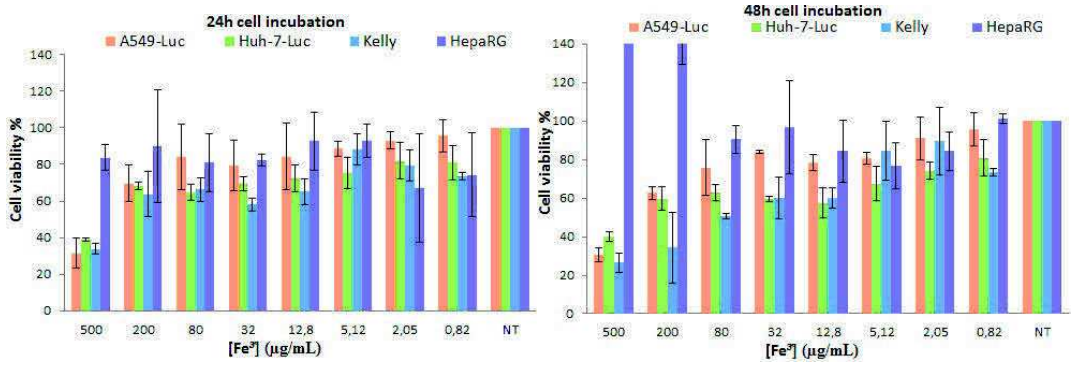

Figure 95: MTT cell viability *transfected* with NPs10@D2 after 24 and 48h incubation.

After 24h incubation with NPs10@D2, all cancer cells viability (A549–luc, Huh7–luc and Kelly) changed from *ca.* 100% to approximately 60% with Fe^{3+} concentrations increasing from 0.8 up to 200µg/mL. At high dose of Fe^{3+}, 500µg/mL, cell viability decreases till 40%. After 48 hours incubation time the cell survival

rate followed almost the same trend. On the other hand, human hepatic stem cells HepaRG, showed very low toxicity (at 24h incubation) or proliferation effect over time (at 48h incubation) at the highest applied concentrations (*i.e.*, 500 and 200µg/mL).

MTT toxicity assay of NPs10@D2–2P demonstrates a moderate to good survival rate after 24h incubation for all cancer cell lines and at Fe^{3+} concentrations up to 200µg/mL **(Fig.96)**. After 48h incubation, A549–luc cells show high proliferation rate even at low concentration and higher cell viability at 500 µg/mL. On the contrary, Huh7–luc shows a drop of cell survival rate to 30% at 500 µg/mL.

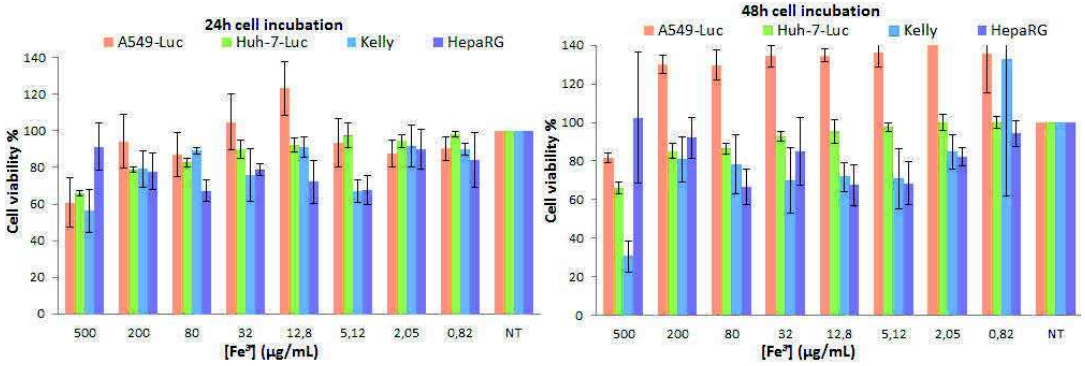

Figure 96: MTT cell viability *transfected* with NPs10@D2–2P after 24 and 48h incubation.

From the MTT results, it is found that IONPs coated with D2 and D2–2P dendrons showed moderate toxic or proliferation effect at the highest applied concentration (*i.e.*, 500 mg/L). The toxicity of dendronized IONPs may be related to their ability to damage DNA via magnetite oxidation as previously shown by Karlsson *et al.* on cultured cell lines.[83]

Also, other factors like the presence of OA on the dendronized NPs' surface, could possibly be responsible for cell toxic responses. Indeed, Delgad *et al.* have recently reported OA influence on normal and cancer cell lines. Their results demonstrated that OA alone promotes apoptosis on different cell lines, even though normal cells were expected to be less sensitive towards OA than cancer cells.[84] As shown earlier on the HR–MAS profiles of NPs10@D2–2P **(Fig. 94)**, OA is still present at the dendronized NPs' surface. This result assess the idea of cytotoxicity induced by the existence of OA in the NPs10@Dendron composition.

Furthermore, for high NPs10@D2–2P concentrations one can notice a promotion of cell proliferation **(Fig.96)**. This promoted cell growth could be due to the ability to diminish intracellular H_2O_2, which plays a pivotal role in the control of proliferation and cell death.[85]

In the literature, the MTT assay method has been prominent among other *in vitro* toxicity assay methods for probing the toxicity of IONPs. This is perhaps due to the fact that the assay allows rapid evaluation of cell viability, cell survival, cell growth and gives good reproducibility.[86]

LDH release test on HepaRG LDH leakage in HepaRG cells was determined using the CytoTox–ONE™ Homogeneous Membrane Integrity Assay from Promega. At the end of cell incubation time (24h or 48h) with different concentrations of NPs10@D2 and NPs10@D2–2P, 100µL of CytoTox–ONE™ Reagent solution supported by the assay kit was added to the cells and incubated for 10min at 25˚C in darkness. Furthermore, triplicate wells were set up in order to determine the Maximum LDH Release Control by adding 2µl of Lysis Solution to the positive control wells before addition of CytoTox–ONE™ Reagent. Subsequently, 50µL of Stop solution was added to each well, and plates were shaken for 30sec at 25˚C. Cells were read under a microplate spectrofluorometer with an excitation wavelength of 560nm and an emission wavelength of 590nm.

The cytotoxicity was calculated according to **Eq.4**, where F_{exp} = measured fluorescence of cells with the testing material; $F_{control}$ = fluorescence of control cells and Max_{LDH} = fluorescence of lysed cells.

$$\%\ Cytotoxicity \frac{F_{exp} - F_{control}}{Max_{LDH} - F_{control}} \times 100\% \tag{4}$$

The cell membrane integrity was determined via quantification of LDH leakage from cells incubated with NPs10@D2 and NPs10@D2–2P **(Fig.97)**. For the shorter incubation period (24h), HepaRG demonstrated low cytotoxicity (below 10%) for entire range of concentrations and for both dendronized IONPs. Else, at 24h incubation for the highest concentrations (above 80µg/mL), one can notice negative cytotoxicity, which is not a calculation error, on the contrary, but is due to the formation of iron chelators which assist cell proliferation.

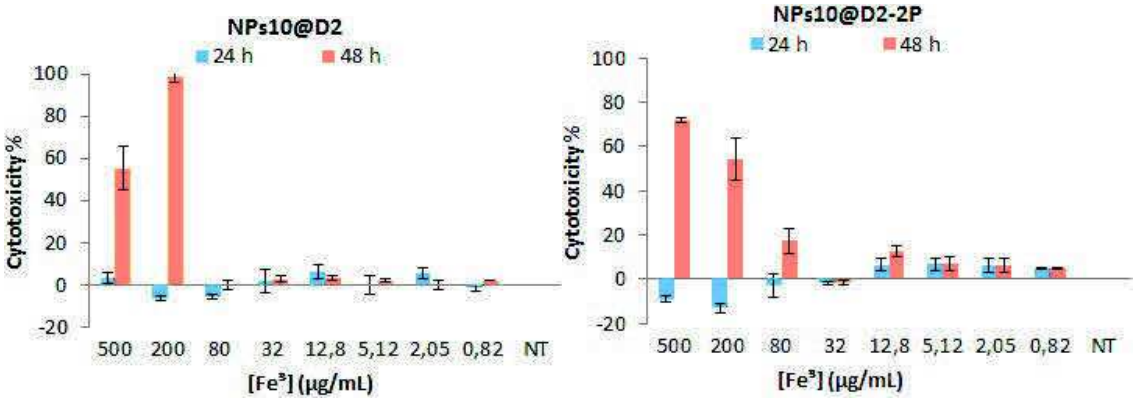

Figure 97: Percentage of HepaRG plasma membrane permeabilization towards dendronized nanoparticles after 24 and 48h incubation.

After 48h incubation the trend was completely different as a significant increase (over 60%) in LDH leakage was observed for the highest Fe^{3+} concentrations and above 200µg/mL, both dendronized nanoparticles presenting low cytotoxicity for iron concentrations up to 80µg/mL.

Regarding those LDH release tests, it is important to point out that such assay measures the fluorescent

signal of membrane–damaged cells, not of the normal ones. Therefore, even though the cell number is increasing as incubation time increases, a natural proliferation process, the LDH leakage assay cannot count the viability of normal cells. It only detects the accumulated LDH derived from continuous leakage of damaged cells which number is proportional to the time, as at 48h incubation a programmed cell death occurs, mediated by an intracellular program.[87] Furthermmore, the real nature of cell membrane morphology change during contact with nanostructures, which may be accredited to endocytosis as well as possible membrane disruption by potential quantum mechanical effect and other nano–activities.[88]

Cellular uptake study by flow cytometry Previously reported studies showed that endocytosis is the main mechanism of cellular internalization of magnetic nanoparticles.[89] In this section we studied NPs10@Dendron internalization in different cancer cell lines, as a function of Fe^{3+} concentration, but also as a function of time and temperature. Indeed, internalization is not only due to one distinct pathway but several processes are possible in parallel. This is mainly why we incubated cells not only at 37˚C, but also at 4˚C, the latter being a condition which blocks all active processes. Indeed it is well known that at 4˚C cell growth and metabolism are clearly limited because of lower membrane fluidity, reduced enzymes' affinity for their substrates, decreased thermal energy and reaction rates and increased aqueous viscosity.[90,91]

Dendronized IONPs were decorated with DY^{TM}– Alexa495 –Amine (Dyomics GmbH) via carbodiimide linkage achieved in the presence of N – Hydroxysuccinimide in water for 2h. NPs10@D2 _ Alexa495 and NPs10@D2–2P _ Alexa495 were characterized by DLS and Zeta potential **(Table 17)**. The Zeta potential shift of dendronized solutions at pH = 7 shows the successful Alexa dye grafting on the NPs' surface. Furthermore, DLS measurements assess colloidal stability of Alexa–coupled nanomaterials.

	NPs10@D2	NPs10@D2–2P	NPs10@D2 _ Alexa495	NPs10@D2– 2P _ Alexa495
d^{DLS} (nm)	17±1.5	14±1.1	18±0.9	21±2.3
PDI	0.33	0.29	0.20	0.37
Zeta potential (mV)	–16.9	–18.5	–11.5	–15

Table 17: Size distribution by volume and Zeta potential before and after Alexa495 decorated dendronized NPs at pH = 7.4.

To study the cellular uptake of NPs10@D2_Alexa495 and NPs10@D2–2P _ Alexa495 with different Fe^{3+} concentrations, analysis of the cell samples were performed using FACScan flow cytometer and Novios software. Briefly, A549–luc, Huh7–luc and Kelly cells, at a density of 2×10^5 cells per well, were seeded in 24 well plates and incubated at 37˚C overnight. After the equilibration time, at 70%–80% confluency, culture media was removed and cells were treated in triplicate with 1mL of NPs10@D2_Alexa495 at 1 and 10µg/mL of Fe^{3+}, or 1mL of NPs10@D2–2P _ Alexa495 at 10 and 50µg/mL of Fe^{3+} suspended in culture

media. Cells were incubated for 4 hours at 4˚C, 4h at 37˚C and for 24h at 37˚C. Cells treated with only medium were used as controls. At the end of the incubation period, cells were washed three times with PBS, to remove non–internalized NPs or different artefacts, which were not taken up by the cells, fixed in 2% Paraformaldehyde solution, and stored overnight in the fridge. In all FACS analysis, cell debris and free particles were excluded by setting a gate on the plot of side–scattered light (SSC) vs forward–scattered light (FSC). Acquisition parameters were optimized for detection of Alexa495 fluorophore, excitation at 488nm wavelength with an argon laser and detection above 505nm. A total of 10,000 gated cells were analyzed for all cell types. The fluorescence increase in the cells treated with dendronized NPs relative to that in the untreated control cells was expressed as mean fluorescence increase relative to control.

The cellular uptake of dendronized NPs10@D2_Alexa495 and NPs10@D2–2P_Alexa495 by three cancer cell lines (Kelly, Huh7–luc and A549–luc) at varying time periods and temperatures was quantified and results are shown in **Fig.98**.

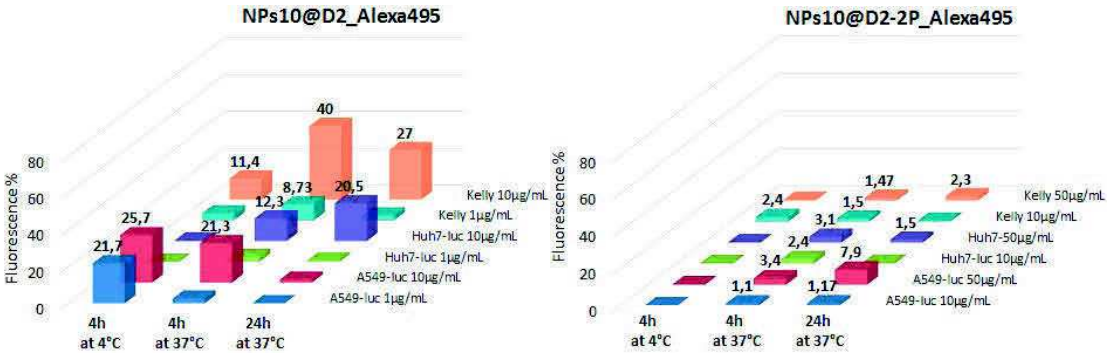

Figure 98: Flow cytometric analysis of A549–luc, Huh7–luc and Kelly cells when incubated at different temperature and time, with different dosages of Alexa495 labeled NPs10@D2 (left) and NPs10@D2–2P (right).

Regarding internalization of NPs10@D2_Alexa495 ***(Fig.98.left)****:* A549–luc cells show a fluorescence intensity of 21 and 25% at 4h incubation at 4˚C with 1 and 10µg/mL of NPs10@D2_Alexa495 respectively. In this case, NPs' internalization process can be considered as a binding (adsorbing) process, since at 4˚C all active internalization mechanisms are blocked. In addition, A549–luc show NPs internalization at 10µg/mL Fe^{3+} concentration and a total exocytosis after 24h incubation. The same phenomena can be noticed for 1µg/mL, A549–luc present internalization at 4h and 4˚C, and a possible exocytosis at 4h and 37˚C. Huh7–luc cancer cells show a slower cellular uptake only for 10µg/mL NPs concentration, reaching a maximum value of 20% after 24h incubation at 37˚C. Kelly cancer cells present also an internalization process for NPs@D2 at 10µg/mL after 4h at 4˚C, yet twice lower than A549–luc for the same conditions. Furthermore, one can notice an increase in cellular uptake of NPs10@D2_Alexa495 at 10µg/mL by Kelly cancer cells after 4h incubation at 37˚C and a clear exocytosis at 24h incubation **(Fig.98)**. It should be noted that the difference in uptake

between cell type could be due to the differences in metabolism, since Kelly cells have a lower metabolism in comparison to A549–luc cells. Nevertheless, for all cancer cell types, 10µg/mL NPs10@D2 concentration appears much relevant for the current study than 1µg/mL.

Regarding internalization of NPs10@D2–2P_Alexa495 ***(Fig.98.right)****:* taking into count the results of cellular uptake for NPs10@D2_Alexa495 (observed almost only for the highest concentration of 10µg/mL), it was decided to increase the concentration of NPs10@D2–2P_Alexa495 and use 10 and 50µg/mL for internalization assessment. The results of flow cytometry after 4 or 24 hours of incubation at 4°C or 37°C revealed no significant uptake of NPs10@D2–2P_Alexa495 by any cancer cell lines.

Such opposite behaviors of D2 and D2–2P dendronized NPs toward cells'viability or internalization could be explained by the presence, at various amounts, of remaining OA at the surface of those nanohybrid structures **(Fig.94)**. Those cytotoxicity assays and cellular uptake tests lean toward the idea that NPs10@D2 present a higher amount of OA in the final structure in comparison with NPs10@D2–2P. Since OA is a well–known penetration enhancer that increases membrane permeability[92,93,94], one can explain the highest cytotoxicity and cellular uptake observed for NPs10@D2.

2.4 *In vivo* studies

The MRI mice (n = 3) were anesthetized with isoflurane by inhalation. The experiments were performed on a 300MHz (7T) Bruker Biospec imaging system. The contrast agent was injected intravenously at a dose of 45µmol [Fe^{3+}]/kg body weight. The signal intensity (SI) was measured in regions of interest (ROIs) drawn on the liver and bladder, and in a region situated out of the image of the animal, representing the noise standard deviation (noise SD). The SI enhancement (Δ SNR%) was calculated according to **Eq.5**, where SI_{post} = post–contrast SI, and SI_{pre} = pre–contrast SI.

$$\Delta \text{ SNR } \% = \left| \frac{SIpost/noiseSD - SIpre/noiseSD}{SIpre/noiseSD} \right| \times 100 \quad (5)$$

The *in vivo* MRI studies were performed on NMRI mice. **Fig.99** shows spin–echo abdomen images of a living mouse acquired before and after intravenous injection of the nanoparticles solution at different times post *iv*. We found a strong negative contrast in the liver in T_2–weighted images 90min after intravenous injection **(Fig.99)** and an increase negative contrast in urinary bladder T_2–weighted axial images over 190min post *iv* **(Fig.100)**. The negative contrast persisted over 10h in liver and for 6h in bladder, but it weakened over time, suggesting that dendronized nanoparticles are susceptible to renal and hepato–biliary excretions.

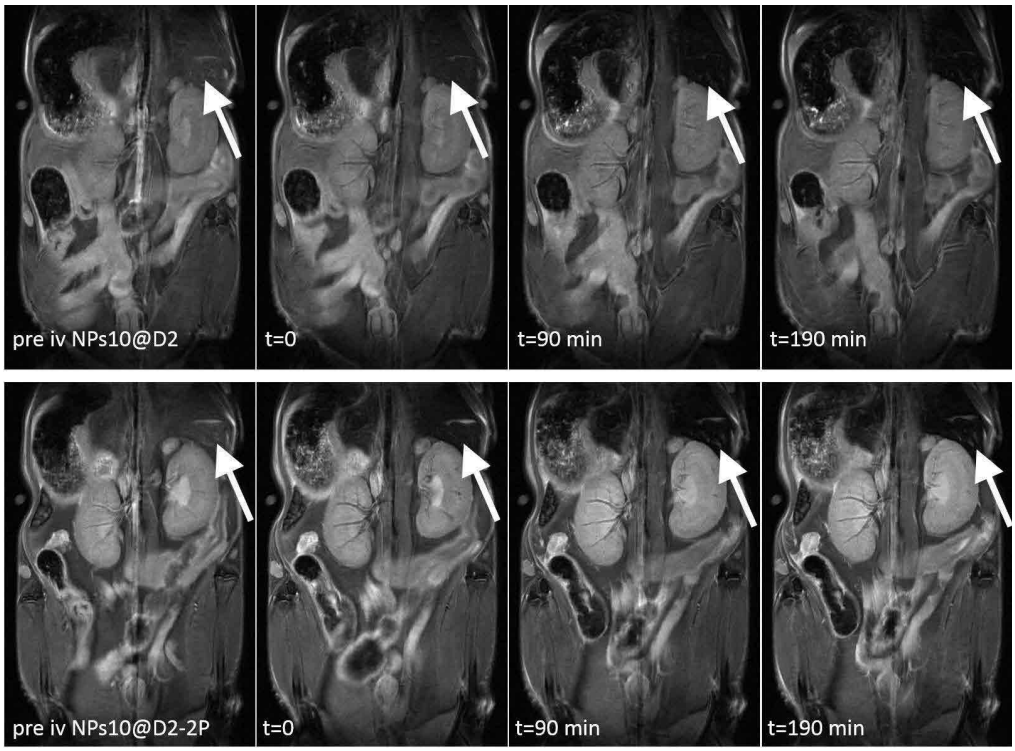

Figure 99: MR images of a live mouse with a T_2–weighted spin–echo sequence (TR 2000, TE 17). Images were acquired before (pre–contrast) and 0, 90 and 190min after intravenous injection of 70 µL of NPs10@D2 (top) and NPs10@D2–2P (bottom) at a concentration of 45 µmol $[Fe^{3+}]$/kg body weight.

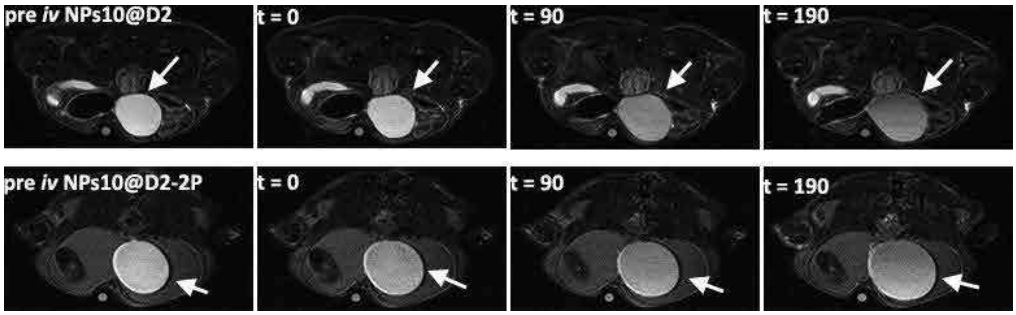

Figure 100: MR images of a live mouse with a T_2–weighted axial sequence (TR 7726, TE 52). Images were acquired before (pre–contrast) and 0, 90 and 190min after intravenous injection of 70 µL of NPs10@D2 (top) and NPs10@D2–2P (bottom) at a concentration of 45 µmol $[Fe^{3+}]$/kg body weight.

The Δ SNR % measured on Rapid Imaging with refocused Echoes (RARE) images of liver and bladder confirmed the negative contrast produced by dendronized nanoparticles **(Fig.101)**. The signal intensity in mice injected with NPs10@D2 reached a maximum at 140min post–injection for liver (55%) and 190min post–injection for bladder (33%) **(Fig.101.left)**. However, mice injected with NPs10@D2–2P showed a maximum of SI at 45min post–injection for liver and at 140min post–injection for bladder **(Fig.101.right)**.

At 24h post injection of NPs10@D2 or NPs10@D2–2P, the negative contrast for both liver and bladder appeared underneath 20%, showing a clear tendency for nanoparticles' excretion or metabolization.

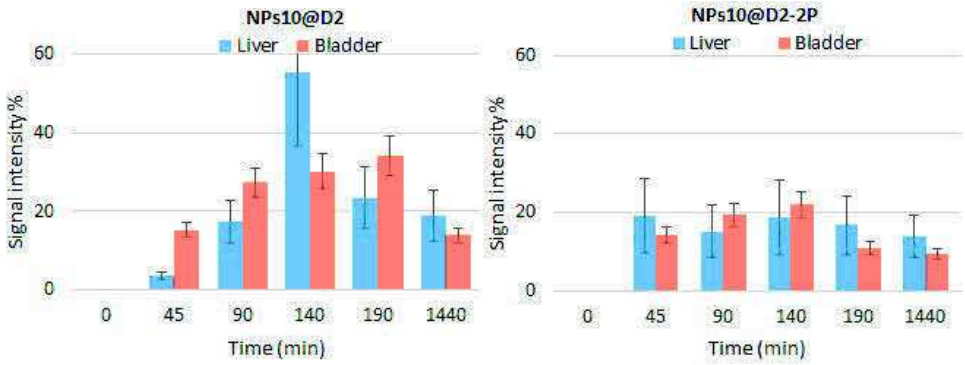

Figure 101: Calculated Δ SNR% for liver and bladder over the time after intravenous injection of (left) NPs10@D2 and (right) NPs10@D2–2P.

Furthermore, despite the administered dose (triple dose used in clinical trials for humans, 15µmoles $[Fe^{3+}]$/kg body weight), all mice showed no toxic signs over 48h, *e.g.* mice showed regular breathing, good quality walkways, no surrounding tissue irritation.

Conclusion In this chapter superparamagnetic IONPs were successfully synthesized and grafted with two different dendrons, 1P_ G_1PEG_ COOH (D2) and 2P_ G_1PEG_ COOH (D2–2P). Physico – chemical characterizations assessed their composition, colloidal stability and interesting magnetic properties as MRI CAs. Both dendronized IONPs showed moderate *in vitro* toxicity towards cancer and primary cell lines. Flow cytometry results showed a non–specific uptake of NPs10@D2 and no internalization of NPs10@D2–2P, which leans toward the idea that NPs10@D2 is not suitable for active targeting. On the other hand, NPs10@D2-2P lack of internalization, makes them a good candidate for active targeting. Furthermore, *in vivo* MRI studies showed high contrast enhancement and renal and hepato–biliary excretions. For these reasons, dendronized IONPs show great potential as early cancer diagnosis imaging and NPs10@D2–2P for active targeting through post–functionalization with targeting ligands.

3 Melanoma Active targeting

Cancer is a worldwide disease with high mortality, accounting for about 595,690 deaths, almost 1,620 people per day in 2016 according to the statistical analysis of American Cancer Society.[95] About 1,685,210 new cancer cases are expected to be diagnosed in 2016. The 5–year relative survival rate for all cancers diagnosed in 2004–2010 was 68%, up from 49% in 1975–1977. The improvement in survival reflects both the earlier

diagnosis of certain cancers and improvements in treatment. However, the number of people living beyond a cancer diagnosis reached nearly 14.5 million in 2014 and is expected to rise to almost 19 million by 2024.[96] Therefore, cancer diagnosis using advanced technologies is essential.

A major issue in current cancer research is the lack of selective diagnosis and treatment. Therefore, researchers have focused on numerous innovative targeting strategies to address this problem with the goal of increasing selectivity and minimize accumulation in healthy tissues.

Active targeting, also called ligand–mediated targeting, involves utilizing affinity ligands on the nanomaterial' surface for specific retention and uptake by the targeted disease cells. To that end, ligands are selected to bind surface molecules or receptors over–expressed in diseased organs, tissues, cells or subcellular domains.[97,98,99,100,101,102] Conversely, the molecular recognition of a ligand coupled to the nanomaterials' surface promotes cellular entry *via* receptor–mediated endocytosis, resulting in enhanced cellular uptake. Therefore, the grafting of targeting ligands should increase internalization of both drug and contrast agent, resulting in improved antitumor activity, reduced toxicity and increased target–to–background contrast during imaging, without altering the overall biodistribution.[103,104,105,106]

The first targeted systems were centered mainly on the use of antibodies as targeting moieties because of their high specificity and wide availability.[107] Since then, other proteins, peptides, nucleic acid–based ligands and small molecules have all been described.[2] Small molecular weight compounds have properties which strongly contrast from usual targeting ligands: small sizes, low production costs, and improved stability. These advantages translate into simple pre–formulation conjugation strategies and simple, tunable nanomaterials' synthesis.[108,109]

3.1 Introduction

The skin is the body's largest organ. It protects against heat, sunlight, injury, and infections. Skin also helps controlling body temperature and stores water, fat, and vitamin D. The skin has several layers, but the two main layers are the epidermis (upper or outer layer) and the dermis (lower or inner layer). Skin cancer begins in the epidermis, which is made up of three kinds of cells **(Fig.102)**:

- Squamous cells: thin, flat cells that form the top layer of the epidermis.
- Basal cells: round cells under the squamous cells.
- Melanocytes: cells that produce melanin and are found in the lower part of the epidermis. Melanin is the pigment that gives skin its natural color. When skin is exposed to the sun or artificial light, melanocytes make more pigment and cause the skin to darken.

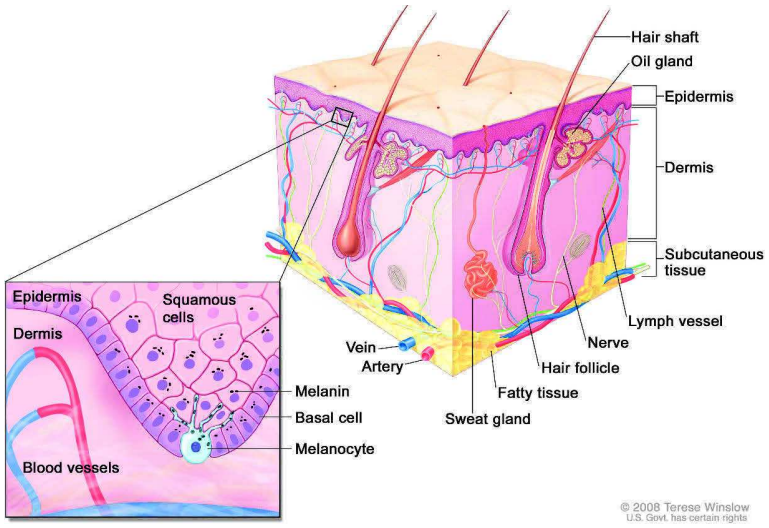

Figure 102: Anatomy of the skin, showing the epidermis, dermis, and subcutaneous tissue. The pullout shows a close–up of the squamous cell and basal cell layers of the epidermis, above the dermis with blood vessels. Melanocytes are in the layer of basal cells at the deepest part of the epidermis.[96]

Melanoma arises from the malignant transformation of melanocytes and is the fifth most common type of new cancer diagnosis in American men and the seventh most common type in American women.[23] The incidence and mortality rates for invasive melanoma are highest in whites, who have a much higher risk of developing melanoma than African Americans. Among people younger than 45 years, incidence rates are higher in women than in men. By age 60 years, melanoma incidence rates in men are more than twice those of women; by age 80 years, men are nearly three times more likely to develop melanoma than women.

Melanoma is more aggressive than most other types of skin cancer. If it isn't diagnosed early, it is likely to invade nearby tissues and spread to other parts of the body. The number of cases of melanoma is increasing each year. Only 2% of all skin cancers are Melanoma, but it causes most deaths from skin cancer.

Melanoma–associated antigens began to be defined and led to Melanoma being among the first tumors to which monoclonal antibodies were produced. Studies with Interferons (IFNs),[110] Interleukin (IL),[111] Dacarbazine (DNA alkylating agent),[112] Ipilimumab (CTLA–4 blockade),[113] Vemurafenib and Dabrafenib (anti–BRAF)[114] demonstrated regressions of metastatic disease and significant improvements in overall survival. Despite promising early results, these treatments are limited by their high relapse rates and undesired side–effects. Among the panel of therapeutic options, targeted radionuclide therapy (TRT) emerged as a potential tool to selectively treat disseminated forms of Melanoma. In this context, radiolabeled ligands directed towards Melanocortin–1 (MC1) receptor or Melanin–producing cells have been the most extensively studied.[115,116,117]

[23] www.cancer.gov

Radio–halogenated (Hetero)arylcarboxamide derivatives (ICF01102[118,119]) targeting Melanocytes seem to be the most promising pigmented melanoma–seeking imaging agents in nuclear imaging,[120,121] while their radio–metallated (*e.g.* ^{99m}Tc) analogues have received little attention due to disappointing results such as compounds washing out from the tumor, prominent uptake in non–target tissues (kidneys, liver) or rapid excretion of the probes.[122,123] In 2015, D. Felder–Flesch and co–workers synthesized ^{111}In–radiolabeled nanoprobes, dendritic and of different generations, G_1 and G_2, bearing respectively 2 and 4 Melanin–targeting ICF01102 ligands.[124] Their *in vitro* and *in vivo* targeting efficiency towards Melanin was assessed in a murine melanoma model. Tumor uptake was correlated to dendrimer multivalency and reached values as high as 12.7 ± 1.6% ID.g^{-1} at 4h post intravenous injection for ^{111}In–G_2 *versus* 1.5 ± 0.5% ID.g^{-1} for the unfunctionalized DP, and over 11% ID.g^{-1} for any tumor weight whatsoever. Considering the cooperative effect and active–targeting properties of those dendrimers, we hypothesized that dendronized NPs would also be optimal candidates as intracellular–melanocytes targeting probes. To confirm such hypothesis and be able to quantify specific tumor uptake, we synthesized ^{177}Lu–DOTA–dendronized IONPs bearing or not Melanin–targeting ligands (ICF01102) and assessed their *in vivo* targeting efficiency in melanoma B16 mice after intravenous injection.

3.2 Synthesis of dendronized nanoparticles functionalized with melanine granules targeting agent

NPs@OA synthesized by thermal decomposition were functionalized with 2P_ $G_{0.5}$PAMAM _ COOH (D1) following the same procedure described in **Section 2.2**. Following purification step, the NPs' surface modification has been assessed by FTIR spectrometry **(Fig.103)** (Digilab FTS 3000).

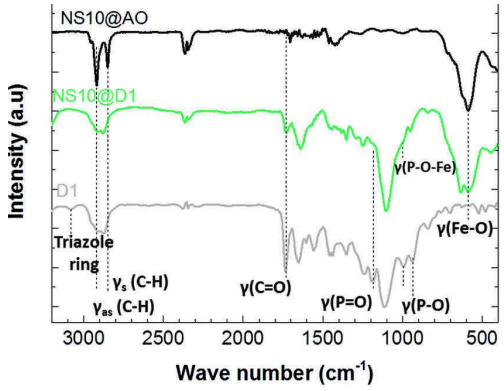

Figure 103: FTIR spactra of dendron D1, of NPs10@OA before and after functionalization with D1.

The FTIR spectrum of D1 displays several bands between 1140 and 1376cm^{-1} and one at 735cm^{-1} corresponding to C–H bonds. The characteristic bands of asymmetric and symmetric vibrations of CH_2

groups are identified at 2920 and 2850cm^{-1}. The band at 1734cm^{-1} belongs to the Carboxylic acid function. The C–O–C groups of PEG chains are characterized by a band at 1100cm^{-1}. The latter band should also include the C–C–C groups of the aromatic cycle. The band at 3083cm^{-1} is characteristic of the triazole cycle and those between 1690 at 1320cm^{-1} to N–H, N–C at C–N=O bonds. The band at 1180cm^{-1} is attributed to the P=O bond and bands at 1054 and 993cm^{-1} to P–OH bonds. After the ligand exchange, the characteristic bands of D1 are identified and in particular the phosphonate bands, which evolved. The P=O band intensity strongly decreased and the P–OH bands disappeared while new bands characteristic of the Fe–O–P bonds appeared especially one at 1035cm^{-1}. Thus, the dendron D1 has been grafted at the surface of NPs10.

DLS and TEM analysis were performed on NPs10@D1 suspensions at pH = 7.4 in order to assess their colloidal stability and size distribution **(Fig.104)**.

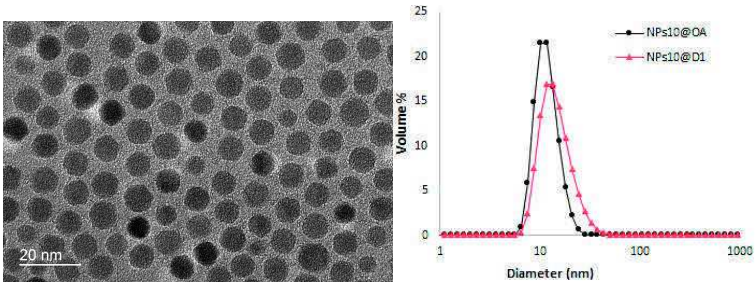

Figure 104: NPs@D1 TEM image (left), size distribution by volume before and after grafting of NPs10@OA with D1 (right).

After ligand exchange, the particle size distributions of functionalized NPs10 suspensions are monomodal (confirmed by TEM images **(Fig.104.left)**) with an average hydrodynamic diameter (16.8nm) slightly larger than that of NPs@OA (12nm) **(Fig.104. right)**.

NPs10@D1 were further conjugated to 2,2',2"–(10– (4– ((2 –Aminoethyl) Amino)–1 – Carboxy – 4 – oxobutyl) –1,4,7,10– Tetraazacyclododecane–1,4,7–triyl) Triacetic acid (NH_2–DOTA[24]) through EDCI–mediated peptide coupling, for further labeling with ^{177}Lu – radionuclide **(Fig.105)**.

For *in vivo* MRI and Scintigraphy studies, NPs10@D1_DOTA was used as control for targeting nanoparticles NPs10@D1_ ICF_ DOTA. Since *ex vivo* Confocal Microscopy (CM) studies (on previously *i.v.* injected mice but also on human excised melanomas) have been planned, we also prepared Alexa–derived NPs such as NPs10@D1_ Alexa495_ DOTA (as control) and NPs10@D1_ ICF_ Alexa647_ DOTA as targeting probe.

Colloidal stability evaluated by DLS **(Fig.105.right)**, and changes in Zeta potential assessed NPs10@D1 functionalization with the different molecules of interest (DOTA, ICF01102 Alexa647 and Alexa495) **(Table 18)**. The change in hydrodynamic volume is in correlation with the added functionalities. Furthermore, **Fig.105.right** shows the preservation of a monomodal size distribution throughout addition of the different

[24]CheMatech, Usual Chemical Name NH2–DOTA–GA and CAS Number: 306776–79–4.

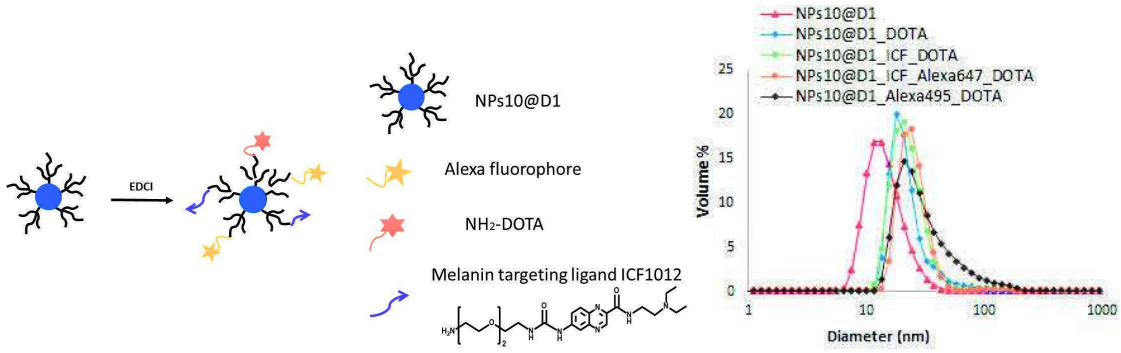

Figure 105: Schematic representation of functionalized NPs10@D1 with different moieties of interest (left) and size distribution by volume of engineered nanoprobes (right).

molecules on the NPs10@D1 periphery, thus enhancing the multivalency of such systems.

	d^{DLS} (nm)	PDI	Zeta potential (mV)
NPs10@D1	16.8	0.138	–15.9
NPs10@D1_DOTA	19.8	0.186	–20.7
NPs10@D1_ICF_DOTA	29.6	0.427	–11
NPs10@D1_ICF_Alexa647_DOTA	35.38	0.512	–5.83
NPs10@D1_Alexa495_DOTA	27.26	0.370	–1.89

Table 18: Size distribution by volume and Zeta potential at pH = 7.4, before and after decoration of dendronized NPs with different molecules of interest.

3.3 *In vitro* and *in vivo* studies

***In vitro* MRI studies** Relaxation properties of NPs10@D1_DOTA and NPs10@D1_ ICF_DOTA colloidal suspensions were studied in order to evaluate their possible use as MRI CAs. T_1 and T_2 values were measured over a concentration range of 1 to 230µM and to 244µM for NPs10@D1_DOTA and NPs@D1_ ICF_DOTA respectively, diluted in doped water (1µM $MnCl_2$). A solution of doped water was used as control sample. Relaxometric rates ($1/T_1$ and $1/T_2$) were calculated and the results were plotted as a function of Fe^{3+} concentration **(Fig.106)**.

Longitudinal relaxivity rates (R_1) were founded in the same range, and of 2.9 and 2.6$mM^{-1}{\cdot}s^{-1}$ for NPs10@D1_DOTA and NPs10@D1_ ICF_ DOTA respectively **(Table 19)**.

Transverse relaxation rates (R_2) vary considerably between NPs10@D1_ DOTA and NPs10@D_ ICF_ DOTA. Indeed, if a r_2 relaxivity value as high as 144.5 $mM^{-1}{\cdot}s^{-1}$ was obtained for NPs10@D1_ DOTA, it lowered down to 99.3 $mM^{-1}{\cdot}s^{-1}$ for NPs10@D1_ ICF_ DOTA **(Table 19)**. Consequently, grafting of ICF01102 at the dendronized NPs' periphery causes a r_2 relaxivity decrease of about 30% which can be attributed to the ligand hydrophobicity, thus precluding water molecules to circulate freely close to the magnetic core.

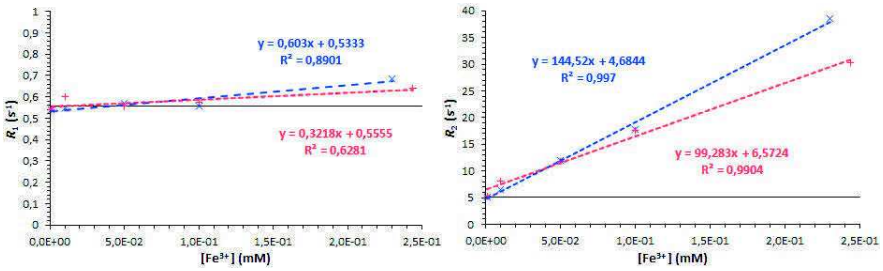

Figure 106: Longitudinal (R_1, left) and transverse (R_2, right) relaxation rates of NPs10@D1_DOTA (blue) and NPs10@D1_ICF_DOTA (red) at different Fe^{3+} concentrations. Black line represents doped water relaxation.

	R_1 (s^{-1})	R_2 (s^{-1})	r_1 ($mM^{-1}{\cdot}s^{-1}$)	r_2 ($mM^{-1}{\cdot}s^{-1}$)	r_2/r_1
Doped Water	0.55	5	N/A	N/A	N/A
NPs10@D1_DOTA ([Fe^{3+}]=230µM)	0.68	38.5	2.9	144.5	49.8
NPs10@D1_ICF_DOTA ([Fe^{3+}]=244µM)	0.64	31.7	2.6	99.3	38.19

Table 19: *In vitro* relaxivity values of dendronized NPs compared to doped water, measured at 1.5T.

The contrast enhancement properties of NPs10@D1_DOTA and NPs10@D1_ICF_DOTA were evaluated. Enhancement contrast ratios (EHC) were extracted from T_{2w} images (TR = 10,000ms) and calculated according to **Eq.6**, where S_{NPs}= signal value of DPs at each Fe^{3+} concentration and S_{water}= signal value of water:

$$EHC\ \% = \frac{S_{NPs} - S_{water}}{S_{water}} \times 100\ \% \tag{6}$$

The high EHC values obtained for both dendronized NPs confirmed their great contrast power **(Fig.107)**. High Fe^{3+} concentrations led to signal loss for both DPs. Higher signal dropouts were noticed for NPs10@D1_ICF_ DOTA at very low Fe^{3+} concentrations.

For an echo time compatible with *in vivo* experiments, TE/TR = 100/2000ms parameters were used and image acquisition was both T_1 and T_2–weighted. **Fig.108.left** shows ghost images as a function of Fe^{3+} concentrations for NPs10@D1_DOTA. For the highest Fe^{3+} concentration, 0.23mM, EHC % as high as 96% was obtained. One must also notice a slight positive contrast at the lowest Fe^{3+} concentrations (1 to 10µm) **(Fig.108.right)**.

Even if ICF–ligand grafting at the dendronized NPs' periphery induced a 30% decrease in r_2 relaxivity *in vitro*, those dendronized NPs10@D1_ICF_DOTA still show an important r_2 value, and high enough for *in vivo* investigations. These interesting properties might be related to the design of the DPs, which permits both preservation of the NPs magnetic properties and the minimization of the organic shell thickness

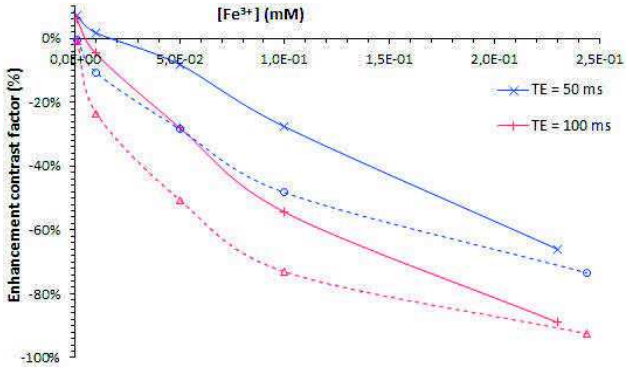

Figure 107: EHC % of NPs10@D1_DOTA (solid line) and NPs10@D1_ICF_DOTA (dotted line) at 50 (blue) and 100ms (red) echo times.

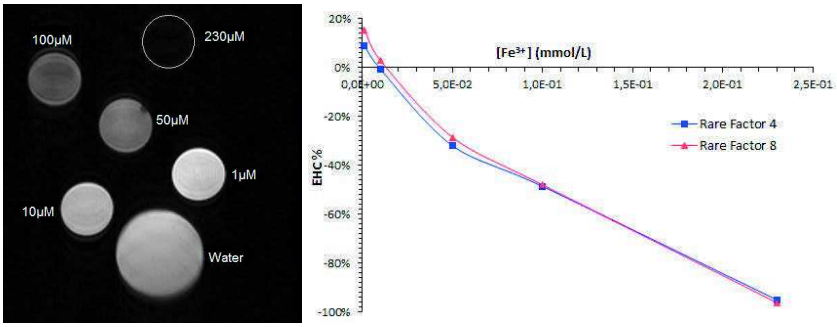

Figure 108: (left) Ghost images of NPs10@D1_DOTA at different Fe^{3+} concentrations, obtained in 100s with a RARE factor of 8 and TE/TR = 100/200ms. (right) Evolution of EHC according to two Rare factors.

necessary for good water diffusion and thus higher MRI responses.

***In vivo* MRI studies** *In vivo* experiments were performed by Dr. Elisabeth Miot–Noirault[25] on C57Bl6J mice carrying interspecies transplants of murine melanoma (B16F0). All experiments were performed 25 days post–transplantation when tumors were tangible (tumors of less than $1cm^3$). MR coronal images were collected using a BioSpec MRI at 11.7T, with a RARE factor of 4 and TE/TR = 12/2500ms.

Before administration of the CA, a T_2–weighted 2D MRI spin echo scan was performed, and coronal images of the animal were acquired **(Fig.109.top)**.

Then, the mice were injected with 200µL of NPs10@D1_ICF_DOTA at 12.2mM, which correspond to a 45µmol $[Fe^{3+}]$/kg body weight dose. Coronal images are represented in **Fig.109.bottom** for slices corresponding to different ROIs: tumor, kidneys, liver and urinary bladder.

At 15 minutes following the injection, NPs10@D1_ICF_DOTA particles provided a clear and immediate liver signal enhancement effect, on the contrary low tumor uptake of DP and no signs of urinary elimination have been noticed, which can be due to the short acquisition time post *iv* injection. During the injection

[25] UMR INSERM /UdA 990, 63005 Clermont–Ferrand, France.

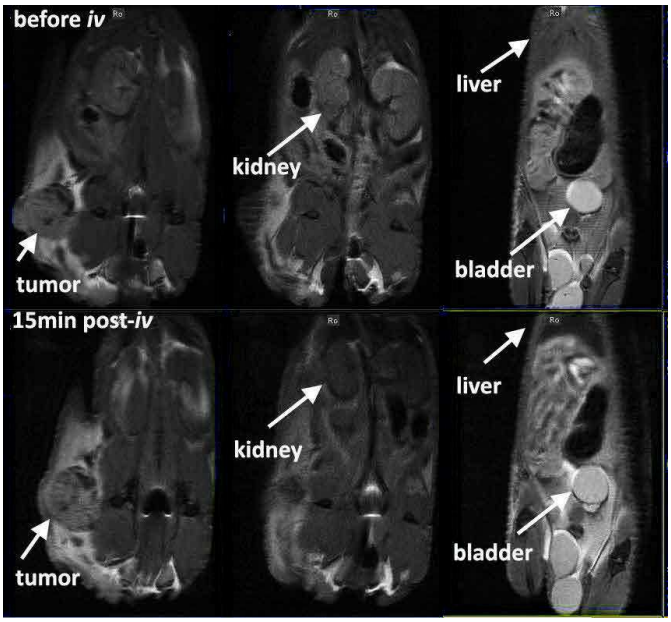

Figure 109: MR images with a T_2–weighted spin–echo sequence (TR 2500, TE 12) of NPs10@D1_ICF_DOTA injected mouse at t = 0 (top) and 15min post *iv* (bottom).

process, the mouse changed the position inside the MRI instrument, thus kidney images differ.

Furthermore, recorded EHC % of each ROI (kidneys, liver, tumor and muscle) allowed comparing the MRI signal effect as a function of the injected NPs' concentration and to follow the biodistribution processes over a longer period of time (100min) after *iv* injection. Injections have been made with either 100µL of NP@D1_ICF_DOTA at low (6.1mM) and high (12.2mM) Fe^{3+} concentration or with 200µl at 12.2mM Fe^{3+} concentration **(Fig.110)**. EHC were calculated according to **Eq.7**, where S_{biv}= signal value of the ROI before *iv* injection and S_{aiv}= signal value of the same ROI after *iv* injection:

$$EHC\ \% = \frac{S_{aiv} - S_{biv}}{S_{biv}} \times 100\% \tag{7}$$

After injection of 12.2mM NPs10@D1_ICF_DOTA for both volumes, a high negative contrast enhancement was observed in the liver (from –40 to – 60% at 15 minutes post–*iv*), and also in the kidneys ($\sim$ –40% at 5 – 10 minutes post–*iv*) with a maximum at 20min post injection; in the muscle and tumor, the obtained EHC values were of $\sim$ –20% and relatively stable over time for injections of 200µL at 12.2mM. Furthermore, for 12.2mM dose injections at different volumes, the decrease of EHC over time in liver and kidneys, points out the potential hepatobiliary and urinary eliminations after short period of time post *iv* injections.

EHC values for low concentration dose, 100µL at 6.1mM, of NPs10@D1_ICF_DOTA show maximum uptake by the liver at 20min post *iv* and positive contrast enhancement for muscle over 40min, kidneys or

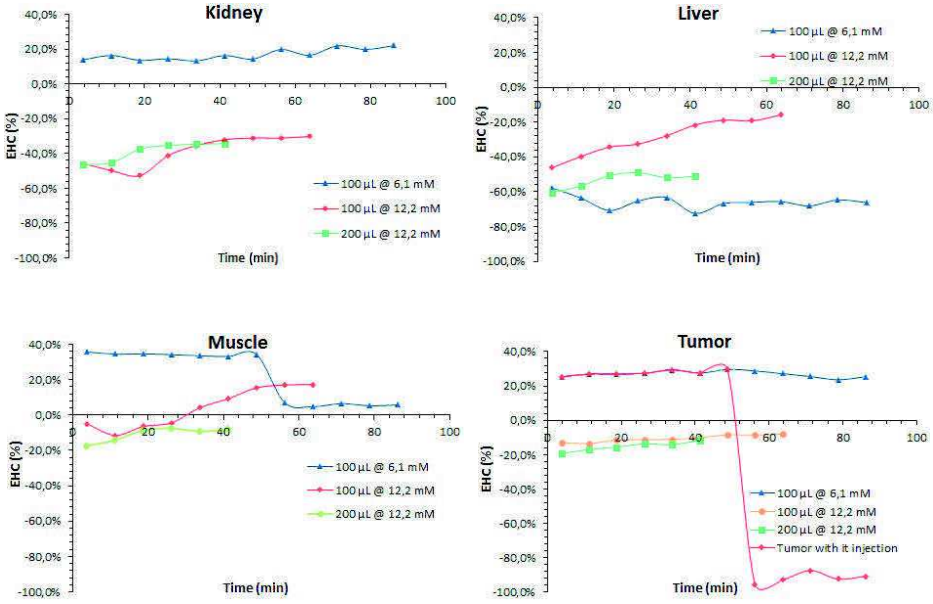

Figure 110: Calculated EHC % for different ROIs over time after intravenous injection of NPs10@D1_ICF_DOTA at various Fe^{3+} concentrations.

tumor over 80min.

In order to assess NPs10@D1_ICF_DOTA contrast in tumor, direct intratumoral (it) injection of 100 µL at 6.1mM was investigated and the MR images were recorded over 40 minutes post–*it* **(Fig.111)**. Recorded EHC values in the tumor **(Fig.110)** show a maximum of –100% at *it* injection time (50min post *iv*) and the slight evolution of the contrast enhancement over 40min confirms the absence of NPs10@D1_ICF_DOTA propagation outside the tumor.

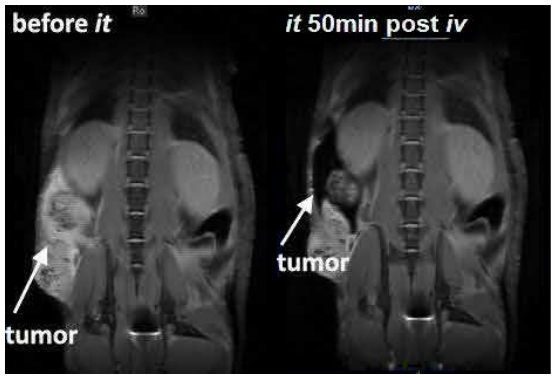

Figure 111: MR images with a T_2–weighted spin–echo sequence (TR 2500, TE 12) of NPs10@D1_ICF_DOTA injected mouse at t = 0 (left) and 50min post–*it* (right).

The biodistribution kinetics of NPs10@D1_DOTA have also been studied after intraperitoneal (*ip*) injection of 100µL at 11.5mM **(Fig.112)**. EHC values showed a maximum liver contrast of –60% at 180min

post–*ip* and very low contrast enhancement in tumor, muscles and bladder. On the other hand, EHC signal started increasing in kidneys at 150min post–*ip*, indicating NPs' accumulation and a possible urinary excretion.

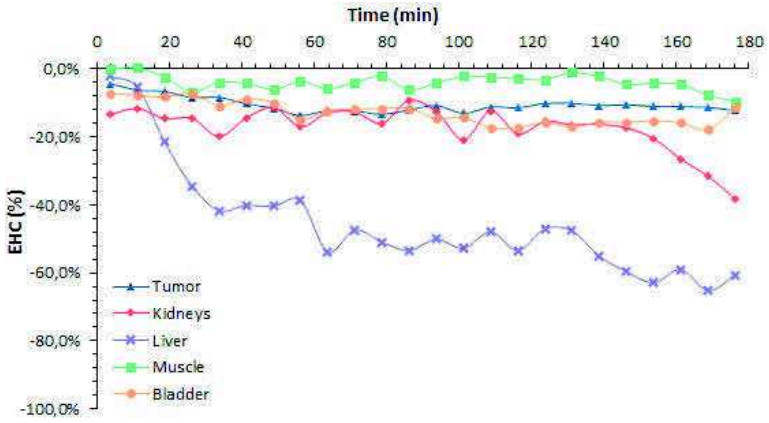

Figure 112: EHC % values for different ROIs over time after intraperitoneal injection of 100µL NPs10@D1_DOTA at 11.5mM of Fe^{3+}.

However, biodistribution kinetics are much slower after *ip* injection as shown by EHC values in bladder and liver. Thus, 180min might not be a timescale long enough to assess the *in vivo* behavior of NPs10@D1_DOTA

Those *in vivo* MRI studies lean toward urinary and hepatobiliary excretions of both DPs although longer timescales have to be explored. The targeting probe NPs10@D1_ICF_DOTA presented low specific tumor uptake as a low EHC value of –20% maximum has been recorded. However a precise quantification through those MRI studies has not been achieved so far. Such results tend to prove that conjugation of ICF01102 onto NPs decreases its binding–power towards Melanocytes.

In vivo planar scintigraphy studies

Radiolabeling with ^{177}Lu For biodistribution studies using planar scintigraphy, dendritic probes (DPs) NPs10@D1_ DOTA and NPs10@ D1_ICF_DOTA were labeled using Lutecium–177 radionuclide (half–life: 6.65 days) in collaboration with Prof. Jean–Michel Chezal[26]. Briefly, 0.6µL of high purity $^{177}LuCl_3$[27] in diluted HCl (0.05N) were added to 0.03mg of DP in 50µL Ammonium acetate buffer. The mixture was incubated for 45min at 60°C. ^{177}Lu–DPs were separated from free $^{177}LuCl_3$ by centrifugation through Amicon Ultracel 50kDa (Merck Millipore) filters. Radiochemical purity of each fraction was performed to ensure that no radiochemical impurities would be present in the radiolabeled complex solution, which could have different patterns of biodistribution render the investigation meaningless. ITLC[28] of the

[26] UMR INSERM /UdA 990, 63005 Clermont–Ferrand, France.
[27] $^{177}LuCl_3$/ 0.05N HCl –Perkin Elmer.
[28] ITLC– Instant Thin Layer Chromatography.

purified ^{177}Lu–DPs were performed using silica gel plates impregnated glass fibber sheets in 1mM EDTA solution as the solvent. ^{177}Lu–DPs remained at the origin with an Rf value of 0, whereas residual $^{177}LuCl_3$ migrated with an Rf of 1. Finally, the fractions with the highest radioactivity and the highest radiochemical purity were pooled. The radiolabeled solution was stable over time, presenting no aggregates, with a high radiochemical purity, 94%. Radiochemical yields of $\backsimeq$ 82% were obtained. At 15 hours post labeling, radiochemical purity decrease was observed for ^{177}Lu–DPs to 89%, which indicate that radiolabeled DPs were kinetically stable and suitable to perform *in vivo* quantitative biodistribution.

ICF01102 have already shown high, specific and long lasting binding to melanin[125] resulting from ionic and hydrophobic interactions.[126] In order to study whether the melanin–targeting ligand derived from ICF01102 remains able to recognize the melanin target once grafted onto the dendronized NPs, *in vitro*, *in vivo* and *ex vivo* experiments have been performed.

In order to evaluate the ability of ^{177}Lu–DPs to target tumors *in vivo*, biodistribution studies were performed in B16F0 melanoma bearing mice at 30min, 2h, 6h and 24h post intravenous injection in the caudal vein. Solutions of NPs10@D1_DOTA_^{177}Lu or NPs10@D1_ICF_DOTA_^{177}Lu were injected in mice at 3.7MBq / mouse and 5MBq / mouse respectively. Tissues distribution is expressed as the average signal intensity of tumor / muscle ratio ($\triangle$TMR%) and was calculated according to **Eq.8**, where S_{tumor} = average signal intensity in tumor and S_{muscle} = average signal intensity in muscle:

$$\triangle TMR\,\% = \frac{S_{tumor} - S_{muscle}}{S_{muscle}} \tag{8}$$

Mice were sacrificed and organs of interest (heart, lungs, spleen, liver, brain, kidneys, bones (one vertebra) and muscles) were weighted and harvested for further *ex vivo* quantification of Fe^{3+}. Planar scintigraphy images are represented in **Fig.113** and show the biodistribution over time in mice injected with the control and melanoma–specific targeting agent ^{177}Lu–DPs.

At 30min post *iv* injection of NPs10@D1_DOTA_^{177}Lu high level of radioactivity were observed in liver and kidneys **(Fig.113.top)**. Highest tumor uptake can also be noticed at such short time delay post *iv* injection. At 24h *pi*, the radioactive signal decreased in liver and increased in lungs, emphasizing the DP metabolization or degradation process over time. Regarding NPs10@D1_ICF_DOTA_^{177}Lu, most of the radioactivity was observed in liver and bladder at 30min *pi* **(Fig.113.bottom)** however its lower biodistribution kinetics was evidenced by the highest radioactivity level in tumor at 6h, whereas NPs10@D1_DOTA_^{177}Lu was uptaken by the tumor at 30min post *iv*. Renal excretion is evidenced by the increase of bladder radioactive signal at 6h *pi*. But one must notice also bone signal due to free ^{177}Lu thus evidencing degradation of NPs10@D1_ICF_DOTA_177Lu a few hours post *iv*. The TMR % was evaluated for both DPs and is

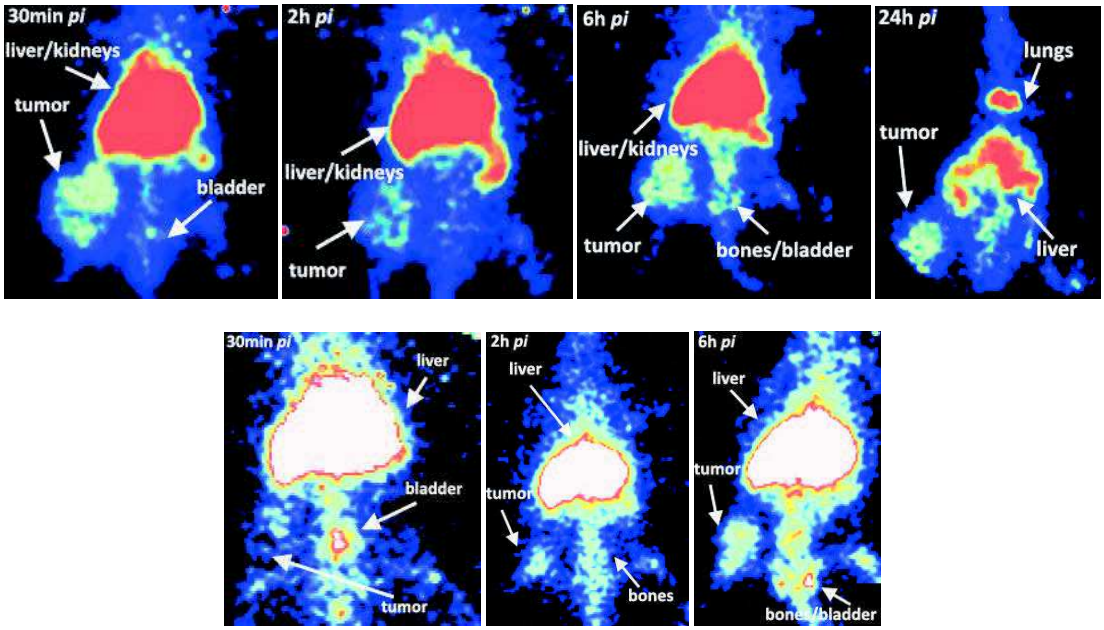

Figure 113: Planar scintigraphy images of mice injected with (top) 5MBq NPs10@D1_DOTA_^{177}Lu and (bottom) 3.7MBq NPs10@D1_ICF_DOTA_^{177}Lu at various time post injection.

represented in **Fig.114**.

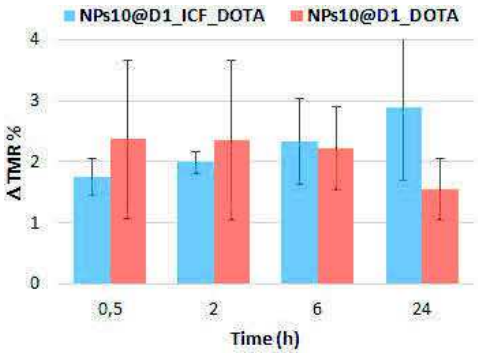

Figure 114: Quantitative analysis of ^{177}Lu – radiolabeled probes at 30min, 2h, 6 and 24h post *iv*, expressed as tumor to muscle ratio (TMR).

NPs10@D1_DOTA_^{177}Lu was predominantly uptaken by the tumor upon first two hours after *iv* injection, showing a TMR ratio of 2.37 ± 0.3 at 2h *pi*. The highest tumor accumulation was observed with NPs10@D1 _ICF_DOTA_^{177}Lu at 24h *pi* (TMD = 2.89 ± 1.2), while at this time, NPs10@D1_DOTA_^{177}Lu radioactive signal in tumor decreased down to a TMR ratio of 1.55 ±0.3.

The TMR signal distribution showed a moderate specific tumor uptake of ICF01102 – functionalized NPs at 24h *pi*, underlining a higher mean blood residence time in comparison with the control sample. Both ^{177}Lu–DPs showed hepatobiliary and urinary excretions. Specific tumor targeting shall further be confirmed

by *ex vivo* Fe^{3+} quantification in organs of interest currently running in the laboratory.

***Ex vivo* Confocal Microscopy (EVCM) studies on Human samples** *Ex vivo* CM (EVCPM) studies on human samples were performed by Dr. Jean–Luc Perrot[29] on a dorsal Melanoma of a male patient **(Fig.115)**. Elliptical excisional biopsy was performed and tumor samples of 4mm thickness were excised.

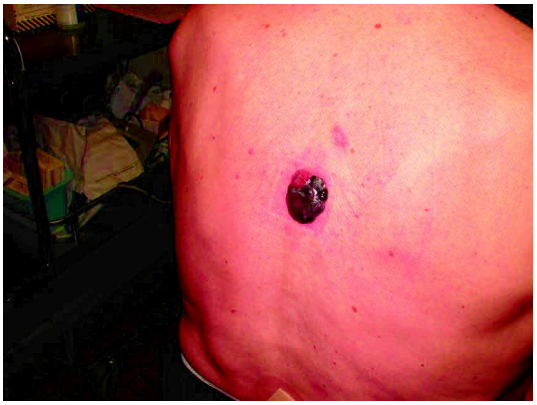

Figure 115: Male patient picture with a dorsal malignant Melanoma, from whom tumor samples were excised for *ex vivo* confocal microscopy (EVCM) studies.

Fresh tissues were incubated with few drops of NPs10@D1 at 1.05mg/mL or NPs10@D1_ ICF_ Alexa647_ DOTA at 0.67mg/mL Fe^{3+} concentration. Confocal images were acquired using a laser scanning fluorescence confocal microscope Vivascope 2500 with 658nm wavelength reflectance / fluorescence filter. Analyses were performed at different incubation times and confocal mosaics were further processed with dark tones.

Confocal images of impregnated malignant Melanoma samples with NPs10@D1 were acquired after 45 and 95min impregnation. Results showed low fluorescence signal at both times, whereas EVCM mosaics of Melanoma sample impregnated with NPs10@D1_ ICF_ Alexa647_ DOTA for 25min, shown in **Fig.116**, showed a moderate fluorescence of the cells co–localized with Melanine granules.

Furthermore, studies have been made at longer impregnation time (75 min) with NPs10@D1_ ICF_ Alexa647_DOTA **(Fig.117)** and in this case EVCM images showed a very high fluorescence signal of tumor cells at 658nm. Co–localization of malignant Melanoma cells with the ICF–labelled DP' fluorescence, illustrates a specific staining of the cells without affecting the surrounding background dermis.

[29]CHU, Dermatology department, 42000 St. Etienne, France.

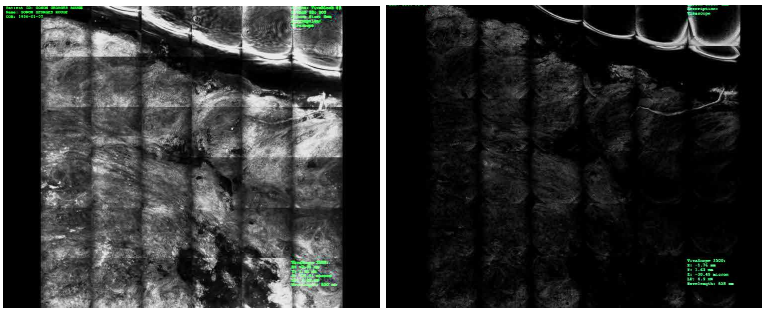

Figure 116: (left) Reflectance confocal microscopy (RCM) image of malignant Melanoma sample and (right) fluorescence confocal microscopy image of malignant Melanoma sample at 25min impregnation with NPs10@D1_ ICF_ Alexa647_ DOTA.

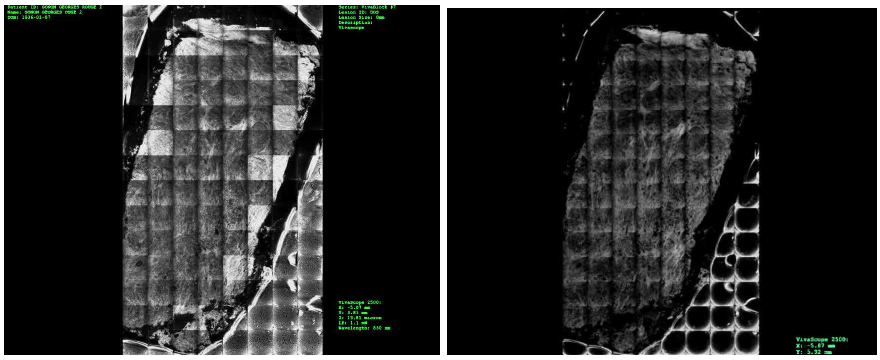

Figure 117: (left) RCM image of malignant Melanoma sample and (right) FCM image of malignant Melanoma sample at 75min impregnation with NPs10@D1_ ICF_ Alexa647_ DOTA.

Conclusion The biodistribution of NPs10@D1_DOTA and NPs10@D1_ICF_DOTA were studied *in vivo* using MRI and planar scintigraphy through ^{177}Lu – radiolabeling. MRI experiments showed high contrast power of both DPs and hepatobiliary and urinary excretions. Little tumor uptake could be highlighted probably as a consequence of the negatively charged DOTA–derivatized shell which reduces the diffusion across the cells' membrane. Planar scintigraphy images demonstrated a moderate specific tumor uptake of melanoma–targeted ^{177}Lu – DPs at 24h post intravenous injection, with a tumor over muscle ratio (TMR) of 2.89±1.2, and a highest tumor uptake of the control probe at 30min *pi*, probably due to the EPR effect. In addition, *ex vivo* confocal microscopy (EVCM) studies showed a high specific targeting of human malignant Melanoma samples impregnated with NPs10@D1_ ICF_ Alexa647_ DOTA. Further EVCM studies on human samples are scheduled on 6 over–expressing melanin and amelanotic Melanomas, 3 basal cell carcinoma and 3 naevus. These studies will assess the ability of ICF–labelled DP to accurately identify cancerous from normal tissues and diagnose correctly a skin tumor. Additionally, studies for fluorescence quantification are to be performed, in order to assess the DP' performance.

References

[1] Berry, C.C., Curtis, A.S.G. Functionalisation of magnetic nanoparticles for applications in biomedicine. *Journal of Physics D Applied Physics*, **2003**, 36, R198-R206.

[2] Bertrand, N., Wu, J., Xu, X., Kamaly, N., Farokhzad, O.C. Cancer nanotechnology the impact of passive and active targeting in the era of modern cancer biology. *Advanced drug delivery reviews*, **2014**, 66, 2-25.

[3] Ghobril, C., Lamanna, G., Kueny-Stotz, M., Garofalo, A., Billotey, C., Felder-Flesch, D. Dendrimers in nuclear medical imaging. *New Journal of Chemistry*, **2012**, 36(2), 310-323.

[4] Jeong, U., Wang, Y., Ibisate, M., Xia, Y. Some New Developments in the Synthesis, Functionalization, and Utilization of Monodisperse Colloidal Spheres. *Advanced Functional Materials*, **2005**, 15(12), 1907-1921.

[5] Gao, J., Gu, H., Xu, B. Multifunctional magnetic nanoparticles design, synthesis, and biomedical applications. *Accounts of chemical research*, **2009**, 42(8), 1097-1107.

[6] Reddy, L.H., Arias, J.L., Nicolas, J., Couvreur, P. Magnetic nanoparticles design and characterization, toxicity and biocompatibility, pharmaceutical and biomedical applications. *Chemical reviews*, **2012**, 112(11), 5818-5878.

[7] Carrillo, A.I., Serrano, E., Luque, R., Garcia-Martinez, J. Microwave-assisted catalysis by iron oxide nanoparticles on MCM-41 Effect of the support morphology. *Applied Catalysis A General*, **2013**, 453, 383-390.

[8] Hutten, A., Reiss, G. Applications beyond data storage. *Nature materials*, **2005**, 4(10), 725-726.

[9] Pereira, C., Pereira, A.M., Fernandes, C., Rocha, M., Mendes, R., Guedes, A., Tavares, P.B., Grene, J., Arau, P., Freire, C. Superparamagnetic MFe 2 O 4 M. *Chemistry of Materials*, **2012**, 24(8), 1496-1504.

[10] Karaagac, O., Kockar, H. Effect of Synthesis Parameters on the Properties of Superparamagnetic Iron Oxide Nanoparticles. *Journal of Superconductivity and Novel Magnetism*, **2011**, 25(8), 2777-2781.

[11] Lu, A., Salabas, E.L., Schuth, F. Magnetic nanoparticles synthesis, protection, functionalization, and application. *Angewandte Chemie International ed. in English*, **2007**, 46(8), 1222-1244.

[12] Grene, J.M., Bernhardt, P., Leuvrey, C., Rogez, G., Pasteur, L., Cedex, S. Hydrothermal Synthesis of Monodisperse Magnetite Nanoparticles. *Chemistry of Materials*, **2006**, 18, 4399-4404.

[13] Chen, D., Xu, R. Hydrothermal Synthesis and Characterization of Nanocrystalline Fe3O4Powders. *Materials Research Bulletin*, **1998**, 33(7), 1015-1021.

[14] Joseyphus, R.J., Kodama, D., Matsumoto, T., Sato, Y., Jeyadevan, B., Tohji, K. Role of polyol in the synthesis of Fe particles. *Journal of Magnetism and Magnetic Materials*, **2007**, 310(2), 2393-2395.

[15] Solinas, S., Piccaluga, G., Morales, M.P., Serna, C.J Sol-gel formation of g-Fe2O3SiO2 nanocomposites. *Acta Materials*, **2001**, 49(14), 2805-2811.

[16] Sun, S., Zeng, H. Size-Controlled Synthesis of Magnetite Nanoparticles. *Journal of American Chemical Society*, **2002**, 124(28), 8204-8205.

[17] Sun, S., Zeng, H., Robinson, D.B., Raoux, S., Rice, P.M., Wang, S.X., Li, G. Monodisperse MFe2O4 M. *Journal of American Chemical Society*, **2004**, 4(1), 126-132.

[18] Park, J., An, K., Hwang, Y., Park, J., Noh, H., Kim, J., Park, J., Hwang, N., Hyeon, T. Ultra-large-scale syntheses of monodisperse nanocrystals. *Nature materials*, **2004**, 3(12), 891-895.

[19] Jeong, U., Teng, X., Wang, Y., Yang, H., Xia, Y. Superparamagnetic Colloids Controlled Synthesis and Niche Applications. *Advanced Materials*, **2007**, 19(1), 33-60.

[20] Baaziz, W., Pichon, B.P., Fleutot, S., Liu, Y., Lefevre, C., Greneche, J., Toumi, M., Mhiri, T., Begin-colin, S. Magnetic Iron Oxide Nanoparticles Reproducible Tuning of the Size and Nanosized-Dependent Composition , Defects , and Spin Canting. *Physical Chemistry*, **2014**, 118, 3795-3810.

[21] Dimo Kashchiev Nucleation Basic theory with applications. *Butterworth-Heinemann*, **2000**.

[22] Wang, Y., Xu, X., Tian, Z., Zong, Y., Cheng, H., Lin, C. Selective heterogeneous nucleation and growth of size-controlled metal nanoparticles on carbon nanotubes in solution. *Chemistry Weinheim an der Bergstrasse, Germany*, **2006**, 12(9), 2542-2549.

[23] van Embden, J., Sader, J.E., Davidson, M., Mulvaney, P. Evolution of Colloidal Nanocrystals Theory and Modeling of their Nucleation and Growth. *The Journal of Physical Chemistry C*, **2009**, 113(37), 16342-16355.

[24] LaMer, V.K., Dinegar, R.H. Theory, Production and Mechanism of Formation of Monodispersed Hydrosols. *Journal of the American Chemical Society*, **1950**, 72(11), 4847-4854.

[25] Derjaguin, B.V., Voropayeva, T.N., Titiyevskaya, A.S., Kabanov, B.N Surface Forces and the Stability of Colloids and Disperse Systems. *Journal of Colloid Science*, **1964**, 19, 113-135.

[26] Derjaguin, B. On the Repulsive Forces between Charged Colloid Particules and on the Theory of slow Coagulation Stability of Lyophobe Sols. *Transactions of the Farady Society*, **1939**, 35, 203-215.

[27] Bacri, J., Perzynski, R., Salin, D. Ionic Ferrofluids A Crossing of Chemistry and Physics. *Journal of Magnetism and Magnetic Materials*, **1990**, 85, 27-32.

[28] Lamanna, G., Kueny-Stotz, M., Mamlouk-Chaouachi, H., Ghobril, C., Basly, B., Bertin, A., Miladi, I., Billotey, C., Pourroy, G., Begin-Colin, S., Felder-Flesch, D. Dendronized iron oxide nanoparticles for multimodal imaging. *Biomaterials*, **2011**, 32(33), 8562-8573.

[29] Duanmu, C., Saha, I., Zheng, Y., Goodson, B.M., Gao, Y. Dendron-Functionalized Superparamagnetic Nanoparticles with Switchable Solubility in Organic and Aqueous Media Matrices for Homogeneous Catalysis and Potential MRI Contrast Agents. *Chemistry of Materials*, **2006**, 18(25), 5973-5981.

[30] Wu, X., He, X., Zhong, L., Lin, S., Wang, D., Zhu, X., Yan, D. Water-soluble dendritic-linear triblock copolymer-modified magnetic nanoparticles preparation, characterization and drug release properties. *Journal of Materials Chemistry*, **2011**, 21(35), 13611-13620.

[31] Rouhollah, K., Pelin, M., Serap, Y., Gozde, U., Ufuk, G. Doxorubicin Loading , Release , and Stability of Polyamidoamine Dendrimer-Coated Magnetic Nanoparticles. *Journal of Pharmaceutical Sciences*, **2013**, 102(6), 1825-1835.

[32] Basly, B., Felder-Flesch, D., Perriat, P., Pourroy, G., Begin-Colin, S. Properties and suspension stability of dendronized iron oxide nanoparticles for MRI applications. *Contrast media molecular imaging*, **2011**, 6(3), 132-138.

[33] BRAGG, W.H. The Structure of Magnetite and the Spinels. *Nature*, **1915**, 95(2386), 561-562.

[34] Fleet, M.E. The structure of magnetite Symmetry of cubic spinels. *Journal of Solid State Chemistry*, **1986**, 62(1), 75-82.

[35] Daou, T.J., Greneeche, J.M., Pourroy, G., Buathong, S., Derory, A., Ulhaq-Bouillet, C., Donnio, B., Guillon, D., Begin-Colin, S. Coupling Agent Effect on Magnetic Properties of Functionalized Magnetite-Based Nanoparticles. *Chemistry of Materials*, **2008**, 20(18), 5869-5875.

[36] Park, J., Lee, E., Hwang, N., Kang, M., Kim, S.C., Hwang, Y., Park, J., Noh, H., Kim, J., Park, J., Hyeon, T. One-nanometer-scale size-controlled synthesis of monodisperse magnetic iron oxide nanoparticles. *Angewandte Chemie*, **2005**, 44(19), 2873-2877.

[37] Demortiere, A., Panissod, P., Pichon, B.P., Pourroy, G., Guillon, D., Donnio, B., Begin-Colin, S. Size-dependent properties of magnetic iron oxidenanocrystals. *Nanoscale*, **2011**, 3(1), 225-232.

[38] Weiss, P. Lhypothese du champ moleculaire et la propriete ferromagnetique. *Journal de Physique Theorique et Appliquee*, **1907**, 6(1), 661-690.

[39] Kittel, C. Physical theory of ferromagnetic domains. *Reviews of modern physics*, **1949**, 21(4), 541-583.

[40] Schneider, C.S. Role of reversible susceptibility in ferromagnetic hysteresis. *Journal of Applied Physics*, **2002**, 91(10), 7637-7639.

[41] Teja, A.S., Koh, P.Y. Synthesis, properties, and applications of magnetic iron oxide nanoparticles. *Progress in Crystal Growth and Characterization of Materials*, **2009**, 55(1-2), 22-45.

[42] Frenkel, J., Doefman, J. Spontaneous and Induced Magnetisation in Ferromagnetic Bodies. *Nature*, **1930**, 126(3173), 274-275.

[43] Chen, D.X., Sanchez, A., Taboada, E., Roig, A., Sun, N., Gu, H.C. Size determination of superparamagnetic nanoparticles from magnetization curve. *Journal of Applied Physics*, **2009**, 105(8), 0839241- 0839246.

[44] Langevin, M.P Magnetism and electron theory. *Annales de chimie et de physique*, **1905**, 5(8), 70-127.

[45] Roch, A., Gossuin, Y., Muller, R.N., Gillis, P. Superparamagnetic colloid suspensions Water magnetic relaxation and clustering. *Journal of Magnetism and Magnetic Materials*, **2005**, 293(1), 532-539.

[46] Laurent, S., Forge, D., Port, M., Roch, A., Robic, C., Vander Elst, L., Muller, R.N. Magnetic iron oxide nanoparticles synthesis, stabilization, vectorization, physicochemical characterizations, and biological applications. *Chemical reviews*, **2008**, 108(6), 2064-2110.

[47] Roch, A., Gillis, P., Ouakssim, A., Muller, R.N Proton magnetic relaxation in superparamagnetic aqueous colloids a new tool for the investigation of ferrite crystal anisotropy. *Journal of Magnetism and Magnetic Materials*, **1999**, 201(1-3), 77-79.

[48] Roch, A., Muller, R.N., Gillis, P. Theory of proton relaxation induced by superparamagnetic particles. *The Journal of Chemical Physics*, **1999**, 110(11), 5403-5411.

[49] Gossuin, Y., Gillis, P., Hocq, A., Vuong, Q.L., Roch, A. Magnetic resonance relaxation properties of superparamagnetic particles. *Nanomedicine and nanobiotechnology*, **2009**, 1, 299-310.

[50] Kaiser, R., Miskolczy, G. Magnetic properties of stable dispersions of subdomain magnetite particles. *Journal of Applied Physics*, **1970**, 41(3), 1064-1072.

[51] Thomas, G., Hutten, A. Characterization of nano-magnetic structures. *Nanostructured Materials*, **1997**, 9, 271-280.

[52] Inouye, K., Endo, R., Otsuka, Y., Mlyashiro, K., Keneko, K., Ishikawa, T. Axygenation of ferrous ions en reversed micelle and reversed microemulsion. *Proceedings Of The American Control Conference*, **1982**, 88(8), 1465-1469.

[53] Calvin, S., Carpenter, E., Harris, V. Characterization of passivated iron nanoparticles by x-ray absorption spectroscopy. *Physical Review B*, **2003**, 68(May), 0334111-0334114.

[54] Rao, S., Houska, C.R. X-ray diffraction profiles described by refined analytical functions. *Acta Crystallographica Section A*, **1986**, 42(1), 14-19.

[55] Rao, S., Houska, C.R. X-ray Particle-Size Broadening. *Acta Crystallographica Section A*, **1986**, A42, 6-13.

[56] Di Marco, M., Sadun, C., Port, M., Guilbert, I., Couvreur, P., Dubernet, C. Physicochemical characterization of ultrasmall superparamagnetic iron oxide particles USPIO for biomedical application as MRI contrast agents. *International Journal of Nanomedicine*, **2007**, 2(4), 609-622.

[57] Miller, C., Krasnow, J., Schwartz, L.H. Medical Imaging in Clinical Trials. *Springer Science Business Media*, **2014**.

[58] Wagner, V., Dullaart, A., Bock, A., Zweck, A. The emerging nanomedicine landscape. *Nature biotechnology*, **2006**, 24(10), 1211-1217.

[59] Kannan, R.M., Nance, E., Kannan, S., Tomalia, D.A. Emerging concepts in dendrimer-based nanomedicine from design principles to clinical applications. *Journal of internal medicine*, **2014**, 276(6), 579-617.

[60] Hadjipanayis, C.G., Machaidze, R., Kaluzova, M., Wang, L., Schuette, A.J., Chen, H., Wu, X., Mao, H. EGFRvIII antibody-conjugated iron oxide nanoparticles for magnetic resonance imaging-guided convection-enhanced delivery and targeted therapy of glioblastoma. *Cancer research*, **2010**, 70(15), 6303-6312.

[61] Liong, M., Lu, J., Kovochich, M., Xia, T., Ruehm, S.G., Nel, A.E., Tamanoi, F., Zink, J.I. Multifunctional inorganic nanoparticles for imaging, targeting, and drug delivery. *ACS nano*, **2008**, 2(5), 889-896.

[62] Pan, B., Cui, D., Sheng, Y., Ozkan, C., Gao, F., He, R., Li, Q., Xu, P., Huang, T. Dendrimer-modified magnetic nanoparticles enhance efficiency of gene delivery system. *Cancer research*, **2007**, 67(17), 8156-8163.

[63] Chang, Y., Liu, N., Chen, L., Meng, X., Liu, Y., Li, Y., Wang, J. Synthesis and characterization of DOX-conjugated dendrimer-modified magnetic iron oxide conjugates for magnetic resonance imaging, targeting, and drug delivery. *Journal of Materials Chemistry*, **2012**, 22(19), 9594-9601.

[64] Maier-Hauff, K., Ulrich, F., Nestler, D., Niehoff, H., Wust, P., Thiesen, B., Orawa, H., Budach, V., Jordan, A. Efficacy and safety of intratumoral thermotherapy using magnetic iron-oxide nanoparticles combined with external beam radiotherapy on patients with recurrent glioblastoma multiforme. *Journal of neuro-oncology*, **2011**, 103(2), 317-324.

[65] Flacke, S., Fischer, S., Scott, M.J., Fuhrhop, R.J., Allen, J.S., Mclean, M., Winter, P., Sicard, G.A., Gaffney, P.J., Wickline, S.A., Lanza, G.M. Novel MRI Contrast Agent for Molecular Imaging of Fibrin Implications for Detecting Vulnerable Plaques. *Circulation*, **2001**, 104, 1280-1285.

[66] Winter, P.M., Morawski, A.M., Caruthers, S.D., Fuhrhop, R.W., Zhang, H., Williams, T.A., Allen, J.S., Lacy, E.K., Robertson, J.D., Lanza, G.M., Wickline, S.A. Molecular imaging of angiogenesis in early-stage atherosclerosis with alphavbeta3-integrin-targeted nanoparticles. *Circulation*, **2003**, 108(18), 2270-2274.

[67] Winter, P.M., Caruthers, S.D., Kassner, A., Harris, T.D., Chinen, L.K., Allen, J.S., Lacy, E.K., Zhang, H., Robertson, J.D., Wickline, S.A., Lanza, G.M. Molecular Imaging of Angiogenesis in Nascent Vx-2 Rabbit Tumors Using a Novel targeted Nanoparticle and 1 . 5 Tesla Magnetic Resonance Imaging. *Cancer research*, **2003**, 63(314), 5838-5843.

[68] Lanza, G.M. Targeted Antiproliferative Drug Delivery to Vascular Smooth Muscle Cells With a Magnetic Resonance Imaging Nanoparticle Contrast Agent Implications for Rational Therapy of Restenosis. *Circulation*, **2002**, 106(22), 2842-2847.

[69] Gillich, T., Acikgo, C., Isa, L., Schlu, A.D., Spencer, N.D., Textor, M. PEG-Stabilized Core Shell Nanoparticles Impact of Linear versus Dendritic Polymer Shell Architecture on Colloidal Properties and the Reversibility of Temperature-Induced Aggregation. *ACS NANO*, **2013**, 7(1), 316-329.

[70] Liu, W., Xue, Y., Peng, N., He, W., Zhuo, R., Huang, S. Dendrimer modified magnetic iron oxide nanoparticleDNAPEI ternary magnetoplexes a novel strategy for magnetofection. *Journal of Materials Chemistry*, **2011**, 21(35), 13306-13315.

[71] Walter, a., Garofalo, A., Parat, A., Jouhannaud, J., Pourroy, G., Voirin, E., Laurent, S., Bonazza, P., Taleb, J., Billotey, C., Vander Elst, L., Muller, R.N., Begin-Colin, S., Felder-Flesch, D. Validation of a dendron concept to tune colloidal stability, MRI relaxivity and bioelimination of functional nanoparticles. *J. Mater. Chem. B*, **2015**, 3(8), 1484-1494.

[72] Boutry, S., Forge, D., Burtea, C., Mahieu, I., Murariu, O., Laurent, S., Elst, L.V., Muller, R.N. How to quantify iron in an aqueous or biological matrix A technical note. *Contrast Media and Molecular Imaging*, **2009**, 4(6), 299-304.

[73] Beilman, G. Pathogenesis of oleic acid-induced lung injury in the rat Distribution of oleic acid during injury and early endothelial cell changes. *Lipids*, **1995**, 30(9), 817-823.

[74] Cury-Boaventura, M.F., Pompeia, C., Curi, R. Comparative toxicity of oleic acid and linoleic acid on Jurkat cells. *Clinical Nutrition*, **2004**, 23(4), 721-732.

[75] Alves, M.M., Mota Vieira, J.A., Alvares Pereira, R.M., Pereira, M.A., Mota, M. Effect of lipids and oleic acid on biomass development in anaerobic fixed-bed reactors. Part I Biofilm growth and activity. *Water Research*, **2001**, 35(1), 255-263.

[76] Polito, L., Colombo, M., Monti, D., Melato, S., Caneva, E., Prosperi, D. Resolving the Structure of Ligands Bound to the Surface of Superparamagnetic Iron Oxide Nanoparticles by High-Resolution Magic-Angle Spinning NMR Spectroscopy Resolving the Structure of Ligands Bound to the Surface of Superparamagnetic Iron Oxide Nanopart. *J. Am. Chem. Soc*, **2008**, 130(4), 12712-12724.

[77] Mosmann, T. Rapid colorimetric assay for cellular growth and survival Application to proliferation and cytotoxicity assays. *Journal of Immunological Methods*, **1983**, 65(1-2), 55-63.

[78] Denizot, F., Lang, R. Rapid colorimetric assay for cell growth and survival. *Journal of Immunological Methods*, **1986**, 89(2), 271-277.

[79] Wan, H., Williams, R.L., Doherty, P.J., Williams, D.F. The cytotoxicity evaluation of Kevlar and silicon carbide by MTT assay. *Journal of Materials Science Materials in Medicine*, **1994**, 5(6-7), 441-445.

[80] Nachlas, M.M., Margulies, S.I., Goldberg, J.D., Seligman, A.M. The determination of lactic dehydrogenase with a tetrazolium salt. *Analytical biochemistry*, **1960**, 1(4-5), 317-326.

[81] Chan, F.K., Moriwaki, K., De Rosa, M.J. Detection of necrosis by release of lactate dehydrogenase activity. *Methods in molecular biology Clifton, N.J*, **2013**, 979, 65-70.

[82] Cole, A.J., David, A.E., Wang, J., Galban, C.J., Hill, H.L., Yang, V.C. Polyethylene glycol modified, cross-linked starch-coated iron oxide nanoparticles for enhanced magnetic tumor targeting. *Biomaterials*, **2011**, 32(8), 2183-2193.

[83] Karlsson, H.L., Cronholm, P., Gustafsson, J., Moller, L. Copper oxide nanoparticles are highly toxic A comparison between metal oxide nanoparticles and carbon nanotubes. *Chemical Research in Toxicology*, **2008**, 21(9), 1726-1732.

[84] Delgado, Y., Morales-Cruz, M., Figueroa, C.M., Hernandez-Roman, J., Hernandez, G., Griebenow, K. The cytotoxicity of BAMLET complexes is due to oleic acid and independent of the alpha-lactalbumin component. *FEBS Open Bio*, **2015**, 5, 397-404.

[85] Huang, D.M., Hsiao, J.K., Chen, Y.C., Chien, L.Y., Yao, M., Chen, Y.K., Ko, B.S., Hsu, S.C., Tai, L.A., Cheng, H.Y., Wang, S.W., Yang, C.S., Chen, Y.C. The promotion of human mesenchymal stem cell proliferation by superparamagnetic iron oxide nanoparticles. *Biomaterials*, **2009**, 30(22), 3645-3651.

[86] Mahmoudi, M., Simchi, A., Milani, A.S., Stroeve, P. Cell toxicity of superparamagnetic iron oxide nanoparticles. *Journal of Colloid and Interface Science*, **2009**, 336(2), 510-518.

[87] Green, D.R. The Grand Finale. *Cell*, **2011**, 144(4), 463-464.

[88] Kroll, A., Pillukat, M.H., Hahn, D., Schnekenburger, J. Current in vitro methods in nanoparticle risk assessment Limitations and challenges. *European Journal of Pharmaceutics and Biopharmaceutics*, **2009**, 72(2), 370-377.

[89] Lu, C., Hung, Y., Hsiao, J., Yao, M., Chung, T. Bifunctional Magnetic Silica Nanoparticles for Highly Efficient Human Stem Cell Labeling. *Nano Letters*, **2007**, 7(1), 149-154.

[90] Gerday, C., Aittaleb, M., Arpigny, J.L., Baise, E., Chessa, J.P., Garsoux, G., Petrescu, I., Feller, G. Psychrophilic enzymes A thermodynamic challenge. *Biochimica et Biophysica Acta - Protein Structure and Molecular Enzymology*, **1997**, 1342(2), 119-131.

[91] Graumann, P., Marahiel, M.A. Some like it cold Response of microorganisms to cold shock. *Archives of Microbiology*, **1996**, 166(5), 293-300.

[92] Nielsen, S.B., Wilhelm, K., Vad, B., Schleucher, J., Morozova-Roche, L.A., Otzen, D. The interaction of equine lysozyme Oleic acid complexes with lipid membranes suggests a cargo off-loading mechanism. *Journal of Molecular Biology*, **2010**, 398(2), 351-361.

[93] Ongpipattanakul, B., Burnette, R.R., Potts, R.O., Francoeur, M.L. Evidence that Oleic Acid Exists in a Separate Phase Within Stratum Corneum Lipids. **1991**.

[94] Turunen, T.M., Urtti, A., Paronen, P., Audus, K.L., Rytting, J.H. Effect of Some Penetration Enhancers on Epithelial Membrane Lipid Domains Evidence from Fluorescence Spectroscopy Studies. **1994**.

[95] Siegel, R.L., Miller, K.D., Jemal, A. Cancer Statistics, 2016. *CA A Cancer Journal for clinicians*, **2016**, 66(1), 7-30.

[96] cancer Institute, National www.cancer.gov.

[97] Peer, D., Karp, J.M., Hong, S., Farokhzad, O.C., Margalit, R., Langer, R. Nanocarriers as an emerging platform for cancer therapy. *Nature nanotechnology*, **2007**, 2(12), 751-760.

[98] Kamaly, N., Xiao, Z., Valencia, P.M., Radovic-Moreno, A.F., Farokhzad, O.C. Targeted polymeric therapeutic nanoparticles design, development and clinical translation. *Chemical Society reviews*, **2012**, 41(7), 2971-3010.

[99] Ullal, A.V., Reiner, T., Yang, K.S., Gorbatov, R., Min, C., Issadore, D., Lee, H., Weissleder, R. Nanoparticle-mediated measurement of target-drug binding in cancer cells. *ACS Nano*, **2011**, 5(11), 9216-9224.

[100] Shi, J., Xiao, Z., Kamaly, N., Farokhzad, O.C. Self-assembled targeted nanoparticles Evolution of technologies and bench to bedside translation. *Accounts of Chemical Research*, **2011**, 44(10), 1123-1134.

[101] Cheng, Z., Al Zaki, A., Hui, J.Z., Muzykantov, V.R., Tsourkas, A. Multifunctional nanoparticles cost versus benefit of adding targeting and imaging capabilities. *Science New York, N.Y*, **2012**, 338(6109), 903-10.

[102] Koshkaryev, A., Sawant, R., Deshpande, M., Torchilin, V. Immunoconjugates and long circulating systems Origins, current state of the art and future directions. *Advanced Drug Delivery Reviews*, **2013**, 65(1), 24-35.

[103] Byrne, J.D., Betancourt, T., Brannon-Peppas, L. Active targeting schemes for nanoparticle systems in cancer therapeutics. *Advanced Drug Delivery Reviews*, **2008**, 60(15), 1615-1626.

[104] Alexis, F., Pridgen, E., Molnar, L.K., Farokhzad, O.C. Factors affecting the clearance and biodistribution of polymeric nanoparticles. *Molecular Pharmaceutics*, **2008**, 5(4), 505-515.

[105] Rosen, J.E., Chan, L., Shieh, D., Gu, F.X. Iron oxide nanoparticles for targeted cancer imaging and diagnostics. *Nanomedicine nanotechnology, biology, and medicine*, **2012**, 8(3), 275-90.

[106] Gindy, M.E., Prudhomme, R.K. Multifunctional nanoparticles for imaging, delivery and targeting in cancer therapy. *Expert opinion on drug delivery*, **2009**, 6(8), 865-878.

[107] Allen, T.M. Ligand-targeted therapeutics in anticancer therapy. *Nature reviews. Cancer*, **2002**, 2(10), 750-763.

[108] Hrkach, J., Von Hoff, D., Ali, M.M., Andrianova, E., Auer, J., Campbell, T., De Witt, D., Figa, M., Figueiredo, M., Horhota, A., Low, S., McDonnell, K., Peeke, E., Retnarajan, B., Sabnis, A., Schnipper, E., Song, J.J., Song, Y.H., Summa, J., Tompsett, D., Troiano, G., Van Geen Hoven, T., Wright, J., LoRusso, P., Kantoff, P.W., Bander, N.H., Sweeney, C., Farokhzad, O.C., Langer, R., Zale, S. Preclinical Development and Clinical Translation of a PSMA-Targeted Docetaxel Nanoparticle with a Differentiated Pharmacological Profile. *Science Translational Medicine*, **2012**, 4(128), 128ra39-128ra39.

[109] Kue, C.S., Kamkaew, A., Burgess, K., Kiew, L.V., Chung, L.Y., Lee, H.B. Small molecules for active targeting incancer. *Medicinal Research Reviews*, **2016**, 36(3), 494-575.

[110] Borden, E.C. Melanoma biologically targeted therapeutics. *Human Press*, **2002**.

[111] Smith, F.O., Downey, S.G., Klapper, J.A., C.Yang, J., Sherry, R.M., Royal, R.E., Kammula, U.S., Hughes, M.S., Restifo, N.P., Levy, C.L., E.White, D., Steinberg, S.M., Rosenberg, S.A. Treatment of metastatic melanoma using Interleukin-2 alone or in conjunction with vaccines. *Clinical Cancer Research*, **2008**, 14(17), 5610-5618.

[112] Jiang, G., Li, R.H., Sun, C., Liu, Y.Q., Zheng, J.N. Dacarbazine combined targeted therapy versus dacarbazine alone in patients with malignant melanoma A meta-analysis. *PLoS ONE*, **2014**, 9(12), 1-13.

[113] Patel, S.P., Woodman, S.E. Profile of ipilimumab and its role in the treatment of metastatic Melanoma. *Drug Design, Development and Therapy*, **2011**, 5, 489-495.

[114] Chapman, P.B., Hauschild, A., Robert, C., Haanen, J.B., Ascierto, P., Larkin, J., Dummer, R., Garbe, C., Testori, A., Maio, M., Hogg, D., Lorigan, P., Lebbe, C., Jouary, T., Schadendorf, D., Ribas, A., ODay, S.J., Sosman, J.A., Kirkwood, J.M., Eggermont, A.M.M., Dreno, B., Nolop, K., Li, J., Nelson, B., Hou, J., Lee, R.J., Flaherty, K.T., McArthur, G.A. Improved survival with vemurafenib in melanoma with BRAF V600E mutation. *The New England journal of medicine*, **2011**, 364(26), 2507-2516.

[115] Thompson, S., Ballard, B., Jiang, Z., Revskaya, E., Sisay, N., Miller, W.H., Cutler, C.S., Dadachova, E., Francesconi, L.C. 166Ho and 90Y labeled 6D2 monoclonal antibody for targeted radiotherapy of melanoma Comparison with 188Re radiolabel. *Nuclear Medicine and Biology*, **2014**, 41(3), 276-281.

[116] Joyal, J.L., Barrett, J.A., Marquis, J.C., Chen, J., Hillier, S.M., Maresca, K.P., Boyd, M., Gage, K., Nimmagadda, S., Kronauge, J.F., Friebe, M., Dinkelborg, L., Stubbs, J.B., Stabin, M.G., Mairs, R., Pomper, M.G., Babich, J.W. Preclinical evaluation of an 131I-labeled benzamide for targeted radiotherapy of metastatic melanoma. *Cancer Research*, **2010**, 70(10), 4045-4053.

[117] Degoul, F., Borel, M., Jacquemot, N., Besse, S., Communal, Y., Mishellany, F., Papon, J., Penault-Llorca, F., Donnarieix, D., Doly, M., Maigne, L., Miot-Noirault, E., Cayre, A., Cluzel, J., Moins, N., Chezal, J.M., Bonnet, M. In vivo efficacy of melanoma internal radionuclide therapy with a 131I-labelled melanin-targeting heteroarylcarboxamide molecule. *International Journal of Cancer*, **2013**, 133(5), 1042-1053.

[118] Chezal, J.M., Papon, J., Labarre, P., Lartigue, C., Galmier, M.J., Decombat, C., Chavignon, O., Maublant, J., Teulade, J.C., Madelmont, J.C., Moins, N. Evaluation of radiolabeled Heteroaromatic analogues of N-2-diethylaminoethyl-4-iodobenzamide for imaging and targeted radionuclide therapy of melanoma. *Journal of Medicinal Chemistry*, **2008**, 51(11), 3133-3144.

[119] Morlieras, J., Chezal, J., Miot-Noirault, E., Roux, A., Heinrich-Balard, L., Cohen, R., Tarrit, S., Truillet, C., Mignot, A., Hachani, R., Kryza, D., Antoine, R., Dugourd, P., Perriat, P., Janier, M., Sancey, L., Lux, F., Tillement, O. Development of gadolinium based nanoparticles having an affinity towards melanin. *Nanoscale*, **2013**, 5(4), 1603-1615.

[120] Cachin, F., Miot-Noirault, E., Gillet, B., Isnardi, V., Labeille, B., Payoux, P., Meyer, N., Cammilleri, S., Gaudy, C., Razzouk-Cadet, M., Lacour, J.P., Granel-Brocard, F., Tychyj, C., Benbouzid, F., Grange, J.D., Baulieu, F., Kelly, A., Merlin, C., Mestas, D., Gachon, F., Chezal, J.M., Degoul, F., DIncan, M. 123I-BZA2 as a Melanin-Targeted Radiotracer for the Identification of Melanoma Metastases Results and Perspectives of a Multicenter Phase III Clinical Trial. *Journal of nuclear medicine official publication, Society of Nuclear Medicine*, **2014**, 55, 15-22.

[121] Rbah-Vidal, L., Vidal, A., Besse, S., Cachin, F., Bonnet, M., Audin, L., Askienazy, S., Dolle, F., Degoul, F., Miot-Noirault, E., Moins, N., Auzeloux, P., Chezal, J.M. Early detection and longitudinal monitoring of experimental primary and disseminated melanoma using 18FICF01006, a highly promising melanoma PET tracer. *European Journal of Nuclear Medicine and Molecular Imaging*, **2012**, 39(9), 1449-1461.

[122] Eisenhut, M., Mohammed, A., Mier, W., Schonsiegel, F., Friebe, M., Mahmood, A., Jones, A.G., Haberkorn, U. Melanoma Uptake of 99m Tc Complexes Containing the N-2-Diethylaminoethylbenzamide Structural Element. *Journal of Medicinal Chemistry*, **2002**, 45, 5802-5805.

[123] Auzeloux, P., Papon, J., Azim, E.M., Borel, M., Pasqualini, R., Veyre, A., Madelmont, J.C. A potential melanoma tracer Synthesis, radiolabeling, and biodistribution in mice of a new nitridotechnetium bisaminothiol derivative pharmacomodulated by a N-diethylaminoethylbenzamide. *Journal of Medicinal Chemistry*, **2000**, 43(2), 190-198.

[124] Parat, A., Kryza, D., Degoul, F., Taleb, J., Viallard, C., Janier, M., Garofalo, A., Bonazza, P., Heinrich-Balard, L., Cohen, R., Miot-Noirault, E., Chezal, J., Billotey, C., Felder-Flesch, D. Radiolabeled dendritic probes as tools for high in vivo tumor targeting application to melanoma. *J. Mater. Chem. B*, **2015**, 3(12), 2560-2571.

[125] Chezal, J., Dolle, F., Maisonial, J.M., Miot-Noirault, E., Moins, N., Papon, J., Kuhnast, B., Tavitian, B., Boigard, R. Labelled analogues of halobenzamides as multimodal radiopharmaceuticals and their precursors. **2008**.

[126] Labarre, P., Papon, J., Moreau, M.-F., Moins, N., Bayle, M., Veyre, A., Madelmont, J.-C Melanin affinity of N-2-diethylaminoethyl-4-iodobenzamide, an effective melanoma imaging agent. *Melanoma Reseach*, **2002**, 12(2), 115-121.

Part IV

Conclusion and Outlooks

Conclusion Nowadays, owing to significant biomedical applications, considerable attention has been devoted to the development of smart dendritic platforms due to their particular intrinsic properties. Indeed, those applications require the elaboration of structures with tunable and precise architecture, multiple functionalities and hydrophilicity. In combination with magnetic nanoparticles (NPs), dendrimers have a strong potential in imaging and therapy applications.

The main challenge of the present work was to create new well-defined small multifunctional Dendrons for diagnosis applications. At first we have developed and successfully synthesized two hydrophilic dendritic Phosphonic acids useful for the functionalization of Iron oxide NPs (IONPs) and two dendritic Lipoic acids for further AuNPs' functionalization for diagnostic medical imaging. We have further shown that organic shells' properties to coat inorganic NPs can be adjusted in order to respond to biomedical issues: biodistribution, toxicity, nanohybrid' integrity. In the present work those issues overcomes are exemplified by molecular engineering of 2P_G_1PEG_PP using Diacetylene moieties for decreasing Cobalt NPs' toxicity and also by engineering 2P_G_1PEG_AIE for assessing the nanomaterial' integrity upon *in vivo* injection.

The second objective of this work was assessing the dendronized NPs' (DPs) bioavailability through several *in vitro* and *in vivo* assays. Subsequently, the synthesis of 10nm IONPs and their grafting with two different dendrons were achieved, and their physicochemical characterizations confirmed their composition, colloidal stability and interesting magnetic properties as MRI contrast agents. Both DPs showed moderate *in vitro* toxicity towards various cancer and primary cell lines. Flow cytometry results indicated great capacity of NPs10@D2-2P for active targeting as no unspecific uptake could be highlighted. Furthermore, *in vivo* MRI studies showed high contrast enhancement and renal and hepatobiliary excretions. For these reasons, IO DPs show great potential as early cancer diagnosis imaging and NPs10@D2–2P for active targeting through post-functionalization with targeting ligands.

The third objective of the present work has been focused on active targeting of solid tumors after intravenous injection of DPs. A proof-of-concept has been made in Melanoma as the IO DPs were further functionalized with a Quinoline derivative (ICF01102, INSERM UMR 990, Clermont-Ferrand) known as Melanine granules targeting agent. Biodistribution was studied *in vivo* using MRI and planar scintigraphy through ^{177}Lu – radiolabeling of the IO DPs. MRI experiments confirmed their high contrast power and hepatobiliary and urinary excretions pathways. Planar scintigraphy images demonstrated a moderate specific tumor uptake of Melanine-targeted ^{177}Lu - DPs at 24h *pi* with a TMR ratio of 2.89±1.2, and a highest tumor

uptake of the control probe (bearing no targeting ligand) at 30min *pi*, probably due to the EPR effect. In addition, *ex vivo* confocal microscopy (EVCM) studies showed a high specific targeting of malignant human Melanoma samples impregnated with ICF-labelled DPs.

The present work has allowed the development of dendritic structures, their bioavailability assessment and successful malignant Melanoma targeting *ex vivo* but also *in vivo* after intravenous injection. With the results obtained herewith, one can definitely infer that, with minor manipulation and fine-tuning, these dendritic structures do possess excellent potential for applications in the field of biotechnology and biochemical engineering.

Outlooks Results of the present work showed an attractive approach for the development of new well-defined dendrons in respond to several biomedical issues. However, there is still work to be accomplished. The most important work remains the completion of 2P_G_1PEG_PP and 2P_G_1PEG_AIE syntheses and their evaluation for toxicity prevention and material integrity assessment respectively. Furthermore, during the elaboration of Diacetylene hydrophilic dendrons, it became clear that the literature is rather poor on this subject, which resulted in an even more challenging project.

As the bioavailability results of the present work extensively demonstrated, there is a substantial scope for applications of dendronized NPs in specific Melanoma targeting. However, it is also clear that there is still need for further research such as *in vitro* studies (toxicity and cellular uptake) on B16 cell lines and *in vivo* Fe^{3+} quantification analyses on animal' organs used in planar scintigraphy are under progress. Of higher importance are EVFCM studies on human samples. Dr. Jean-Luc Perrot has already scheduled EVFCM tests of ICF-labelled DPs through impregnation of 6 Melanin and Amelanotic human Melanomas (3 basal cell carcinoma and 3 naevus). These studies will assess the ability of ICF-labelled DPs to accurately identify cancerous from normal tissues and diagnose correctly a skin tumor without the need of a time-consuming histological analysis.

From a practical point of view, results obtained within the laboratory IPCMS in Strasbourg showed a number of key innovations and breakthrough made on dendronized IONPs in the last few years. Some of the major ones include:

- synthesis of IONPs of tunable shape and size;
- synthesis of well-defined small dendrons allowing a strong anchoring at metal oxides or metallic NPs' surfaces;
- assessment of dendronized IONPs biocompatibility, excretion pathways, cellular uptake and their assets for *ex vivo* malignant Melanoma targeting;

These outlooks give the opening to exciting future work, in particularly commercialization of DPs platforms for various biomedical applications.

Part V

Experimental part

Instrumentation

Nuclear magnetic resonance (NMR) spectra (^{1}H, ^{13}C and ^{31}P) were recorded on a Bruker spectrometer (300MHz). Chemical shifts for ^{1}H and ^{13}C spectra are recorded in parts per million and are calibrated to solvent residual peaks (for example: $CHCl_3$: ^{1}H 7.26 ppm and^{13}C 77.16 ppm; MeOH: ^{1}H 3.31 ppm and ^{13}C 49.00 ppm) according to **Ref.[1]**. Multiplicities are indicated by s (singlet), bs (broad singlet), d (doublet), t (triplet), q (quadruplet), quint (quintuplet) and m (multiplet). Coupling constants, *J*, are reported in Hertz.

Exact mass analyses were performed with matrix assisted laser desorption ionization time of flight mass spectrometry (MALDI–TOF MS). Analyses were performed at Laboratoire de Spectrométrie de Masse Bio–Organique, Département des Sciences Analytiques, Institut Pluridisciplinaire Hubert Curien, UMR 7178 (CNRS–UdS) ECPM, Bat. R5–N0, 25 rue Becquerel F67087 – Strasbourg, France.

Fourier transform infrared (FTIR) spectra were performed on Perkin ELmer Spectum 100. Spectra were recorded using KBr disks and transmittance wes measured with a wavenumber between 450 and 4000cm^{-1}.

Relaxometry measurements were performed at 37°C on Bruker Minispec systems mq–60 working at 60MHz. The longitudinal relaxation times (T_1) were measured thanks to inversion recovery sequence and transversal relaxation times (T_2) were measured using Carr–Purcell–Meiboom–Gill sequence. Each experiment was performed with 300µL solution. For Fe^{3+} quantification, T_1 was measured of mineralized NPs in2% HNO_3 solution.

^{1}H NMRD profiles were obtained at 37°C using Stela fast cycling relaxometer over a range of magnetic fields extending from 0.25mT to 0.94T (0.01 – 40MHz). For each experiment 300µL suspension was used. The theoretical adjustment of NMRD profiles was performed using classical relaxation models (Fitting2000 software) assuming diffusion coefficients of $3.53 \cdot 10^{-5} cm^2 s^{-1}$. NMRD diameter, saturation magnetization were estimated using Fitting200 software.

Dynamic light scattering (DLS) was performed using Zetasizer NanoZS from Malvern Intruments. Measurements of hydrodynamic size distribution were performed at 25°C with IONPs refractive index of 2.42. For water solutions, media viscosity was set at 0.89mPa.s and the refractive at 1.33. For THF solutions, solvent viscosity was set at 0.456mPa.s and the index of refraction at 1.40.

Zeta potential measurements were performed using the same instrument as for DLS measurements. Analysis were performed at 25°C on aqueous suspensions, placed in a standard cell and pH value was adjusted

using solutions of NaOH and HCl (0.01, 0.1, and 1M).

Transmission electron microscopy (TEM) analysis were performed using a Jeol 2100F (200kV, Cs–corrected condenser, imaging filter, EDX, biprism, 2 CCD cameras) – Topcon 002B (200kV, EDX, CCD camera) microscope. Samples were prepared by placing a drop of diluted solution on a carbon–coated copper grid (300mesh). The statistical treatment of TEM images was performed using ImageJ software. Counted nanoparticle number was in 200–400 range.

Magnetization curves were obtained using MPMS SQUID–VSM instrument at applied field between –5 and 5T. The fitting of the curves with Langevin functions gives several parameters as the crystal radius and saturation magnetization.

High resolution magic–angle spinning NMR (HR–MAS NMR) experiments were carried out on a Bruker FT–NMR Avance 500 equipped with a 11.75T superconducting ultrashield magnet. All the experiments were performed at spinning rate of 5kHz with a 50µL zirconium rotor.

ICP–MS (Inductively Coupled Plasma Mass Spectrometry) measurements were performed on a Jobin Yvon JY70^{+} instrument at Inorganic and analytic laboratory, Mons University, Mons, Belgium.

Atomic absorption spectrometry (AAS) analysis were performed using Varian 55B Atomic Absorption Spectrophotometer with air–Acetylene flame at a temperature above 2300°C and hollow cathode lampe specific for Iron. Fe^{3+} concentration was determined using the Beer–Lambert law in a range of 0 to 5ppm.

Ultraviolet–visible measurements were performed using Cary 300UV–Vis, Agilent Technologies instrument in 200–800nm range.

Methods

General All dry solvents, Dichloromethane (CH_2Cl_2), Tetrahydrofurane (THF), Acetonitrile (CH_3CN), Toluene, Acetone, Ethanol (EtOH), Methanol (MeOH), Chloroform ($CHCl_3$), Dimethylformamide (DMF), Ethyl acetate (EtOAc), and Cyclohexane (CyHex), were of HPLC grade (chromasolvs, Sigma–Aldrich) further purified in a solvent system containing drying columns or dried over 4Å molecular sieves. All commercially available reagents were used without further purification. Flash column chromatography was performed on silica gel (high–purity grade, 230–400mesh, 40–63mm, Sigma–Aldrich) according to a standard technique. The experimental section is composed of the syntheses of compounds published by Garofalo *et al.*[2].

Compound 1: A solution of *para*–Toluenesulfonyl chloride (22.3g, 105mmol, 1.1eq.) in THF (35mL) was added dropwise to a solution of Tetraethyleneglycol methyl ether (20.0g, 96mmol) and NaOH (6.7g, 166mmol, 1.7eq.) in a mixture of THF/H2O (135mL / 45mL) at 0°C. After 1 hour stirring at 0°C, the

reaction was allowed to warm to room temperature and was stirred 20 additional hours. The solution was then poured into 200mL of brine and the volatiles were evaporated. The resulting mixture was extracted several times with DCM and the combined organic layers were washed with brine, dried over $MgSO_4$ and filtered. The solvent was evaporated under reduced pressure and the so–obtained oil was purified by column chromatography on silica gel eluting with DCM / MeOH (98/2). Compound **1** was obtained as pale yellow oil in 94% yield. ^{1}H NMR (300MHz, $CDCl_3$) δ 7.73 (d, J = 1.5 Hz, 2H, Ar–2,6–H), 7.28 (d, J = 1.5 Hz, 2H, Ar–3,5–H), 4.11 – 4.08 (m, 2H, $ArSO_2OCH_2$), 3.64 – 3.47 (m, 14H, OCH_2CH_2O), 3.31 (s, 3H, OCH_3), 2.39 (s, 3H, $ArCH_3$); ^{13}C NMR (75 MHz, $CDCl_3$) δ 144.9 (ArS), 133.2 ($ArCH_3$), 130.0 (Ar), 72.1 (PEG), 70.9 (PEG), 70.7 (PEG), 70.6 (PEG), 69.5 (PEG), 68.8 (PEG), 59.1 (OCH_3), 21.8 (CH_3); MS (MALDI–TOF) m/z calculated for $C_{16}H_{26}NaO_5S$: 385.14, obtained: 385.13.

Compound 2: A solution of Methyl gallate (20.0g, 108.6mmol), Benzyl bromide (14.2mL, 119mmol, 1.1eq.), $KHCO_3$ (32.4g, 324mmol, 3eq.) and KI (0.1g, 0.6mmol) in DMF (100mL) was stirred during 4 days at 30°C. The reaction mixture was poured into 1L of water and Sulfuric acid was added to reach neutral pH. The aqueous layer was then extracted 3 times with DCM (150mL) . The combined organic layers were washed three times with brine (50mL), dried ($MgSO_4$) and filtered. The solvent was removed by evaporation and the residue was purified by column chromatography on silica gel eluting with DCM / MeOH (98/2) to provide a yellow oil. The obtained residue was filtered and washed with petroleum ether to provide **2** as a white solid in 70% yield. ^{1}H NMR (300MHz, CD_3OD–d) δ 7.52 (d, J = 7.5Hz, 2H, Ar^{Bz}– 2,6 –H), 7.31 (m, 3H, Ar^{Bz} – 3,4,5 –H), 7.13 (s, 2H, Ar – 2,6 –H), 5.18 (s, 2H, $Ar^{Bz}OCH_2$), 3.83 (s, 3H, $COOCH_3$); ^{13}C NMR (75MHz, CD_3OD–d) δ 167.1 ($COOCH_3$), 150.5 (ArOH), 138.2 ($ArOCH_2$), 137.2 ($Ar^{Bz}CH_2$), 128.5 (Ar^{Bz}), 128.0 (Ar^{Bz}), 127.8 (Ar^{Bz}), 125.0 ($ArCOOCH_3$), 108.8 (Ar), 73.8 (OCH_2), 51.2 ($COOCH_3$); MS (MALDI–TOF) m/z calculated for $C_{10}H_{12}NaO_5$: 225.20, obtained: 225.09.

Compound 3: A solution of **2** (9.2g, 33.4mmol), **1** (26.9g, 74.3mmol, 2.2eq.), K_2CO_3 (28.0g, 200mmol, 6eq.) and KI (0.6g, 3.3mmol, 0.1eq.) in Acetone (600mL) was stirred during 30 hours at 65°C. The reaction mixture was filtered over Celite and the solvent was evaporated. The resulting crude product was diluted in DCM (200mL) and washed twice with an aqueous saturated solution of $NaHCO_3$ and with brine. After drying over $MgSO_4$, filtration and evaporation of the solvent, the crude product was purified by column chromatography over silica gel column (DCM / MeOH 98/2 to 95/5) to afford **3** as a colorless oil in 75% yield. ^{1}H NMR (300MHz, $CDCl_3$) δ 7.48 (d, J = 7.7Hz, 2H, Ar^{Bz}– 2,6 –H), 7.28 (m, 5H, Ar^{Bz}– 3,4,5 –H and Ar – 2,6 – H), 5.12 (s, 2H, $Ar^{Bz}OCH_2$), 4.20 – 4.17 (t, J = 4.8Hz, 4H, $ArOCH_2$), 3.90 (s, 3H, $COOCH_3$), 3.88 – 3.85 (t, J = 4.8Hz, 4H, OCH_2CH_2O), 3.74 – 3.69 (m, 4H, OCH_2CH_2O), 3.67 – 3.60 (m,

16H, OCH_2CH_2O), 3.54 – 3.50 (m, 4H, OCH_2CH_2O), 3.35 (s, 6H, $OCH_2CH_2OCH_3$); ^{13}C NMR (75MHz, $CDCl_3$) δ 166.9 ($COOCH_3$), 152.5 (Ar), 142.2 (Ar), 138.2 ($Ar^{Bz}CH_2$), 128.2 (Ar^{Bz}), 128.0 (Ar^{Bz}), 127.8 (Ar^{Bz}), 125.3 ($ArCOOCH_3$), 109.1 (Ar), 74.8 (OCH_2), 72.3 (PEG), 71.2 (PEG), 71.0 (PEG), 70.9 (PEG), 70.8 (PEG), 70.0 (PEG), 69.2 (PEG), 59.3 (OCH_3), 52.5 ($COOCH_3$); MS (MALDI–TOF) m/z calculated for $C_{33}H_{50}NaO_{13}$: 677.33, obtained: 677.03.

Compound 4: Sodium hydroxide (5.1g, 127mmol, 10eq.) was added to a solution of **3** (8.3g, 12.7mmol) in a mixture of Methanol / Water 4/1 (150mL). The reaction mixture was stirred 2h at 85°C and stopped. The mixture was concentrated *in vacuo* and hydrolyzed (200mL). The pH was adjusted to 3 by HCl 12N and the aqueous solution was extracted with DCM (3 x 100mL). The combined organic phase was washed with brine and water, dried over $MgSO_4$, filtered and concentrated under reduced pressure. Purification by column chromatography on silica gel eluting with DCM / MeOH (95/5) afforded **4** as a colorless oil in 90% yield. ^{1}H NMR (300MHz, $CDCl_3$) δ 7.50 (d, J = 7.8Hz, 2H, Ar^{Bz} – 2,6 – H), 7.38 (s, 2H, Ar – 2,6 – H), 7.35 – 7.28 (m, 3H, Ar^{Bz} – 3,4,5 – H), 5.13 (s, 2H, $Ar^{Bz}OCH_2$), 4.20 – 4.16 (t, J = 4.8Hz, 4H, $ArOCH_2$), 3.87 – 3.82 (t, J = 4.8Hz, 4H, OCH_2CH_2O), 3.74 – 3.69 (m, 4H, OCH_2CH_2O), 3.67 – 3.61 (m, 16H, OCH_2CH_2O), 3.54 – 3.50 (m, 4H, OCH_2CH_2O), 3.37 (s, 6H, $OCH_2CH_2OCH_3$); ^{13}C NMR (75MHz, $CDCl_3$) δ 169.6 (COOH), 152.8 (Ar), 142.4 (Ar), 137.9 ($Ar^{Bz}CH_2$), 128.2 (Ar^{Bz}), 128.0 (Ar^{Bz}), 127.8 (Ar^{Bz}), 124.8 (ArCOOH), 109.2 (Ar), 74.8 (OCH_2), 72.3 (PEG), 71.2 (PEG), 71.0 (PEG), 70.9 (PEG), 70.8 (PEG), 70.0 (PEG), 69.2 (PEG), 59.1 (OCH_3); MS (MALDI–TOF) m/z calculated for $C_{32}H_{48}O_{13}$: 640.31, obtained: 640.24; calculated for $C_{29}H_{48}NaO_{13}$: 627.30, obtained: 627.13; calculated for $C_{29}H_{48}KO_{13}$: 643.27, obtained: 643.09.

Compound 5: A solution of 1–(Benzyloxy)– 4 –(chloromethyl) Benzene (2.0g, 8.6mmol) in $P(OEt)_3$ (3mL) was stirred 2 hours at 160°C. The excess of $P(OEt)_3$ was evaporated under reduced pressure. The crude product was purified by column chromatography on silica gel eluting with DCM / MeOH (95/5) to afford **5** as a white solid in 92% yield. ^{1}H NMR (300MHz, $CDCl_3$) δ 7.50 – 7.35 (m, 5H, Ar^{Bz} –H), 7.21 (d, J = 8.1Hz 2H, Ar – 2,6 – H), 6.95 (d, J = 8.1Hz 2H, Ar – 3,5 – H), 5.07 (s, 2H, $ArOCH_2$), 4.02 (q, J = 7.1Hz, 4H, $PO(OCH_2CH_3)_2$), 3.12 (d, J = 21.1Hz, 2H, $ArCH_2P$), 1.27 (t, J = 7.1Hz, 6H, $PO(OCH_2CH_3)_2$); ^{13}C NMR (75MHz, $CDCl_3$) δ 157.7 (J = 3.8Hz, Ar), 137.1 ($Ar^{Bz}CH_2$), 130.8 (J = 6.0Hz, Ar), 128.6 (Ar^{Bz}), 128.0 (Ar^{Bz}), 127.5 (Ar^{Bz}), 123.7 (J = 9.3Hz, Ar), 115.0 (J = 2.7Hz, Ar), 70.0 (OCH_3), 62.1 (J = 6.5Hz, PCH_2CH_3), 32.7 (J = 139.4Hz, CH_2–P), 16.4 (J = 6.0Hz, PCH_2CH_3); ^{31}P NMR (81MHz, $CDCl_3$) δ 26.79; MS (MALDI–TOF) m/z calculated for $C_{18}H_{24}O_4P$: 335.13, obtained: 335.16.

Compound 6: Palladium activated on carbon 10% (0.5eq.) was added to a solution of **5** (2.0g, 6mmol) in Ethanol absolute (60mL). The mixture was stirred under a hydrogen atmosphere at room temperature

for 16h. The crude mixture was filtered through a plug of Celite before being concentrated under reduced pressure. Phenol **6** was obtained as white solid in 92% yield. ^{1}H NMR (300MHz, $CDCl_3$) δ 7.05 (dd, J = 2.8 and 8.0Hz, 2H, Ar – 2,6 – H), 6.61 (d, J = 8.0Hz 2H, Ar – 3,5 – H), 4.02 (q, J = 7.1Hz, 4H, $PO(OCH_2CH_3)_2$), 3.08 (d, J = 21.0Hz, 2H, $ArCH_2P$), 1.27 (*t*, J = 7.1Hz, 6H, $PO(OCH_2CH_3)_2$); ^{13}C NMR (75MHz, $CDCl_3$) δ 156.1 (J = 3.8Hz, Ar), 130.6 (J = 6.6Hz, Ar), 121.0 (J = 9.3Hz, Ar), 116.0 (J = 3.2Hz, Ar), 62.4 (J = 7.1Hz, PCH_2CH_3), 32.3 (J = 139.4Hz, CH–P), 16.4 (J = 6.0Hz, PCH_2CH_3); ^{31}P NMR (81MHz, $CDCl_3$) δ 27.58; MS (MALDI–TOF) m/z calculated for $C_{11}H_{18}O_4P$: 245.09, obtained: 245.13.

Compound 7: (2–bromo–ethyl)Carbamic acid *tert*–butyl ester (1.4g, 6.3mmol, 3eq.), K_2CO_3 (0.87g, 6.3mmol, 3eq.) and KI (0.05g, 0.4mmol, 0.2eq.) were added to a solution of **6** (0.5g, 2.1mmol) in Acetone (25mL). The mixture was stirred during 72h at 65°C, filtered over Celite and concentrated under reduced pressure. The resulting crude product was diluted in DCM (50mL) and washed twice with an aqueous saturated solution of $NaHCO_3$ and with brine. After drying over $MgSO_4$, filtration and evaporation of the solvent, the crude product was purified by column chromatography over silica gel (DCM / MEOH 98/2 to 95/5) to afford *tert*–butyl protected compound as yellow oil in 75% yield. Trifluoroacetic acid (1.1mL, 13mmol, 10.0eq.) was added dropwise to a solution of this product (0.5g, 1.3mmol) in DCM (15mL) at 0°C. The reaction mixture was stirred overnight at room temperature, the volatiles were then evaporated. The crude product was dissolved in a solution of DCM / MeOH (9/1) (20mL) and was washed with NaOH 1N (2 x 10mL). The organic layer was dried over $MgSO_4$, filtered and concentrated under reduced pressure to afford **7** as a white solid in 94% yield. ^{1}H NMR (300MHz, $CDCl_3$) δ 7.20 (dd, J = 2.7 and 8.0Hz, 2H, Ar – 2,6 – H), 6.85 (d, J = 8.0Hz 2H, Ar – 3,5 – H), 4.02 (m, 6H, $OCH_2CH_2NH_2$ and $PO(OCH_2CH_3)_2$), 3.08 (m, 4H, $OCH_2CH_2NH_2$ and $ArCH_2P$), 1.21 (t, J = 7.0Hz, 6H, $PO(OCH_2CH_3)_2$); ^{13}C NMR (75MHz, $CDCl_3$) δ 157.8 (J = 3.3Hz, Ar), 130.7 (J = 6.6Hz, Ar), 123.6 (J = 9.3Hz, Ar), 114.6 (J = 2.7Hz, Ar), 70.0 (OCH_2), 62.0 (J = 6.6Hz, PCH_2CH_3), 41.4, 32.5 (J = 138.9Hz, CH–P), 16.3 (J = 6.1Hz, PCH_2CH_3); ^{31}P NMR (81MHz, $CDCl_3$) δ 26.81; MS (MALDI–TOF) m/z calculated for $C_{13}H_{23}NO_4P$: 288.13, obtained: 288.19.

Compound 8: BOP (0.66g, 1.5mmol, 1.3eq.) was added under argon to a solution of Carboxylic acid **4** (0.74g, 1.15mmol, 1eq.) in dry DCM (20mL). After 5min stirring, Amine derivative **7** (0.3g, 1.05mmol 1eq.) and *N,N*–Diisopropylethylamine (0.7mL, 4.2mmol, 4eq.) were added. The reaction mixture was stirred overnight at room temperature. 40mL of DCM were added and the organic layer was washed with a solution of NaOH 1N (2 x 20mL), HCl 1N (2 x 20mL), brine (2 x 20mL) and water (1 x 20mL), dried over $MgSO_4$, filtered and concentrated under reduced pressure. The crude product was purified by column chromatography over silica gel (DCM / MeOH 98/2 to 95/5) to afford **8** as colourless oil in 70% yield. ^{1}H NMR (300MHz,

$CDCl_3$) δ 7.50 (d, J = 8.1Hz, 2H, Ar^1 – 2,6 – H), 7.35 – 7.25 (m, 3H, Ar^{Bz} – 3,4,5 – H), 7.20 (dd, 2H, J = 2.4 and 8.5Hz, Ar^{Bz} – 2,6 – H), 7.08 (s, 2H, Ar^2 – 2,6 – H), 6.85 (d, J = 8.1Hz, 3H, Ar^1 – 3,5 – H and $Ar^1OCH_2CH_2NH$), 5.08 (s, 2H, $Ar^{Bz}OCH_2$), 4.18 (t, 4H, J = 4.8Hz, $Ar^2OCH_2CH_2O$), 4.11 (t, 2H, J = 5.3Hz, $Ar^1OCH_2CH_2NH$), 4.08 – 3.96 (m, 4H, $PO(OCH_2CH_3)_2$), 3.85 – 3.78 (m, 6H, $Ar^1OCH_2CH_2NH$ and OCH_2CH_2O), 3.70 –3.50 (m, 24H, OCH_2CH_2O), 3.33 (s, 6H, $OCH_2CH_2OCH_3$), 3.08 (d, J = 21.1Hz, 2H, Ar^1CH_2P), 1.22 (t, J = 7.1Hz, 6H, $PO(OCH_2CH_3)_2$); ^{13}C NMR (75MHz, $CDCl_3$) δ 167.2 (NHCO), 157.5 (J = 3.3Hz, Ar), 152.6 (Ar), 140.7 (Ar), 137.6 (Ar), 130.8 (J = 6.6 Hz, Ar), 129.6 (Ar), 128.4 (Ar), 128.1 (Ar), 127.8 (Ar), 123.9 (J = 8.7 Hz, Ar), 114.6 (J = 3.3 Hz, Ar), 107.0 (Ar), 74.8 (OCH_2), 71.8 (PEG), 70.65 (PEG), 70.5 (PEG), 70.45 (PEG), 70.4 (PEG), 70.35 (PEG), 69.8 (PEG), 68.8 (PEG), 66.6 (OCH_2CH_2NH), 62.0 (J = 6.6 Hz, CH_2CH_3), 58.9 (OCH_3), 39.5 ($CH_2NHCOAr$), 32.8 (J = 138.9Hz, CH_2P), 16.3 (J = 6.0Hz, CH_2CH_3); ^{31}P NMR (81MHz, $CDCl_3$) δ 26.63; MS (MALDI–TOF) m/z calculated for $C_{45}H_{69}NO_{16}P$: 910.43, obtained: 910.34; calculated for $C_{45}H_{68}NaNO_{16}P$: 932.43, obtained: 932.35; calculated for $C_{45}H_{68}KNO_{16}P$: 948.40, obtained: 948.30.

Compound 9: **8** (0.6g, 0.66mmol) was dissolved in Ethanol absolute (10mL) and Palladium activated on carbon 10% (0.5eq.) was added. The mixture was stirred under a hydrogen atmosphere at room temperature for 16h. The product was filtered through a plug of Celite before being concentrated and purified by column chromatography on silica gel eluting with DCM / MeOH (98/2 to 95/5) to afford phenol **9** as a colorless oil in 85% yield. ^{1}H NMR (300MHz, $CDCl_3$) δ 7.21 (dd, J = 2.5 and 8.1Hz, 2H, Ar^1 – 2,6 – H), 7.15 (s, 2H, Ar^2 – 2,6 – H), 6.86 (d, J = 8.1Hz, 2H, Ar^1 – 3,5 – H), 6.78 (t, J = 5.6Hz, 1H, $Ar^1OCH_2CH_2NH$), 4.21 (t, 4H, J = 4.8Hz, $Ar^2OCH_2CH_2O$), 4.11 (t, 2H, J = 5.2Hz, $Ar^1OCH_2CH_2NH$), 4.05 – 3.95 (m, 4H, $PO(OCH_2CH_3)_2$), 3.88 – 3.80 (m, 6H, $Ar^1OCH_2CH_2NH$ and OCH_2CH_2O), 3.72 – 3.50 (m, 24H, OCH_2CH_2O), 3.34 (s, 6H, $OCH_2CH_2OCH_3$), 3.07 (d, J = 21.1Hz, 2H, Ar^1CH_2P), 1.22 (t, J = 7.0Hz, 6H, $PO(OCH_2CH_3)_2$); ^{13}C NMR (75MHz, $CDCl_3$) δ 168.1 (CONH), 157.3 (J = 3.3Hz, Ar), 146.8 (Ar), 141.3 (Ar), 130.6 (J = 6.6Hz, Ar), 124.6 (Ar), 123.9 (J = 9.3Hz, Ar), 114.6 (J = 3.3Hz, Ar), 108.6 (Ar), 71.8 (PEG), 70.6 (PEG), 70.5 (PEG), 70.4 (PEG), 70.3 (PEG), 69.6 (J = 7.1Hz, PEG), 66.8 (OCH_2CH_2NH), 61.9 (J = 7.1Hz, CH_2CH_3), 58.9 (OCH_3), 39.4 ($CH_2NHCOAr$), 32.8 (J = 139.5Hz, CH_2P), 16.3 (J = 6.0 Hz, CH_2CH_3); ^{31}P NMR (81MHz, CDCl3) δ 26.64; MS (MALDI–TOF) m/z calculated for $C_{38}H_{63}NO_{16}P$: 820.38, obtained: 820.41; calculated for $C_{38}H_{62}NaNO_{16}P$: 842.38, obtained: 842.40.

Compound 10: NEt_3 (840µL, 6.0mmol, 3.0eq.) and *para*–Toluenesulfonyl chloride (570mg, 3.0mmol, 1.5eq.) were added to a solution of Hydroxy–dPEG™8–*t*–butyl ester (1.00g, 2.0mmol) in DCM (20mL) kept at 0°C. After 40h stirring at room temperature, the reaction mixture was diluted with DCM (70mL). The

organic phases were combined, washed with brine, dried over $MgSO_4$, filtered and concentrated under reduced pressure. The crude product was purified by column chromatography over silica gel (EtOAc / MeOH 95/5 to 90/10) to afford **10** as a colourless oil in 85% yield. ^{1}H NMR (300MHz, $CDCl_3$): δ 7.81 (2H, BB' part of an AA'BB' system), 7.34 (2H, AA' part of an AA'BB' system), 4.16 (t, J = 4.9Hz, 2H, OCH_2CH_2O), 3.58 – 3.73 (m, 32H, OCH_2CH_2O), 2.50 (t, J = 6.6Hz, 2H, $CH_2COOC(CH_3)_3$), 2.45 (s, 3H, $ArCH_3$), 1.44 (s, 9H, $CH_2COOC(CH_3)_3$); ^{13}C NMR (75MHz, $CDCl_3$): δ 170.20 ($COOC(CH_3)_3$), 144.32 (ArS), 132.74 ($ArCH_3$), 129.47 (Ar), 127.46 (Ar), 79.78 ($COOC(CH_3)_3$), 70.08 (PEG), 69.00 (PEG), 68.15 (PEG), 66.40 (PEG), 35.84 ($CH_2COOC(CH_3)_3$), 27.65 ($OC(CH_3)_3$), 21.14 ($ArCH_3$); MS (MALDI–TOF) m/z calculated for $C_{10}H_{20}LiO_5$: 227.15, obtained: 227.08; calculated for $C_{26}H_{44}LiO_{12}S$: 587.27, obtained: 587.13.

Compound 11: K_2CO_3 (0.19g, 1.38mmol, 3eq.) and KI (21mg, 0.13mmol, 0.3eq.) were added to an equimolar solution of **9** (0.38g, 0.46mmol) and **10** (0.34g, 0.56mmol) in Acetone (15mL). The reaction mixture was stirred at 60°C during 24h. After filtration over Celite, the solvent was evaporated and the residue was diluted in DCM (50mL). The organic layer was washed twice with a saturated solution of $NaHCO_3$, then with brine, filtered and concentrated under reduced pressure. The crude product was purified by column chromatography on silica gel eluting with DCM / MeOH (98/2 to 95/5) to afford **11** as a colorless oil in 70% yield. ^{1}H NMR (300MHz, $CDCl_3$) δ 7.20 (dd, J = 2.5 and 8.1Hz, 2H, Ar^1 – 2,6 – H), 7.11 (s, 2H, Ar^2 – 2,6 – H), 6.91 (t, J = 5.6Hz, 1H, $Ar^1OCH_2CH_2NH$), 6.84 (d, J = 8.1Hz, 2H, Ar^1 – 3,5 – H), 4.20 – 4.15 (m, 6H, $Ar^2OCH_2CH_2O$), 4.11 (t, 2H, J = 5.1Hz, $Ar^1OCH_2CH_2NH$), 4.05 – 3.95 (m, 4H, $PO(OCH_2CH_3)_2$), 3.85 – 3.77 (m, 8H, $Ar^1OCH_2CH_2NH$ and OCH_2CH_2O), 3.70–3.50 (m, 54H, OCH_2CH_2O), 3.33 (s, 6H, $OCH_2CH_2OCH_3$), 3.07 (d, J = 21.1Hz, 2H, Ar^1CH_2P), 2.49 (t, 2H, J = 6.6Hz, $OCH_2CH_2COOC(CH_3)_3$), 1.43 (s, 9H, $COOC(CH_3)_3$), 1.22 (t, J = 7.1Hz, 6H, $PO(OCH_2CH_3)_2$); ^{13}C NMR (75MHz, $CDCl_3$) δ 171.0 ($COO(CH_3)_3$), 167.1 (NHCO), 157.6 (J = 3.3 Hz, Ar), 152.5 (Ar), 141.6 (Ar), 130.8 (J = 6.6 Hz, Ar), 129.5 (Ar), 124.1 (J = 9.3Hz, Ar), 114.6 (J = 2.7Hz, Ar), 107.4 (Ar), 80.3 ($C(CH_3)_3$), 72.2 (PEG), 71.9 (PEG), 70.7 (PEG), 70.6 (PEG), 70.5 (PEG), 70.55 (PEG), 70.4 (PEG), 70.3 (PEG), 69.7 (PEG), 69.1 (PEG), 66.8 (OCH_2CH_2NH), 66.6 (CH_2CH_2COO), 62.0 (J = 7.1Hz, CH_2CH_3), 58.9 (OCH_3), 39.8 ($CH_2NHCOAr$), 35.4 (CH_2COO), 32.8 (J = 138.9Hz, CH_2P), 28.4 ($C(CH_3)_3$), 16.3 (J = 6.0Hz, CH_2CH_3); ^{31}P NMR (81MHz, $CDCl_3$) δ 26.65; MS (MALDI–TOF) m/z calculated for $C_{61}H_{106}NaNO_{26}P$: 1322.60, obtained: 1322.58; calculated for $C_{61}H_{106}KNO_{26}P$: 1338.60, obtained: 1338.55.

Compound 12: TMSBr (0.29mL, 2.2mmol, 20eq.) was added dropwise to a solution of **11** (0.14g, 0.11mmol) in dry DCM (5mL) kept at 0°C. After stirring overnight at room temperature, the volatiles were evaporated and MeOH was added to the crude product and evaporated several times. The Phosphonic

acid **12** was obtained as orange oil in 90% yield without further purification. ^{1}H NMR (300MHz, CD_3OD) δ 7.307.25 (m, 4H, $Ar^1 - 2,6 - H$ and $Ar^2 - 2,6 - H$), 6.97 (d, J = 8.3Hz, 2H, $Ar^1 - 3,5 - H$), 4.31 – 4.18 (m, 8H, $Ar^1OCH_2CH_2NH$ and $Ar^2OCH_2CH_2O$), 3.93 (m, 6H, OCH_2CH_2O), 3.85 – 3.50 (m, 56H, OCH_2CH_2O), 3.41 (s, 6H, $OCH_2CH_2OCH_3$), 3.12 (d, J = 21.3Hz, 2H, Ar^1CH_2P), 2.63 (t, 2H, J = 6.1Hz, OCH_2CH_2COOH); ^{13}C NMR (75MHz, CD_3OD) δ 171.8 (COOH), 167.8 (NHCO), 157.2 (Ar), 151.8 (Ar), 140.4 (Ar), 130.1 (J = 6.0Hz, Ar), 128.5 (Ar), 124.3 (J = 9.3Hz, Ar), 113.8 (Ar), 106.1 (Ar), 71.8 (PEG), 71.0 (PEG), 69.9 (PEG), 69.8 (PEG), 69.7 (PEG), 69.6 (PEG), 69.4 (PEG), 69.3 (PEG), 68.9 (PEG), 68.2 (PEG), 65.8 (PEG), 65.6 (OCH_2CH_2NH), 57.2 (CH_2CH_2COOH), 50.1 (OCH_3), 39.0 (CH_2P), 33.9 (CH_2CH_2NH), 32.8 (J = 135.5Hz, CH_2CH_2COOH); ^{31}P NMR (81MHz, CD_3OD) δ 25.32; MS (MALDI–TOF) m/z calculated for $C_{53}H_{90}NaNO_{26}P$: 1210, 55 obtained: 1220.57; calculated for calculated for $C_{61}H_{106}KNO_{26}P$: 1226.55, obtained: 1226.58.

Compound 13: Concentrated Sulfuric acid (0.6mL) was slowly added to a solution of 5–Hydroxyisophtalic acid (1g, 5.49mmol) in MeOH (15mL). After stirring the reaction at 70°C for 4h, water (100mL) was added and product was extracted using DCM. Organic phase was washed with saturated solution of $NaHCO_3$, brine and water, dried over $MgSO_4$, filtered and concentrated under reduced pressure. The product was obtained as a white solid in 97% yield. ^{1}H NMR (300MHz, CD_3OD) δ 8.17 (t, J = 1.5Hz, 1H, $Ar - 4 - H$), 7.69 (d, J = 1.4Hz, 2H, $Ar - 2,6 - H$), 3.98 (s, 6H, $COOCH_3$); ^{13}C NMR (75MHz, CD_3OD) δ 167.2 ($COOCH_3$), 162.3 (Ar), 134.8 (Ar), 128.4 (Ar), 56.5 ($COOCH_3$).

Compound 14: $LiAlH_4$ 0.5M in THF (36.0mmol, 1.8eq.) was added dropwise at 0°C to a solution of **13** (4.20g, 20.0mmol) in anhydrous THF (21mL). After 3h stirring under reflux, the mixture was cooled to room temperature and MeOH, water and was added then acidified with H_2SO_4 (30mL, 10%). The THF was evaporated under reduced pressure and the resulting aqueous phase was extracted several times (at least 6 times, TLC control) with EtOAc. The organic phase was dried over $MgSO_4$, filtered and concentrated under reduced pressure to afford **14** (18.8mmol, 95%). White foam. ^{1}H NMR (300MHz, CD_3OD–d) δ 6.82 (s, 1H, $Ar - 4 - H$), 6.71 (s, 2H, $Ar - 2,6 - H$), 4.52 (d, J = 5.8Hz, 4H, $ArCH_2OH$); ^{13}C NMR (75MHz, CD_3OD–d) δ 157.2 (Ar), 143.7 (Ar), 115.1 (Ar), 112.1 (Ar), 63.0 (CH_2OH); MS (MALDI–TOF) m/z calculated for $C_{10}H_{12}NaO_5$: 225.20, obtained: 225.09.

Compound 15: A solution of HBr 30% in Acetic acid (36.0mmol, 1.8eq.) was added dropwise at 0°C to a solution of **14** (2.00g, 13.0mmol) in Acetic acid (21mL). The mixture was stirred 24h at room temperature, and then 80mL of distilled water were added. A white precipitate was formed and the mixture was stirred for additional 10 minutes. The resulting aqueous phase was extracted 3 times with DCM (200mL) and the

organic layer was washed with distilled water (2 x 120mL), a saturated solution of $NaHCO_3$ (2 x 120mL), and with brine (80mL). The organic phase was dried over $MgSO_4$, filtered and concentrated under reduced pressure to afford **15** (12.5mmol, 96%). White solid. ^{1}H NMR (300MHz, $CDCl_3$) δ 6.99 (t, J = 1.3Hz, 1H, Ar – 4 – H), 6.04 (d, J = 1.3Hz, 2H, Ar – 2,6 – H), 5.38 (bs, 1H, OH), 4.40 (s, 4H, $ArCH_2Br$); ^{13}C NMR (75MHz, $CDCl_3$) δ 155.8 (Ar), 140.0 (Ar), 122.2 (Ar), 116.2 (Ar), 32.7 (CH_2Br).

Compound 16: A solution of **15** (2.24g, 8.0mmol) in $P(OEt)_3$ (4.0 eq., 5.0mL) was stirred 2h at 160°C. The excess of $P(OEt)_3$ was evaporated under reduced pressure at 70°C. The crude product was purified by column chromatography (SiO_2, DCM / MeOH 95:5) to afford **16** (7.6mmol, 95%) as a yellowish oil. ^{1}H NMR (300MHz, $CDCl_3$) δ 6.82 (bs, 2H, Ar – 2,6 – H), 6.62 (bs, 1H, Ar – 4 – H), 3.99 (m, 8H, $PO(OCH_2CH_3)_2$), 3.49 (d, J = 21.9Hz, 4H, $ArCH_2P$), 1.23 (t, J = 7.1Hz, 12H, $PO(OCH_2CH_3)_2$); ^{13}C NMR (75MHz, $CDCl_3$) δ 157.9 (Ar), 132.6 (J = 10.6Hz, Ar), 122.4 (J = 6.7Hz, Ar), 115.8 (Ar), 62.5 (J = 6.6Hz, CH_2CH_3), 33.6 (J = 138.8Hz, PCH_2CH_3), 16.5 (J = 5.2Hz, PCH_2CH_3); ^{31}P NMR (81MHz, $CDCl_3$) δ 26.72; MS (MALDI–TOF) m/z calculated for $C_{16}H_{29}O_7P_2$: 395.14, obtained: 394.96.

Compound 17: (2–bromo–ethyl) Carbamic acid *tert*–butyl ester (0.86g, 3.82mmol, 3eq.), K_2CO_3 (1.11g, 8.03mmol, 3eq.) and KI (0.042g, 0.25mmol, 0.2eq.) were added to a solution of **16** (0.5g, 1.27mmol) in Acetone (25mL). The mixture was stirred during 72h at 65°C, filtered over Celite and concentrated under reduced pressure. The resulting crude product was diluted in DCM (50mL) and washed twice with an aqueous saturated solution of $NaHCO_3$ and with brine. After drying over $MgSO_4$, filtration and evaporation of the solvent, the crude product was purified by column chromatography over silica gel (DCM / MEOH 98/2 to 95/5) to afford *tert*–butyl protected compound as yellow oil in 70% yield. ^{1}H NMR (300MHz, $CDCl_3$) δ 6.8 (s, 1H, Ar – 4 – H), 6.75 (s, 2H, Ar – 2,6 – H), 3.97 – 4.07 (m, 10H, $PO(OCH_2CH_3)_2$and CH_2CH_2NH), 3.5 (dd, J = 10.1 and 4.5Hz, CH_2CH_2NH), 3.08 (d, J = 21.8, 4H, $ArCH_2P$), 1.44 (s, 9H, $COO(C(CH_3)_3)$, 1.25 (t, J = 21.8Hz, 12H, $PO(OCH_2CH_3)_2$); ^{13}C NMR (75MHz, $CDCl_3$) δ 158.5 (Ar), 155.7 ($NHCOOC(CH_3)_3$), 133.1 (Ar), 123.9 (J = 6.9Hz, Ar), 114.5 (Ar), 79.4 ($COO(C(CH_3)_3$), 67.0 (CH_2CH_2NH), 62.1 (J = 6.6Hz, PCH_2CH_3), 39.9 (CH_2CH_2NH), 33.6 (J = 138.2Hz, CH_2P), 28.3 ($PO(OCH_2CH_3)_2$), 16.4 ($C(CH_3)_3$); ^{31}P NMR (81MHz, $CDCl_3$) δ 26.09; MS (MALDI–TOF) m/z calculated for $C_{23}H_{41}NO_9P_2$: 537.23, obtained 538.53.

Compound 18: Trifluoroacetic acid (1.1mL, 13mmol, 10.0eq.) was added dropwise to a solution of **17** (0.5g, 1.3mmol) in DCM (15mL) at 0°C. The reaction mixture was stirred overnight at room temperature, the volatiles were then evaporated. The crude product was dissolved in a solution of DCM / MeOH (9/1) (20mL) and was washed with NaOH 1N (2 x 10mL). The organic layer was dried over $MgSO_4$, filtered and

concentrated under reduced pressure to afford **18** as a white solid in 70% yield. ^{1}H NMR (300MHz, $CDCl_3$) δ 6.72 (m, 3H, Ar – 2,4,6 – H), 5.25 (bs, 2H, $OCH_2CH_2NH_2$), 4.03 – 3.92 (m, 10H, $PO(OCH_2CH_3)_2$ and $OCH_2CH_2NH_2$), 3.10 (d, J = 21.7Hz, 4H, $ArCH_2P$), 3.02 (m, 2H, $OCH_2CH_2NH_2$), 1.25 (t, J = 7.1Hz, 12H, $PO(OCH_2CH_3)_2$); ^{13}C NMR (75MHz, $CDCl_3$) δ 159.0 (J = 2.8 Hz, Ar), 133.1 (J = 6.0Hz, Ar), 123.8 (J = 6.8Hz, Ar), 114.5 (J = 5.0Hz, Ar), 70.0 (OCH_2), 62.1 (J = 7.0Hz, CH_2CH_3), 41.5 (CH_2NH_2), 33.5 (J = 138.2Hz, CH_2P), 16.5 (J = 2.7Hz, CH_2CH_3); ^{31}P NMR (81MHz, $CDCl_3$) δ 26.24; MS (MALDI–TOF) m/z calculated for $C_{18}H_{34}NO_7P_2$: 438.17, obtained: 438.18; calculated for $C_{18}H_{34}NaO_7P_2$: 460.17, obtained: 460.16.

Compound 19: NEt_3 (8.1mL, 58.91mmol, 2.3eq.) and *para*–Toluenesulfonyl chloride (5.86g, 30.73mmol, 1.2eq.) were added to a solution of N–*Z*–Ethanolamine (5g, 25.61mmol) in DCM (20mL) kept at 0°C. After 16h stirring at room temperature, the reaction mixture was diluted with DCM (70mL). The organic phases were combined, washed with brine, dried over $MgSO_4$, filtered and concentrated under reduced pressure. The crude product was purified by column chromatography over silica gel (CyHex/Acetone gradient) to afford **19** as a white solid in 75% yield. ^{1}H NMR (300MHz, $CDCl_3$): δ 7.79 (2H, AA' part of an AA'BB' system), 7.34 (m, 7H, BB' part of an AA'BB' system and Ar^{Cbz}), 5.15 (bs, 1H, NH), 5.06 (s, 2H, CH_2Ar^{Cbz}), 4.1 (t, J = 5.1Hz, 2H, OCH_2CH_2NH), 3.45 (q, J = 5.4Hz, 2H, OCH_2CH_2NH), 2.4 (s, 3H, CH_3Ar); ^{13}C NMR (75MHz, $CDCl_3$) δ 156.12 (NHCOO), 145.04 (Ar), 136.2 (Ar), 132.6 (Ar^{Cbz}), 129.9 (Ar), 128.5 (Ar^{Cbz}), 128.15 (Ar), 127.97 (Ar^{Cbz}), 127.87 (Ar^{Cbz}), 69.05 (CH_2Ar^{Cbz}), 66.8 (OCH_2CH_2NH), 40.2 (OCH_2CH_2NH), 21.6 ($ArCH_3$); MS (MALDI–TOF) m/z calculated for $C_{17}H_{19}NO_5S$: 349.10, obtained 350.93.

Compound 20: K_2CO_3 (3.68g, 26.63mmol, 3eq.) was added to a solution of **19** (3.41g, 9.76mmol, 1.1eq.) and **16** (3.5g, 8.88mmol) in Acetone (150mL). The reaction mixture was stirred at 60°C during 48h. After filtration over Celite, the solvent was evaporated and the residue was diluted in DCM (50mL). The organic layer was washed twice with brine, filtered and concentrated under reduced pressure. The crude product was purified by column chromatography on silica gel eluting with EtOAc / MeOH (98/2 to 95/5) to afford **20** as a yellowish oil in 85% yield. ^{1}H NMR (300MHz, $CDCl_3$) δ 7.35 (bs, 5H, Ar^{Cbz}), 6.8 (s, 1H, Ar – 4 – H), 6.7 (s, 2H, Ar – 2,6 – H), 5.2 (bs, 1H, NH), 5.1 (s, 2H, CH_2Ar^{Cbz}), 3.99 – 4.12 (m, 10H, $PO(OCH_2CH_3)_2$ and OCH_2CH_2NH), 3.6 (bs, 2H, OCH_2CH_2NH), 3.08 (d, J = 21.9Hz, 4H, CH_2P), 1.25 (t, J = 6.9Hz, 12h, $PO(OCH_2CH_3)_2$); ^{13}C NMR (75MHz, $CDCl_3$) δ 158.2 (J = 2.8 Hz, Ar), 155.9 (NHCOO), 136.8 (Ar^{Cbz}), 133.5 (Ar), 127.5 (Ar^{Cbz}), 126.9 (Ar^{Cbz}), 123.6 (Ar), 114.5 (Ar), 68.2 (CH_2CH_3NH), 66.9 (CH_2Ar^{Cbz}), 41.1 (CH_2NH_2), 33.2 (J = 138.4Hz, CH_2P), 16.3 (CH_2CH_3); ^{31}P NMR (81MHz, $CDCl_3$) δ 26.07; MS (MALDI–TOF) m/z calculated for $C_{26}H_{39}NO_9P_2$: 571.21, obtained: 572.16.

Compound 21: BOP (2.7g, 6.1mmol, 1.3eq.) was added under argon to a solution of Carboxylic acid **4** (2.93g, 4.57mmol, 1eq.) in dry DCM (120mL). After 5min stirring, Amine derivative **18** (2g, 4.57mmol, 1eq.) and *N,N*–Diisopropylethylamine (3.19mL, 3.32mmol, 4eq.) were added. The reaction mixture was stirred overnight at room temperature. 40mL of DCM were added and the organic layer was washed with a solution of NaOH 1N (2 x 20mL), HCl 1N (2 x 20mL), brine (2 x 20mL) and water (1 x 20mL), dried over $MgSO_4$, filtered and concentrated under reduced pressure. The crude product was purified by column chromatography over silica gel (DCM / MeOH 98/2 to 95/5) to afford **21** as colorless oil in 66% yield. ^{1}H NMR (300MHz, $CDCl_3$) δ 7.50 (d, J = 7.7Hz, 2H, Ar^{Bz} – 2,6 – H), 7.35 – 7.28 (m, 3H, Ar^{Bz} – 3,4,5 – H), 7.07 (s, 2H, Ar^2 – 2,6 – H), 6.88 (t, J = 5.7Hz, 1H, OCH_2CH_2NH), 6.85 – 6.78 (m, 3H, Ar^1 – 2,4,6 – H), 5.07 (s, 2H, $Ar^{Bz}CH^2O$), 4.20 – 4.17 (t, J = 4.8Hz, 4H, Ar^2OCH_2), 4.15 – 4.11 (t, J = 5.0Hz, 2H, OCH_2CH_2NH), 4.08 – 3.96 (m, 8H, $PO(OCH_2CH_3)_2$), 3.88 – 3.78 (m, 6H, OCH_2CH_2NH and OCH_2CH_2O), 3.71 – 3.68 (m, 4H, OCH_2CH_2O), 3.65 – 3.58 (m, 16H, OCH_2CH_2O), 3.55 – 3.49 (m, 4H, OCH_2CH_2O), 3.35 (s, 6H, $OCH_2CH_2OCH_3$), 3.08 (d, J = 21.5Hz, 4H, Ar^1CH_2P), 1.25 (t, J = 7.0Hz, 12H, $PO(OCH_2CH_3)_2$); ^{13}C NMR (75MHz, $CDCl_3$) δ 167.2 (NHCO), 158.6 (J = 2.8Hz, Ar), 152.8 (Ar), 141.0 (Ar), 137.8 (Ar), 133.1 (J = 6.0Hz, Ar), 129.6 (Ar), 128.2 (Ar), 128.0 (Ar), 127.8 (Ar), 124.0 (J = 6.8 Hz, Ar), 114.6 (J = 4.8 Hz, Ar), 107.0 (Ar), 74.9 (OCH_2), 72.0 (PEG), 70.8 (PEG), 70.7 (PEG), 70.6 (PEG), 69.8 (PEG), 69.1 (PEG), 66.8 (OCH_2CH_2NH), 62.1 (J = 3.4Hz, $PO(OCH_2CH_3)_2$), 58.9 (OCH_3), 39.5 ($CH_2NHCOAr$), 33.5 (J = 138.3Hz, CH_2P), 16.5 (J = 2.7Hz, $PO(OCH_2CH_3)_2$); ^{31}P NMR (81MHz, $CDCl_3$) δ 26.08; MS (MALDI–TOF) m/z calculated for $C_{50}H_{79}NaNO_{19}P_2$: 1082.87, obtained: 1082.51.

Compound 22: **21** (2.03g, 1.91mmol) was dissolved in Ethanol absolute (50mL) and Palladium activated on carbon 10% (0.5eq.) was added. The mixture was stirred under a hydrogen atmosphere at room temperature for 16h. The product was filtered through a plug of Celite before being concentrated and purified by column chromatography on silica gel eluting with DCM / MeOH (98/2 to 95/5) to afford phenol **22** as a colorless oil in 83% yield.^{1}H NMR (300MHz, $CDCl_3$) δ 7.16 (s, 2H, Ar^2 – 2,6 – H), 6.85 – 6.78 (m, 3H, Ar^1 – 2,4,6 – H), 6.65 (m, 1H, OCH_2CH_2NH), 4.27 – 4.21 (t, J = 4.7Hz, 4H, Ar^2OCH_2), 4.15 – 4.10 (t, J = 5.0Hz, 2H, OCH_2CH_2NH), 4.08 – 3.98 (m, 8H, $PO(OCH_2CH_3)_2$), 3.88 – 3.78 (m, 6H, OCH_2CH_2NH and OCH_2CH_2O), 3.75 – 3.60 (m, 20H, OCH_2CH_2O), 3.56 – 3.51 (m, 4H, OCH_2CH_2O), 3.35 (s, 6H, $OCH_2CH_2OCH_3$), 3.09 (d, J = 22.0Hz, 4H, Ar^1CH_2P), 1.26 (t, J = 7.1Hz, 12H, $PO(OCH_2CH_3)_2$); ^{13}C NMR (75MHz, $CDCl_3$) δ 167.3 (NHCO), 158.7 (J = 2.8Hz, Ar), 146.8 (Ar), 141.0 (Ar), 133.1 (J = 6.0Hz, Ar), 124.0 (Ar), 114.6 (Ar), 108.4 (Ar), 72.0 (PEG), 70.8 (PEG), 70.7 (PEG), 70.6 (PEG), 69.8 (PEG), 69.1 (PEG), 66.8 (OCH_2CH_2NH), 62.1 (J = 3.4Hz, $PO(OCH_2CH_3)_2$), 58.9 (OCH_3), 39.5 ($CH_2NHCOAr$), 33.4 (J = 138.1Hz, CH_2P), 16.4 (J = 2.7Hz, $PO(OCH_2CH_3)_2$); ^{31}P NMR (81MHz, $CDCl_3$) δ 26.10; MS (MALDI–TOF) m/z calculated for

$C_{43}H_{74}NO_{19}P_2$: 970.43, obtained: 970.44; calculated for $C_{43}H_{73}NaNO_{19}P_2$: 992.43, obtained: 992.44.

Compound 23: K_2CO_3 (1.59g, 11.51mmol, 6eq.) was added to a solution of **22** (1.86g, 1.92mmol) and **10** (1.75g, 2.68mmol, 1.4eq.) in dry Acetone (200mL). The reaction mixture was stirred at 60°C during 24h. After filtration over Celite, the solvent was evaporated and the residue was diluted in DCM (50mL). The organic layer was washed twice with a saturated solution of $NaHCO_3$, then with brine, filtered and concentrated under reduced pressure. The crude product was purified by column chromatography on silica gel eluting with DCM / MeOH (98/2 to 95/5) to afford **23** as a colorless oil in 70% yield. ^{1}H NMR (300MHz, $CDCl_3$) δ 7.10 (s, 2H, $Ar^2 - 2,6 - H$), 6.87 (t, J = 5.1Hz, 1H, $Ar^1OCH_2CH_2NH$), 6.80 (t, 1H, J = 2.0Hz, $Ar^1 - 2 - H$), 6.76 (q, 2H, J = 2.0Hz, $Ar^1 - 4,6 - H$), 4.22 – 4.15 (m, 6H, $Ar^2OCH_2CH_2O$), 4.12 (t, 2H, J = 5.1Hz, OCH_2CH_2NH), 4.05 – 3.95 (m, 8H, $PO(OCH_2CH_3)_2$), 3.85 – 3.75 (m, 8H, OCH_2CH_2NH and OCH_2CH_2O), 3.70 – 3.50 (m, 54H, OCH_2CH_2O), 3.33 (s, 6H, OCH_3), 3.07 (d, J = 21.7Hz, 4H, Ar^1CH_2P), 2.48 (t, 2H, J = 6.6Hz, $CH_2CH_2COOC(CH_3)_3$), 1.42 (s, 9H, $COOC(CH_3)_3$), 1.22 (t, J = 7.0Hz, 12H, $PO(OCH_2CH_3)_2$); ^{13}C NMR (75MHz, $CDCl_3$) δ 170.9 ($COO(CH_3)_3$), 167.1 (NHCO), 157.5 (Ar), 152.4 (Ar), 141.6 (Ar), 133.2 (J = 6.0Hz, Ar), 129.4 (Ar), 124.1 (Ar), 114.6 (J = 5.0Hz, Ar), 107.3 (Ar), 80.4 ($COOC(CH_3)_3$), 72.2 (PEG), 71.9 (PEG), 70.7 (PEG), 70.6 (PEG), 70.55 (PEG), 70.5 (PEG), 70.4 (PEG), 70.3 (PEG), 69.7 (PEG), 69.1 (PEG), 66.8 (OCH_2CH_2NH), 66.6 (CH_2CH_2COO), 62.1 (J = 7.0Hz, $PO(OCH_2CH_3)_2$), 58.9 (OCH_3), 39.6 (CH_2NHCO), 35.2, (CH_2COO), 33.8 (J = 137.8Hz, CH_2P), 27.9 ($C(CH_3)_3$), 16.4 (J = 6.0Hz, $PO(OCH_2CH_3)_2$); ^{31}P NMR (81MHz, $CDCl_3$) δ 26.06; MS (MALDI–TOF) m/z calculated for $C_{66}H_{117}NaNO_{29}P_2$: 1472.72, obtained: 1472.65.

Compound 24: TMSBr (0.55mL, 3mmol, 30eq.) was added dropwise to a solution of **23** (0.2g, 0.14mmol) in dry DCM (5mL) kept at 0°C. After stirring overnight at room temperature, the volatiles were evaporated and MeOH was added to the crude product and evaporated several times. The Phosphonic acid **24** was obtained as orange oil in 93% yield without further purification. ^{1}H NMR (300MHz, CD_3OD) δ 7.28 (s, 2H, $Ar^2 - 2,6 - H$), 6.92 – 6.86 (m, 3H, $Ar^1 - 2,4,6 - H$), 4.35 – 4.20 (m, 8H, $Ar^2OCH_2CH_2O$ and $Ar^1OCH_2CH_2NH$), 3.92 – 3.82 (m, 8H, $Ar^1OCH_2CH_2NH$ and OCH_2CH_2O), 3.80 – 3.53 (m, 54H, OCH_2CH_2O), 3.38 (s, 6H, OCH_3), 3.18 (d, J = 21.8Hz, 4H, Ar^1CH_2P), 2.62 (t, 2H, J = 6.0Hz, OCH_2CH_2COOH); ^{13}C NMR (75MHz, CD_3OD) δ 172.2 (COOH), 167.1 (NHCO), 158.8 (Ar), 152.3 (Ar), 141.0 (Ar), 134.8 (J = 6.0Hz, Ar), 128.8 (Ar), 123.8 (Ar), 114.3 (Ar), 106.4 (Ar), 72.2 (PEG), 71.7 (PEG), 70.4 (PEG), 70.25 (PEG), 70.15 (PEG), 70.1 (PEG), 70.0 (PEG), 69.95 (PEG), 69.4 (PEG), 68.8 (PEG), 66.3 (OCH_2CH_2NH), 66.1 (CH_2CH_2COO), 57.8 (OCH_3), 50.8, 39.6 (CH_2NHCO), 34.6 (CH_2COOH), 33.6 (J = 134.5Hz, CH_2P); ^{31}P NMR (81MHz, CD_3OD) δ 25.19; MS (MALDI–TOF) m/z calculated for $C_{54}H_{94}NO_{29}P_2$: 1282.53, obtained:

1282.46; calculated for $C_{54}H_{93}NaNO_{29}P_2$: 1304.53, obtained: 1304.45.

Compound 26: A solution of Sodium trimethylsilanolate (TMSONa, 1M) in DCM (66mL, 66mmol) was added to a solution of $G_{0.5}$ PAMAM dendron (5g, 22mmol) in DCM (90mL). The mixture was stirred for 16h at room temperature. The solvent was then evaporated in vacuo and the residue was precipitated in EtOAc. The solid was filtered and **26** was obtained (22mmol, quant) as yellow solid. ^{1}H NMR (300MHz, D_2O) δ 3.36 (s, 2H, CH_2 alkyne), 2.38 (dd, J = 10.6 and 11.9Hz, 4H, NCH_2), 1.63 (dd, J = 12.2 and 10.6Hz, 4H, CH_2COONa), 0.84 (s, 1H, CH alkyne); ^{13}C NMR (75MHz, D_2O) δ 181.1 (COO), 77.9 (C alkyne), 74.5 (CH alkyne), 49.7 (NCH_2), 41.1 (alkyne–CH_2), 34.9 (CH_2COONa); MS (MALDI–TOF) m/z calculated for $C_9H_{11}NNa_2O_4$: 243.05, obtained 242.28.

Compound 27: N– (3– Dimethylaminopropyl)– N′– ethylcarbodiimide hydrochloride (EDCI, 0.38g, 1.97mol), HOBt (0.05 g, 0.33 mmol) and DIPEA (0.31mL, 1.8mmol) were added to a suspension of **26** (0.2g, 0.82mmol) and H_2N–$dPEG_4$–tBu (0.58g, 1.8mmol) in CH_3CN (9mL). The mixture was stirred at room temperature for 16h and then the solvent was evaporated. The crude mixture was purified by column chromatography (SiO2, DCM / MeOH 90:10) to yield **27** (1.05mmol, 67%) as yellow oil. ^{1}H NMR (300MHz, $CDCl_3$) δ 7.38 (m, 2H, NH), 3.70 – 3.42 (m, 34H, OCH_2CH_2O), 3.39 (m, 4H, NCH_2), 2.81 (dd, J = 6.36 and 6.36Hz, 4H, $CONHCH_2CH_2O$), 2.48 (dd, J = 6.57 and 6.57Hz, 4H, NCH_2CH_2CONH), 2.36 (dd, J = 6.12 and 6.36Hz, 4H, $CH_2COOC(CH_3)_3$), 2.23 (dd, J = 2.2 and 2.4Hz, 1H, H alkyne),1.45 (s, 18H, $OC(CH_3)_3$); ^{13}C NMR (75MHz, $CDCl_3$) δ 171.9 (CONH), 170.8 ($COOC(CH_3)_3$), 80.5 ($C(CH_3)_3$), 77.8 (C Alkyne), 73.6 (CH Alkyne), 70.6 (PEG), 70.5 (PEG), 70.4 (PEG), 70.3 (PEG), 70.2 (PEG), 69.9 (PEG), 66.8 (OCH_2CH_2COO), 49.5 (NCH_2CH_2), 41.5 (alkyne–CH_2), 39.1 ($CONHCH_2CH_2O$), 36.2 ($CH_2COOC(CH_3)_3$), 33.9 (CH_2CONH), 27.9 ($C(CH_3)_3$). MS (MALDI–TOF) m/z calculated for $C_{39}H_{71}N_3O_{14}$: 805.49, obtained $[M+H]^+$ = 806.55.

Compound 28: A solution of Methyl 3,5–dimethylbenzoate (20g, 121.8mmol), N–Bromosuccinimide (47.69g, 267.86mmol, 2.2eq.), and Benzoyl peroxide (1.48g, 6.09mmol, 0.05eq.) in dry $CC1_4$ (200mL) was refluxed for 3 h. After the solution cooled, the precipitate (Succinimide) was separated and washed with $CC1_4$. The filtrate was washed with H_2O, dried ($MgSO_4$), and evaporated. The thick residue was suspended in petroleum ether and refrigerated. The product crystallized to yield compound **28** (28g, 72%). ^{1}H NMR (300MHz, $CDCl_3$) δ 8.0 (s, 2H, Ar), 7.6 (s 1H, Ar), 4.5 (s, 4H, CH_2Br), 3.9 (s, 3H, CH_3COO); ^{13}C NMR (75MHz, $CDCl_3$) δ 165.7 ($COOCH_3$), 138.3 (Ar), 135.6 (Ar), 130.6 (Ar), 129.7 (Ar), 52.3 (CH_3COO), 31.9 (CH_2Br).

Compound 29: A mixture of DIBALH (4.7g, 32.74mmol, 2.2eq.) and Toluene (25ml) was cooled to 0 °C under argon. A solution of **28** (5g, 14.88mmol) in Toluene (45ml) was added dropwise and the reaction mixture was stirred for 3h at 0°C. A solution of HCl 1N was added until pH = 1. The phases were separated; the organic phase was washed with water, dried over $MgSO_4$, filtered and concentrated at reduced pressure. The crude was purified by silica gel chromatography (CyHex / EtOAc 70/30) to yield compound **29** as a white solid (92%). ^{1}H NMR (300MHz, $CDCl_3$) δ 7.34 (bs, 3H, Ar), 4.7 (s, 2H, CH_2OH), 4.5 (s, 4H, CH_2Br); ^{13}C NMR δ 141.3 (Ar), 138.3 (Ar), 130.6 (Ar), 129.7 (Ar), 65.3 (CH_2OH), 32.3 (CH_2Br).

Compound 30: The Dibromide **29** (3g 10.2mmol) was heated at 140 °C in the presence of $P(OEt)_3$ (6.78g, 40.82mmol, 4eq.) for 2h. The excess of $P(OEt)_3$ was then removed under reduced pressure to yield a white solid **30** quantitatively, which was used in the next step without further purification. ^{1}H NMR (300MHz, $CDCl_3$) δ 7.01 (s, 1H, Ar), 6.83 (bs, 2H, Ar), 4.72 (s, 2H, CH_2OH), 4.2 – 4.07 (m, 8H, $PO(OCH_2CH_3)_2$), 3.29 (d, J = 21.7Hz, 4H, $ArCH_2P$), 1.23 (t, J = 6.8Hz, 12H, $PO(OCH_2CH_3)_2$); ^{13}C NMR (75MHz, $CDCl_3$) δ 147.9 (Ar), 132.6 (Ar), 128.4 (Ar), 122.3 (Ar), 68.9 (CH_2OH), 62.5 ($PO(OCH_2CH_3)_2$), 35.2 (CH_2P), 16.5 ($PO(OCH_2CH_3)_2$); ^{31}P NMR (81MHz, $CDCl_3$) δ 26.7; MS (MALDI–TOF) m/z calculated for $C_{17}H_{30}O_7P_2$: 408.15, obtained $[M+H]^+$ = 409.4

Compound 31: Thionyl chloride (2.33g, 19.59mmol, 2eq.) was added to a solution of **30** (4g, 9.8mmol) in $CHCl_3$ (3mL). The solution was refluxed under argon for 1h. The organic phase was washed with a solution of NaOH 0.1N and brine, then dried over $MgSO_4$, filtered and concentrated under reduced pressure to yield **31** in 60%. It was used in the next step without further purification. ^{1}H NMR (300MHz, $CDCl_3$) δ 7.23 – 7.19 (m, 3H, Ar), 4.55 (s, 2H, CH_2Cl), 4.02 (qt, J= 7.23Hz, 8H, $PO(OCH_2CH_3)_2$), 3.14 (d, J = 21.9Hz, 4H, CH_2P), 1.25 (dd, J = 6.99Hz, 12H, $PO(OCH_2CH_3)_2$); ^{13}C NMR (75MHz, $CDCl_3$) 137.8 (J = 2.72Hz, Ar), 132.3 (J = 6.54Hz, Ar), 131.0 (J = 6.54Hz, Ar), 128.4 (J = 4.91Hz, Ar), 62.1 (J = 6.54Hz, $PO(OCH_2CH_3)_2$), 45.6 (CH_2Cl), 33.2 (J = 137.46Hz, CH_2 P), 16.2 (J = 6.00Hz, $PO(OCH_2CH_3)_2$); ^{31}P NMR (81MHz, $CDCl_3$) δ 26.45; MS (MALDI–TOF) m/z calculated for $C_{17}H_{29}ClO_6P_2$: 426.11, obtained $[M+H]^+$ = 427.06.

Compound 32: Sodium azide (2.02g, 31mmol) was added to a solution of **31** (6.63g, 15.5mmol) in CH_3CN (78mL) and the resulting mixture was refluxed under argon for 16h. The solvent was then removed under reduced pressure and the residue taken in DCM or EtOAc. The organic phase was washed with water, dried over $MgSO_4$, filtered and concentrated under reduced pressure. The crude mixture was purified by column chromatography (SiO2, DCM / MeOH 95:5) to yield **32** (4.61mmol, 70%) as yellow oil. ^{1}H NMR (300MHz, $CDCl_3$) δ 7.21 – 7.16 (m, 3H, Ar), 4.31 (s, 2H, CH_2N_3), 4.00 (qt, J = 7.23Hz, 8H, $PO(OCH_2CH_3)_2$), 3.14 (d, J = 21.93Hz, 2H, CH_2P), 1.25 (t, J = 7.02Hz, 12H, $PO(OCH_2CH_3)_2$); ^{13}C NMR (75MHz, $CDCl_3$) δ

135.7 (J = 2.72Hz, Ar), 132.5 (J = 6.54Hz, Ar), 130.8 (J = 6.54Hz, Ar), 127.9 (J = 4.91Hz, Ar), 61.9 (J = 7.08Hz, CH_2P), 54.0 (CH_2N_3), 33.2 (J = 136.92Hz, $PO(OCH_2CH_3)_2$), 16.1 (J = 5.46Hz, $PO(OCH_2CH_3)_2$); ^{31}P NMR (81MHz, $CDCl_3$) δ 26.48; MS (MALDI–TOF) m/z calculated for $C_{17}H_{29}N_3O_6P_2$: 433.15, obtained $[M+H]^+$ = 434.10.

Compound 33: A mixture of Azide **32** (0.070g, 0.25mmol, 1.1 equiv) and Propargyl derivative **27** (0.2g, 0.27mmol) in THF/H_2O (4/1, v/v, in mL) in the presence of 5% mol of Cu(II)SO_4·$5H_2O$ and 10% mol of Sodium ascorbate was stirred at room temperature for 16h. The reaction mixture was then quenched with brine and the aqueous phase extracted with EtOAc. The organic phase was dried over $MgSO_4$, filtered and concentrated under reduced pressure. The crude mixture was purified by column chromatography (SiO_2, DCM / MeOH 90:10). **33** was obtained (0.15mmol, 75%) as yellow oil. ^{1}H NMR (300MHz, $CDCl_3$) δ 7.53 (s, 1H, CH triazole), 7.37 (m, 2H, NH), 7.11 – 7.10 (m, 3H, Ar), 5.47 (s, 2H, CH_2 triazole), 4.00 (qt, J = 7.23Hz, 8H, $PO(OCH_2CH_3)_2$), 3.79 (s, 2H, CH_2N triazole), 3.72 – 3.51 (m, 34H, OCH_2CH_2O), 3.39 (m, 4H, NCH_2 PAMAM), 3.1 (d, J = 21.9Hz, 4H, CH_2P), 2.75 (dd, J = 6.12 and 6.3Hz, 4H, $CONHCH_2$), 2.49 (dd, J = 6.6 and 6.57Hz, 4H, CH_2CONH), 2.39 (dd, J = 6.32 and 6.15Hz, 4H, CH_2COO), 1.43 (s, 18H, $COOC(CH_3)_3$), 1.23 (t, J = 7.02 Hz, 12H, $PO(OCH_2CH_3)_2$); ^{13}C NMR (75MHz, $CDCl_3$) δ 171.9 (COO), 170.6 (CONH), 143.9 (Ar^2), 135.3 (C triazole), 132.9 (J = 6.00Hz, Ar^1), 131.2 (Ar^1), 127.7 (J = 4.91Hz, Ar^2), 122.8 (CH triazole), 80.2 ($COOC(CH_3)_3$), 70.4 (PEG), 70.3 (PEG), 70.2 (PEG), 69.9 (PEG), 69.6 (PEG), 66.6 (CH_2CH_2CONH), 62.0 (J = 7.09Hz, $PO(OCH_2CH_3)_2$), 53.4 (CH_2 triazole), 49.3 (NCH_2), 47.7 (CH_2N triazole), 38.8 ($CONHCH_2$), 36.0 (CH_2CONH), 33.8 (J = 137.46Hz, CH_2P), 32.2 (CH_2COO), 27.9 ($C(CH_3)_3$), 16.2 (J = 6.00Hz, $PO(OCH_2CH_3)_2$); ^{31}P NMR (81MHz, $CDCl_3$) δ 25.60; MS (MALDI–TOF) m/z calculated for $C_{56}H_{100}N_6O_{20}P_2$: 1238.65, obtained $[M+H]^+$ = 1239.58.

Compound 34: TMSBr (3.46g, 2.98mL, 30eq.) was added dropwise to a solution of **33** (0.93g, 0.75mmol) in dry DCM (10mL) kept at 0°C. After stirring overnight at room temperature, the volatiles were evaporated and MeOH was added to the crude product and evaporated several times. The Phosphonic acid **34** was obtained as orange oil in 66% yield without further purification. ^{1}H NMR (300MHz, CD_3OD) δ 8.45 (bs, 1H, H triazole), 7.32 (s, 1H, Ar), 7.27 (s, 2H, Ar), 5.73 (s, 2H, CH_2N next to triazole), 4.69 (s, 2H, CH_2N PAMAM), 3.80 – 3.41 (m, 40H, PEG), 3.21 (d, J = 21.66Hz, 4H, CH_2P), 2.93 (bs, 4H, CH_2CONH), 2.63 (s, 4H, CH_2COOH); ^{13}C NMR (75MHz, CD_3OD) δ 173.4 (COOH), 171.9 (COOH), 170.3 (CONH), 135.4 (Ar), 134.7 (Ar^2), 134.4 (triazole), 133.8 (Ar^1), 130.7 (Ar^1), 127.0 (Ar^2), 126.5 (CH triazole), 69.7 (PEG), 69.6 (PEG), 69.5 (PEG), 69.3 (PEG), 68.4 ($CH_2OCH_2CH_2COOH$), 65.9 (CH_2CH_2COOH), 65.7 (CH_2CH_2COOH), 53.0 (CH_2 next to triazole), 50.3 (NCH_2 PAMAM), 49.2 (NCH_2 PAMAM), 45.6 (CH_2N

PAMAM), 38.6 ($CONHCH_2$), 34.6, 32.8 (J = 132.54Hz, CH_2P), 33.9 (CH_2COOH), 27.8 (CH_2CONH); ^{31}P NMR (81MHz, CD_3OD) δ 24.92; MS (MALDI–TOF) m/z calculated for $C_{40}H_{68}N_6O_{20}P_2$: 1014.40, obtained $[M+H]^+$ = 1015.36.

References

[1] Gottlieb, H.E., Kotlyar, V., Nudelman, A. NMR Chemical Shifts of Common Laboratory Solvents as Trace Impurities In the course of the routine use of NMR as an aid for organic chemistry , a day-to-day problem is the identifica- tion of signals deriving from common contaminants literature , but the. *The Journal of Organic Chemistry*, **1997**, 62(3), 7512-7515.

[2] Garofalo, A., Parat, A., Bordeianu, C., Ghobril, C., Kueny-Stotz, M., Walter, A., Jouhannaud, J., Begin-Colin, S., Felder-Flesch, D. Efficient synthesis of small-sized phosphonated dendrons potential organic coatings of iron oxide nanoparticles. *New Journal of Chemistry*, **2014**, 38, 5226-5239.

Part VI

Publications and contributions

Posters

1. Bi–phosphonate tweezer and clickable PEGylated PAMAM dendrons for the elaboration of functional iron oxide nanoparticles displaying renal and hepatobiliary eliminations. Bordeianu C., Ghobril C., Parat A., Billotey C., Taleb J., Bonazza P., Begin–Colin S., Felder–Flesch D. Winter School 'Surface–Confined Synthesis of Nanostructures', Baden–Baden, Germany, 2014.

2. Dendrimer–nanoparticle conjugates as Nanomedicine tools. Catalina Bordeianu, Aurelie Walter, Claire Billotey, Sophie Laurent, Robert Muller, Sylvie Begin–Colin, Delphine Felder–Flesch. Fourth International Conference on Multifunctional, Hybrid and Nanomaterials (Hybrid Materials 2015), Sitges, Spain, 2015.

3. Dendronized superparamagnetic nanoparticles as tools for high *in vivo* cancer targeting: application to melanoma. Catalina Bordeianu, Aurélie Walter, Claire Billotey, Sophie Laurent, Robert Muller, Sylvie Begin–Colin, Delphine Felder–Flesch. *Poster Award /Best poster* of the "Contrast Agents" Session–European Society for Molecular Imaging, Tübingen, Germany, 2015.

4. Dendrimer–nanoparticle conjugates as Nanomedicine tools. Catalina Bordeianu, Aurélie Walter, Claire Billotey, Sophie Laurent, Robert Muller, Sylvie Begin–Colin, Delphine Felder–Flesch. 4th Sino–French Workshop on Macromolecules and Soft Matter, Strasbourg, France, 2015.

Oral contributions

1. Dendronized nanoparticles for Multimodal Imaging. Catalina Bordeianu, Audrey Parat, Antonio Garofalo, Aurélie Walter, Cynthia Ghobril, Claire Billotey, Jacqueline Taleb, Pauline Bonazza, Sophie Laurent, Robert Muller, Sylvie Begin–Colin, Delphine Felder–Flesch. Nanohybride, Bastia, France, 2015.

2. Synthesis of biocompatible dendritic nanoparticles for Multimodal Imaging. Catalina Bordeianu, Audrey Parat, Antonio Garofalo, Aurélie Walter, Cynthia Ghobril, Claire Billotey, Jacqueline Taleb, Pauline Bonazza, Sophie Laurent, Robert Muller, Sylvie Begin–Colin, Delphine Felder–Flesch. International Conference on Nanotheranostics (ICoN 2015), Limassol, Cyprus, 2015.

Publications

1. Efficient synthesis of small sized phosphonate dendrons: potential organic coatings of iron oxide nanoparticle. Special SUPRABIO Issue of New Journal of Chemistry, 2014, 38, 5226 (Garofalo *et al.*, 2014).

2. Dendrimer–Nanoparticle conjugates in Nanomedicine. Invited review in Nanomedicine (Future Medicine), 2015, 10(6), 977–992 (Parat *et al.*, 2015).

3. Preparation of core/shell NaYF:Yb,Tm@dendrons nanoparticles with enhanced upconversion luminescence for *in vivo* imaging. Nanomedicine: Nanotechnology, Biology, and Medicine, 2016, doi: 10.1016/j.nano.2016.05.020 (Francolon *et al.*).

4. Design of iron oxide–based nanoparticles for MRI and magnetic hyperthermia. Invited review in Nanomedicine (Future Medicine), 2016, doi: 10.2217/nnm–2016–5001 (Blanco–Andujar *et al.*).

Book chapter

1. Dendrimer–nanoparticles conjugates in Nanomedicine, in "Dendrimers for Nanomedicine", Ed. D. Felder–Flesch, Panstanford Editions, to be published Aug. 2016.

RESUME

Le cancer est une cause majeure de décès dans le monde, 7,6 millions de décès en 2008, (mortalité de 13%) selon l'OMS. La chirurgie, la chimiothérapie et la radiothérapie sont les traitements conventionnels les plus courants actuellement utilisés. Bien que de nombreux progrès ont été réalisés dans le traitement du cancer, de nouvelles approches sont nécessaires pour améliorer les techniques de traitement existantes ou pour développer de nouvelles techniques, ceci afin de minimiser les effets secondaires délétères et d'augmenter le taux de survie des patients. Par conséquent, il existe un réel besoin médical de nouveaux nano-objets efficaces pour le traitement du cancer. La thérapie guidée par l'image sera également cruciale pour le développement de ces nouveaux traitements. Par conséquent, l'avenir de la nanomédecine réside dans le développement de nano-plateformes multifonctionnelles qui combinent à la fois des composants thérapeutiques et de l'imagerie multimodale et qui agissent également localement uniquement au niveau des tumeurs pour éviter les effets secondaires.

La fondation Européenne de la Science, appelle à une stratégie coordonnée pour fournir de nouveaux outils médicaux basés sur les nanotechnologies, à des fins de diagnostic et de thérapie. Ceci est démontré par l'émergence dans ce domaine de nombreuses nouvelles revues à fort impact, symposium internationaux, sociétés médicales et start-ups, et une croissance exponentielle du nombre de publications, de brevets, d'essais cliniques. Au rythme actuel de croissance annuelle de 12,3% les marchés mondiaux de nanomédecine devraient atteindre 177,6 milliards $US en 2019.[1]
Les domaines de plus forte croissance de la nanomédecine sont prévus pour être principalement la neurologie, l'oncologie, la cardiologie, les maladies inflammatoires et infectieuses.

Les nanoparticules d'oxyde de fer (IONPs), de par leurs propriétés physiques et leurs interactions avec les tissus vivants, sont très largement étudiées pour leurs applications dans le domaine biomédical. En particulier, elles sont déjà commercialisées comme agent de contraste pour l'IRM et sont particulièrement intéressantes car biodégradables et non toxiques par rapport à d'autres familles d'agents de contraste (complexes macromoléculaires de gadolinium Gd^{3+}).

[1] www.transparencymarketresearch.com

Dans toutes les applications biologiques la stabilité colloïdale des IONPs est de la plus haute importance. Il a été montré que la demi-vie sanguine, l'opsonisation, la biocinétique et la biodistribution des IONPs sont déterminées à la fois par la nature chimique de la surface et la taille des particules.[2] Les IONPs doivent satisfaire certaines caractéristiques pour avoir une utilité pratique dans le domaine biomédical: (1) hydrophilicité et biocompatibilité; (2) furtivité; (3) stabilité dans le milieu physiologique; (4) taille hydrodynamique <100 nm. Par conséquent, en plus d'une fonctionnalisation multiple et contrôlée, les dendrimères et les unités dendron permettent une polyvalence de taille et des propriétés physico-chimiques (hydrophiles, lipophiles) modulables avec précision en fonction de leur génération (**Figure 1**). Il ne fait aucun doute que les hybrides organique / inorganique à base de dendrimères représentent des outils pharmaceutiques très avancés, capables de cibler un type de cellules spécifiques ou un organe en particulier et d'être suivis par imagerie dans le même temps.

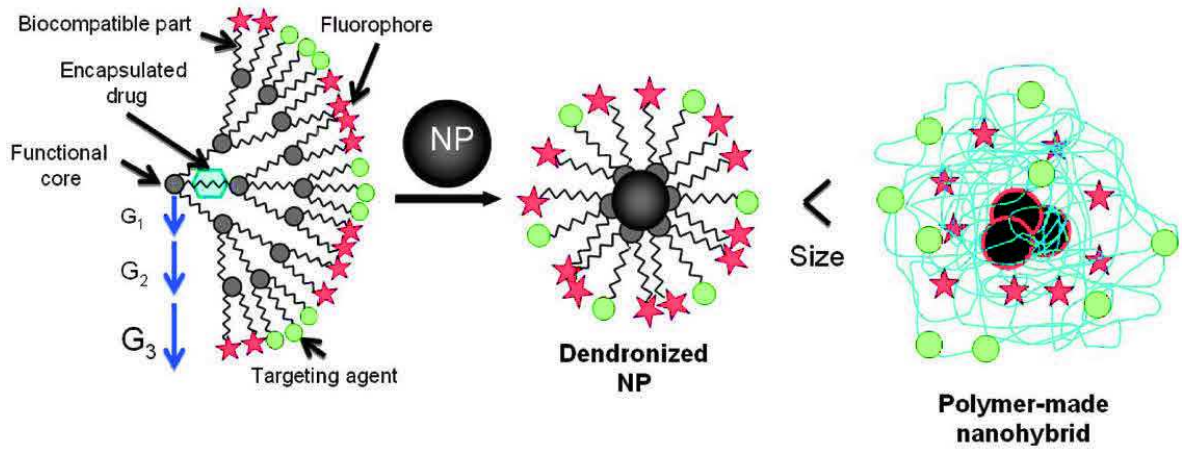

Figure 1: Comparaison entre la taille des nanoparticules dendronisées et leur homologue présentant un enrobage à base de polymère.

Dans ce contexte, les objectifs de cette thèse sont non seulement la conception de nano-objets magnétiques dendronisés multifonctionnels biocompatibles permettant à la fois le diagnostic par imagerie à résonance magnétique (IRM) ainsi que par imagerie

[2] Berry, C. C., & Curtis, A. S. G. (2003). Functionalization of magnetic nanoparticles for applications in biomedicine. Journal of Physics D: Applied Physics, 36, R198–R206

optique (IO) mais également la validation *in vitro* et *in vivo* des propriétés de ces nano-objets et la démonstration de leur efficacité pour le ciblage spécifique de tumeurs.

Le premier objectif du projet de thèse est l'élaboration de dendrons hydrophiles bifonctionnels qui seront greffés de façon covalente d'une part à un agent de ciblage (ex. Pour Apoptose, Inflammation) ou une sonde fluorescente, et d'autre part aux nanoparticules d'oxydes métallique (par phosphonate) ou métalliques (par le biais des groupes thiol) (**Figure 2)**. Une fois les nanomatériaux préparés, une série de tests sera effectuée afin de vérifier leur biocompatibilité et stabilité dans des conditions physiologiques, leurs propriétés magnétiques, leur « non-captation » par le système réticulo-endothélial (RES), leur biodistribution et bioélimination.

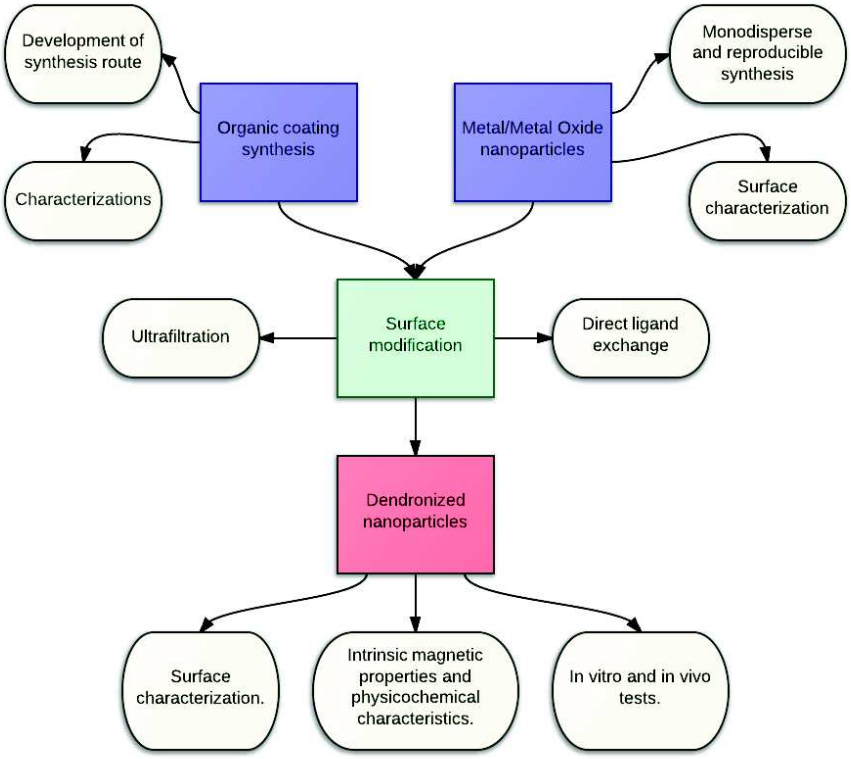

Figure 2: Description générale de la stratégie scientifique de la thèse

Le premier défi de la thèse se concentre sur la synthèse de différents dendrons en optimisant la taille, l'hydrophilie et leur multifonctionnalité.

Le second défi est la synthèse de nanoparticules monodisperses d'oxyde de fer et leur conversion en systèmes reproductibles et biocompatibles par greffage dendritique.

L’ingénierie des dendrons

Nous avons développé une approche convergente impliquant une série de réactions organiques classiques pour la synthèse des dendrons mono- et bis-phosphonate, avec un corps gallate-PEG ou PAMAM-PEG (**Figure 3**).

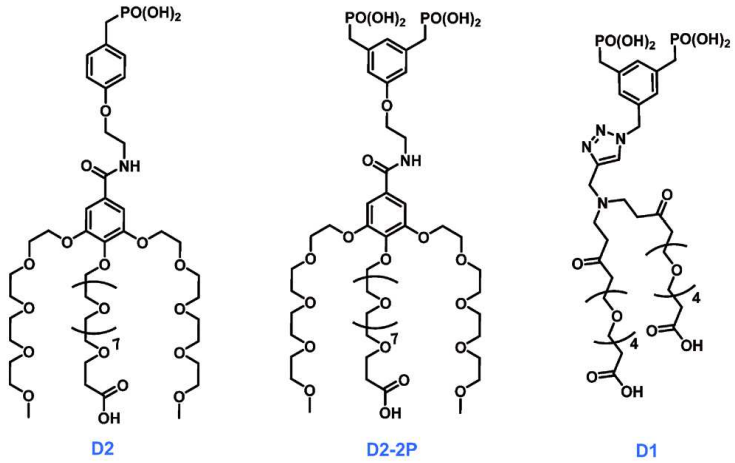

Figure 3: Structure des trois dendrons employés pour la stabilisation des IONPs.

Synthèse du dendron D2

La synthèse du dendron mono-éthyl-phosphonate (D2) est obtenue à partir de l’intermédiaire clé **4** qui a été obtenu en 4 étapes avec un rendement global de 44% (**Figure 5**). Tout d'abord le *para*-benzyle méthyle gallate **2** et le tétraéthylèneglycol monométhylether tosylé **1** ont été obtenus avec de bons rendements à partir du méthyl de gallate commercial et du tetraéthylèneglycol monométhyléther respectivement. Une étherification de Williamson entre **1** et **2** dans l'acétone à 60 ° C, en présence de carbonate de potassium (K_2CO_3) et d'iodure de potassium (KI), a permis la préparation de l'ester **3** avec un rendement de 75%. Ce dernier subi une saponification en milieu basique pour donner le composé **4** avec un rendement de 90%.

La voie de synthèse de l'éthyl phosphonate **7** est représentée sur la **Figure 4**. Le composé a été obtenu en 4 étapes avec un rendement global de 54%. Tout d'abord, le chlorure de 4- (benzyloxy) benzyle est amené à réagir au reflux avec du $P(OEt)_3$ pour donner **5** (92%). Le phénol **6** a été obtenu après hydrogénolyse en présence de Pd/C (10%) avec un rendement de 92%, et a été ensuite engagé dans une réaction d'étherification en

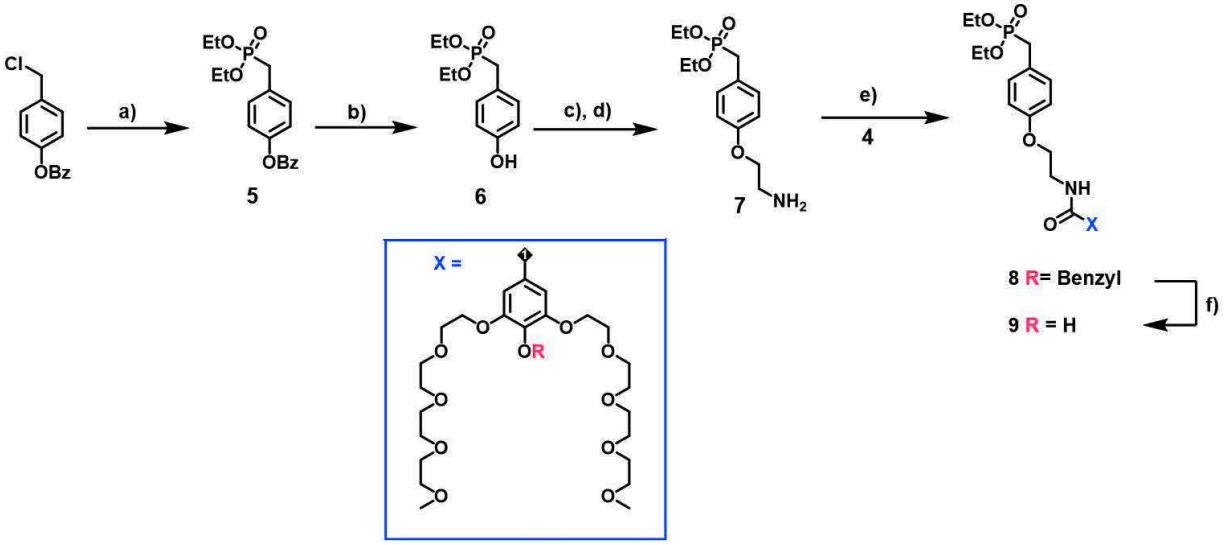

*Figure 4: Synthése du mono–ethylphosphonate **9** : a) $P(OEt)_3$, 160°C, 3h, 92%; b) Pd/C 10%, H_2, EtOH, Ta, 16h, 92%; c) Boc–2–bromo–ethylamine, K_2CO_3, KI, acetone, reflux, 16h, 75%; d) TFA, CH_2Cl_2, 0°C à Ta, 16h, 94%; e) **4**, BOP, DIPEA, CH_2Cl_2, Ta, 24h, 70%; f) Pd/C 10%, H_2, EtOH, rt, 16h, 85%.*

présence de Boc-2-bromo-éthylamine. Un traitement ultérieur avec de l'acide trifluoracétique (TFA) permet d'obtenir le composé **7** (94%).Celui-ci subit une réaction de couplage peptidique avec l'acide carboxylique **4** en présence de (benzotriazol-1-yloxy) tris (diméthylamino) -phosphonium (BOP) et de N, N - diisopropyléthylamine (DIPEA) pour obtenir le composé benzylé **8** (70%). Enfin, l'hydrogénolyse de **8** en présence de Pd / C a conduit au phosphonate d'éthyle **9** correspondant, avec un rendement de 85%.

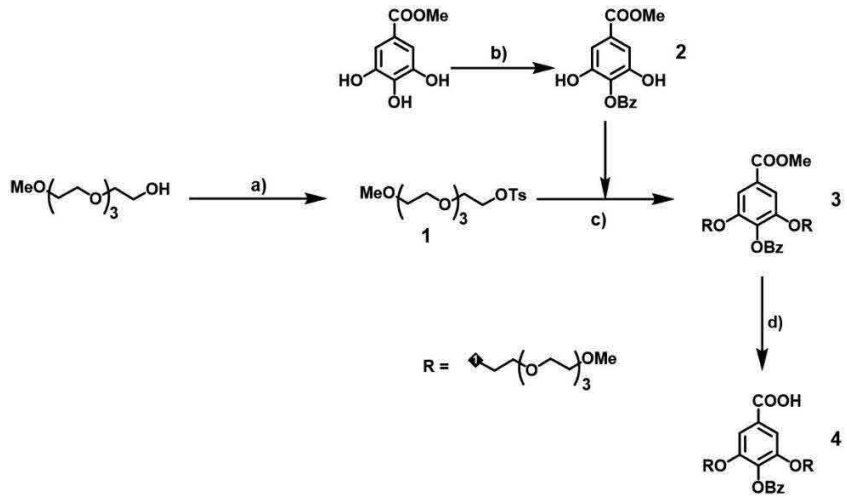

*Figure 5: Synthése du para–Benzyl (meta–tetraethyleneglycol monomethyl ether) methyl gallate **4**: a) TsCl, NaOH, THF/H_2O, T_a, 24h, 94%; b) Bromo Benzyl, $KHCO_3$, KI, DMF, 30°C, 72h, 70%; c) K_2CO_3, KI, Acetone, reflux, 24h, 75%; d) NaOH, $MeOH/H_2O$, reflux, 2h, 90%.*

Afin de parvenir à la synthèse de l'acide phosphonique **12** portant une chaîne oligoéthylèneglycol fonctionnalisé en position para, la première étape est la synthèse de l'intermédiaire commun **10** (**Figure 6**), qui a été obtenu avec un bon rendement à partir de l'hydroxy-dPEGs®8-tert-butyle commercial. **10** a ensuite subi une réaction de Williamson avec l'éthylphosphonate **9** dans l'acétone à 60 ° C en présence de K_2CO_3 et KI pour donner le précurseur correspondant, l'éthyl phosphonate **11**, avec un rendement de 85%. Le traitement de **11** avec un fort excès de TMSBr a permis d'obtenir le composé **12** avec un rendement de 90%.

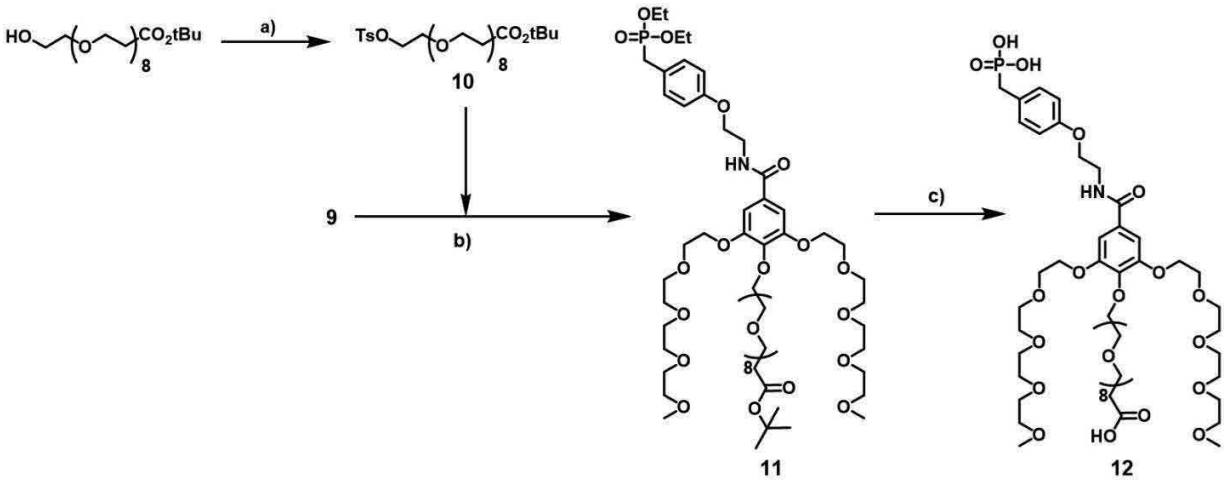

*Figure 6: Synthèse du dendron acid mono–phosphonic COOH–fonctionalisé **12** : a) TsCl, NEt_3, CH_2Cl_2, Ta, 24h, 85%; b) K_2CO_3, KI, Acetone, reflux, 16h, 70%; c) TMSBr, CH_2Cl_2, rt, 16h, 90%.*

Synthèse du dendron D2-2P

La synthèse de la structure complexe de D2-2P est divisée en deux parties, comme celle du dendron précédent (D2). D2-2P a été synthétisé par un procédé convergent, en couplant le segment de couplage que l'on appelle « Nord », le composé **18**, avec le segment « Sud », le composé **4**. La synthèse de la pince bis-éthylphosphonate **18** est détaillée sur la **Figure 7**.

Son précurseur, l'acide 5-hydroxyisophtalique, a été convertie en 5-Diméthyl hydroxyisophtalate correspondant, **13**, en utilisant une quantité catalytique de H_2SO_4 dans du méthanol à reflux, avec un rendement quantitatif (plus de 98%). La réduction du diester **13** par un excès de $LiAlH_4$ dans du THF à température ambiante, a fourni le triol **14**. Toutefois, le rendement de cette réaction a été jugée peu reproductible (50-95%). Ceci

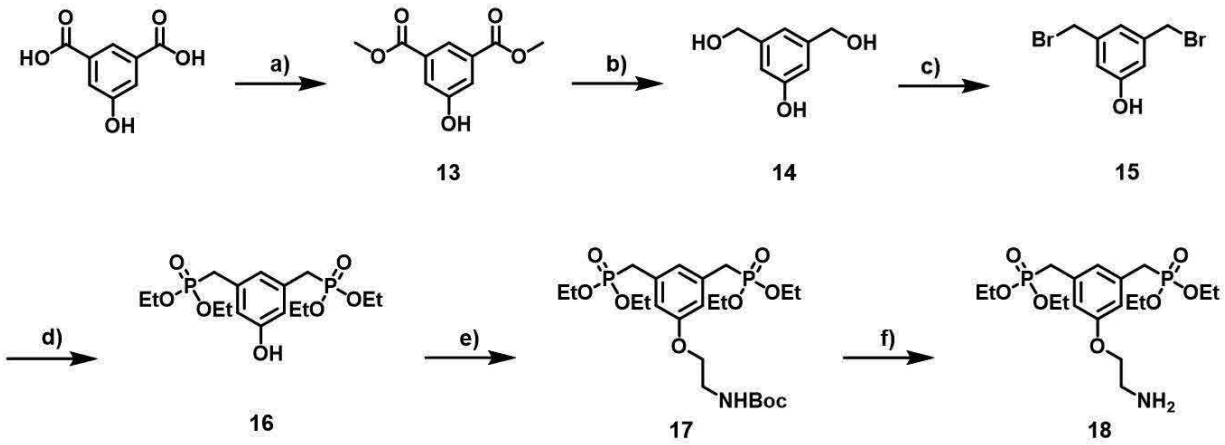

*Figure 7: Synthèse de l'ancrage bis–ethylphosphonate **18** : a) MeOH, H_2SO_4, reflux, 4h, quant.; b) $LiAlH_4$, THF, Ta, 3h, 50 – 95%; c) HBr 30%, Acid Acetic, Ta, 24h, 96%; d) $P(OEt)_3$, reflux, 2h, 95%; e) Boc–2–bromo–ethylamine, K_2CO_3, KI, Acetone, reflux, 16h, 53 – 70% ; f) TFA, DCM, Ta, 24h, 88%.*

est principalement associé à la faible solubilité du composé **14** dans les solvants organiques usuels et à sa tendance à coller aux sels d'aluminium résultant de l'oxydation de $LiAlH_4$.

Les alcools primaires du composé **14** sont soumis à une substitution nucléophile en présence de HBr pour donner **15** avec un rendement de 96%. La conversion du brome à l'aide du phosphonate de triéthyle à reflux a donné le composé **16** avec un rendement de 95%.

Un couplage de Williamson a été réalisé entre **16** et un fort excès de Boc-2-bromo-éthylamine, en présence de K_2CO_3 et KI, pour obtenir le composé **17** avec 70% de rendement, au maximum. L'éthérification a été suivie par la déprotection de l'amine à l'aide de TFA, ce qui donne **18** avec un rendement de 88%.

Le composé **21** a été obtenu par couplage peptidique de l'amine **18** avec l'acide carboxylique **4**, en présence de BOP et de DIPEA sous atmosphère d'argon, avec 66% rendement (**Figure 8**). Après hydrogénolyse du groupe benzyle, le composé **22** est obtenu avec un rendement de 83%.

Le phénol **22** a ensuite subi un couplage de Williamson avec TsO-dPEGs®8-*tert*-butyl dans l'acétone à 60 ° C en présence de K_2CO_3 pour donner le phosphonate de bis-éthyl correspondant **23** avec 70%. Le traitement de **23** avec un fort excès de TMSBr a généré les fonctions acides phosphonique au point d'ancrage et converti le groupe ester de *tert*-

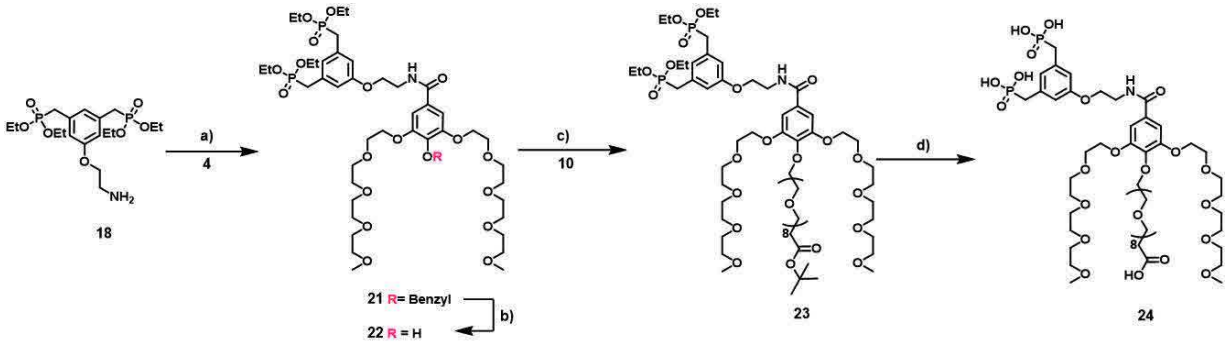

*Figure 8: Synthèse du D2-2P **24** : a) BOP, DIPEA, CH_2Cl_2, Ta, 24 h, 66%; b) Pd/C 10%, H_2, EtOH, Ta, 6h, 83%; c) K_2CO_3, Acetone, 60°C, 24h, 70%; d) TMSB, DCM, Ta, 10h, 93%.*

butyl terminal en acide carboxylique correspondant. Cette étape a permis d'obtenir le composé **24** avec 93% de rendement sous forme d'huile jaunâtre.

Synthèse du dendron D1

Un autre concept de dendron de petite taille a été basé sur une petite structure poly (amido)amine. Précisément, le monomère alcyne **25** a subi une déprotection des deux esters méthyliques par le triméthylsilanolate de sodium (TMSONa), ce qui donne **26** sous forme de solide jaune avec un rendement quantitatif (**Figure 9**). Disponibles dans le commerce, les chaînes PEG amine ont été introduites au sein du monomère **26** par une réaction de couplage peptidique, en présence de 1- éthyl- 3- (3- diméthylaminopropyl) carbodiimide (EDCI), hydroxybenzotriazole (HOBt) et de N, N - diisopropyléthylamine (DIPEA). Le composé acétylénique **27** a été obtenu avec 67% de rendement sous forme d'huile jaunâtre.

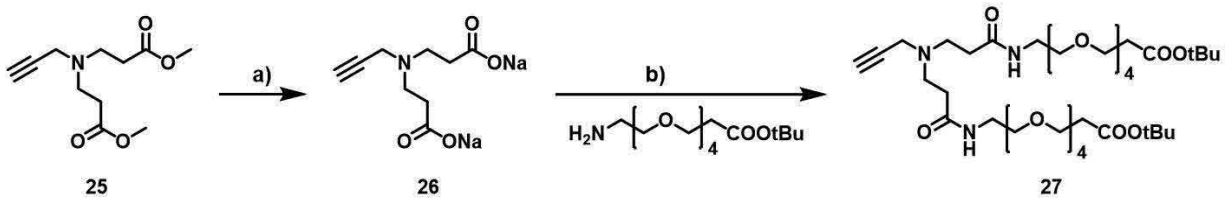

*Figure 9: Synthèse du composé **27** : a) TMSONa 1M, CH_2Cl_2, Ta, 16 h, quant.; b) EDCI, HOBt, DIPEA, CH_3CN, Ta, 16 h, 67%.*

En parallèle, le précurseur azoture bis-éthylphosphonate **32** a été synthétisé en cinq étapes avec un rendement global de 18%, comme décrit sur la **Figure 10**. Disponible dans le commerce, le 3,5- diméthylbenzoate de méthyle a été soumis à une bromation

benzylique en utilisant le N-bromosuccinimide (NBS) et le peroxyde de benzoyle, ce qui a donné le composé **28** avec un rendement de 72%.

Le composé **28** a ensuite été réduit en utilisant l'hydrure de diisobutylaluminium (DIBAL)

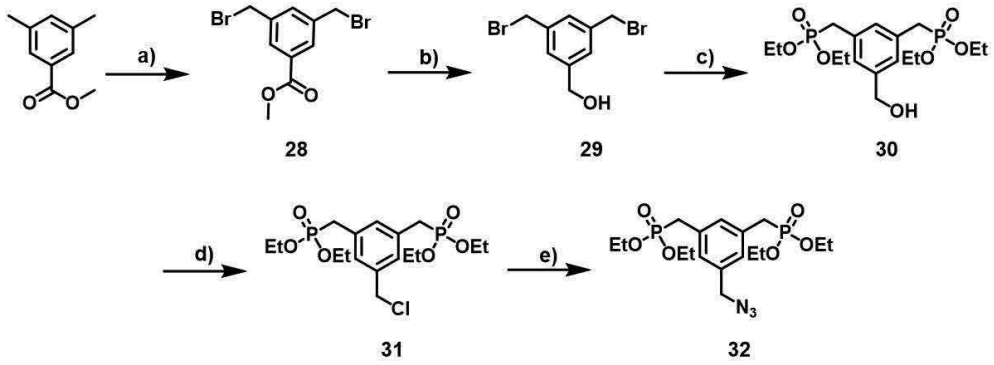

Figure 10: Synthèse du précurseur azoture Bis–phosphonate ***32*** *: a) NBS, Benzoyl peroxide, CCl_4, Ta, 3h, 72%; b) DIBAl, Toluene, 0°C, 3h, 92%; c) $P(OEt)_3$, 160°C, 2h, 88%; d) $SOCl_2$, $CHCl_3$, reflux, 1h, 40–60%; e) NaN_3, CH_3CN, reflux, 16h, 50 – 70%.*

pour former le dibromoéthyle alcool correspondant **29** avec un rendement de 92%. **29** subit une réaction d'Arbuzov en présence de triéthylphosphite pour obtenir le composé **30** sous forme d'huile transparente. Ensuite l'alcool **30** a été converti en chlorure **31** correspondant, en présence de chlorure de thionyle. Le composé **32** a été obtenu suite à la substitution nucléophile du chlore par l'azoture de sodium avec un rendement de 45% sous forme d'une huile incolore.

La cycloaddition 1,3-dipolaire Huisgen, catalysée par le cuivre a été réalisée entre l'azoture **32** et l'alcyne **27**, donnant le triazole **33**, 1,4-disubstitué, avec 75% rendement (**Figure 11**). La réaction dite «clic», a été réalisée en utilisant un sel de Cu (II) en présence

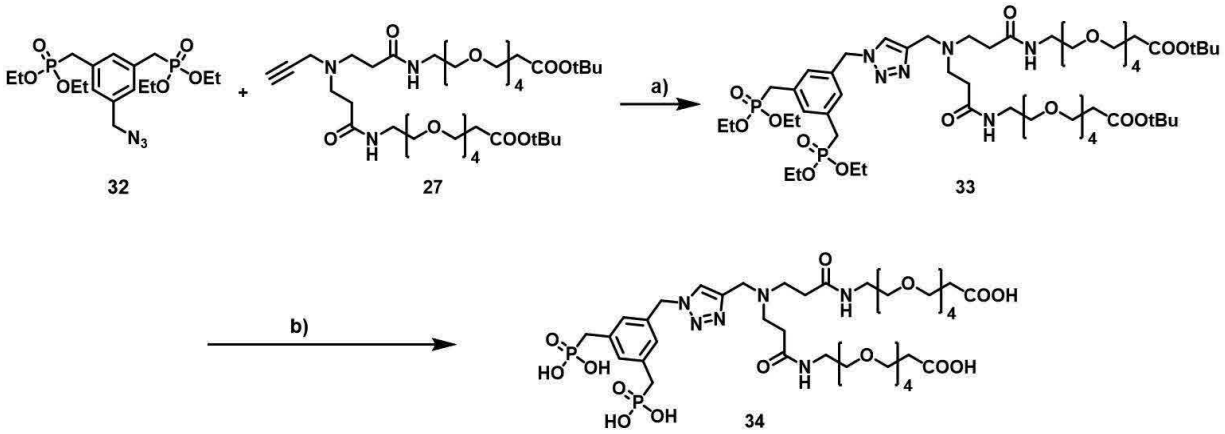

Figure 11: Synthèse du D1 ***34*** *: a) $CuSO_4 \cdot 5H_2O$, L–ascorbate, THF, H_2O, ACN, Ta, 16h, 75%; b) TMSBr, Ta, 4h, 66%.*

d'ascorbate de sodium dans un mélange de solvants : tétrahydrofurane (THF), eau et acétonitrile (ACN).

La déprotection finale du bis-ethylphosphonate a été réalisée en présence de TMSBr, qui a permis la déprotection simultanée des esters de *tert*-butyl ainsi que des phosphonates d'éthyle, donnant **34** sous forme d'huile incolore avec un rendement de 66%.

Après une étape de purification par chromatographie à exclusion de taille, LH-20, les dendrons ont été caractérisés par RMN ^{1}H, ^{31}P et ^{13}C, spectrométrie de masse et par Spectroscopie Infrarouge à transformée de Fourier.

La synthèse des nanomatériaux

Des nanoparticules sphériques d'oxyde de fer de 10nm de diamètre ont été synthétisées par décomposition thermique en présence d'acide oléique dans le diocthyl éther à reflux. En variant le gradient de température ainsi que le temps des étapes de décomposition, germination et croissance, les nanoparticules synthétisées sont obtenues avec une forme sphérique de 10nm en diamètre (Figure 12: Images TEM de NS10 @ AO à 20 nm zoom (à gauche) et à haute résolution (au milieu); DLS et distribution de taille au TEM de NPs 10 @ OA (à droite).**Figure 12**).

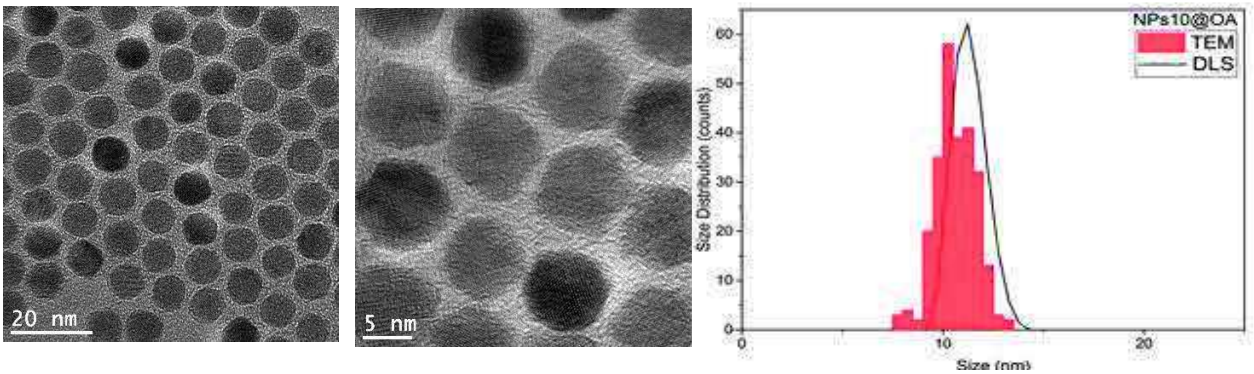

Figure 12: Images TEM de NS10 @ AO à 20 nm zoom (à gauche) et à haute résolution (au milieu); DLS et distribution de taille au TEM de NPs 10 @ OA (à droite).

Le greffage des différentes molécules dendritiques (D2, D2-2P et D1) par un protocole d'échange direct de ligands en milieu organique s'en suit.

Les propriétés physiques des nanoparticules dendronisées ont été caractérisées par différentes méthodes: Diffusion dynamique de la lumière (DLS), potentiel zêta, Spectroscopie Infrarouge à transformée de Fourier (FTIR), microscopie électronique en

transmission (TEM), Magnétométrie (SQUID) et spectrométrie de masse de type rotation à l'angle magique (HR-MAS). Les trois nanomatériaux, NPs10 revêtues des dendrons D2, D2-2P ou D1, présentent une distribution en taille monodisperse.

Les images TEM (**Figure 13** (en haut)), montrent une distribution en diamètre de 10 ± 0.9nm. La **Figure 13** (en bas) représente la distribution en diamètre hydrodynamique par mesure DLS (16 ± 2nm) (gauche) ainsi que les potentiels Zêta (droite) obtenus pour les 3 types de nano-matériaux.

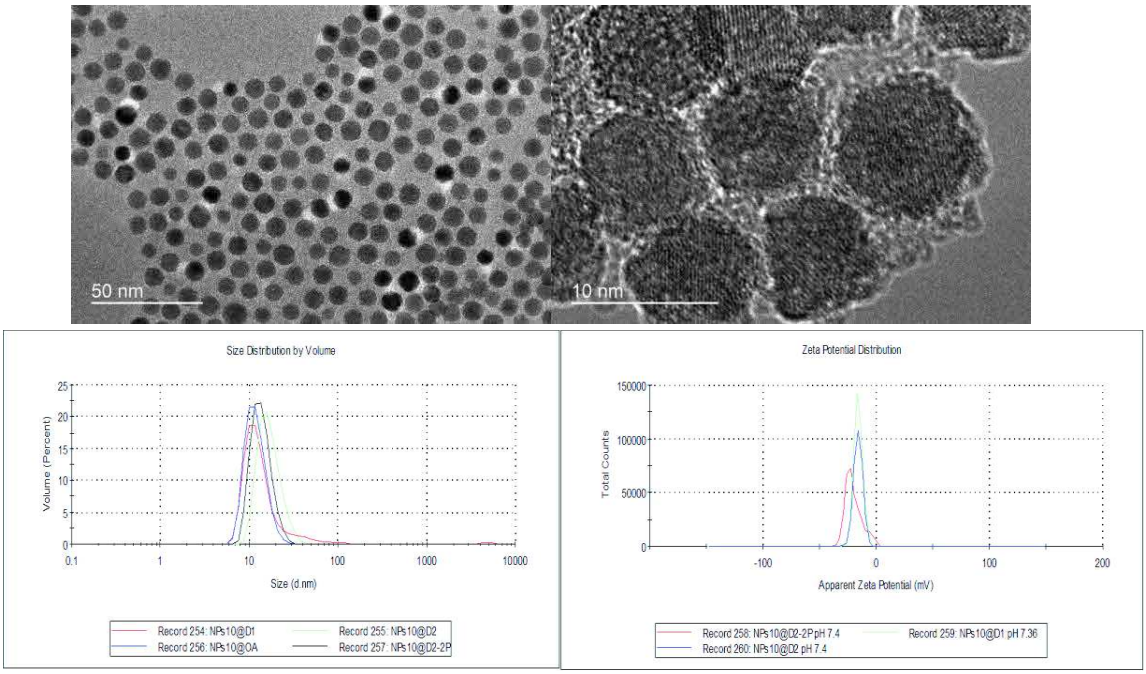

Figure 13: (haut) Images TEM des NPs10@D2 à différentes échelles (50 et 10nm); (bas) Distribution en diamètre hydrodynamique ainsi que le potentiel Zeta des NPs10@D2/D2-2P et D1 au pH = 7.4.

Les mesures SQUID montrent un comportement superparamagnétique pour tous les hybrides dendronisés. Le potentiel Zêta obtenu met en relief une densité de charge proche pour tous les nanohybrides, même si le nombre de groupements acide carboxylique à la périphérie est différent entre D2, D2-2P et D1. Par conséquent, les études HR-MAS sont très importantes pour comprendre la composition de la coque organique et pour déterminer le taux de greffage des dendrons à la surface des nanoparticules. En effet, la corrélation entre le taux de greffage et la structure du dendron permettra de mieux comprendre l'influence du groupe d'ancrage (acide mono-phosphonique par rapport à une pince bi-phosphonique) sur l'efficacité du greffage.

Analyses *in vitro* et *in vivo*

La biocompatibilité *in vitro* a été déterminée sur des modèles 2D de culture cellulaires, en évaluant la biodisponibilité de nanoparticules dendronisées vers quatre types cellulaires différents: i) Lignée de cellules souches hépatiques humaines (HepaRG), ii) Lignée cellulaire de carcinomes cellulaires dérivés d'hépatocytes (HuH7-luc), iii) Cellules épithéliales basales alvéolaires humaines adénocarcinomiques (A549-luc) et iv) Lignée cellulaire de neuroblastome humain (Kelly). La cytotoxicité a été établie par le test MTT[3] et le test de libération LDH[4].

La viabilité cellulaire a été déterminée par un essai colorimétrique MTT développé par Mosmann pour des mesures de cytotoxicité *in vitro* et de prolifération cellulaire. Il a été rapporté que l'enzyme mitochondriale succinate-déshydrogénase dans les cellules viables est capable de cliver le sel MTT en le transformant en Formazan, un produit de couleur bleue. La quantité de Formazan produite, lue sur le spectrophotomètre multi - puits à balayage, est proportionnelle au nombre de cellules viables présentes, examinant ainsi le pourcentage de cellules mortes causé par des facteurs externes, dans notre cas - IONP dendronisé.

L'analyse LDH complémentaire, quantifie l'enzyme Lactate déshydrogénase, qui est une enzyme cytoplasmique soluble et présente dans presque toutes les cellules. Elle est libérée dans l'espace extracellulaire lorsque la membrane plasmique est endommagée. La LDH réduit le chlorure d'INT (chlorure de 2- (4-iodophényl) -3- (4-nitrophényl) -5-phényl tétrazolium) en présence de NADH + H^+ (adénine dinucléotide β-nicotinamide réduit) donnant un Formazan hydrosoluble rouge, quantifié par mesure d'absorption de lumière. La membrane plasmique endommagée amorce une réponse inflammatoire dans les tissus environnants, empêchant ainsi les phagocytes d'éliminer les cellules mortes. La perte de l'intégrité de la membrane cellulaire est une signature clé de la nécrose.

La demi-vie dans le sang *in vivo* des IONP varie en fonction de la taille des particules et des propriétés de surface, de 2 heures pour les particules de Ferumoxyde

[3] MTTMTT-3- (4,5-diméthylthiazol-2-yl) -2,5-diphényl-tétrazolium ou le bromure de thiazolyl bleu de tétrazolium.
[4] LDH - lactate déshydrogénase.

revêtues de Dextran 120-180 nm (Endorem®, Feridex®) à 24-36 heures pour le Dextran-enrobées de 15 à 30 nm de particules de Ferumoxtran (Sinerem®, Combidex®). Dans une étude récente, on a trouvé que la demi-vie des IONP revêtus d'amidon et ceux avec des revêtements de PEG de 5 et 2 kDa étaient respectivement de 0,12, 7,3 et 11,8 h chez des rats mâles. Pour imiter le potentiel temps de contact *in vivo*, les effets de biocompatibilité / toxicité ont été étudiés pendant des périodes de 24 ou 48 h d'incubation, à 37 ° C, avec 5% de CO_2. Les cellules ont été étalées dans des plaques à fond plat de 96 puits à une densité de départ de 104 cellules par puits. Après un temps d'équilibrage (12 à 24h pour A549-luc, Huh7-luc et Kelly et 7 jours pour HepaRG), jusqu'à ce qu'ils atteignent 70 à 80% de confluence, le milieu de culture est éliminé et les cellules sont traitées en triple avec des concentrations croissantes 0,82, 2,05, 5,12, 12,8, 32, 80, 200 et 500 µg / mL) de NPs10@D2 et de NPs10@D2-2P en suspension dans des milieux de culture.

Test MTT

En bref, l'essai MTT a été réalisé en incubant les cellules avec une solution de 2 mg/mL de MTT (50 µL) pendant 3 heures. On a ensuite aspiré le surnageant et on a appliqué aux cellules 150 µL de diméthylsulfoxyde (DMSO) pour solubiliser les cristaux de Formazan formés. Les plaques ont été agitées et ensuite 100 µL du surnageant ont été recueillis et transférés dans une plaque de 96 puits à fond plat propre. La densité optique a été mesurée à 570 nm et une longueur d'onde de référence à 630 nm a été utilisée. La viabilité de la viabilité cellulaire a été calculée comme le rapport de l'absorbance moyenne des lectures en triple des puits d'échantillon (A_{sample}) par rapport à l'absorbance moyenne des puits de contrôle ($A_{control}$). A chaque expérience, le DMSO a été utilisé comme témoin négatif, A_{DMSO}, comme indiqué dans l'équation :

$$Viabilité\ cellulaire\ \% = \frac{A_{sample} - A_{DMSO}}{A_{control} - A_{DMSO}}$$

L'analyse de cytotoxicité par MTT de cellules transfectées avec NPs10@D2 a démontré à la fois un temps d'incubation et une perte de cellules dépendant de la concentration (**Figure 14**). L'effet toxique a été pris en considération lorsque le taux de survie était inférieur à 80%.

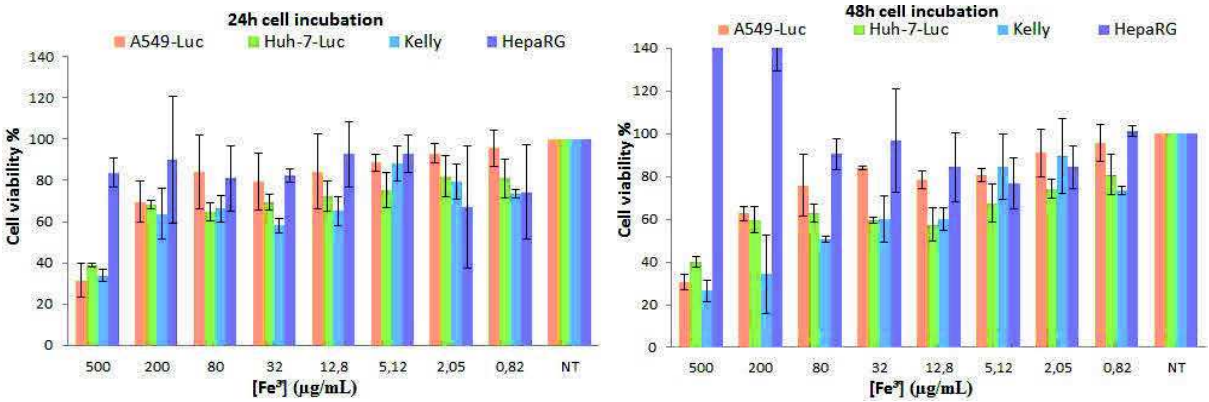

Figure 14: La viabilité des cellules MTT transfectées avec NPs10@D2 après 24 (gauche) et 48h (droite) d'incubation

Après 24h d'incubation avec NPs10@D2, la viabilité de toutes les cellules cancéreuses (A549-luc, Huh7-luc et Kelly) a changé de 100% à environ 60% avec des concentrations de Fe^{3+} augmentant de 0,8 à 200 µg/mL. À des doses élevées de Fe^{3+}, 500 µg/mL, la viabilité cellulaire diminue jusqu'à 40%. Après 48 heures d'incubation, le taux de survie des cellules suivait pratiquement la même tendance. D'autre part, les cellules souches hépatiques humaines HepaRG présentent une très faible toxicité (à 24h d'incubation) ou un effet de prolifération au cours du temps (à 48h d'incubation) aux concentrations appliquées les plus élevées (c'est-à-dire 500 et 200 µg/ml).

L'essai de toxicité MTT de NPs10@D2-2P démontre un taux de survie modéré à bon après 24h d'incubation pour toutes les lignées cellulaires cancéreuses et à des concentrations de Fe^{3+} allant jusqu'à 200 µg/mL (**Figure 15**). Après 48 h d'incubation, les cellules A549-luc présentent un taux de prolifération élevé même à faible concentration et une viabilité cellulaire supérieure à 500 µg / mL. Au contraire, Huh7-luc montre une baisse du taux de survie cellulaire à 30% à 500 µg / ml.

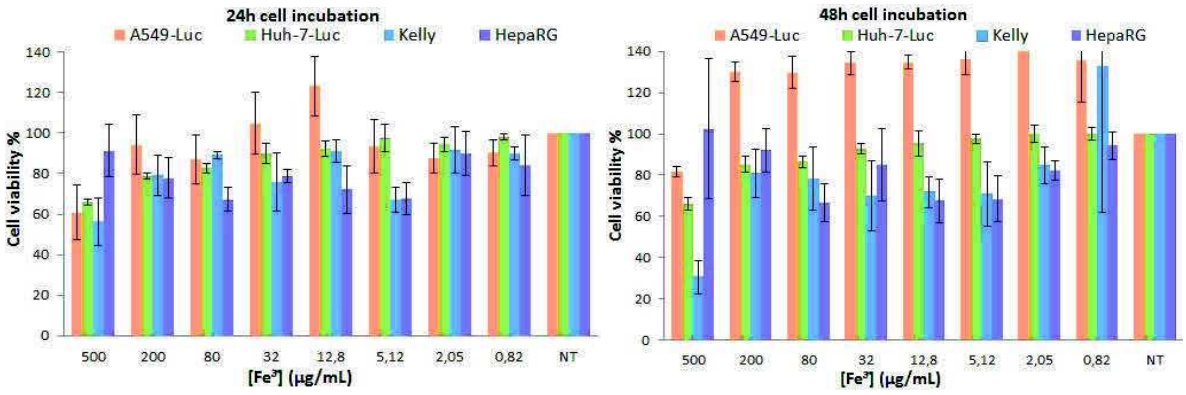

Figure 15: La viabilité des cellules MTT transfectées avec NPs10 @ D2-2P après 24 et 48h d'incubation.

A partir des résultats du MTT, on constate que les IONP revêtues de dendrons D2 et D2-2P présentent un effet toxique ou de prolifération modéré à la concentration appliquée la plus élevée (c'est-à-dire 500 mg/L). La toxicité des IONP dendronisées peut être liée à leur capacité à endommager l'ADN par l'oxydation de la magnétite comme précédemment montré par Karlsson *et al*. sur des lignées cellulaires cultivées.[5]

De plus, d'autres facteurs comme la présence d'acide oléique (OA) sur la surface des NP dendronisés pourraient être responsables de réactions toxiques cellulaires. En effet, Delgad *et al.* ont récemment signalé une influence de l'OA sur les lignées cellulaires normales et cancéreuses. Leurs résultats ont démontré que l'OA seule favorise l'apoptose sur différentes lignées cellulaires, même si les cellules normales étaient censées être moins sensibles à l'OA que les cellules cancéreuses.[6] Comme indiqué par les profils HR-MAS de NPs10@D2-2P, OA est toujours présent à la surface des NPs dendronisées. Ce résultat évalue l'idée de cytotoxicité induite par l'existence d'OA dans la composition de NPs10@Dendron.

De plus, pour des concentrations élevées de NPs10@D2-2P, on peut remarquer une promotion de la prolifération cellulaire (**Figure 15**). Cette croissance cellulaire pourrait être due à la capacité des IONPs de diminuer l'H_2O_2 intracellulaire, qui joue un rôle pivot dans le contrôle de la prolifération et la mort cellulaire.[7]

Test de libération LDH

La libération de LDH dans les cellules HepaRG a été déterminée en utilisant le CytoTox-ONE ™ Homogeneous Membrane Integrity Assay de Promega. A la fin du temps d'incubation des cellules (24h ou 48h) avec différentes concentrations de NPs10@D2 et NPs10 @ D2-2P, on a ajouté 100 µL de solution de réactif CytoTox-ONE supportée par le kit de test, et on a incubé les cellules pendant 10 min à 25 ° C dans l'obscurité. De plus, des puits en triple ont été mis en place afin de déterminer le contrôle de libération de LDH maximum en ajoutant 2 µl de solution de lyse aux puits témoins positifs avant l'addition

---

[5] Karlsson, H. L., Cronholm, P., Gustafsson, J., Möller, L. Copper oxide nanoparticles are highly toxic: A comparison between metal oxide nanoparticles and carbon nanotubes. *Chem. Res. Toxicol.* 21, 1726–1732 (**2008**).

[6] Delgado, Y. et al. The cytotoxicity of BAMLET complexes is due to oleic acid and independent of the α-lactalbumin component. *FEBS Open Bio* 5, 397–404 (**2015**)

[7] Huang, D. M. et al. The promotion of human mesenchymal stem cell proliferation by superparamagnetic iron oxide nanoparticles. *Biomaterials* 30, 3645–3651 (**2009**).

du réactif CytoTox-ONE. Ensuite, on ajoute 50 µL de solution d'arrêt à chaque puits et on agite les plaques pendant 30 secondes à 25 °C. Les cellules ont été lues sous un spectrofluoromètre en microplaque ayant une longueur d'onde d'excitation de 560 nm et une longueur d'onde d'émission de 590 nm.

La cytotoxicité a été calculée selon l'équation suivante : où F_{exp} = fluorescence mesurée des cellules avec la solution d'essai; $F_{control}$ = fluorescence des cellules témoins et Max_{LDH} = fluorescence des cellules lysées.

$$\% \, Cytotoxicité = \frac{F_{exp} - F_{control}}{Max_{LDH} - F_{control}} \times 100\%$$

L'intégrité de la membrane cellulaire a été déterminée par la quantification de LDH à partir des cellules incubées avec NPs10@D2 et NPs10@D2-2P (**Figure 16**). Pour la période d'incubation plus courte (24h), HepaRG a démontré une faible cytotoxicité (inférieure à 10%) pour toute la gamme de concentrations et pour les deux IONP dendronisés. Sinon, à 24h d'incubation pour les concentrations les plus élevées (supérieures à 80µg / mL), on peut remarquer une cytotoxicité négative, ce qui n'est pas une erreur de calcul, au contraire, due à la formation de chelates de fer qui aident la prolifération cellulaire.

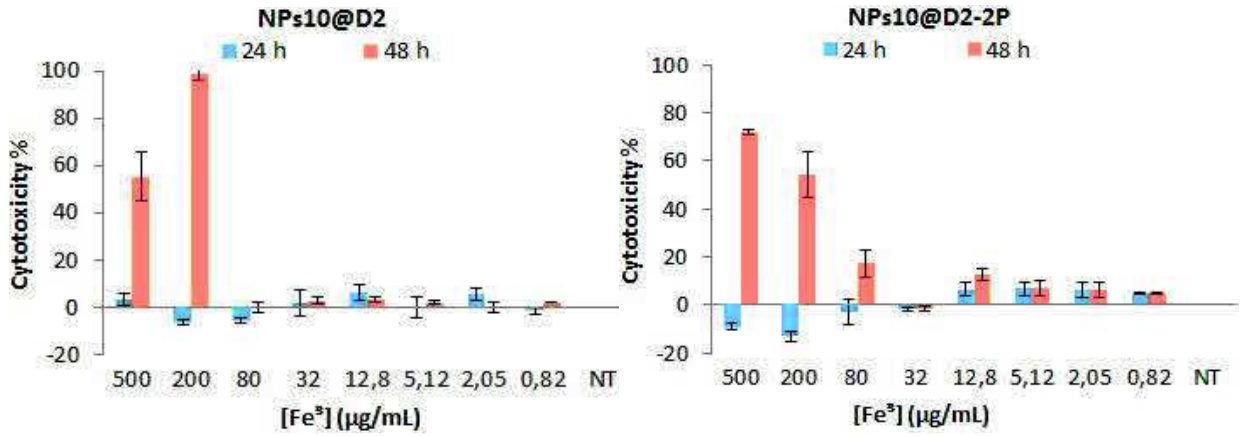

Figure 16: Pourcentage de perméabilisation de la membrane plasmique des HepaRG envers les nanoparticules dendronisées après 24 et 48h d'incubation.

Après 48h d'incubation, la tendance était complètement différente, une augmentation significative (plus de 60%) des libérations de LDH a été observée pour les concentrations de Fe^{3+} et 200 µg/mL, les deux nanoparticules dendronisées présentant une faible cytotoxicité pour des concentrations de fer allant jusqu'à 80 µg/mL.

En ce qui concerne ces tests de libération de la LDH, il est important de souligner qu'un tel test mesure le signal fluorescent des cellules endommagées par les membranes, et non celles saines. Par conséquent, même si le nombre de cellules augmente à mesure que le temps d'incubation augmente, un processus de prolifération naturel se met en place, ainsi le test de liération de LDH ne compte pas la viabilité des cellules saines. Il ne détecte que la LDH accumulée dérivée de la fuite continue des cellules endommagées, ce nombre étant proportionnel au temps. De plus, à 48h d'incubation une mort cellulaire programmée, médiée par un programme intracellulaire.[8] De plus, la nature réelle de la morphologie de la membrane cellulaire change au cours du contact avec les nanostructures, qui peut être accrédité à l'endocytose ainsi que possible rupture de la membrane par l'effet mécanique potentiel et d'autres nano-activités.[9]

Étude de l'absorption cellulaire par cytométrie en flux

Pour étudier l'absorption cellulaire de NPs10@D2_Alexa495 et NPs10@D2-2P _ Alexa495 avec différentes concentrations de Fe^{3+}, l'analyse des échantillons de cellules a été réalisée en utilisant le cytomètre de flux FACScan et le logiciel Novios. En bref, les cellules A549-luc, Huh7-luc et Kelly, à une densité de 2×10^5 cellules par puits, ont été ensemencées dans des plaques à 24 puits et incubées à 37 ° C pendant une nuit. Après le temps d'équilibrage, à 70-80% de confluence, les milieux de culture ont été éliminés et les cellules ont été traitées par triplicat avec 1 mL de NPs10@D2_Alexa495 à 1 et 10 µg/ml de Fe^{3+}, ou 1 mL de NPs10@D2-2P_Alexa495 à 10 et 50 µg/mL de Fe^{3+} en suspension dans un milieu de culture. Les cellules ont été incubées pendant 4 heures à 4 °C, 4 h à 37 °C et pendant 24 h à 37 °C. Des cellules traitées avec un seul milieu ont été utilisées comme témoins. A la fin de la période d'incubation, les cellules ont été lavées trois fois avec du PBS, pour éliminer les NP non internalisés ou des différents artefacts, qui n'ont pas été absorbés par les cellules. Aune fois lavée, les cellules sont fixées dans une solution de Paraformaldehyde à 2% et stockées au réfrigérateur pendant une nuit. Dans toutes les analyses FACS, les débris cellulaires et les particules libres ont été exclus en plaçant une grille sur le diagramme de la lumière diffusée latéralement (SSC) contre

[8] Green, D. R. The Grand Finale. *Cell* 144, 463–464 (**2011**).
[9] Kroll, A., Pillukat, M. H., Hahn, D. & Schnekenburger, J. Current in vitro methods in nanoparticle risk assessment: Limitations and challenges. *Eur. J. Pharm. Biopharm*. 72, 370–377 (**2009**).

la lumière diffusée vers l'avant (FSC). Les paramètres d'acquisition ont été optimisés pour la détection du fluorophore Alexa495, l'excitation à 488 nm avec un laser à l'argon et la détection au-dessus de 505 nm. Un total de 10 000 cellules ont été analysées pour tous les types de cellules. L'augmentation de la fluorescence dans les cellules traitées avec des NP dendronisées par rapport à celles des cellules témoins non traitées a été exprimée comme une augmentation moyenne de la fluorescence par rapport au témoin.

On a quantifié les captures cellulaires de NPs10 @ D2_Alexa495 et NPs10 @ D2-2P_Alexa495 par trois lignées de cellules cancéreuses (Kelly, Huh7-luc et A549-luc) à des périodes et à des températures variables, et les résultats sont représentés sur la **Figure 17**.

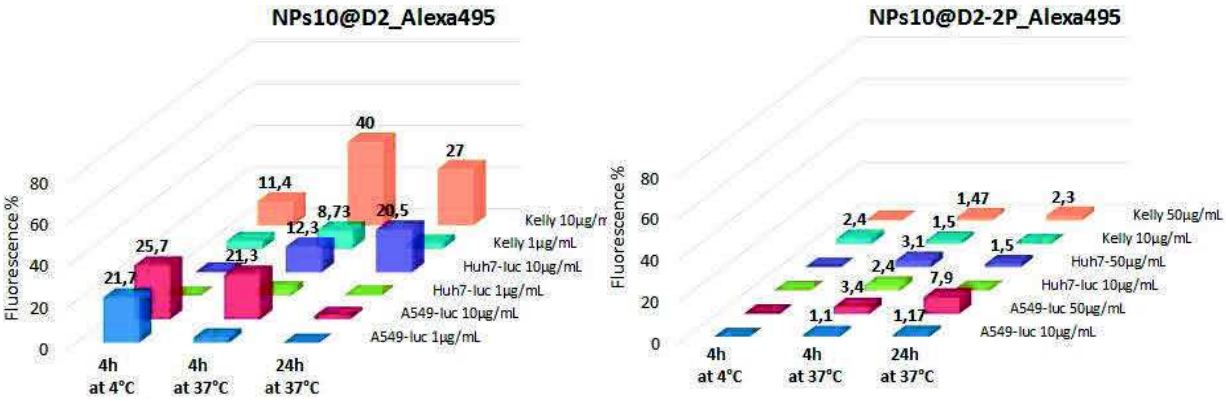

Figure 17: Analyse cytométrique de flux de cellules A549-luc, Huh7-luc et Kelly, incubées à différentes températures et à différentes températures, avec des doses différentes de NPs10 @ D2 marquées avec Alexa495 (à gauche) et NPs10 @ D2-2P (à droite).

Etudes *in vivo*

Les souris IRM (n = 3) ont été anesthésiées avec de l'isoflurane par inhalation. Les expériences ont été effectuées sur un système d'imagerie Biospec de Bruker de 300 MHz (7T). L'agent de contraste a été injecté par voie intraveineuse à une dose de 45 µmol [Fe^{3+}]/kg de poids corporel. L'intensité du signal (SI) a été mesurée dans les régions d'intérêt (ROI) dessinées sur le foie et la vessie, et dans une région située hors de l'image de l'animal, représentant l'écart-type de bruit (bruit SD). L'augmentation du SI (Δ SNR%) a été calculée selon l'équation suivante, où SI_{post} = post-contraste SI, et SI_{pre} = pré-contraste SI.

$$\Delta\, SNR\ \% = \frac{{SI_{post}}/{bruitSD} - {SI_{pre}}/{bruitSD}}{{SI_{pre}}/{bruitSD}} \times 100\%$$

Les études IRM *in vivo* ont été réalisées sur des souris NMRI. La **Figure 20** montre des images d'abdomen de spin-écho d'une souris vivante, acquise avant et après injection intraveineuse de la solution de nanoparticules à différents moments après iv. Nous avons constaté un fort contraste négatif dans le foie dans les images pondérées en T_2 – 90 min après injection intraveineuse (**Figure 20**) et une augmentation du contraste négatif dans les images axiales pondérées T_2 de la vessie sur 190min après iv (**Figure 18**). Le contraste négatif persistait plus de 10h dans le foie et pendant 6h dans la vessie, mais il s'est affaibli au fil du temps, ce qui suggère que les nanoparticules dendronisées sont sensibles aux excrétions rénales et hépatico-biliaires.

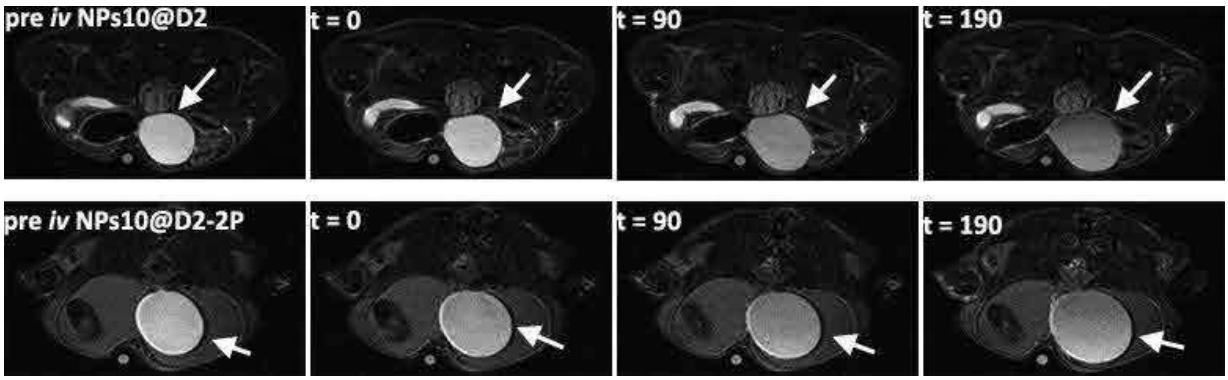

Figure 18: Images RM d'une souris vivante avec une séquence axiale pondérée en T2 (TR 7726, TE 52). Les images ont été acquises avant (pré-contraste) et 0, 90 et 190min après injection intraveineuse de 70µL de NPs10 @ D2 (haut) et NPs10 @ D2-2P (bas) à une concentration de 45µmol [Fe3 +] / kg de poids corporel.

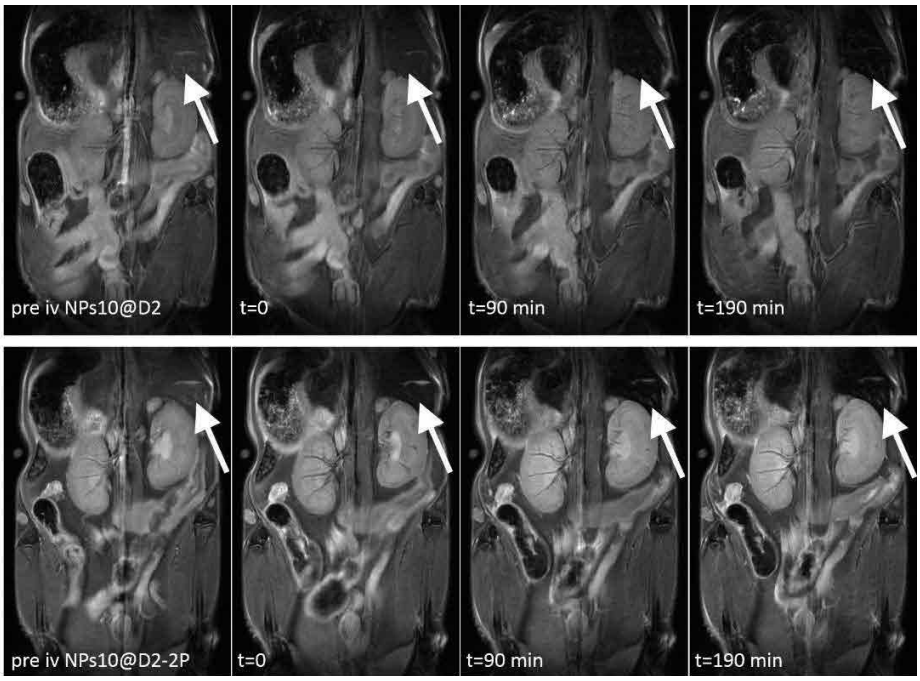

Figure 20: Images IRM in vivo d'une souris avec une séquence d'écho de spin pondérée en T_2 (TR 2000, TE 17). Les images ont été acquises avant (pré-contraste) et 0min, 90min et 190min après injection intraveineuse de 70µL de NPs10 @ D2 (en haut) et NPs10 @ D2-2P (en bas) à une concentration de 45µmol [Fe^{3+}] / kg.

Les valeurs de Δ SNR% mesurées sur l'imagerie rapide avec des images RARE du foie et de la vessie ont confirmé le contraste négatif produit par les nanoparticules dendronisées (**Figure 19**). L'intensité du signal chez les souris injectées avec NPs10@D2 a atteint un maximum à 140 minutes après l'injection pour le foie (55%) et 190 minutes après l'injection pour la vessie (33%) (**Figure 19.gauche**). Cependant, les souris injectées

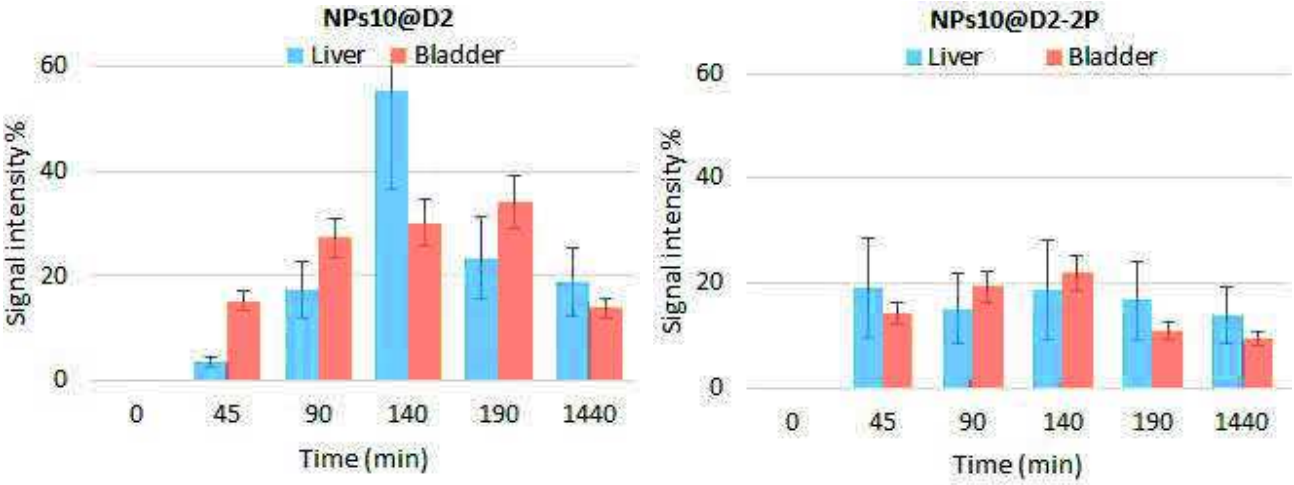

Figure 19: Δ SNR% calculé pour le foie et la vessie sur le temps après injection intraveineuse de (gauche) NPs10@D2 et (droite) NPs10@D2-2P.

avec NPs10@D2-2P ont montré un maximum de SI à 45 minutes après l'injection pour le foie et à 140 minutes après l'injection pour la vessie (**Figure 19.droite**). À 24 h après l'injection de NPs10 @ D2 ou NPs10 @ D2-2P, le contraste négatif du foie et de la vessie apparaît sous 20%, montrant une nette tendance à l'excrétion ou à la métabolisation des nanoparticules.

En outre, malgré la dose administrée (dose triple utilisée dans les essais cliniques chez l'homme, 15 µmoles [Fe^{3+}] / kg de poids corporel), toutes les souris ne présentaient pas de signes toxiques sur 48h, *e.g.* les souris ont montré une respiration régulière, des passerelles de bonne qualité, pas d'irritation des tissus environnants.

Conclusion

De nos jours, grâce à des applications biomédicales importantes, une attention considérable a été consacrée au développement de plates-formes dendritiques intelligentes en raison de leurs propriétés intrinsèques particulières. En effet, ces applications nécessitent l'élaboration de structures avec une architecture réglable et précise, avec une grande balance hydrophile – lipophile ainsi que de multiples fonctionnalités. En combinaison avec les nanoparticules magnétiques (NP), les dendrimères ont un fort potentiel dans les applications d'imagerie et de thérapie.

Les résultats obtenus dans ce travail constituent une base solide pour de futures études dans le développement de nano-conjugués présentant un fort contraste en IRM ainsi que pour le ciblage actif de tumeurs mélaniques (preuve de concept) ou plus généralement de l'hypoxie (phénomène impliqué dans la résistance tumorale au traitement de chimiothérapie).

Catalina BORDEIANU

Ingénierie d'architectures dendritiques pour la résolution de problématiques de Nanomédecine – biodistribution, toxicité, pharmacocinétique ou ciblage actif

Résumé

Le cancer est une cause majeure de décès dans le monde, 7,6 millions de décès en 2008. Bien que de nombreux progrès ont été réalisés dans le traitement du cancer, de nouvelles approches sont nécessaires afin de minimiser les effets secondaires délétères et d'augmenter le taux de survie. Par conséquent, l'avenir de la nanomédecine réside dans le développement de nano-plateformes multifonctionnelles.

Il ne fait aucun doute que les hybrides organique / inorganique à base de dendrons représentent des outils très avancés, capables de cibler spécifiquement et d'être suivis par imagerie en même temps.

Dans ce contexte, les objectifs de cette thèse sont non seulement la conception de nano-objets magnétiques dendronisés biocompatibles permettant à la fois le diagnostic par imagerie à résonance magnétique (IRM) ainsi que par imagerie optique (IO) mais également la validation in vitro et in vivo des propriétés de ces nano-objets et la démonstration de leur efficacité pour le ciblage spécifique de tumeurs.

Mots clés : Dendrimer/dendron, biodistribution, ciblage actif, nanoparticules d'oxyde de fer, nanoparticules dendronisées.

Résumé en anglais

Cancer is a worldwide leading cause of death, 7.6 million deaths in 2008 with 13% mortality. Although much progress has been made in early cancer diagnosis and treatment, new approaches are needed to minimize the deleterious side effects while increasing survival rate. Therefore, the future of Nanomedicine relies in the development of multifunctional nano-platforms that combine therapeutic components, multimodal imaging and active targeting.

Organic/inorganic dendrimer-based hybrids are very advanced tools, especially for targeting a specific cell type or a particular organ and for being followed by imaging techniques at the same time.

In this context, the objective of this thesis is not only the design of multifunctional magnetic dendronized nano-objects, but also their in vitro and in vivo validation and assessment of their active targeting effectiveness.

Key words: Dendrimer/dendrons, biodistribution, active targeting, iron oxide nanoparticles, dendronized nanoparticles.